LAPPEENRANTA
UNIVERSITY OF TECHNOLOGY

Pekka Rajamäki

FUSION WELD METAL SOLIDIFICATION: Continuum from weld interface to centerline

Thesis for the degree of Doctor of Science (Technology) to be presented with due permission for the public examination and criticism in the Auditorium 1383 at Lappeenranta University of Technology, Lappeenranta, Finland on the 7th of March, 2008, at noon

Acta Universitatis
Lappeenrantaensis
301

Supervisor	Professor Jukka Martikainen Department of Mechanical Engineering Lappeenranta University of Technology Finland
Reviewers	Professor Victor Karkhin St. Petersburg State Polytechnic University Russia
	Professor Risto A. J. Karppi The Technical Research Centre of Finland Finland
Opponents	Professor Carl Cross Bundesanstalt für Materialforschung und –prüfung Germany
	Professor Victor Karkhin St. Petersburg State Polytechnic University Russia

ISBN 978-952-214-536-9
ISBN 978-952-214-537-6 (PDF)
ISSN 1456-4491
Lappeenrannan teknillinen yliopisto
Digipaino 2008

ABSTRACT

Rajamäki Pekka

Fusion weld metal solidification:
Continuum from weld interface to centerline

Lappeenranta 2008
148 p
Acta Universitatis Lappeenrantaensis 301
Diss. Lappeenranta University of Technology
ISBN 978-952-214-536-9 ISBN 978-952-214-537-6 (PDF)
ISSN 1456-4491

We present a brief résumé of the history of solidification research and key factors affecting the solidification of fusion welds. There is a general agreement of the basic solidification theory, albeit differing - even confusing - nomenclatures do exist, and *Cases 2* and *3* (the *Chalmers'* basic boundary conditions for solidification, categorized by *Savage* as *Cases*) are variably emphasized.

Model Frame, a tool helping to model the continuum of fusion weld solidification from start to end, is proposed. It incorporates the general solidification models, of which the pertinent ones are selected for the actual modeling. The basic models are the main solidification *Cases 1…4*. These discrete *Cases* are joined with *Sub-Cases*: models of Pfann, Flemings and others, bringing needed *Sub-Case variables* into the model. *Model Frame* depicts a grain growing from the weld interface to its centerline. Besides modeling, the *Model Frame* supports education and academic debate. The new mathematical modeling techniques will extend its use into multi-dimensional modeling, introducing new variables and increasing the modeling accuracy.

We propose a model: *melting/solidification-model* (*M/S-model)* - predicting the solute profile at the start of the solidification of a fusion weld. This *Case 3*-based *Sub-Case* takes into account the melting stage, the solute back-diffusion in the solid, and the growth rate acceleration typical to fusion welds.

We propose – based on works of *Rutter* & *Chalmers*, *David* & *Vitek* and our experimental results on copper – that **NEGS-EGS**-transition is not associated only with cellular-dendritic-transition.

Solidification is studied experimentally on pure and doped copper with welding speed range from 0 to 200 cm/min, with one test at 3000 cm/min. Found were only planar and cellular structures, no dendrites - columnar or equiaxed. Cell sub structures: rows of cubic elements we call "*cubelettes"*, "*cell-bands"* and "*micro-cells",* as well as an anomalous crack morphology "*crack-eye",* were detected, as well as microscopic hot crack nucleus we call *"grain-lag cracks",* caused by a grain slightly lagging behind its neighbors in arrival to the weld centerline.

Varestraint test and R-test revealed a change of crack morphologies from centerline cracks to grain- and cell boundary cracks with an increasing welding speed. High speed made the cracks invisible to bare eye and hardly detectable with light microscope, while electron microscope often revealed networks of fine micro-cracks.

Keywords: welding metallurgy, fusion weld, weld solidification, solidification growth rate, solute distribution, rejected solute, solute pileup, temperature gradient, constitutional supercooling, cell, columnar dendrite, equiaxed dendrite, melting, diffusion, modeling, weld interface, copper, hot cracking, easy growth direction, NEGS, EGS, teardrop weld pool, cell tip concentration, stagnant layer, marginal stability, solute trapping

UDC 621.791.053 : 669-19 : 66.065.5

FOREWORD

The present work was carried out at the Welding Laboratory, Lappeenranta University of Technology, during the period of 2000 to 2007.

First of all, I wish to express my gratitude to the supervisor of the dissertation, Professor Jukka Martikainen, for his invaluable guidance and commitment to the work. The able staff of LUT Welding Laboratory deserves the warmest thanks for the work, especially Special Laboratory Masters Antti Kähkönen for building the Varestraint apparatus, Antti Heikkinen for metallography and Harri Rötkö for carrying out the welding experiments.

The Metals Laboratory of Outokumpu Poricopper Oy can not be sufficiently thanked for their part – albeit abruptly ended because of the dissolution of the company. The greatest overall support to this work in general - and to the experimental work especially - came from Lic. Sc. (Tech.) Jouko Koivula. Under the able supervision of Directors of Laboratory Olli Naukkarinen and Tuomas Parviainen, the Masters of Laboratory Jukka Jokisalo and Marja Valtanen did the best optical- and SEM-microscopy of this work. Master of Laboratory Timo Välimäki's advices are appreciated; his greatest single contribution was the production of the 99.9995 %-purified copper test material.

This work is indebted to the Outokumpu OYJ not only by the invaluable technical support, but also for the lengthy direct financial support of the Outokumpu Oyj Foundation. Special thanks go to Foundation Director Markku Kytö and Foundation Secretary Riitta Tolonen.

This dissertation was endowed with strong and active Preliminary Examiners. Professor Victor A. Karkhin gave a major contribution advising with acute physical and mathematical problems associated with the modeling. Professor, President of The Welding Society of Finland Risto A. J. Karppi – not saving his efforts – gave his ample experience of both theoretical and experimental welding research in use. I am truly indebted to these wise and experienced scientists.

The Editor-in-Chief, DI Juha Lukkari benefited this work with suggestions based on his wide experience in the field of welding.

Finally, I thank my wife Ella, my mother and my sons Jari-Petteri and Pasi, and for the love, support and understanding during the work.

Lappeenranta, January 2008

Pekka Rajamäki

CONTENTS

LIST OF SYMBOLS

a - thermal diffusivity, m^2s^{-1}
C - concentration
C_0 - initial concentration
C_{max} - peak concentration
$c\rho$ - volume-specific heat capacity, $Jm^{-3}K^{-1}$
D - diffusion coefficient, m^2s^{-1}
E_{EGS} - free energy of *NEGS-EGS-transition J.* {f(R- $R_{NEGS-EGS}$), Ch. 2.9}
f - function, e.g. App. 38
f_S - solidified fraction
$1- f_S$ - proportion of the remaining melt
G - temperature gradient in liquid side of S/L, Km^{-1}
k_0, k - equilibrium distribution coefficient
k_e - effective distribution coefficient
L - weld pool length, m
L - specific latent heat of solvent Jm^{-3}
l - length of trailing end of the weld pool, m
P_C - Péclet-number *Pe* for solute. The ratio of relative flow rate to diffusion rate, ~ r·R/2D, ~ r/2ξ_0 [5 p.75]
P_t - thermal Péclet number
Q - activation energy, $Jmol^{-1}$
q - net heat power, W
R - growth rate of melting and solidification, ms^{-1}
- gas constant, $Jmol^{-1}K^{-1}$
R_3 - growth rate at the onset of *Case3* solidification, ms^{-1}
R_a - growth rate at the onset of *capillarity limit-induced planar* solidification, ms^{-1}
R_C - growth rate at the onset of *cellular* solidification, ms^{-1}
R_{CD} - growth rate at onset of *columnar dendritic* solidification, ms^{-1}
R_{DC} - growth rate at the onset of *capillarity limit-induced cellular* solidification, ms^{-1}
R_{st} - growth rate at the onset of solute trapping, ms^{-1}
$\dot{R}$ - *dR/dt,* ms^{-2}
R_∞ - ultimate cooling rate (Ch. 3.4), Ks^{-1}
r - tip radius, m
S - solubility
s - plate thickness, m
t - time, s
T - temperature, K
T_0 - initial temperature, K
T_L - melting (solidification) temperature, K
$\dot{T}$ *-dT/dt,* cooling rate, Ks^{-1}
U - mass transfer potential
v - welding speed, ms^{-1}
W - bead width, m
x, y, z - fixed coordinate system, m
x' - ξ', distance from solid/liquid interface, coordinate moving with S/L, m
α - angle between G and welding direction
δ - ξ_{CG}, width of the concentration gradient (pileup) of the rejected solute, m
δ_h - thickness of stagnant layer, m
δi - characteristic distance of diffusion jump, m
γ - specific free energy of S/L-interface, Jm^{-2}
Γ - capillary constant γ/L, [77 p.446], Jm^{-2}
Γ - Gibbs-Thompson coefficient $\sigma/\Delta s_f$, [5], Km
ΔH - latent heat of fusion and Solidification, J kg^{-1}
Δs_f - specific entropy of fusion, $Jm^{-3}K^{-1}$
ψ - angle between R and *EGD*
Ω - solute supersaturation (Ch. 2.8.5)
λ - thermal conductivity, $Wm^{-1}K^{-1}$
ξ - crystal axis, m
ξ' - x', distance from solid/liquid interface, m
ξ_0 - characteristic width of the solute pileup (concentration gradient), m
ξ_{CG} - $5\xi_0$, δ, ~ width of solute concentration gradient (pileup), m
ξ_{SL} - coordinate of solid/liquid interface, m

Indices

L - liquid, liquidus
S - solid, solidus
CG - concentration gradient

Concepts and abbreviations

Acc - accelerating (in *SCV*, Ch. 4.1.3)
At-solidification – a term differentiating solidification proper from pre- and post-solidification phenomena
Back-diffusion – post solidification diffusion in solid
Bulldozing – solute transport in liquid, in front of planar or bluntly cellular S/L fronts, see *Plowing*

Capillarity limit – limit where radius of cell tip approaches the critical nucleation radius, creating circumstances for *marginal stability* (Fig. 2.30)

Case - the basic model (limiting condition) for solidification. (Ch's 1.2, 3 and 5.8)

Case 1 - equilibrium solidification

Case 2 - no diffusion in solid, total mixing in liquid

Case 3 - no diffusion in solid, no mixing except by diffusion in liquid

Case 4 - splat cooling

CB - cell boundary

CG - concentration gradient (used often as a synonym of the solute pileup on liquid side of the S/L-interface)

CS - constitutional supercooling

C/L - centerline (of a weld, grain or cell)

Cross-jump cracks –cracks, crossing the cell, resulting fine meshes of cracks, *spongy crack areas* (Ch. 6.2.8).

Dec -decelerating (in *SCV*, Ch.4.1.3)

DS - diffusion in solid

EGD - easy growth direction

EGS - easy growth solidification

EQZ - equiaxed grain zone, non-dendritic, Ch. 1.1.15(ii)

Fenced-in – solute, caught in between sharp tipped cells or dendrites. (≠ solute trapping Ch. 1.1.27)

FL - fusion line, isotherm of the weld pool liquidus. (Pool solidus = *WiF*)

GB - grain boundary

HAZ - heat affected zone

K&F - Kurz and Fisher-approach. (Ref. [5])

Knee - sharp bend in a grain due to shift of *EGD* (Ch.1.1.20)

Lausanne (EPFL) approach –solidification research line, preferring *Case 2*-based models. See Ch's 2.8 & 5.7.

Marginal stability limit – limiting $\mathbf{R=R_a}$, rendering S/L-interface planar Fig's 4.5 and 5.4.

MGB - migrated *SGB*, having lowered its surface energy by post-solidification migration

Microscopic equilibrium – equilibrium existing in a few atoms thick layer on both sides of the S/L-interface

M/S-model – melting/solidification-model, taking into account the pre-solidification melting stage

M&S - Mullins and Sekerka

NEGS - non-easy growth solidification; solidification in the G-direction

PMZ - partially melted zone

Plowing – solute transport in front of sharp-tipped cells/dendrites. See *bulldozing*

$R_{NEGS\text{-}EGS}$ - rate, above which the solidification transforms from NEGS- to EGS-mode

RPI-approach - solidification research line, preferring *Case 3*- models. See Ch's 2.7 & 5.7.

Scheil partitioning – *Case 2*-regulated solute distribution at final transient and across a cell

SCS Savage Casing System, (Ch's 2.7.1 and 5.7)

SCS2 - SCS modified with Sub-Cases, (Ch's 4 and 5.7)

SCTR - solidification cracking temperature range

SGB - solidified grain boundary prior to any post-solidification phenomena

S/L - solid/liquid (interface)

Snow cap - a dope-rich layer on the top surface of the weld

Solute pileup ~ concentration gradient (CG)

Solute trapping – non-diffusional and non-equilibrium freezing of solute atoms at high R (Ch. 1.1.7).

Spongy crack area – an area, where meshes of microscopic cracks are formed by cell boundary cracks, intersected by *cross-jump cracks*. (Fig. A35.3). Associates with high **v**

SSGB- solidification subgrain (cell- or dendrite) boundary.

Sub-Case – a mathematical equation, modeling a certain aspect of the solidification. (Ch's 4 and 5.7)

SCA- *Sub-Case Aspect*, phenomenon modeled with the *Sub-Case.* (often the longitudinal solid solute profile).

SCV - *Sub-Case Variable*, a *TMV* (such as **R, G,** $\mathbf{D_L}$, Péclet-number, viscosity, C_0, etc.) or their combination (such as $\mathbf{D_L/R, \Omega}$, Burton-Primm-Slichter-equation etc.), substantially affecting fusion weld solidification. (Ch. 5.7)

TMV -thermo-metallurgical variable, the physical element of a *SCV*

WiF - weld interface, isotherm of weld pool solidus. (Pool liquidus = *FL*)

ORIGINAL FEATURES OF THIS DISSERTATION

This dissertation casts light on how the existing theories of fusion weld solidification have evolved, and how to use these theories to model the solute distribution and microstructure of an actual weld. The work acts on five levels; it

- **(i)** makes a *historical review* of metal solidification research,
- **(ii)** organizes the models needed for modeling an actual weld in two categories: *Cases*[1] and *Sub-Cases*[2]
- **(iii)** designs a tool *(Model Frame)* for modeling welds with the help of the *Cases* and the *Sub-Cases*[3]*,*
- **(iv)** proposes one *Sub-Case* (the *M/S-model*[4]) for the very start of the solidification and
- **(v)** verifies experimentally the applicability of the theory on copper welds.

The Chapters contain original features of ours as follows:

Chapter 2: *The historical review* shows that the weld solidification theory is uniform historically and geographically. Nomenclatural ambiguities were found; the term *columnar dendritic* had earlier a different meaning[5]. Further, the grain substructure, which *B. Chalmers* named and *W.F Savage* called *cellular dendrites* are called *columnar dendrites* nowadays. These are trivialities compared with the fact that the preceding researchers left us a legacy of sound solidification theory trusted, used and developed further around the world.

Albeit the basic solidification theory is uniform, two schools were found in the historical review, the first emphasizing *Case 3*, the second *Case 2* in solidification.

Chapter 3.4 proposes expanding of the range of *Case 4* to start from the onset of *solute trapping* and extend it to an *ultimate massive solidification* at $\mathbf{R=R_{\infty}}$.

Chapter 4 presents the concept *Sub-Case*, which is essential for the *Model Frame***.** The *Sub-Cases* categorize existing solidification models, extending the region of a *Case* and sometimes even uniting *Cases* with one another. The models have been solved mathematically by leading solidification scientists; the author can or will take no credit for the models, but their explicit sequencing (as *Sub-Cases)* in the welding continuum the way we do, is new.

Chapters 5.1…5.5 analyze modeling of the fusion weld solidification in its entirety – from start to end. The author proposes a tool for this – the *Model Frame*, presenting the central elements of a model, helping the modeler to make rational choices between non-pertinent and pertinent elements and to arrange the latter in a logical sequence. This is an original feature of this dissertation.

Chapter 5.6 and **Appendix 38** present the *melting/solidification*-model (M/S-model), predicting the solute distribution at the very start of the weld. The basic metallurgical idea is the author's. The idea could not have been materialized as a mathematical model without the help of Professor V.A. Karkhin, his research assistant P.N Homich and their numerical finite difference model, as well as their usage of the mass transfer potential *U*, facilitating the continuous modeling across the S/L-interface.

Chapters 5.6.6 and **A42.3** present initial proposals for *Sub-Case 3(-)"CG cut-off"* and *Sub-Case 3(-) [δ_n/ξ_{CG}]* respectively. These models would help unite the Mullins & Sekerka-analysis with the final and initial transients.

---

[1] The *Cases* see Chapter 1.2 and in detail Chapter 3.
[2] The *Sub-Cases,* see Chapter 4, a short round-up in Ch. 4.1.4.
[3] Special emphasis is given to the rigorous continuum these must preserve from the start of the solidification to its end.
[4] For the relation of the *Sub-Cases, Model Frame* and *M/S-model* in short*,* see *Explanatory insert* in Appendix 38.
[5] For a short round-up, see Appendixes 36 and 37

Chapter 6 shows that the theories apply for copper. The lack of the dendritic modes is unexpected. Hot-crack morphologies changed from well visible centerline cracks to a network of fine micro cracks with increasing welding speed. New to us morphologies: *crack eyes, cubelettes*, *micro-cells* and *cell-bands* are presented. Reports were found of the *cubelette*, but not of its location as rows at the cell centerline, or of its tendency to grow and *smother* the cell it is in.

We show *easy growth solidification* **EGS** occurring in *cells* of copper, which slightly contradicts other results for other metals. (Ch. 2.9).

Our proposal of *grain-lag cracks* is an original feature (Ch. 6.3.4 and Appendixes 9A & 22C).

INTRODUCTION

The Dancing Girl of Mohenjodaro, a 4600 year old 10.8 cm high bronze statue from the Indus Valley culture.
The National Museum in New Delhi

Metal solidification has interested man from the times of making of the first metal artifact; the oldest known such may be a copper pendant found near Shanidar in Iraq, dating back over 10000 years. That dating is under dispute, but there is a common agreement that the elegant young lady to the right has performed her proud dance for 4600 years. If – as some assume - she stood joined onto a pedestal, the statue manifests – besides stunning artistry – mastering of joining. Unfortunately, we may also witness ancient problems associated with joining, as the joints of her legs proved the weakest points, and were not preserved. The joining method was hardly fusion welding but brazing, but the problem was – we suggest - associated with the distribution of the solute in the braze metal, rendering the joints and their vicinity brittle.

The area of this dissertation. The fusion weld solidification consists of the *pre-, at-* and *post-solidification* phenomena; we concentrate to the two first ones[6]. The theory divides further into the solidification of *pure metals, binary alloys* and *multi-component alloys*. We concentrate to the two firstly mentioned[7]. A third division is between the *singe-phase-* and the *multi-phase* solidification; we concentrate to the first of these[8].

The history. The current comprehension of metal solidification is reviewed in Ch. 2 with a historical viewpoint. However, some general aspects are presented in Ch. 1 without their historical context.

The Savage's *Cases.* From the start, we use RPI Professor Savage's *Casing System* we call ***SCS***, for the basic solidification models. To differentiate Savages *Cases* from other cases, we print them in italics with a capital letter. Much of the mainstream research classifies the basic solidification models with explicit descriptions (Ch. 1.2). Here is no conflict; both classifications are based on or at least coherent with Chalmers' "three simple cases" [35 pp. 251-253]. However, the *SCS* is irreplaceable in the analysis of the mutual relations of the various models.

Gulliver & Scheil. *Case 1* theory (maintaining the equilibrium) was known in the 19th century; we omit its history and start with *Case 2*; its numerical solution was published by G. H. Gulliver in 1913, and developed further by E. Scheil in 1942.

The Bell Laboratories. The location of the inventing of the transistor - the Bell Laboratories – hosted foundational research simultaneously with and even before the Toronto pioneers; it appears that J.A. Burton, R.C. Prim and W.P. Slichter, as well as W.G. Pfann were the first to present the Gulliver-Scheil equation in its present analytic form (Equation $2.4.1_{GS}$).

The Toronto pioneers. University of London professor Bruce Chalmers gathered the mentioned and other knowledge of the time in University of Toronto, where he participated in and headed research that solved the *Case 3* solidification. One of the basic findings of the Canadian researchers was the division a growing grain into *cells*. Their modeling – based on *constitutional supercooling* (**CS**) - is still valid, further developed by Mullins & Sekerka, Flemings, Kurz and others.

---

[6] The post-solidification *migration of solidified grain boundaries,* solid-state back-diffusion, as well as *recovery* & *recrystallization* cannot be totally avoided, however. The pre-solidification phenomena associated with the melting stage are handled in the *Melting/Solidification-model.*
[7] Some references to the multi-component solidification are inevitable.
[8] Again, some references to the eutectic reaction and other multi-phase phenomena could not be avoided.

RPI and Professors Savage & Nippes. The existing theories were adapted to welding by a work group in Rensselaer Polytechnic Institute, RPI. This work – headed by professors Warren F. Savage and Ernest F. Nippes – gave a vital boost to our present understanding of weld metal solidification.

Professor Savage classified fundamental solidification regimes in *Cases 1…4*. We use this *SCS*-system throughout this dissertation.

SCS2* and *Sub-Cases*.** Weld solidification continuum (the continuous sequence of metallurgical events in the actual solidification) leads to a continuous sequence of microstructures from the start of the solidification to its end. The model of this actual solidification must have an identical continuum. To help imitate the nature's solidification continuum with the existing models, we developed the *Savage Casing System* version 2 (SCS2***), adding intermediate *Sub-Cases* between the "discrete" main *Cases*. They help form a continuum between the *Cases* with **(i)** increasing solid diffusion (From *Case 2* towards *Case 1,* Ch. 4.1.1), with **(ii)** increasing solute pileup (From *Case 2 towards 3*, Ch. 4.1.2) and with **(iii)** accelerating/decelerating solidification rate **R** (Ch. 4.1.3), to name just a few**.** *Sub-Cases* form a system, categorizing generally accepted mathematical models. We add to these one – the *M/S-model* - and outline two others (Fig's 5.16 and A42.2).

- *You can model the solidification continuum of a weld without the Sub-Cases - using only the Cases (in practical welding only the Cases 2 or 3 come into question), but if your actual weld includes non-constant thermo-metallurgical variables - or SCV's as we call them or their combinations - you must add a Sub-Case into the model.*

- *The RPI research recognized a unique structure we call "culumnar dendritic", (preserving a misprint from reference [12]), to differentiate this structure from the "columnar dendritic", which in today's mainstream usage denotes what Savage and Chalmers [13 p.164] called "cellular dendritic". The nomenclatural discrepancy in this area still reflects in modern works, complicating the scientific debate occasionally.*

MIT, Mullins & Sekerka. Modeling of the cells was renewed by an analysis of the break-down of the planar interface by Mullins & Sekerka at MIT (Ch. 2.6.2). This approach is an indispensable addition to the classical **CS**-approach in the occasions, where the solidification forms cells or dendrites. The MIT-professors Clyne, Flemings and Aziz modeled the solid-state back-diffusion (Ch. 2.8.2), the growth rate variations (Ch. 4.1.3) and the solute trapping (Ch. 1.1.27), respectively.

EPFL-Lausanne. *Ecole Polytechnique Fédérale de Lausanne* EPFL developed – headed by Professor Wilfried Kurz – both the *Case 3* and especially the *Case 2*-based approach further; the **Σ**- and **Ω**- solutions (Ch's 2.8.4 and 2.8.5) are *Sub-Cases* between *Cases 1* to *2* and *Cases 2* to *3* respectively (Ch. 4). These approaches are neither the only, nor the simplest, but they are the best quantified and readiest for practical use.

The Lausanne-approach – or at least several of its branches - emphasizes Case 2 and the Gulliver-Scheil-equation, equipped with a concentration gradient, making it a Sub-Case 2(+)CG. If this – the most advanced today approach – could be repeated with genuine Case 3-based models (Sub-Cases going from Case 3 downwards to Case 2), the theory would get a valuable comparison point in the area of faster growth rates. In the areas, where Case 3 is valid – and a wide enough stagnant layer may make it so – utilizing Case 2-derivatives may invite inaccuracy to the model.

Easy Growth and Non-Easy Growth Solidification (**EGS** and **NEGS).** Uniting research of the Toronto pioneers, David & Vitek from Oak Ridge National Laboratory and our own experiments, we propose that a sufficiently low growth rate **R** favors *Non Easy Growth Solidification,* turning to *Easy Growth Solidification* at a higher, material specific growth rate $\mathbf{R=R_{NEGS\text{-}EGS}}$ (Ch. 2.9).

Model Frame. The *Cases* and *Sub-Cases* are placed into a *Weld Solidification Continuum Model Frame*, in short *Model Frame*, which is proposed as a framework for all known and future models (categorized in *Sub-Cases*) of any possible solidification regime. When modeling an actual weld, the models (*Cases* and *Sub-Cases*) judged as non-pertinent are excluded, while the models judged pertinent *Cases/Sub-Cases* are ordered in a logical sequence. The result is the model of the actual weld, containing the solute profile and estimated microstructures (preferably in 3-D, which at the

present is beyond reach). If the model does not comply with the experimentally determined features of the actual weld, it must be taken back to the *Model Frame* where a new combination of *Cases* and *Sub-Cases* is chosen. With such an iterative process, a sufficiently accurate model for the actual weld will eventually be designed. The active exclusion of the non-pertinent models forces the designer to make conscious judgments concerning each *Case* and *Sub-Case*.

The new mathematical modeling techniques will extend the use of the *Model Frame* into geometrically 3-D modeling, facilitating handling of perpendicular diffusion – and thermo-metallurgically multi-dimensional modeling, facilitating simultaneous handling of such variables (called *SCV*'s) as the growth rate **R**, the temperature gradient **G**, the diffusion in the solid, the weld pool flows, a.s.o., including future ones not yet known.

The basic Model Frame-A is for an elliptic weld pool. It includes all the microstructural morphologies of the Kurz & Fisher model up until the fastest growth rates. Many of those may never occur in fusion welding due to the fact that its solidification regime tends to change at higher growth rates. For this, there are variants of the Model Frame for a teardrop pool and for a pool with equiaxed dendrites (Model Frame-B and -C respectively). Either variant may replace the basic Model Frame-A at some point during the accelerating solidification of a fusion weld.

M/S-model. We propose a new *Melting/Solidification-model (M/S-model)*, which is a *Sub-Case* for *Case 3*. It takes into consideration the melting stage prior to solidification. The model also takes into account the acceleration of **R** and the diffusion in solid. The effect of the melting stage is restricted to the very start of the solidification at weld interface (WiF), where also the effect of the growth rate acceleration is the greatest. Therefore, the solidification starts with the regime of M/S-model, and transforms to pure *Case 3* not later than where the planar front breaks to cells. From there, the Mullins & Sekerka- model takes over.

The experimental work on copper – pure and doped – revealed planar and cellular structures only; dendrites of any sorts were not detected. Peculiar cell sub structures: rows of cubic elements we call "*cubelettes"*, "*cell-bands"* and "*micro-cells",* as well as an anomalous crack morphology "*crack-eye",* were detected. The top surface of the weld was covered with a thin solute-rich layer, *snow cap*. The thickest and most evident *Snow cap* can be seen in Fig.A15.2, one of the thinnest in Fig. A3A. Its cracking shows that the layer is not just a metallographic edge-phenomenon.

Varestraint test and a modified R-test revealed a change of crack morphologies from centerline cracks to *grain boundary* and *cell boundary* cracks, with an increasing welding speed. Increasing speed made the cracks invisible to bare eye and hardly detectable with light microscope; in some occasions, electron microscope revealed networks of fine micro cracks (*"spongy crack areas"*). It is not impossible that some of these networks - detected with light microscopy - were not in fact cracked, but only preferentially etched in the preparation. At least in these occasions, the overall susceptibility to cracking diminished with an increasing growth rate.

The figures, graphs and formulas from other sources in this non-commercial, academic dissertation have been taken and modified to illuminate a specific point they are associated with in this work. The modifications include changing the solidification direction from left to right, adding definitions and markers, replacing v and r with R and r_0 etc.

To avoid confusion and clashes with copyrights, we request that these objects not be borrowed from this dissertation, but from the original sources. The author's own figures - identifiable by not having markings of references - are free to be borrowed and referred to.

Chapter 1 GENERAL ASPECTS OF SOLIDIFICATION

This work handles solidification of bead-on-plate fusion welds in pure metals and single-phase binary alloys in flat position. Only drooping solidus and liquidus lines (k_0 <1) and positive temperature gradients are handled. Stresses, strains and the atmospheric pressure, and their effects on solidification, are framed out of this dissertation.

1.1 Solidification basics

1.1.1 Normal, zone and crystal pulling freezing

Historically, solidification (freezing) was divided in *normal-* (the entire charge is solidified with a plane front), *zone-* and *crystal pulling solidification* (referring to specific methods), [1 p.32][2 p.9]. Fusion welding does not quite fit into this classification and *fusion weld solidification* may be considered a class of its own.

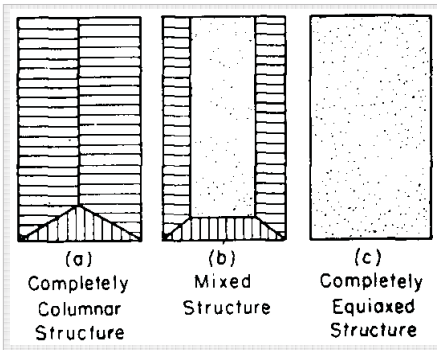

Fig. 1.1.Three main solidification types. Tiller 1959 in [6] Cahn Tiller 1970,

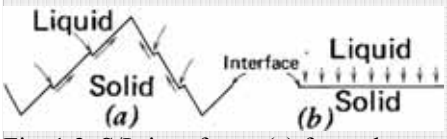

Fig. 1.2. S/L-interfaces, (a) faceted, (b) non-faceted. Verhoeven 1975 [8]

1.1.2 Constrained and unconstrained

Growth with neighboring grains allowing growth only longitudinally is traditionally defined as *constrained*, (or *directional* or *Columnar*) Fig. 1.1 (a) [6]. In the *fusion weld solidification* the definition must include the solidification rate **R** as well as the direction; the welding speed **v** controls the **R** (more in Ch. 1.1.18).

- Free growth in all three directions is unconstrained Fig. 1.1 (c). In a fusion weld, there may be equiaxed grains near the weld centerline, growing unconstrained; they are free of the direct control by ***v.***

- In the constrained growth, the temperature of the growing crystal is cooler than the temperature of the melt it is forming from, in the unconstrained growth, the melt must be cooler than the growing crystal.

1.1.3 Faceted and non-facetted

Solid/Liquid (S/L) interface may grow facetted, Fig. 1.2 **(a),** or *non-facetted* **(b)**. Both interfaces may have *ledges* helping atoms to attach. The non-facetted growth is also called *continuous growth* and the facetted growth *stepwise growth*, Aziz 1982 [7 p.1159].

1.1.4Growth ledges

Atoms with one side attached to the S/L- front (*bond number 1*) have high risk of dissolving back to liquid (Fig. 1.3). If surface diffusion leads them to a *ledge*, they attach from two sides. Diffusion along the ledge may lead them to a corner attaching them from three sides. The process continues until the atom is connected from all six sides (*bond number* 6) Fig. 1.4 shows two surface ledges growing in opposite directions and annihilating one another.

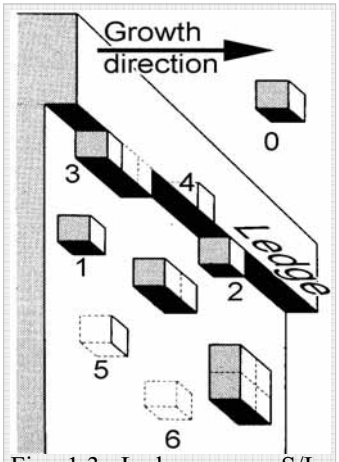

Fig. 1.3. Ledge on an S/L-interface. Atoms finding a place with a high *bond number* have a high probability to fix into the lattice. Kurz, Fisher 1998 [5] Modif.

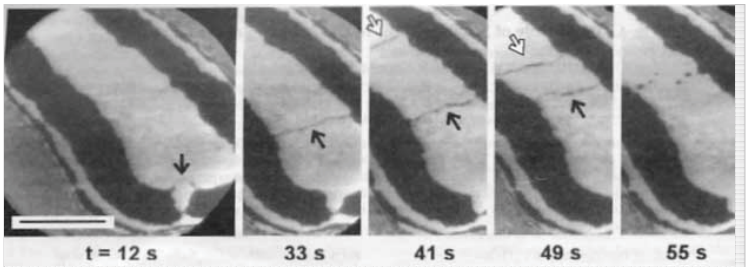

Fig. 1.4. Migration and eventual annihilation of two surface ledges (black & white arrows). Light areas are Ge on darker Si surface Scale bar = 2µm. Hanon et al. 2004[9]

1.1.5 Birth of cells and dendrites - Rising and Drooping G

A positive melt temperature gradient **G** in Fig. 1.5 **(a)** melts any protrusion from the planar S/L-line, enhancing planar growth. With the negative **G** in Fig. 1.5 **(b),** the tip of the protrusion is in a temperature below freezing and it grows; a negative temperature gradient enhances protrusions. In fusion welds, **G** is always positive; protrusions (*cells* and *dendrites*) must be explained otherwise. The explanation is the *constitutional supercooling* ***CS***, handled by the *Classic-* and the *Mullins & Sekerka* approaches (Ch's 1.1.25 and 2.6.2).

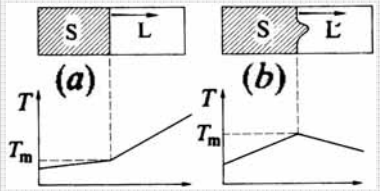

Fig. 1.5. Solidification with **(a)** positive temperature gradient enhancing planar growth and **(b)** negative temperature gradient making protrusions possible. Haasen 1996 [10 p.61]

1.1.6 Latent heat of fusion vs. thermal gradient at S/L-interface

Liberation of the latent heat of fusion alone can not form a negative **G** during fusion welding and never leads to local supercooling in front of the S/L interface (Fig. 1.6); unless the weld is specially cooled, **G** is always positive in a fusion weld.

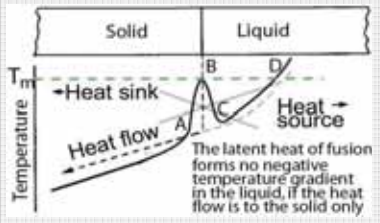

Fig. 1.6. Latent heat of fusion does not cause undercooling at S/L-interface between **B-C-D** if heat dissipates to the solid only.

The only recognized undercooling (protrusion forming) mechanisms for fusion welding are the negative temperature gradient in Fig. 1.5b (possible only with specific cooling of the weld surface) and the constitutional supercooling.

1.1.7 Grains and cells - solute distribution

A planar S/L-interface has solidification grain boundaries (**SGB**'s): high-angle boundaries with dislocation networks. A collision of competing grains leaves SGB's with an elevated solute concentration, which is a remnant of the final transient of the grain having lost the competition.

Longitudinal solute transport. A planar (and blunt-tipped cellular) interface transports solute in the longitudinal growth direction. This *macroscopic segregation* is studied with the longitudinal volume elements (**PrC** Fig. 1.7a) (*large systems*, [5 p.117-]).

Transverse solute transport. Sharp-tipped cells transport solute transversely towards the cell boundaries. This *microscopic segregation* is studied with the transverse volume elements **inC** in Fig. 1.7a (*small systems*, [5 p.122-]).

If cells form secondary arms, (transform to dendrites), their longitudinal growth (macroscopic segregation) is studied with the volume element ***PrD*** *and inter-cellular (microscopic) growth with the volume element* ***inD*** *in Fig. 1.7b.*

Much of the modeling of fusion welds deals with the solute profile in the longitudinal and transverse directions. The transverse segregation divides yet to the segregation between the *cells* and between the *grains.*

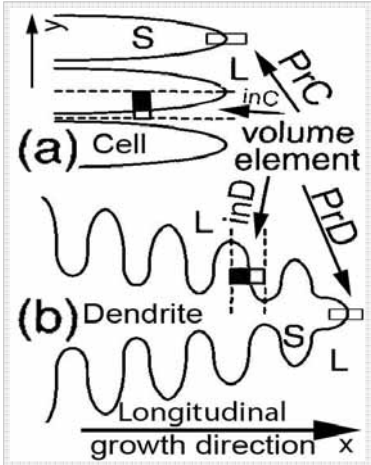

Fig.1.7. Volume elements in **(a)** a cell, **PrC**=in principal growth direction. **inC**=inter-cellular **(b)** a dendrite **PrD** = in principal, **inD** = inter-dendritic direction. Volume elements should be in the solidification direction. Based on [3]

1.1.8 Dendrites

In most metals, an increasing **R** transforms in some point the *cellular growth* into *columnar dendritic growth*. We failed in creating dendrites in experiments on copper and leave these important micro-constituents with the photo-collage in Fig. 1.8, collected from various references. Fig. 1.8A shows a dendrite with needle like secondary arms in a Ti-6% Mn weld. Savage, the author, writes that it took years to find this structure, evidently formed by a grain, not cells, as discussed in Fig. 2.23A. This mechanism is no more recognized; we refer to it with the misprinted form *culumnar dendritic* [12].

The dendrites in Fig. 1.8B were presented and named by Chalmers as *cellular dendrites* [13 p. 164]. This morphology is still recognized, but it is named *columnar dendritic* nowadays (more in detail in Appendix 37).

Fig. 1.8E shows an equiaxed dendrite, sometimes forming near the weld centerline.

The Fig's 1.8C-D and F-O present various types of dendrites, actual micrographs and models. The dendrites may acquire an abundant selection of morphologies.

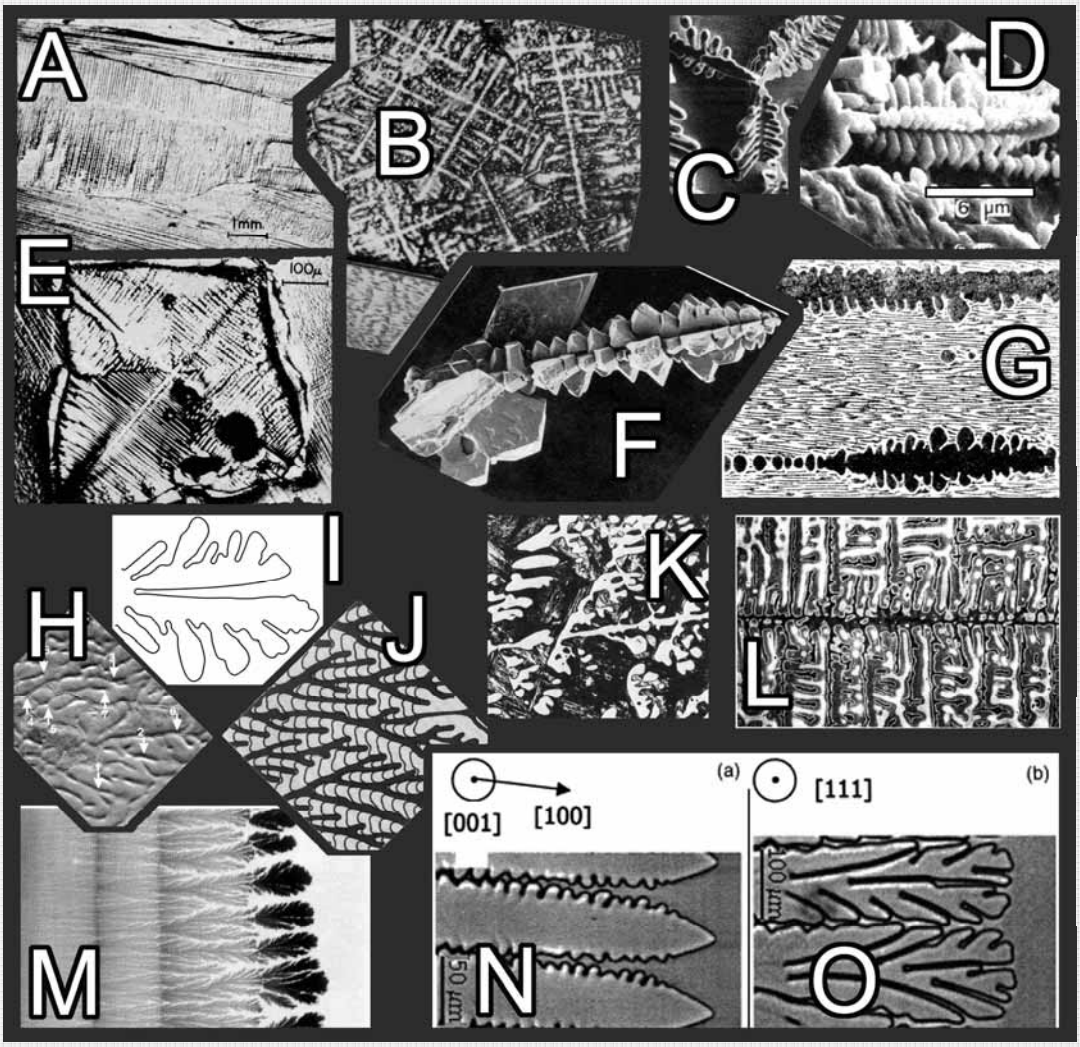

Fig 1.8. Arbitrarily chosen dendrites with a variety of morphologies.

A and E: Savage 1980 [12], **B:** Chalmers 1963 [13], **C:** [14 p.614], **D:** [15 p.891], **F:** [16 p.94 Fig32], **G:** [14 p.613], **H, I and J:** [17], **K:** [14], **L:** [14 p680Fig21], **M:** [18 p717], **N and O:** [19].

1.1.9 Solute rejection and Microscopic equilibrium

In the solidification of a liquid with a composition $\mathbf{C_0}$, only the fraction $\mathbf{C_S = k_0 \cdot C_0}$ of the solute atoms is accepted into the forming solid lattice (Fig. 1.9). The rejected solute atoms stay in the liquid raising its concentration $\mathbf{C_L}$. Atoms raising $\mathbf{C_L}$ above $\mathbf{C_0/k_0}$ are forced to make diffusion jumps in to the melt to give way to the advancing solid.

The equilibrium is preserved in a few atoms thick layer on both sides of the S/L interface. This is called the *microscopic equilibrium* (*local equilibrium* [5 p.135], *interfacial equilibrium* [8 p.247].

The microscopic equilibrium breaks down not later than at the sufficiently high growth rate $\boldsymbol{R_{st}}$ *at the onset of solute trapping, Ch. 1.1.27. It may happen earlier, at Ra, Ch. 4.2.1 Fig. 4.5* [5 p.135][7].

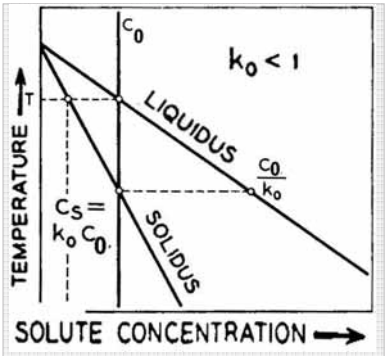

Fig. 1.9. Binary equilibrium.

1.1.10 Equilibrium distribution coefficient k_0

The term *equilibrium distribution coefficient* $\mathbf{k_0}$ (also *marked* **k** and named *equilibrium partition ratio* or *equilibrium concentration constant*) is central in analytical solute distribution models.

$\mathbf{k_0} = Cs / C_L$, (Fig. 1.9)

The analytical solution of Case 2 (Eq. $2.4.1_{GS}$*) is found only with* $\boldsymbol{k_0}$*; the earlier solutions of Gulliver and Scheil were numerical (Ch 2.2).*

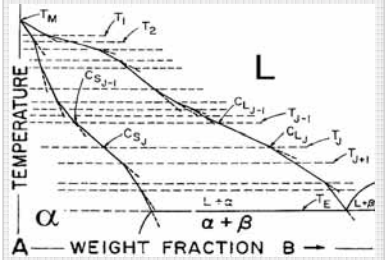

Fig. 1.10. Liquidus and solidus by straight-line segments. Brody, Flemings 1966 [20]

1.1.11 Non-linear solidus and liquidus

$\mathbf{k_0}$ is constant if solidus and liquidus are linear. Brody and Flemings developed a method with arbitrary forms of constitution, Fig. 1.10.

1.1.12 Epitaxial nucleation and growth

Weld pool is bordered by solid base metal of the same or analogous composition, providing an ideal base for heterogeneous nucleation with minimal supercooling.

The term "Epitaxial" (from Greek: epi = on taxis = be organized) refers primarily to the initiation – i.e. ideally heterogeneous nucleation–stage. The growing grain inherits its orientation from the mother grain; preserving its lattice orientation, Fig. 1.11.

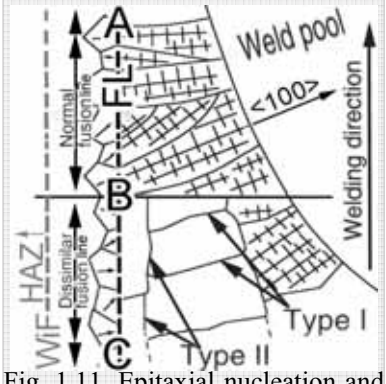

Fig. 1.11. Epitaxial nucleation and growth. [11] *WiF added from Fig. 1.15.*

Epitaxiality in welding was proven and verified by Savage et al. [21][22][23 p.331-s]. The use of the word in this context has been criticized [25]; however, the concept is globally accepted.

1.1.13 Post-solidification SGB Migration

The solidified grains boundaries (*SGB*'s) may migrate during sufficiently slow cooling, allowing back-diffusion. Low welding speeds and high preheating temperatures enhance this. Fig. 1.13 shows one such migrated grain boundary (*MGB*). The segregations along *SGB*'s do not necessarily follow and may remain decorating the area of the original *SGB* [26 p.63].

The solidification subgrain boundaries (SSGB's) are usually not as prone to migration, but they too tend to turn obscure by back-diffusion with time at elevated temperatures.

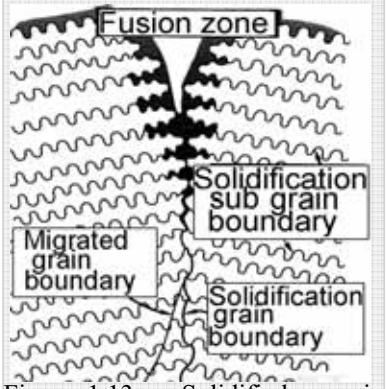

Fig. 1.13. Solidified grain boundary (***SGB***) migrating to the location of the ***MGB.*** Lippold, Kotecki 2005 [11]

1.1.14 Fusion line and Weld Interface

Textbooks often show fusion line **FL** as a distinct line (**ABC** in Fig's 1.14 and 1.18), as do all weld-associated standards. This leaves in trouble the poor welding engineer positioning his Charpy-V notches in a certain distance from **FL**: the fact is that fusion line **FL** seldom shows up this distinctly. The perfect match between the epitaxially nucleated grain and mother grain most often conceals the **FL**.

Fig. 1.14 a) shows schematically a typical feature cells: if cells follow an easy growth direction, they tend to follow it more accurately than the grains do.

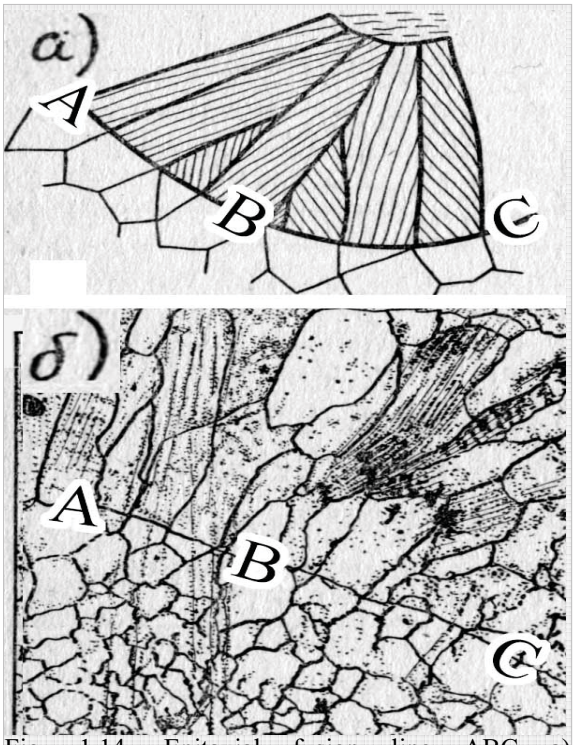

Fig. 1.14. Epitaxial fusion line ABC a) schematically, and б) in a micrograph. Petrov, Tumarev 1977 [27]

WiF and FL

We define the weld lines according to Fig. 1.15 (ASM Hand Book [28][4]). The *weld interface* **WiF** is the line where the maximum temperature reached the solidus temperature $\mathbf{T_S}$. It is the line between 99.9 % solid and 100% solid. (590 C^0 in Fig. 1.16). The *fusion line* **FL** is the line where the maximum temperature reached the liquidus temperature $\mathbf{T_L}$; the line between 100% and 99.9…% liquid (640 C^0 in Fig. 1.16). Between these two lines is the *partially melted zone* **PMZ**.

The single line 4.32 replaces both these contours in the European standard, Fig. 1.17. There is a nomenclatural gap between science and standards in Europe. Our US colleagues are not more fortunate:

ANS/AWS A3.0-94 Standard Welding Terms and Definitions define "Fusion line: a nonstandard term for weld interface". "Weld interface": The interface between weld metal and base metal in a fusion weld; There is a gap between research and standards in USA as well.

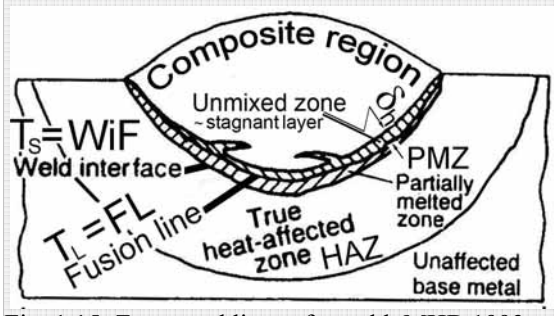

Fig. 1.15. Zones and lines of a weld. MHB 1993 v.6, from Messler 1999[4][28] *T_S=WiF, T_L=FL Fusion line, PMZ, ~ stagnant layer and δ_n added.*

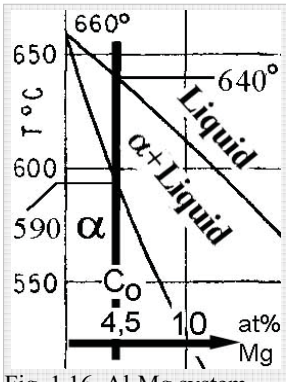

Fig. 1.16. Al-Mg system.

This dual nomenclature must be accepted, but the definitions of all the parties should be un-ambiguous (Appendix 36).

The stagnant layer - and unmixed zone are taken in this dissertation as one and the same, which is an approximation (Fig. 1.15, Ch. 1.1.24 and Appendix 42).

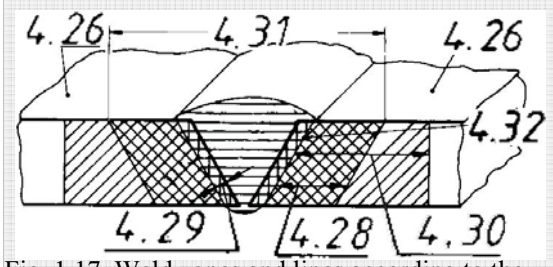

Fig. 1.17. Weld zones and lines according to the European/Finnish standard SFS 3052 Fig. 69. **4.26**: base metal, **4.28**: HAZ, 4.**29**: fusion zone **4.30**: heat affected area, **4.31**: weld zone, **4.32**: fusion line. [29]

Visible Fusion Lines

The fusion line (**FL**) appears rather seldom, as in Fig 1.17; usually special metallography is required (Fig's A24E and A35.2C).

Lines easily mistaken as fusion lines

Fig. 1.18 shows two candidates for the fusion line, lines **ABC** and **DE.** The correct **FL** is the former. Line **DE** marks "abrupt change to a coarser structure" in the fusion zone.

The planar to cellular change causes similar lines in copper [32] and Fig. A35.2.A. Line P/C-P/C

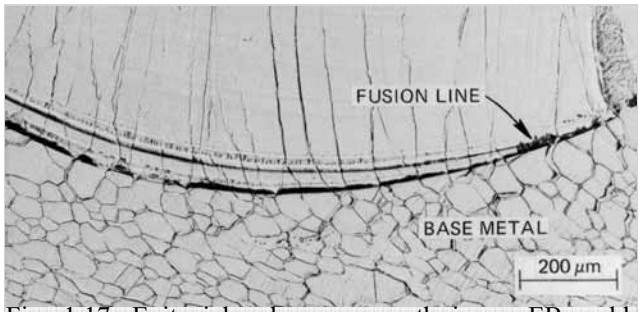

Fig. 1.17. Epitaxial columnar growth in an EB weld. Distinct fusion line. David, Vitek 1993 [30]

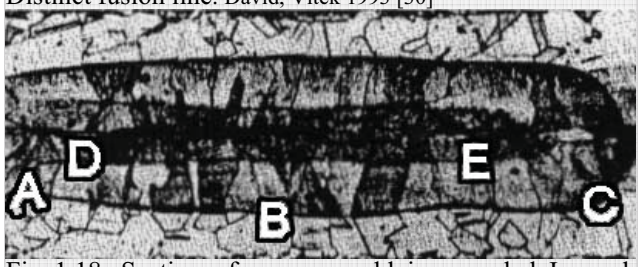

Fig 1.18. Section of a seam weld in annealed Inconel. **ABC** = Fusion line, **DE** = line of transformation in melt. ~100x. Savage, Lundin, Aronson 1965 [31]

1.1.15 Proposed non-epitaxial nucleation and growth in fusion welding

In vast majority of cases, the weld pool solidifies and grows epitaxially. Our survey revealed two occasions of proposed non-epitaxial nucleation.

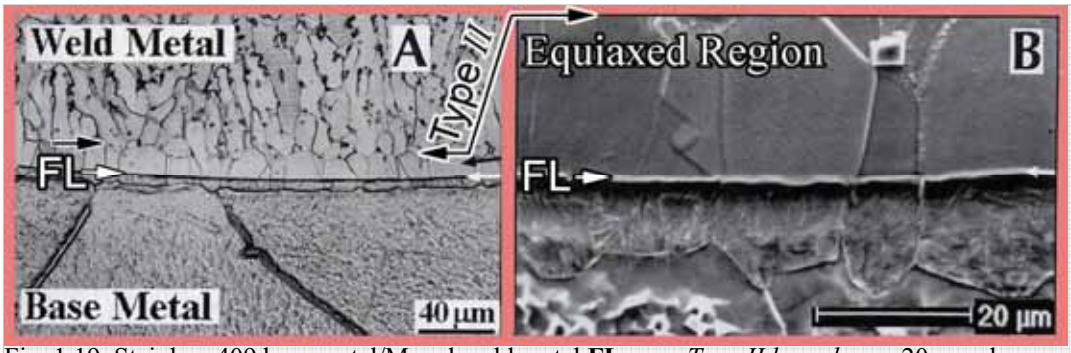

Fig. 1.19. Stainless 409 base metal/Monel weld metal **FL** area. *Type II boundary* ~ 20 μm above **FL**. The grains in the untypical *Equi axed region* between **FL** and ***Type II*** boundary have no common orientation with Base Metal. Nelson, Lippold, Mills 1999 [23]

(i) ***Stainless 409 base metal / Monel weld metal.***

Epitaxial nucleation was proposed not to have occurred in a stainless steel 409 base metal/Monel weld metal welds by Nelson, Lippold, and Mills [23].

Absence of common base metal-weld metal orientation across **FL** in **Fig** 1.19 in electron back scatter diffraction EBSD tests and the fact that the boundaries of the growing grains do not cross the **FL** in Fig. 1.20 suggest heterogeneous nucleation along **FL** [23 p.329-s].

Our experiments suggest a similar lines in e.g. La-doped Cu in Fig. A27 B.

The Type I Boundary in Fig.1.19 results from columnar growth from base metal grains into the weld metal running roughly perpendicular to the ***FL.*** *Type II boundaries run typically parallel to* ***FL*** *> 200μm above it, as in Fig. 1.11 [26 p. 291].*

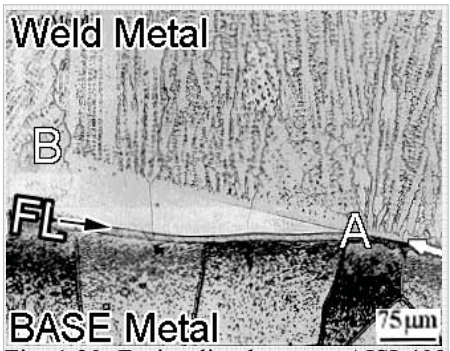

Fig. 1.20. Fusion line between AISI 409 base metal and Monel weld metal. Grain boundaries do not cross the fusion line FB. Nelson, Lippold, Mills 1999 [23]

(ii) *Equi-axed Grain Zone, EQZ*

The *non-dendritic equiaxed grain zone EQZ* in Fig. 1.21 is reported only in Li-alloyed aluminum Al 2195, and even there only under certain circumstances. The figure suggests that a weld may nucleate non-epitaxially [23 p.331-s] and [3]. Near the **FL,** a vigorous homogenous nucleation occurs with moderate nuclei growth rate. **EQZ** is susceptible to hot cracking, which suggests existence of segregation between grains. With the low melting point of lithium (180 ^{0}C as compared with 660 ^{0}C of Al), emergence of hot crack by Li segregation is not surprising.

Al 2195 shows an exceptionally high difference between the Nil Strength- and solidus temperatures, relating to the hot cracking susceptibility (Ch. 1.1.28). This does not shed light to the birth mechanism of the rather mysterious EQZ.

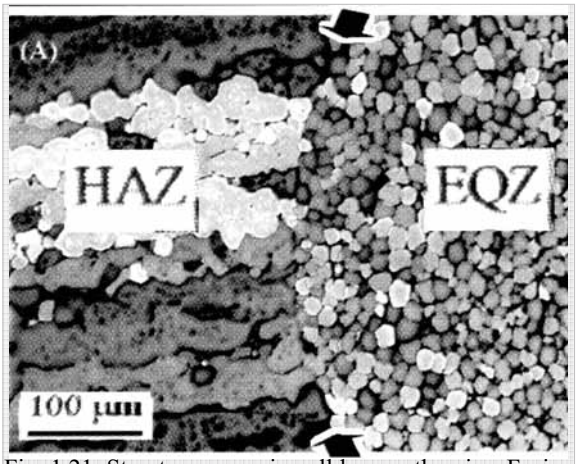

Fig. 1.21. Structure, opposing all known theories: Fusion zone with *non-dendritic equiaxed grain zone EQZ*. Al 2195-T8, simulated fusion line. Kostrivas Lippold 2000 [33]

1.1.16 Backfilling

The last solidifying grain- and cell boundaries may form canals from the pool towards and sometimes into the HAZ (Fig's 1.22, 1.37 and 1.40). Contraction may form a vacuum, pulling liquid from the pool backwards in these canals, with positive or adversary results. If a crack opens in a just solidified grain boundary, this crack may be filled from weld pool; this gives some aluminum alloys good resistance to cracking [4 p.444] and (Fig. 1.41 region III→IV).

Adversary backfilling may pull low-melting and crack prone liquid into PMZ, even expanding the PMZ deep into the HAZ and even base metal, causing cracking, as in (Fig's 1.22, 1.23 and A11A)[9]. Cracks extending into the base metal (~70%Cu, 30%Ni) were backfilled from the Ni-depleted liquid ahead of the S/L line. *(The Ni-content of the backfill was ~ k_0C_0, this was the first experimental proof of the existence of the concentration gradient in a weld)*.

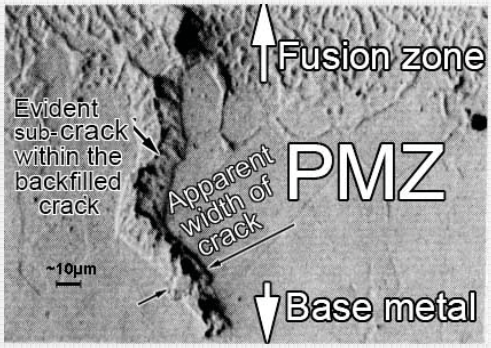

Fig. 1.22. Crack – back filled with molten metal from the weld pool - extending from fusion zone into base metal. ~120x [34] *Texts added.*

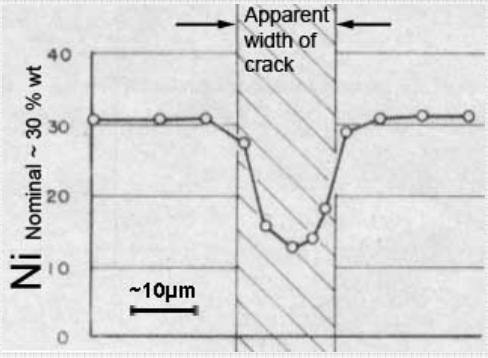

Fig. 1.23. Ni-content analysis across a back filled crack in Fig. 1.22. Savage, Nippes, Miller1976 [34]. *The µm-scale added*

1.1.17 Inverse segregation

Inverse segregation involves segregation against concentration gradient [35][36][37]. This complex phenomenon is known in continuous casting but rare in welding. It should be differentiated from backfilling. *We seem to have encountered inverse segregation in the La-doped copper welds with v=10 cm/min (Fig. A24 G) and 200 cm/min.(not presented). The circumstances (x ~ -5mm) and the structure are non-typical to welds and this topic is limited to this mention in this dissertation.*

[9] This cracking is sometimes called *liquation cracking.* Kou advocates reserving the term for cracking from *constitutional liquation* [4 p.509]. Thus we use the term *adversary backfilling* or *PMZ cracking* [3 p.321] (see Appendix 36).

1.1.18 Relation of R and v in welding

Weld solidifies as the welding heat and the latent heat of fusion are liberated to the surroundings over the line **A'E'D'C'** in Fig 1.24. The line-like welding arc or beam points at **O;** temperature gradient **G** rises monotonously towards this spot. The vectors of **G** and growth rate **R** are parallel. At the fusion line **FL,** they are perpendicular to **FL**. The growth - not following the easy growth direction **EGD** and proceeding in **G** direction - is called *non-easy growth solidification* **NEGS.** Its rate is:

$$\mathbf{R} = \mathbf{v} \cos \phi \qquad \text{(Eq. 1.1.18A)}$$

If the growth does follow the **EGD**, the solidification is called *easy growth solidification* (**EGS**) and its rate is:

$$R_{EGS} = R / \cos \Psi, \qquad \text{(Eq. 1.1.18B)}$$

Ψ is the angle between EGD and **G** (Fig.1.24).

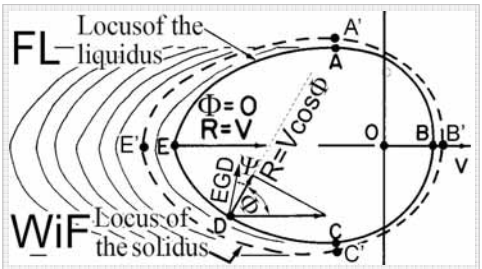

Fig. 1.24. Elliptic weld pool, line source (arc or beam) location at **O**. **v** = welding speed, **R** = grain growth rate (**NEGS**), ϕ = angle between **R** and **v**. $\phi = 90^0$ at **FL,** 0 at weld centerline. **ABCDE**= pool liquidus. **FL**= fusion line. Outer dashed line **A'B'C'E'**= pool solidus. **WiF =** Weld interface. **NEGS** = non easy growth solidification, Ψ = angle between **R** and easy growth direction **EGD**. Based on [12]

1.1.19 Elliptic and teardrop pool form vs grain curvature

Slow welding speed **v** favors an elliptic weld pool (Fig.1.25b), while fast **v** tends to cause a teardrop-shaped pool (Fig. 1.25a). The grains in an elliptic weld pool are curved and **G** and **R** change gradually from perpendicular to parallel with **v**, (Eq. 1.1.18A).

*At high **v,** an exceeding amount of latent heat may lead to reduction of the growth component in welding direction, grains start growing straight and the weld pool assumes a teardrop shape* [4 p.398]. [3 pp.53-58, 174-178].

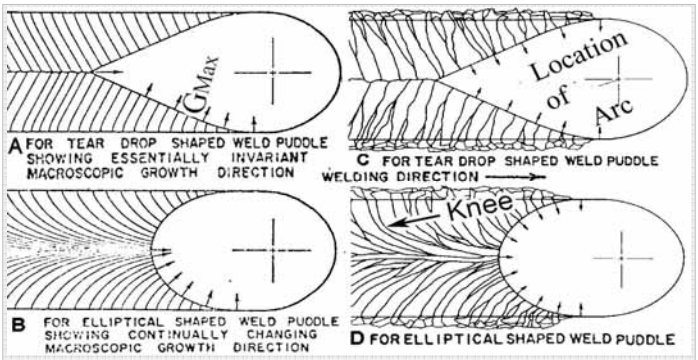

Fig. 1.25. Effect of welding speed **v** on puddle shape and form of **G** (***A** and **B***), and grain morphology (***C** and **D***).
Upper: High speed **v:** teardrop pool, **Lower**: Low **v:** elliptic pool
A and **C)** Maximum temperature gradient **G** direction is constant in teardrop welds; grains grow straight. **B)** In elliptic pools **G** curves; grains grow curved from **FL** to weld centerline. **D**) If they solidify EGS, change from one EGD to another, forms a **knee.** Based on Savage et al. [21][12]

1.1.20 Easy growth, grain shape and knees

The *easy growth directions* **EGD** of the cubic metals, most often <100> or <110>, enhance *easy growth solidification* **EGS** in the **EGD** closest to **G.** As **G** curves, a new **EGD** is chosen. This makes a knee into the grain (Fig 1.25 D).

Fig. 1.26 shows horizontal sections of Al welds. In **view a)** the grain marked **A** follows the temperature gradient **G,** which is

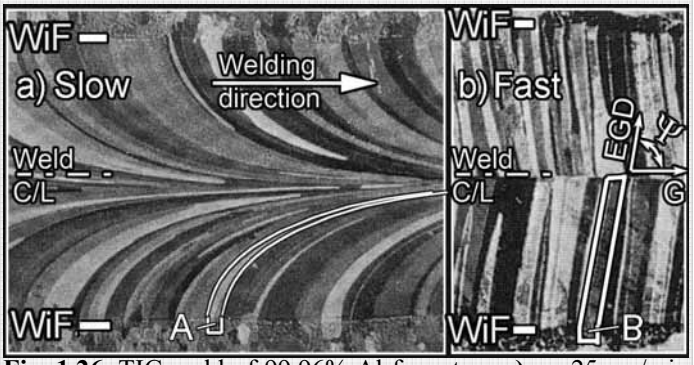

Fig. 1.26. TIG-weld of 99.96% Al from top. **a)** v= 25 cm/min **b)** v= 100 cm/min. Grains **A** and **B** are grains in HAZ, initiating growth from **FL** to weld C/L. Kou [3] orig. Arata et al. 1973: Trans JWRI, 2: 55. Modified

perpendicular to welding direction at **FL**, parallel to it at weld C/L and tilted in between. It has no distinct knees: either it experienced a *non-easy growth solidification* (**NEGS**), or its knees are quite subtle**.** In **view b),** the growing grain **B** ignores the **G** and follows tenaciously its **EGD** from **FL** to weld C/L**.** The angle **Ψ** in Fig. 1.26 for grain **B** at weld C/L is large: ~80^0.

1.1.21 Segregation to cell boundaries

Brooks and Garrison quenched stainless steel weld pool, obtaining a cooling rate high near the weld pool (right in Fig's 1.27A and 1.28). Fig's 1.27B and C show the microsegregation to solidification subgrain boundaries (SSGB's, subgrains in this occasion being cells), resulting from the transverse growth of the cells.

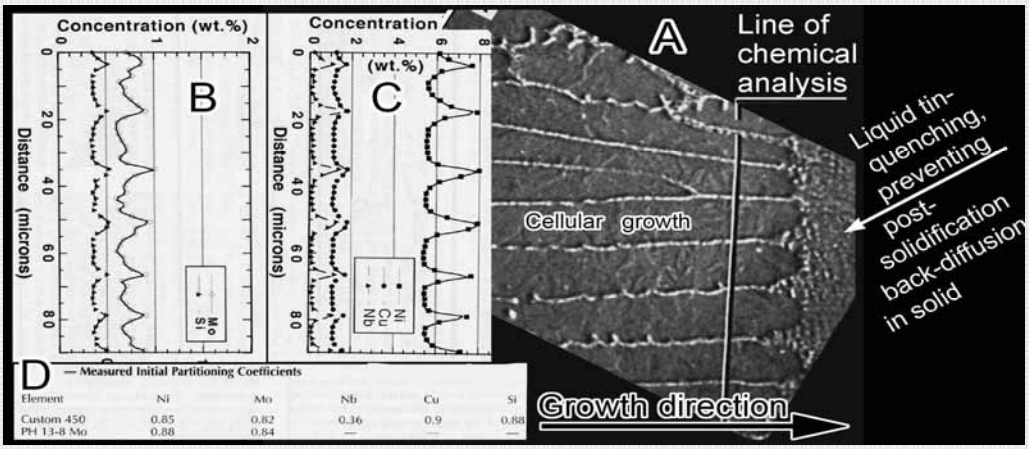

Fig. 1.27. Chemical line-analyses of the perpendicular microsegregation to the solidification subgrain boundaries SSGB (cell lines). **A:** Micrograph, **B** and **C:** Chemical line-analyses, **D:** Measured equilibrium distribution coefficients $\mathbf{k_0}$. Brooks, Garrison 1999 [38]

1.1.22 Post-solidification back-diffusion in welding

The quenching caused a cooling rate high near the weld pool (right in Fig. 1.28), slowing towards left in the figure. The cell lines are blurred towards left, evidently due to the *post-solidification back-diffusion*: diffusion during the weld cooling-stage. Chemical line-analysis corroborates this evening out of the cell line concentrations (Fig. 1.27 C, lower lines).

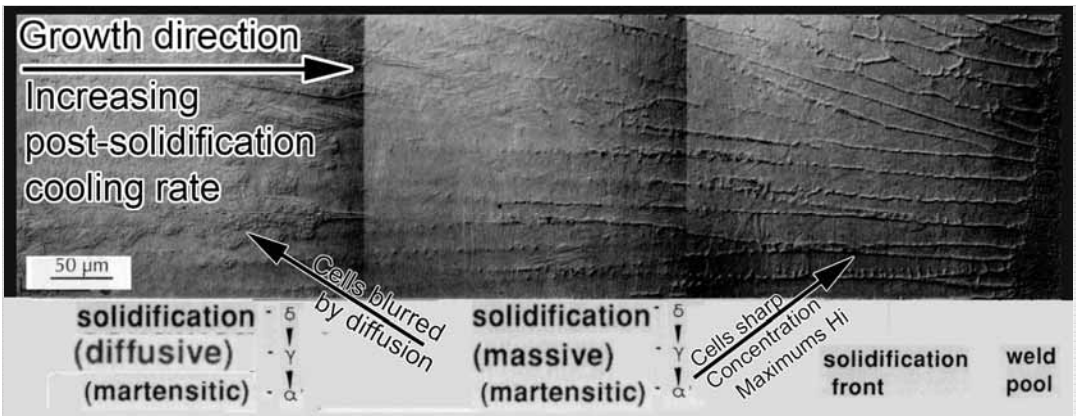

Fig 1.28. The area with increased post-solidification cooling rate (right side) has sharp cells, while in slow post-solidification cooling (on the left) the cells are blurred due to back-diffusion in solid immediately after solidification. Brooks, Garrison 1999 [38].

1.1.23 Weld pool forces and flows

A fusion weld pool is subjected to thermal, mechanical and electro-magnetic stirring. Its surface is stirred by temperature- and filler-dependent *surface tensions* [39][3], *electromagnetic forces* [40][41], weld arc with possible filler metal droplets causing *arc pressure* [42], and gas flow causing *gas shear (plasma drag)*. In the pool, an electric welding current causes electromagnetic *Lorenz forces*; *buoyancy* causes its temperature-dependent forces. All these cause flows in the pool, affecting its shape, penetration and solidification.

Direction of surface tension (γ) force (named also "*Maragoni force*" or "*surface gradient force"* referring to the gradient $d\gamma/dT$ [4]) may be altered, even reversed. Minute additions reversed the flow direction in Fig's 1.30 and 1.31.

The flows affect the weld form and penetration, mixing of the elements and evening out of temperature gradients. They affect also the solidification. Solute is rejected to liquid at the S/L-interface, and one of the central questions is what happens to this rejected solute. If the melt is thoroughly stirred, it distributes evenly in the remaining melt. With no stirring, the rejected solute remains in the melt near **C/L** and forms a pileup evening out only by diffusion. These two cases with seemingly small differences play a central role in solidification.

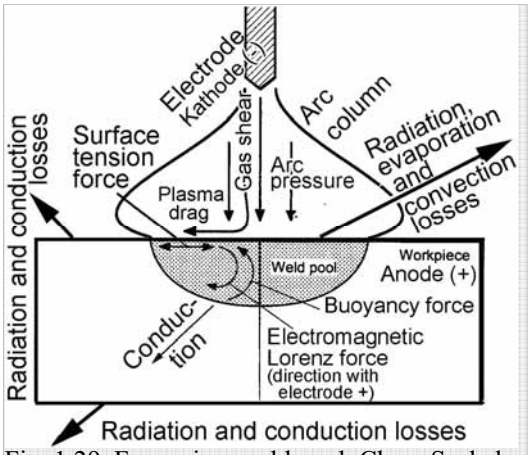

Fig. 1.29. Forces in a weld pool. Choo, Szekely, Westhof. 1992 [43] and Vilpas 1999 [57], origin. Winkler, Amberg, Inoue, Koseki. 1997 [44]

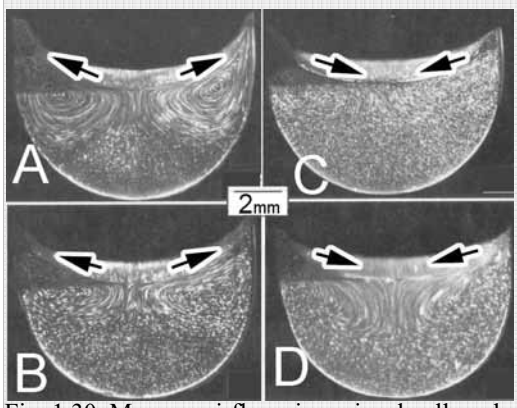

Fig. 1.30. Marangoni-flows in variously alloyed $NaNO_3$-basematerial laser welds. **(A)** No C_2H_5COOK, **(B)** 0,5% C_2H_5COOK. **(C)** 1.0 % C_2H_5COOK **(D)** 1.6% C_2H_5COOK. Arrow marks flow direction. Limmaneevichitr, Kou 2000 [45]

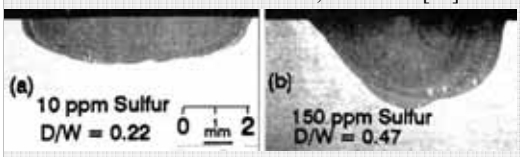

Fig. 1.31. Effect of sulphur on steel weld penetration. a) 10 ppm S, b) 150 ppm S Pierce, Burgardt, Olson. 1999 [46]

1.1.24 Stagnant layer

The speed of liquid running in a vessel is zero or insignificant from the vessel wall to a distance δ_h, forming the *stagnant layer,* where the melt is *unmixed* (Fig. 1.15). This layer forms the environment for the rejected solute pileup at the S/L-interface, it can only diffuse through the stagnant layer; there is no mechanical mixing.

The width of the stagnant layer δ_h is complex (Appendix 42), but we consider it wider than the width of the concentration gradient (ξ_{CG} in Fig. 2.13B); it usually is sufficient to hamper the total mixing of the rejected solute in a weld pool.

Absolute stagnancy of moving liquid at solid surface is questioned by Lichter et al. [47]. Faisst and Eckhardt published Fig. 1.32 showing local zero-velocities along tube wall. The existence of the stagnant layer is not questioned, only its evenness.

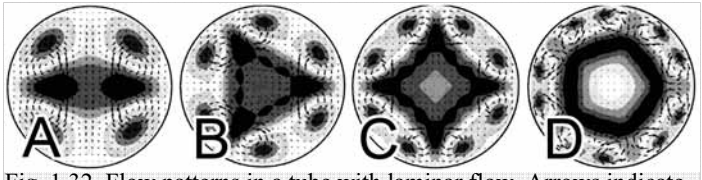

Fig. 1.32. Flow patterns in a tube with laminar flow. Arrows indicate transverse velocity component of liquid. Minute changes in conditions alter flow patterns radically. Faisst, Eckhardt 2003 [48]

1.1.25 Constitutional supercooling

A solute pileup (concentration gradient) at S/L-front (Fig. 1.33) lowers the solidification temperature with respect to melt further away. With gentle *actual temperature gradient* **G** (dashed line), the actual temperature stays below the effective solidification temperature over the distance **0-ξ_{CG}**; this is called *constitutional supercooling* **CS**. The effect of **CS** in microstructure is presented in Fig. 1.45 and its limit in Eq. 2.5.16.

If a chance protuberance forms on the S/L-interface, its tip is below the effective melting/solidification temperature of the surrounding liquid. This enhances cellular or dendritic growth.

*The temperature gradient **G** is always positive in a fusion weld and a pure metal - with no possibility to **CS** - will always solidify planar, with no cells or dendrites.*

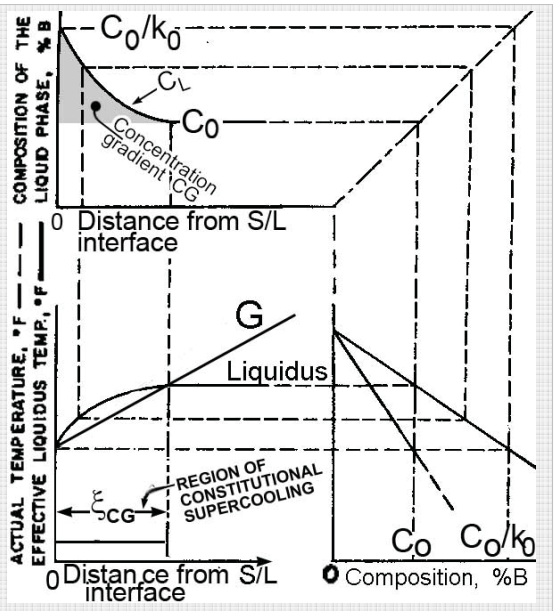

Fig. 1.33. Constitutional supercooling (**CS**). Concentration gradient **CG** lowers liquidus temperature towards S/L front. Adapted fr. Savage, Nippes, Miller 1976 [34] and Kou 2003[3 p.158]

1.1.26 Relation of Growth and Cooling rates and temperature gradient

Central parameters of solidification (Fig. 1.34): the S/L-interface growth rate *R,* the cooling rate $\Delta T/\Delta t = \dot{T}$ and the temperature gradient G, are interdependent according to Eq. 1.1.26, Kurz 1995 [50]:

$$\dot{T} = -GR \qquad \text{Eq. 1.1.26}$$

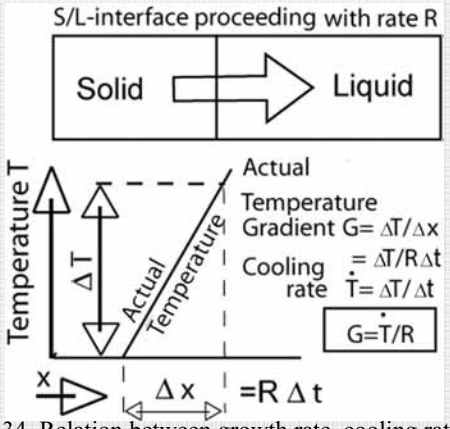

Fig.1.34. Relation between growth rate, cooling rate and temperature gradient on liquid side of S/L interface. Kurz Fisher 1998 [5] Eq. 4.20.

Vilpas measured solidification rates and growth rates in stainless steel welds in temperature region 800 to 1200^{0}C and added to these measurements similar data from literature, Fig. 1.35 [51], shows the temperature gradient varying between 100 – 1000 K/mm. We added our calculations for copper, marked **x,** into the figure

Equation 1.1.26 makes results of a vide variety of solidification types comparable. The plot in Fig. 1.35 is material-specific; the thermal conductance affects it, as the Vilpas' analysis on stainless steel - and our addition of results of copper to it - shows; temperature gradients are steeper in materials with higher thermal conductivities.

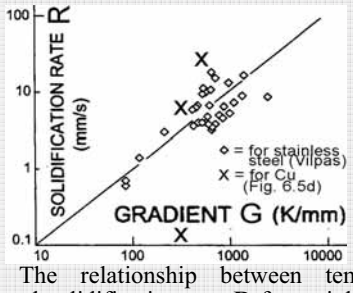

Fig. 1.35. The relationship between temperature gradient **G** and solidification rate **R** for stainless steel, calculated by Vilpas from his own measurements and data from literature. Vilpas 1999 [51], Suutala 1981 [52], Elmer 1988 [53], Katayamaja, Matsunawa 1984 [54]. Point x added by us from our calculations for Cu in Fig. 6.5d

1.1.27 Solute trapping

The rejected from S/L front solute atoms (Fig. 1.9) remain in melt and give way to the oncoming front by stepping back with diffusion jumps. As the increasing growth rate **R** reaches a critical value $\mathbf{R_{st}}$, a rejected solute atom has no time to make the diffusion jump into the melt and is *trapped* into the on-avalanching solid.

In Fig. 1.36 A) $\boldsymbol{\delta i}$ is the width of the zone from where the solute atom may escape to liquid in one jump; the S/L interface crosses it in time $\boldsymbol{\tau = \delta i/R}$. With Fick's laws, the diffusion time for the same distance is $\boldsymbol{\delta i^2/Di}$. This is a base for the mathematical modeling of this process.

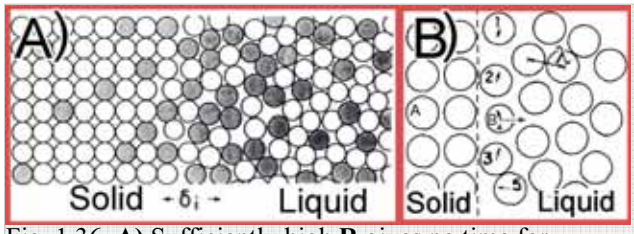

Fig. 1.36. **A)** Sufficiently high **R** gives no time for rejected solute atoms to diffuse from S/L line into melt; they get *trapped* in the fast approaching solid; equilibrium in not reached**.** $\boldsymbol{\delta i}$ is the *characteristic distance* (~atomic distance). Kurz, Fisher [5 p.135 and 220] **B)** *Rearrangement step* from liquid to solid lattice of atoms (vectors in atoms 1. 2, 3 and 5) is shorter than the distance between these atoms in liquid (λ).
A rejected solute atom **B** (number 4) should find its low-energy state in the melt (dashed longer arrow); the lattice (the solid arrow) - however- is closer. Aziz 1982 [7].

Solute trapping marks the end of microscopic equilibrium and the solidification mechanism changes radically, Aziz 1982 [7]. No cell formation can be expected; the front grows planar.

A growth rate increasing past the critical $\mathbf{R_{st}}$ leads to further changes: grains reducing to nano-cells and ultimately to amorphous metallic glasses with no detectable lattice We propose existence of an ultimate growth rate $\mathbf{R_\infty}$, after which increasing **R** brings about no changes to the solidified structure.

There is a critical $\boldsymbol{R_a}$*, above which the cellular structure also turns planar (Fig. 4.5). This is due to cell tip radius reducing below critical; it should not be confused with solute trapping*.

1.1.28 Hot cracking

We limit the hot cracking discussion to the following nine points:

<u>*1. Dendrite coherency*</u> <u>and *back-filling.*</u> The *back-filling* may be beneficial, as in the non-coherent region of Fig 1.37, or detrimental as with *backfill cracking,* (Ch. 1.1.16). The name with the dash seems to be used for the beneficial one in several references. *Dendrite coherency* hampers the back-fill healing of cracks. Maximum cracking is expected where *Solidification Cracking Temperature Range* (**SCTR**, Lippold, Lin 1996 [55]) coincides with a region of maximal coherency, which most likely is at the maximum solubility, point **B** in the upper, and region **II** in the lower part of Fig. 1.38. The shaded region is the coherent zone.

<u>*2. Eutectic reaction*</u>: Increasing eutecticum is expected to lessen the susceptibility to hot cracking (Fig. 1.38 at concentration C_e).

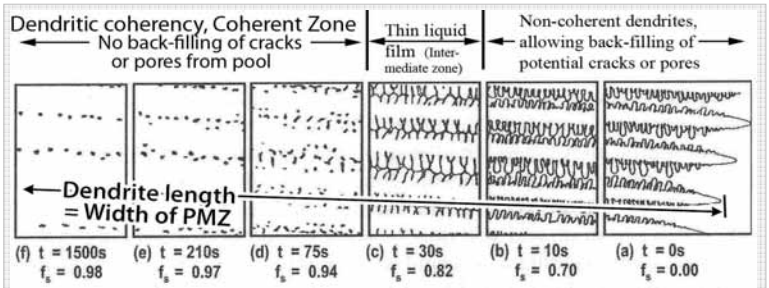

Fig. 1.37. Progressive stages of dendritic solidification demonstrating regions of liquid back-filling (**a-b**), thin liquid film (**c**), and dendrite coherency (Coherent Zone) (**d-f**). Cross2005 [56]

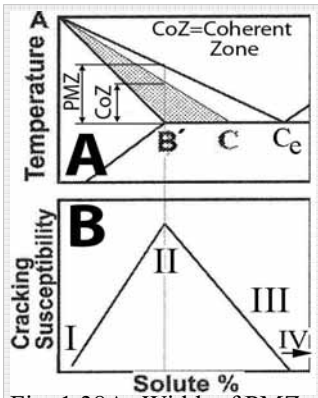

Fig. 1.38**A:** Width of PMZ and *Coherent Zone* in eutectic system. Maximum width at maximum solubility, point **B´**.
B: Cracking susceptibility. Cross 2005 [56] after Pumphrey [57]

The solidification range and the hot cracking susceptibility are inter-connected in eutectic systems, Fig.1.38. The solidification temperature range, divided by **G,** gives the width of **PMZ**, or the dendrite length from tip to the last non-solidified liquid in the coherency region in Fig.1.37. The maximum **SCTR** occurs in the alloy with solute content of maximum solubility (Fig. 1.38). This is the alloy with maximum hot cracking propensity..

3. Liquid rupture. Crack initiates only after the liquid films, *fenced-in* between the dendrites, rupture..

4. Centerline and grain/cell boundary hot cracks. As seen in Fig.1.39 (and our experiments), two types of fusion zone hot cracks are prominent in practice, namely: **(A)** hot cracks along the weld centerline (Fig.1.39**A**) and **(B)** hot cracks along grain and cell boundaries (Fig. 1.39**B**). Combinations of the two - **(C)** - are common. *Our results endorse the theory that a planar solidification front bulldozes the concentration gradient to the centerline [4 p.446][3 p.291], while solidification fronts consisting of needle-tipped cells and dendrites* ***fence-in*** *a part of the solute gradient at the cell/dendrite lines, spreading the solute more evenly across the fusion zone.*

5. Meshes of cracks. Fig. 1.39**B5** shows what appear to be meshes of cell boundary cracks intersected by perpendicular *cross-jump cracks.* These are similar to our findings in welds in Cu with **v**<100 cm/min, (see Ch.6.3.2).

The cracks in Fig. 1.39 ***B1*** *curve - along the cell- and grain boundaries - asymptotically towards the weld C/L. High welding speed may make the grains straight, non-curving, resulting in a head-on collision with the C/L, as with the two protuberances of the centerline crack* ***CL*** *in the laser weld in* ***C2*** *(see tear-drop weld pool form in Ch. 1.119).*

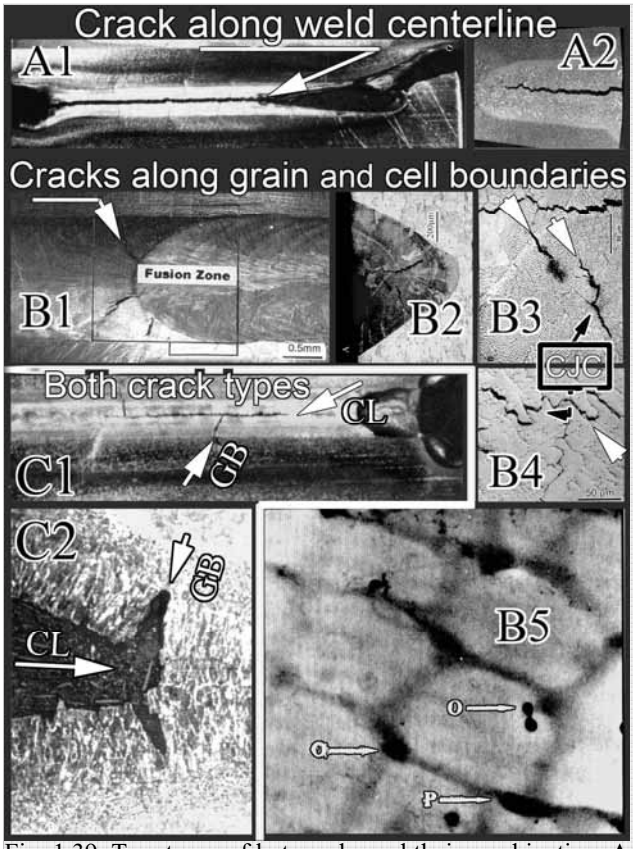

Fig. 1.39**.** Two types of hot cracks and their combination. **A:** Hot crack along center line. **A1** from Top; **A2** from side. **B:** Hot cracks along grain and cell boundaries. **B1** from top, **B2…4** from side.

CL= cracks in centerline and **GB** in grain boundary direction. **C:** Combination of the two from top and side.

Cracks in **B3…B5** form a mesh similar to found in our experiments on Cu. With inclusions (arrows **O** and **P**) they form what we call "*spongy cracking").* *B1: Lundin et al. [101], Brooks, Robino 2003[102]; C1:Feng et al. [103]; C2:Cam et al, [104]*

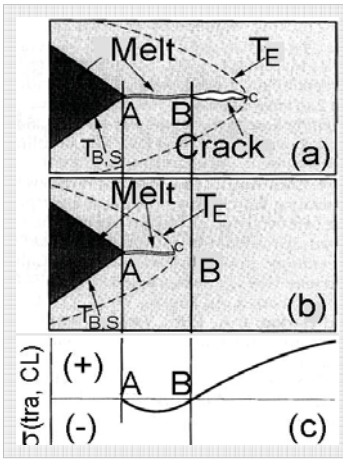

Fig. 1.40. Transverse stress $\sigma_{tra,CL}$ at the centerline behind the weld pool. Contraction of solidifying weld metal is balanced by compression of the solid. Zacharia 1994 [58] *Welding direction is from right to left.*

6. Equiaxed dendrites. The least susceptible growth morphology to hot cracking appears to be the equiaxed dendritic. It distributes the solute most evenly in the weld, albeit in the centerline region [3 p.188][4 p.445].

7. Dynamic stresses in weld metal hot cracking. Zacharia proposes the stress distribution in Fig. 1.40 Zacharia 1994 [58], showing a tensile (+) stress behind line **B** in the just solidified weld metal. *Visual inspection in our experiments suggests that cracks open a few millimeters behind the trailing pool end.* It is not impossible that between the lines **A** and **B** the crack is back-filled from the pool, and after line **B** the crack is in the *dendrite coherency region*, with the remaining liquid – not yet *rupturing* - giving the structure resilience. With this assumption, Fig. 1.40 would be well in accordance with Fig. 1.37

8.Hot cracking in aluminum.

Nil-segregation causes negligible hot cracking susceptibility in pure aluminum (Fig 1.41 a, b, c and d, area **I**). Increasing alloy composition increases this susceptibility to maximum at area **II**, where the amount of segregated low-melting alloy is sufficient to form a continuous network surrounding the grains but insufficient to back-fill the forming cracks. The decreasing hot cracking susceptibility in the region **II-III-IV** is due to an increasing amount of low-melting solute-rich melt - in these Al-alloys - not increasing cracks, but healing them by back-filling.

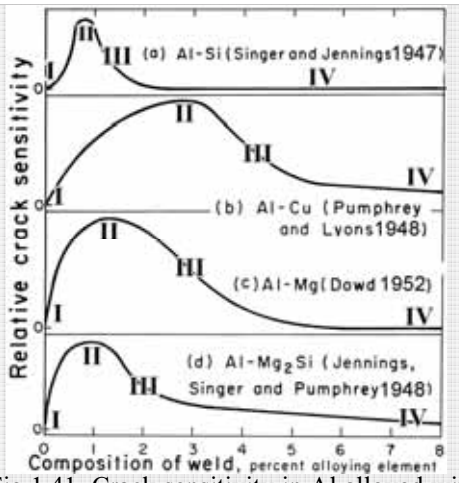

Fig.1.41. Crack sensitivity in Al alloyed with **(a)** Si, **(b)** Cu, **(c)** Mg and **(d)** Mg_2Si. Dudas and Collins 1966 [59]

9. Hot cracking in carbon steel.

In carbon steel, the cracking susceptibility is minimal at and below region **I** of Fig. 1.42 because high amount of δ-ferrite is able to dissolve harmful P [60]. The susceptibility may be minimal also at region **II** – following the dotted line in Fig 1.42 (a) - if no peritectic reaction occurs. Generally hot cracking susceptibility increases outside range of the peritectic reaction in region **III** with increasing **γ+L** range.

The possible peritectic reaction may cause deleterious hot cracking (Fig. 1.42 (a) solid line in the region **II**). This is a complex process including *weld metal shrinkage*, *changes of P solubility, of δ–γ- transformation kinetics* among others [60 p.31]. The peritectic reaction is problematic and the hot cracking occurs in it with varying kinetics, but the process has common features with the afore-described Al alloy cracking.

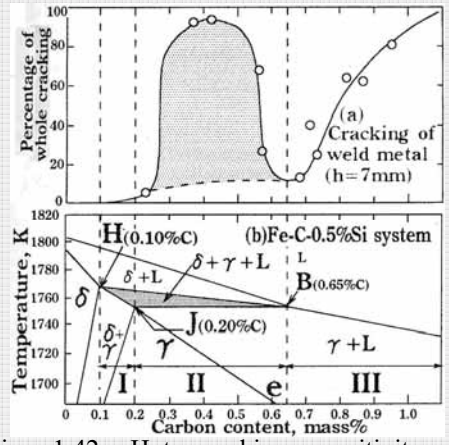

Fig. 1.42. Hot cracking sensitivity vs. equilibrium diagram of the Fe-C-0,5% Si system. Tamaki, Kawakami, Suzuki 2003 [60]

Fig. 1.43 is included as an example of an approach dividing the dendritic sub structures into cellular dendritic and columnar dendritic at least seemingly similarly as Savage (Fig's 2.19B, 2.22, 2.23 and Appendix 37).

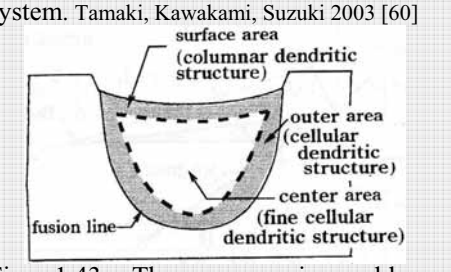

Fig. 1.43. Three areas in weld metal classified by the type of the dendritic structure. Tamaki et al. 2003 [60]

1.1.29 G, R, GR and G/R in welding

Fig. 1.44 presents the basic morphologies and thermal factors in a weld. Much of the general solidification theory is associated with single crystal manufacturing, zone melting and casting. Most of this theory applies readily to fusion welding, but some of its specifics should be appreciated. The nucleation stage and curved growth differentiate welding from most other processes. The growth rate **R** accelerating from zero to the welding speed in Fig. 1.44 **(b)** is a feature specific to fusion welding, seldom encountered in other applications. (This work handles fusion welding, other welding methods may - and often do - behave differently.) The plot of the temperature gradient of a fusion weld in Fig. 1.44 **(c)** experiences greater changes than in most other solidification types.

The cell width grows inversely to the product **GR**. The Fig. 1.44 **(d)** shows a maximum, after which the width grows with the decreasing product GR. *Cells* in cellular mode start wide, grow narrowing, but may – after the maximum - grow wider, and then begin to develop secondary arms. This is corroborated by Messler [4 p. 429].

In out experiments, both the product GR and the cell width grew smaller during the solidification (Fig. 6.5).

The **G/R** ratio, determining the morphology, usually diminishes monotonously from WiF to weld C/L, Fig. 1.44 **(e)**.

1.2 Descriptive classification vs. "Cases"

The oft-mentioned *descriptive classification* of the main solidification regimes is: **(1)** Equilibrium maintained at all times, **(2)** Liquid uniform in composition at all times, no solid diffusion, **(3)** No solid diffusion, no mixing except by diffusion in liquid, Chalmers 1962 [35 p. 251-253]. The wording alters by the author, but the idea is the same. The *Savage Casing System* (SCS) used in this dissertation for this classification calls the **(1), (2)** and **(3)** above *Case 1, Case 2 and Case 3* respectively and adds *Case 4 (Splat cooling).* The history of the SCS is discussed in Ch. 2.7.1 and its detailed résumé is in Ch. 3.

1.3 Growth modes

To finalize the general aspects in welding, Fig. 1.45 presents the solidification growth modes with the nomenclature used by today's mainstream research and this dissertation [3 p.159][4 p. 428][5 p.88][61].

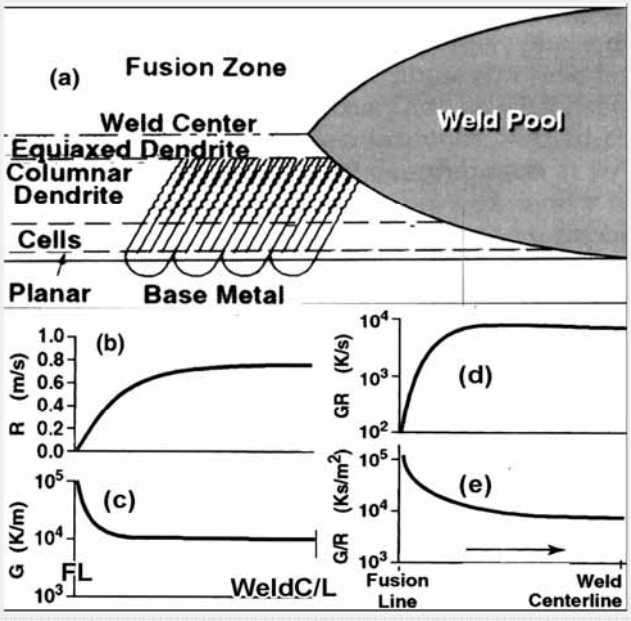

Fig. 1.44. **(a)** Weld microstructures **(b)** solidification rate **R**, **(c)** temperature gradient **G**, **(d)** product **GR** and **(e)** ratio **G/R.** David, Vitek, Babu, Boatner, Reed 1999 [62]

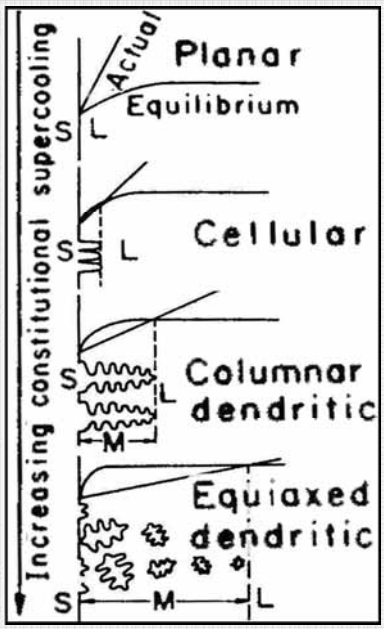

Fig 1.45. Solidification growth modes vs. the relative degree of constitutional supercooling. The present mainstream classification. Kou 2003 [3],Messler 1999 [4 p.428]

Chapter 2 SOLIDIFICATION RESEARCH IN THE 20th CENTURY

This chapter attempts to recapitulate evolution of solidification theory until the turn of the millennium. *Savage Casing System SCS* is used throughout the text with *Cases 1* to *4*, not known at the time.

2.1 Equilibrium solidification; Case 1

The mathematical modeling of the equilibrium solidification has been a milestone in the history of solidification. The solid solute concentration is controlled by Equation 2.1.1 and the development of the solute profile is in Fig. 3.1. The history of this equation dates further than the time span we searched. Gulliver seems to assume it to be known and does not present it in his works [63][64]. He does refer to Roozeboom 1899 [65], which was left out of our study. Obviously, the *lever rule equation* was known in the 19th century.

$$c_s^* = \frac{k_0 c_0}{1 + g(k_0 - 1)}$$

Eq. 2.1. The "lever rule equation". Solid solute concentration c_s^* during *Case 1* (equilibrium) solidification, after fraction **g** of the initial liquid has frozen. Pfann 1978 [2 p.10 Eq. 2.1]. The symbols correspond to Fig. *3.1* by Flemings 1974 [1 p. 33]

Equation 2.1 gives in the beginning – with solidified fraction **g** = 0 - the solid concentration $\mathbf{c_s^* = k_0 C_0}$. In the end - with **g** = 1 - the solid concentration $\mathbf{C_S = C_0}$. This seemingly primitive chain of events is the basis for the more complex solidification regimes.

2.2 Start of modern solidification theory; Gulliver and Case 2

Case 2 solidification was first mathematically modeled by G. H. Gulliver in 1913 [63]. Assuming no solid diffusion / perfect liquid mixing and using the notations in Fig. **2.1** with impressive calculus he worked out the Equation **2.2** for the proportion of the remaining liquid as a function of temperature. Then having the temperature, initial concentration and the constitution diagram, he solved the liquid as well as solid concentration at any proportion of the remaining melt numerically.

Gulliver himself called the solution a mathematical approximation but it may be as exact as the present ones.

The modern Gulliver-Scheil equation unites two factors **Θ** and **Φ** in Fig. 2.1 into one $\mathbf{k_0}$, thus facilitating the analytic solution Eq. $2.4.1_{GS}$.

From the times of Gulliver until mid of the century the only "solidification cases" were *equilibrium solidification* (*Case 1*) and this "*rapid cooling"* meaning *Case 2*.

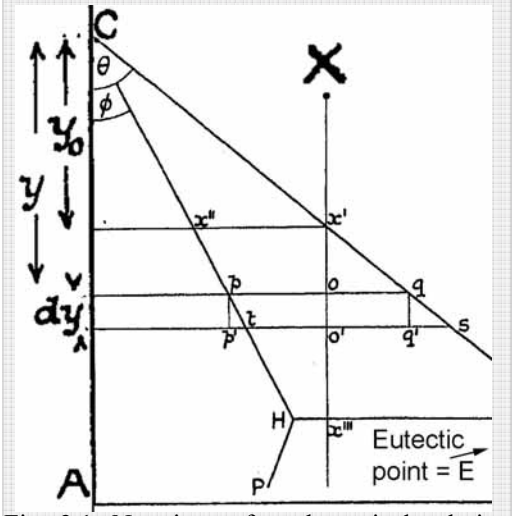

Fig. 2.1. Notations of mathematical solution Gulliver equation. Temperature **y** is measured down from melting point of the pure metal.

$$\text{Proportion of liquid (rapid cooling)} = \epsilon^{-\frac{\tan\theta}{\tan\theta - \tan\phi} \cdot \log_e \frac{y_r}{y_0}}$$

Eq. 2.2. Proportion of liquid as a function of the temperature difference **y**. **ε** = Euler's base of the natural logarithm. Factors as in Fig. 2.1, Gulliver G.**H**. 1913 [63 p.134]

2.3 Scheil during WWII

Erich Scheil developed a second solution for the *Case 2* solidification in 1942 [66]. The approach is similar (not identical) to that of Gulliver's, made 29 years earlier[10]. He came to the seemingly simple equation 2.3.A using terms of Fig 2.2. Further Scheil analyzed numerically binary constitutional diagrams and plotted the width **Δx** vs. proportion of remaining liquid/initial liquid ($\mathbf{m_S/m_{S0}}$, Fig. 2.3 with plots for three binary alloys). Using this data and a solution of the equation 2.3.A he solved the $\mathbf{m_S/m_{S0}}$ -relation and the portion of remaining liquid. Equation 2.3.b and Fig 2.4 have this relation for Au-Ag-system.
Scheil enlarged this method into eutectic, peritectic and simple ternary systems.

The next step in the evolution of the modern *Scheil-* or *Gulliver-Scheil-equation* is the analytical solution presented by *Pfann*.

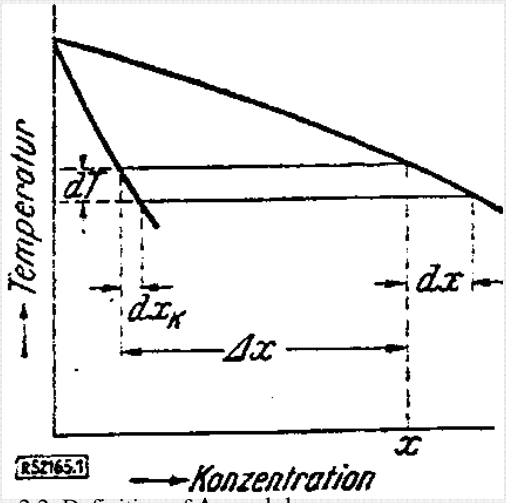

Fig 2.2. Definition of **Δx** and dx

$$\frac{dm_s}{m_s} = -\frac{dx}{\Delta x}$$

Eq. 2.3A. Amount of remaining liquid (Schmelze) $\mathbf{m_s}$ over initial liquid $\mathbf{m_{s0}}$. as a function of the terms in the previous figure. Scheil 1942 [66]

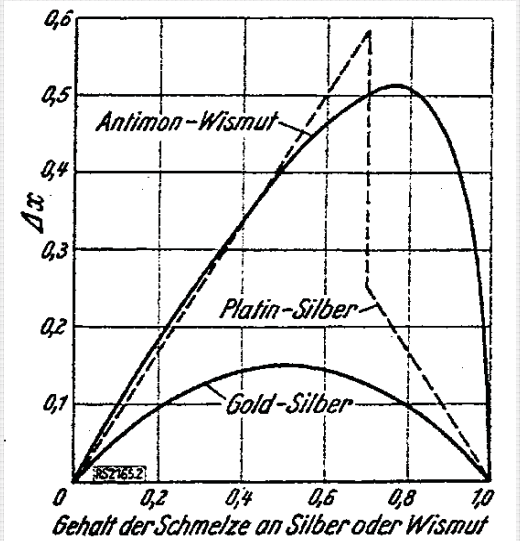

Bild 2. Breite Δx des Zweiphasengebietes dreier Legierungsreihen

Fig 2.3. The width of Δx vs. the proportion of remaining liquid for three alloy metal systems. Scheil 1942 [66]

$$\frac{m_s}{m_{s0}} = \left(\frac{x_0}{x}\,\frac{1-x}{1-x_0}\right)^{\frac{1}{0,6}}$$

Eq. 2.3.B.

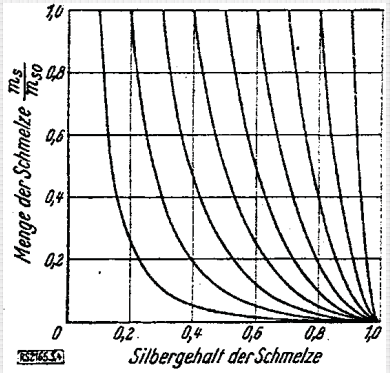

Bild 3. Konzentration-Mengen-Kurven bei der Erstarrung von Gold-Silber-Legierungen

Fig2.4. **Δx** vs. the proportion of remaining liquid for three alloy metal systems. Scheil 1942 [66]

[10] Scheil writes: "At the end, the author was made aware of a work by J.M.Gulliver handling the same area" [66 p.72]. This may mean that he did his work independently of Gulliver. It may also be the best a German researcher could say of a Briton in 1942.

2.4 Bell Laboratories; Burton, Primm & Slichter, Pfann's Cases

Working in The Bell Laboratories – the birth place of the transistor - *Burton, Primm, Slichter* and *Pfann* made impressive solidification research, as the examples in Fig. 2.5: **A):** Controlling growth rate with a concentration-dependent resistivity-drop, crystals with even concentration are produced. **B):** Bands in Ge-Sb crystal cause fluctuations in physical properties *(radiograph density **BA**, electrical resistivity **BB** and hole lifetime **BC**)*. **C):** Bands form in mildly stirred Ge-crystals *(CA and CB, 4rpm stirring)*. **D):** No bands in well-stirred crystals *(DA and DB >60rpm)*: stirring destroys bands. These arbitrarily chosen examples represent remarkable expertise in 1953.

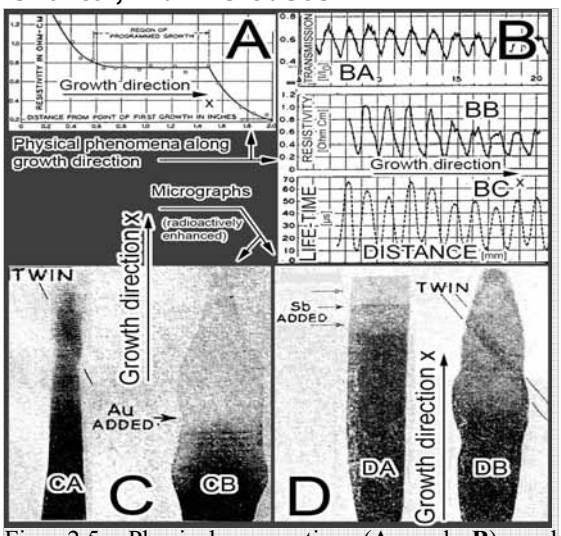

Fig. 2.5. Physical properties (**A** and **B**) and morphology (**C** and **D**) along single crystals. Burton, Prim, Slichter 1953[67]

2.4.1 Gulliver-Scheil equation with k_0

The same Burton, Primm, Slichter and Pfann seem to present first the *Gulliver-Scheil equation* in its present analytic form (Eq. $2.4.1_{GS}$). Authoritative back up for this comes from Chalmers, who, discussing this equation in *Principles of Solidification* [13 p.140] refers to Pfann [2]. New is $\mathbf{k_0}$, *equilibrium distribution coefficient*. The solid concentration is plotted in Fig. 2.6.

$$C_s = k_0 C_0 (1 - f_s)^{k_0 - 1}$$

Eq. 2.4.1GS. The Gulliver-Scheil equation by Pfann. C_s = *Solid concentration* f_s = *solidified fraction* k_0 = *equilibrium distribution coefficient.* C_0 = *Nominal composition. Pfann 1978 [2]*

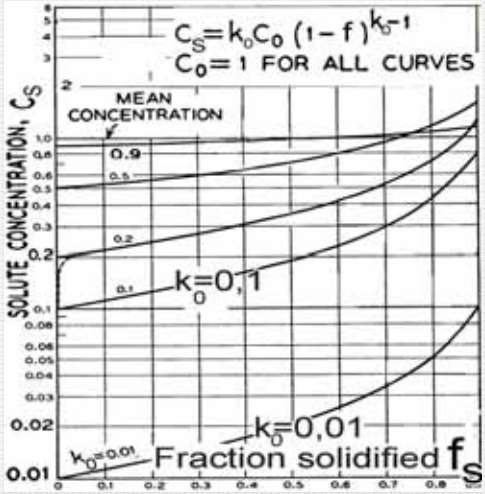

Fig. 2.6. *Case 2* solid solute concentration $\mathbf{C_s}$.

2.4.2 Pfann's Cases - Concentration gradient

Pfann divided *normal freezing* (no solid diffusion) into three cases: **(1)** complete liquid mixing **(2)** partial liquid mixing and **(3)** no stirring in the liquid solute transport by diffusion only.

This is not the Savage system *SCS*[11]: Pfann's case **(1)** = *SCS Case* 2, Pfann's case **(2)** = *SCS2 Sub-Case 2(+)CG (Ch. 4),* Pfann's case **(3)** = Savage's *Case 3*

Pfann's Casing System deserves all respect, but we must not confuse the two systems. In this dissertation, *Case* (in italics) refers to the Savage's *Cases* (Ch. 1.2).

Pfann added a concentration gradient to *Case 2*, and modeled this combination using the Gulliver-Scheil equation replacing its $\mathbf{k_0}$ with the *Burton-Primm-Slichter-effective distribution coefficient* $\mathbf{k_e}$, Equation $2.4.2_{BPS}$ [2][67]. The terms **f** and δ are test parameters of [67] and their determination is outside the scope of this dissertation, (the exploitation of this approach as a *Sub-Case* is discussed in Ch's 4.1.2 and 4.1.4).

Flemings 1974 [1 p41] handles this "Sub-Case", referring to Wagner 1954 [68], with no cross-reference to Pfann, Burton, Primm or Slichter. Pfann also refers to it briefly [2 p.22]. We have not studied this research line.

$$k_e = \frac{1}{1 + \left(\frac{1}{k_0} - 1\right) e^{-f\delta/D}}$$

Eq. 2.4.2BPS. Burton-Primm-Slichter-*Pfann* equation. $\mathbf{k_e}$ = *Effective Distribution Coefficient* (Eq. 2.4.1GS gives solute distribution of *Sub-Case 2*(+)CG, if $\mathbf{k_0}$ **is** replaced with $\mathbf{k_e}$), f=flow velocity, δ=layer thickness. **D** = diffusion coeff. Pfann 1978 [2 p. 15 Eq. 2.7].

[11] SCS, mentioned in Ch. 1.2, will be discussed more in detail later in Ch. 2.7.1.

2.5 University of Toronto; ~1950, Chalmers, Rutter & Tiller

2.5.1 Cells

Professor Chalmers and his graduate student Rutter of University of Toronto published in 1953 evidence of *cells* ("corrugations") on tin single crystals (Fig. 2.7). The cell centers protruded above and the boundaries lagged behind the solidification front. Solute redistribution controlled the solidification even in the 99.9 pure Sn.

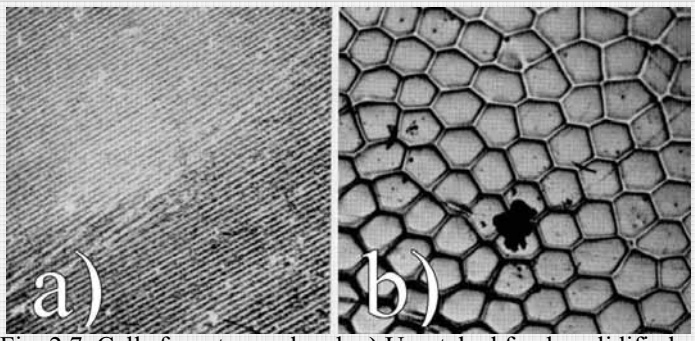

Fig. 2.7. Cells from top and end. **a)** Un-etched freely solidified single crystal top with cells in solidification direction. ~20x. **b)** Decanted cell ends with hexagonal structure. Cell peaks are above and the boundaries are below the surface. ~100x. 99.986% Sn. Rutter and Chalmers 1953 [69]

2.5.2 Cell width, R and G

Increasing growth rate **R** reduced cell width; tips grew more convex. In addition, increasing temperature gradient **G** reduced cell width. (Fig 2.8).

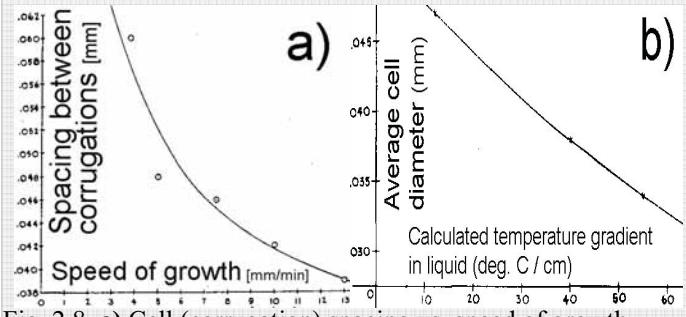

Fig. 2.8. **a)** Cell (corrugation) spacing vs. speed of growth **b)** Cell diameter vs. temperature gradient **G** in liquid at FL. **R** = 5mm /min. Rutter and Chalmers: 1953 [69]

2.5.3 Preferred growth orientation

At <u>low growth rates</u> cells grew opposite to heat flow direction, at <u>high growth rates</u> in the tin lattice [110] direction (Fig.2.9 **a**). This was detected also by Teghtsoonian and Chalmers 1951 [70]. Later were found other easy growth directions, e.g. [100].

2.5.4. Transverse diffusion

Rutter and Tiller proposed transverse solute diffusion enhancing growth of the first born protrusion **B**, which feeds solute from its gradient sideways towards point **C,** thus lowering freezing point at **C,** Fig. 2.9 **b)** This hampers initiation of potential protrusions at **A**.

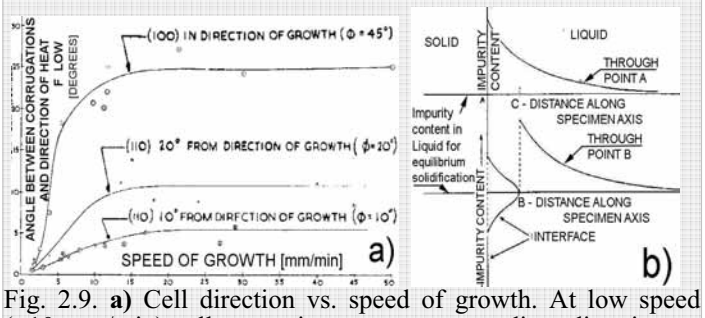

Fig. 2.9. **a)** Cell direction vs. speed of growth. At low speed (<10 mm/min) cells grow in temperature. gradient direction, <u>at high speed</u> (>15mm/min) in easy growth direction [69 Fig. 19]. **b)**. Planar S/L-interface with a first born protrusion at **B** feeding solute in transverse direction. [69 Fig.29]

2.5.5 Bands

Bands running ~ perpendicular to overall growth direction were found, Fig. 2.10; Tiller, Jackson, Rutter and Chalmers [71] interpreted banding as growth rate **R** fluctuations, affecting solute distribution as in Fig. 4.4. A profound explanation was given by Chalmers [13 pp.152-154], based mainly on Landau 1958 [72]. This explanation is still accepted, Flemings. 1974 [1], David, Vitek 1989 [61], Kou 2003 [3 p.163], Messler 1999 [4 p. 307 and 364] and others.

Theory of banding has been clarified and affirmed experimentally by Mollard and Flemings 1967 [73, Sn-Pb-alloy] and Kou [3 p.250].

2.5.6 From cellular to planar structure with growing G/R

The cellular structure was found to break down to *planar* at high gradients **G** and low growth rates **R** (Fig 2.11)[12]. This first finding of the planar growth remained poorly understood for long; it did not find its way to Fig. 2.12 a) or b). Its renaissance came with study of fusion welds with their $\mathbf{G=G_{Max}}$ **and R** = 0 at the fusion line (Fig. 2.19B).

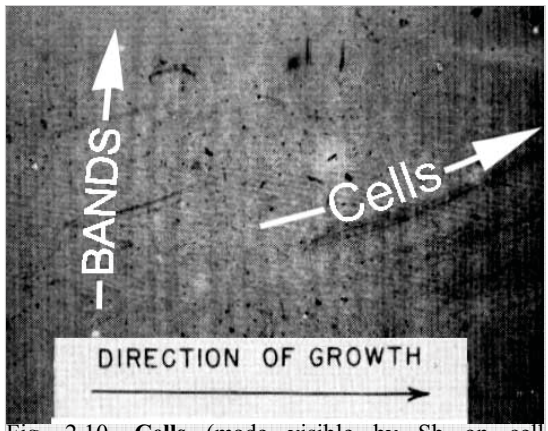

Fig. 2.10. **Cells** (made visible by Sb on cell boundaries) and **Bands**. Autoradiograph of lead containing approx. 0,05% radioactive antimony, added to 99,999% pure Pb. ~ 4x. Rutter and Chalmers 1953 [69]]

2.5.7 $G/\sqrt{R}$ - C_0 analysis

Cell diameter was found to increase with growing initial solute concentration $\mathbf{c_0}$. [69].

The $G/\sqrt{R}$ - concentration analysis from 1957 appears up to date today. That it lacks the planar zone may be because the crystal pulling conditions do not include sufficiently high **G** to produce one.

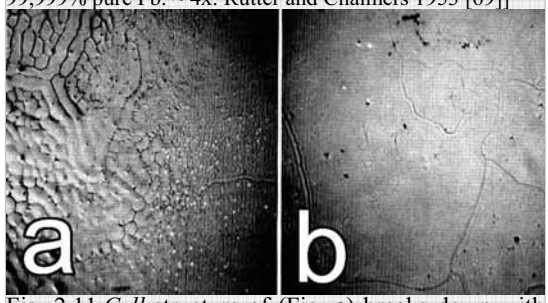

Fig. 2.11.*Cell* structure of (Fig. **a**) breaks down with high **G** or slow **R** (Fig. **b)**. Rutter and Chalmers 1953 [69]

2.5.8 R-G analysis

Fig. **2.12**. **b)** displays an early solidification analysis with **R-G** coordinates. The *degenerate* (or *lamellar* structure) is where modern knowledge places *planar* structure (Fig. 5.1). One reason why the planar growth was discovered relatively late (Ch. 2.7.4) may be that it occurs with low cooling rates allowing post-solidification SGB migration (Ch. 1.1.13), which was identified as *degenerate.*.

2.5.9Facetted growth

Tiller proposed that slow growth rate and minute super-cooling enhance d facetted growth, Fig. 2.12 **b**).

2.5.10. Sub-structure within cells.

The pioneers found cell sub-structures they called facetted and lamellar (Fig. 2.12. **c)** and **d)**. The cells apparently may have various sub-structures.

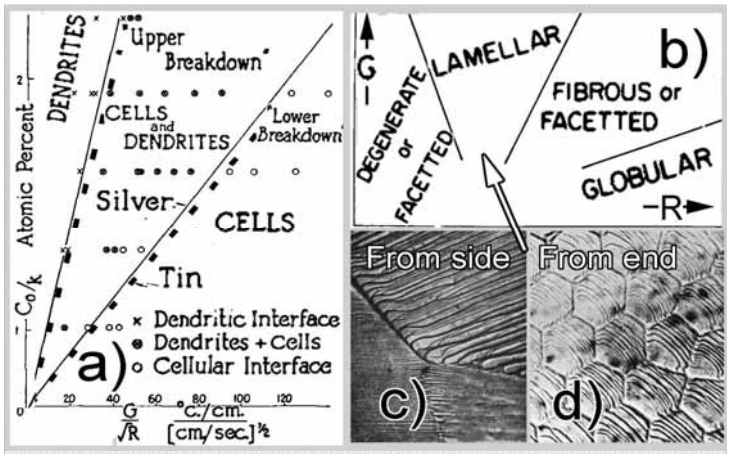

Fig. 2.12. Early presentations of solidification morphologies. **a)** $G/\sqrt{R}$ **-C_0/k-**analysis (Pb-*Ag (solid line) Sn-Ag (dashed, x-scale qualitative)*).
b) in **R-G** field. No planar mode. **c)&d)** cells with substructure from side and from end. Pb +500ppm Ag. **a)** Holmes, Rutter, Winegard 1957 [74], **b)…d)** Tiller Cahn (ed) 1970 [6 p.403]

[12] This is a reversible process. In fusion welding the ratio G/R diminishes along the solidification; first forms usually a *planar zone*, followed by a *cellular zone*.

2.5.11 Solute redistribution in *Case 3*, Classic approach

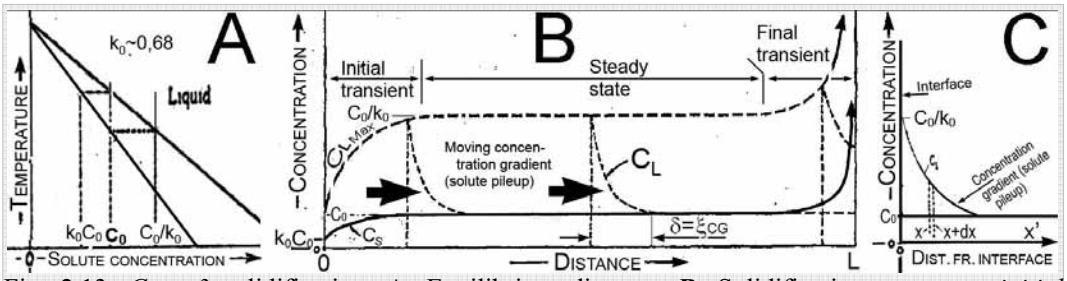

Fig. 2.13. *Case 3* solidification. **A**. Equilibrium diagram. **B.** Solidification sequence: *initial transient* (left), steady state (middle) and final transient (right). $\mathbf{C_S}$ and $\mathbf{C_L}$ in the liquid. $\mathbf{C_T}$ is the top concentration of the concentration gradient. **C.** Steady state Liq. concentration gradient C_L, at C/L. Tiller, Jackson, Rutter, Chalmers 1953 [71]

Rutter, Chalmers, Tiller, Jackson and Smith 1953-1955 [71][49] solved the concentration distribution in *Case 3* solidification (Fig. 2.13 **B** and **C**).

2.5.12 Concentration gradient

In Eq. 2.5.12 diffusion lowers the concentration in the volume element in Fig 2.13 **C** as much as the velocity - bringing new atoms - raises it. Equation 2.5.13 is the solution for the gradient.

D/R = characteristic distance; multiplied by 5, it gives an approximate value for the width of the concentration gradient) ξ_{CG} *[4 p.417].*

$$\xi_{CG} = 5\ D/R \qquad \text{(Eq. 2.5.12A)}$$

$D=5\cdot10^{-5}cm^2/s$ and R=0.2cm/min [12p19] gives ξ_{CG}= 5 3=~15μm.

2.5.13 Initial transient solution

Eq. 2.5.14 is the solid concentration in the initial transient *(More exact in [49 Eq.10][5 Eq.13.60 p.421]).*
k_0=0.86, $D=5\cdot10^{-5}cm^2/s$ and R= 0.2cm/min give the initial transient an approximate width 20μm[12p19].

2.5.14 Final transient solution

Equation 2.5.15 is an approx. solid concentration of the final transient. Its width ξ_G= ~15μm

2.5.15 Constitutional supercooling

Combining Equation 2.5.13 with temperature gradient **G** gives limit for constitutional supercooling, Equation 2.5.16.

2.5.16 Cellular to dendritic change – $G/\sqrt{R}$

In 1956 Tiller and Rutter [75] reported that the planar to cellular transition relates to G/R and in 1957 that the transition from the cellular to dendritic interface relates to $G/\sqrt{R}$ (Fig. 2.12 **a**).

$$D\frac{d^2C_L}{dx'^2}+R\frac{dC_L}{dx'}=0$$

Eq. 2.5.12. The solute pileup in Fig. 2.13 **C.**
x'= distance from S/L-interf.

$$C_L = C_0\left\{1+\frac{1-k_0}{k_0}\exp\left(-\frac{R}{D}x'\right)\right\}$$

Eq. 2.5.13. The solution for the former for the steady state. Tiller et al, 1953 [71].

$$C_S=C_0\left\{(1-k_0)\left[1-\exp\left(-k_0\frac{R}{D}x\right)\right]+k_0\right\}$$

Eq. 2.5.14. Solid concentration in initial transient (Fig. 2.13 **B**) [71]. *Characteristic distance D/k_0R.*

$$\frac{C_S(x_2)}{C_0} = 1+3\left(\frac{1-k_0}{1+k_0}\right)\epsilon^{-2(R/D)x_2}+5\frac{(1-k_0)(2-k_0)}{(1+k_0)(2+k_0)}\epsilon^{-6(R/D)x_2}+\ldots +(2n-1)\frac{(1-k_0)(2-k_0)\ldots(n-k_0)}{(1+k_0)(2+k_0)\ldots(n+k_0)}\epsilon^{-n(n+1)(R/D)x_2}+\ldots$$

Eq. 2.5.15. Solid concentration in final transient in Fig. 2.13 **B.** Tiller, Jackson, et al. 1953 [49]

$$\frac{G}{R}=\frac{mC_0}{D}\frac{1-k_0}{k_0}$$

Eq. 2.5.16. Limit for constitutional supercooling; **m**=liquidus slope. Tiller, Jackson, et al 1953 [71][75]
$\mathbf{k_0}$ = equilibrium distribution coefficient,
$\mathbf{c_0}$ = nominal concentration, $\mathbf{c_L}$, $\mathbf{c_S}$ = liquid and solid concentrations, **D** =solute diffusion coefficient in the liquid, **R** = solidification rate
x = distance, **x'** = distance in liquid from S/L-front

2.6 MIT; Flemings and Mullins & Sekerka

2.6.1 Flemings

This dissertation attempts to limit to monophase alloys, but eutectics could not be avoided in the experiments.

If $\mathbf{C_0} > \mathbf{C_{SM}}$ in Fig 2.14A, the solidification includes a eutectic reaction. Flemings presents for it a *Sub Case 2(+)CG-type* model (see Ch. 4.1.2) in Fig. 2.14C [1 p.128-130]. This model leads to morphology of the type in Fig. 2.15.

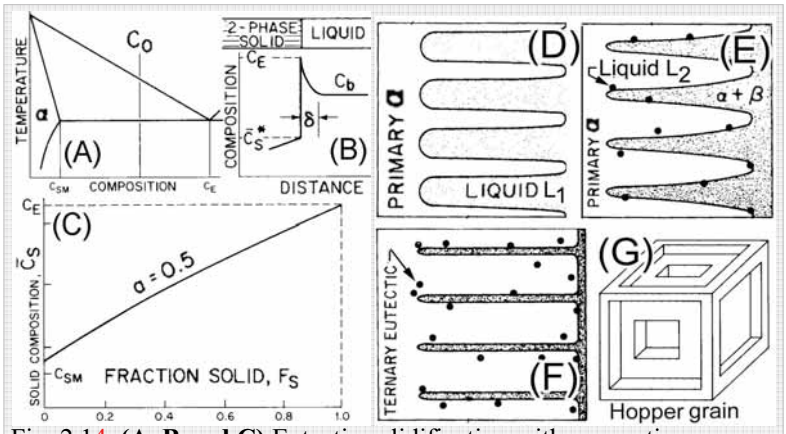

Fig. 2.14. **(A, B and C)** Eutectic solidification with convection. **(D, E and F):** Ternary alloy solidifying. **(D)**: Primary α phase forms **(E)**: *Divorced* pseudobinary eutectic forms isolated liquid L_2 droplets. **(F):** The L_2 droplets solidify as ternary eutectic globules. **(G)**: Hopper crystal, found in facetted growing metals, e.g. Bi. Flemings 1974 [1][73]

For reasons discussed in Ch. 6.2.7, this binary model does not seem to apply to our experiments. The presented in Fig's 2.14 D, E and F solidification mechanism of ternary eutectics lead to isolated ternary eutectic globules. Such globules were typical in our experiments; our doping led obviously to ternary reactions. .

The hopper crystals in Fig 2.14 G resemble the *cubelettes* found in copper. Their behavior remained unsolved by us.

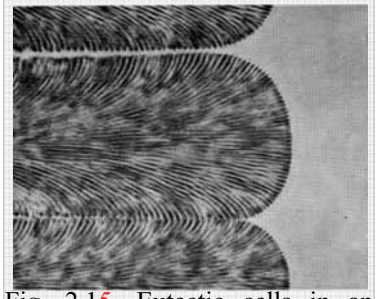

Fig. 2.15. Eutectic cells in an organic alloy [1], Jackson 1972 [76]

2.6.2 Mullins & Sekerka – interface stability

Case 3 theory based on *constitutional supercooling* concept (**CS**) is criticized for **(i)** not taking into consideration energy of the newly forming cell/dendrite surfaces, **(ii)** considering only temperature gradient **G** and **(iii)** not giving any indication of the scale of the cells/dendrites [5 p226][77].

The Mullins & Sekerka-approach models slow breakdown of an initially stable S/L interface (with a small initial perturbation **2ε**, Fig. 2.16) with the initial equations 2.6.2; concentration is only for liquid. This method has largely replaced the traditional **CS**-approach of Ch. 2.5.11 for *Case 3*. M&S-approach applies to the range of **R** from the S/L front instability $\mathbf{R=R_C}$ (start of cellular growth) until the *marginal stability limit* $\mathbf{R=R_a}$ (Fig's 4.5 and 5.4); the method serves as an intermediate *Sub-Case* in this **R**-range (Ch. 4.2.2).

Fig. 2.16. Mullins & Sekerka S/L-interface. y-axis is parallel to S/L-interface growing in z-direction. The analysis resolves whether or not the small turbulence 2ε will grow (cellular growth with inter-cellular width λ) or decay (planar growth)

$$\frac{\partial^2 C}{\partial y^2}+\frac{\partial^2 C}{\partial z^2}+\frac{R}{D}\frac{\partial C}{\partial z}=0 \quad [a]$$

$$\frac{\partial^2 T_l}{\partial y^2}+\frac{\partial^2 T_l}{\partial z^2}+\frac{R}{a_l}\frac{\partial T_l}{\partial z}=0 \quad [b]$$

$$\frac{\partial^2 T_s}{\partial y^2}+\frac{\partial^2 T_s}{\partial z^2}+\frac{R}{a_s}\frac{\partial T_s}{\partial z}=0 \quad [c]$$

Eq. 2.6.2. Mullins & Sekerka fields of liquid concentration **C** [**a**], and temperature field $\mathbf{T_l}$ for liquid[**b**] and T_s for solid [**c**]. **R**=growth rate and **D**=diffusion coefficient. Kurz, Fisher [5 p.226], Mullins, Sekerka 1964 [77]

2.7 RPI; Savage

A group of scientists in Rensselaer Polytechnic Institute or RPI (USA) concentrated in mid-19th century in welding and weld solidification. Professors W.F. Savage and E.F. Nippes with their associates started applying solidification theory in welding. With proliferated publishing and two major experiment methods - *Gleeble* and *Varestraint* - this work still affects modern welding metallurgists.

2.7.1. Savage Casing System *SCS*

In this dissertation, we use what we call *Savage Casing System SCS* used by Professor Savage in teaching and research (Fig. 2.17). He did not introduce it as his own. In [12 p.93] he refers to Smith et al. 1955 [49], which – however – does not contain any Case-classification, but refers to Pfann. Pfann 1952 [78] does divide solidification regimes in Cases, but his casing system is different (see Ch. 2.4.2).

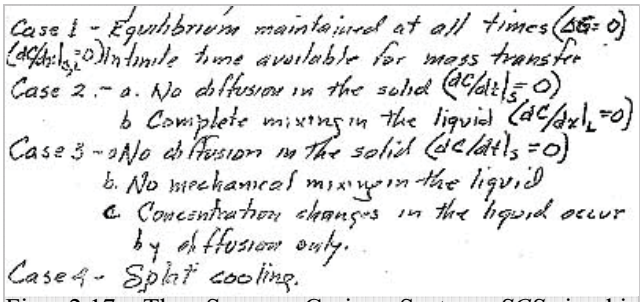

Fig. 2.17. The Savage Casing System *SCS* in his handwriting. From his notes [79], "priceless (but unpublished) purple-on-white mimeo notes" Messler [4, p. 463]. *We interpret Case 4 as the region from start of the solute trapping to the ultimate instantaneous cooling.*

Chalmers numbered "three simple cases 1, 2 and 3" identically with *SCS,* [35 pp. 251-253], but he never returned to this numbering thereafter; in *Principles of Solidification* [13] he used the descriptive classification.

We advocate *SCS* for its shortness. The descriptive classification suits to the study of the particulars of a regime: *SCS* is better suited for comparing the regimes and visualizing their mutual relations. (The descriptive classification and its comparison with the *SCS* are discussed in Ch. 1.2.)

David and Vitek [30][61] and DebRoy & David [80 p.104] use the three first *Cases* identically to *SCS*. This approach may have born independent of Savage. Messler [4 p.407] includes the fourth *Case*.

2.7.2. Cells

Fig. 2.18a shows a weld from top; the grains grow from the fusion line towards the weld C/L. Distinct *knees* are seen (Ch.1.1.20); the growth forms *axial grains* aligning with the welding direction.

Inside, the RPI group found the first *cells* in welds, Fig 2.18b, much like the Toronto pioneers did for single crystals in Fig. 2.7. The basic geometry is similar, the hexagonality may be questioned but the cell tips protrude above the cell boundaries.

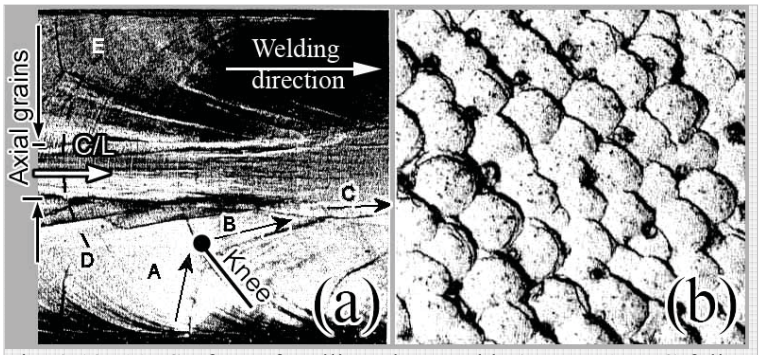

Fig. 2.18. **(a).** Surface of a silicon iron weld. Arrows **A-B-C** follow *cells,* changing growth direction from one *easy growth direction* **EGD** to the next at a *knee*. Lines **DE** are *ripples*. Note the *axial grains* at the C/L. Approx. 10x.
(b). Perpendicular cross-section. Special etching reveals a 3-dimesional surface relief of the cells. Approx. 500X. Savage, Lundin. Aronson 1965 [31].

2.7.3 From four to five weld metal solidification modes

Savage continued the work of Holmes et al. (Fig. 2.12a) in Fig. 2.19. In 1965 the number of proposed weld solidification growth modes was four (Fig. 2.19 A), in 1980 five (Fig. 2.19 B): **(1)** Planar, **(2)** Cellular, **(3)** Cellular dendritic *(named originally so by Chalmers [13 p.164], nowadays Columnar dendritic),* **(4)** Culumnar dendritic *(misprint left intentionally)* and **(5)** Equiaxed dendritic growth, showing their continuum by the *solidification factor* $G/\sqrt{R}$ and nominal concentration $\mathbf{C_0}$.

This dissertation uses the modern mainstream classification of growth modes in Fig. 1.45, differing from Fig's 2.19.

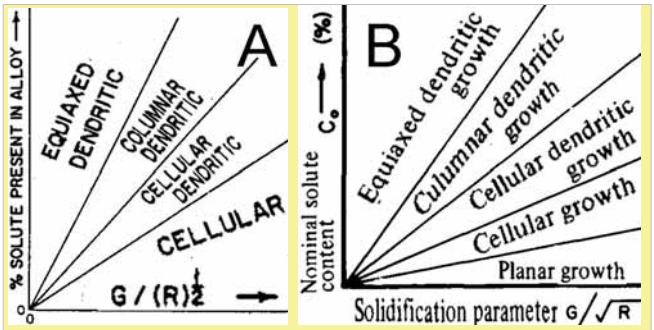

Fig. 2.19. Two $(G/\sqrt{R})$-C_0-analyses of solidification modes from RPI: **A:** in 1965, without planar growth and **B: in** 1980, with planar growth added. Modern versions of this analysis are presented in Fig. 5.1.

A: Savage, Lundin. Aronson 1965 [31] **B**: Savage 1980 [12]

2.7.4 Planar growth

Although the early discussions [75][81] seem to know the possibility of an existence of a planar growth (**PG**), this growth mode emerged to general scientific debate first in the 1970'ies; the earlier - $G/\sqrt{R}$ -$\mathbf{C_0}$-growth mode analyses in Figures. 2.12 **a**), and **b**) and 2.19 **A** did not recognize it.

A prerequisite for **PG** is **(i)** *Case 1*, *2* or *4* solidification, or **(ii)** in *Case 3* the non-existence of constitutional supercooling **CS**: i.e. a high **G/R** in the Eq. 2.5.16. In fusion welding, the **R** is **0** and **G** is high at **FL,** which is why a **PG**-zone so often decorates the fusion weld **FL,** as in Fig's 2.21. That the earlier researchers did not recognize **PG** is not necessarily that they failed to see it: may be no **PG-**zone existed in their experiments. Not even all welds have it because only fusion welds have the **R=0** condition at the **FL**; Fig. 5.11 shows a spot weld with no clear **PG** region. The **PG** zone width may alternate sharply even between fusion welds. Of the two stainless steel welds below, the one in Fig. 2.21 S has a **PG**-zone width ~ 250 µm. while in the second in Fig. 2.21 **M** this width is only ~3 µm.

2.7.5 Cellular growth

Fig. 2.21 shows the *planar growth* turn *cellular*. If **FL** is placed correctly, the planar growth area in Fig. **S** is ~ 150µm and in Fig. **M** ~3 µm wide. In welding, the width of the planar zone may alter within broad limits, but it is usually substantially less than the width of the cellular zone.

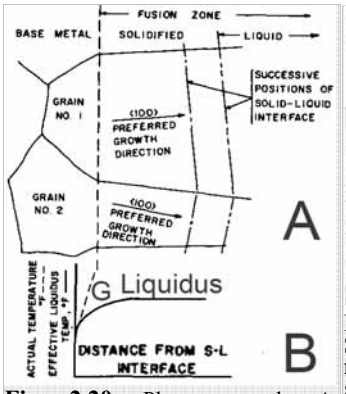

Fig. 2.20. Planar growth. **A**: outlook, **B**: Steep **G** prerequisite. [34]

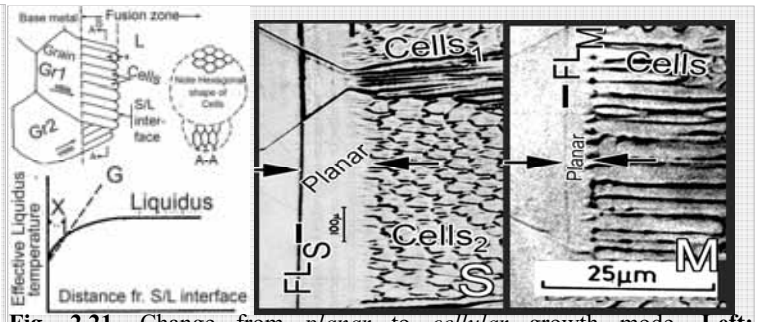

Fig. 2.21. Change from *planar* to *cellular* growth mode. **Left:** Schematically. *Savage, Nippes, Miller 1976 [34]* **Right.** In the two micrographs **FL** = fusion line. **S:** Fe-49%Ni alloy. **Cells$_1$** have a [100] easy growth direction parallel to micrograph. **Cells$_2$** have this direction at an angle to the micrograph plane.
Savage 1980 [12] ***M:** Austenitic stainless steel, Moisio1977 [82]*

2.7.6 Columnar-dendritic growth (Chalmers' and Savage's *cellular dendritic)*

With increasing constitutional supercooling **CS**, the solidifying cells form dendritic: cell walls grow secondary arms. (Fig. 2.22). Dendritic mode does not always start from fusion line, as in Fig. 2.22/**1**; planar and cellular growths often emerge before that in fusion welding.

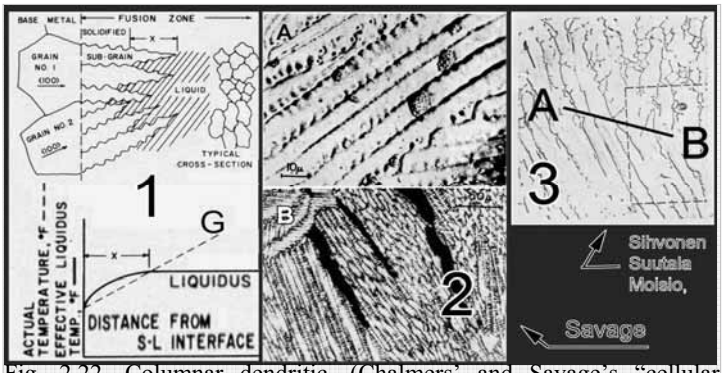

Fig. 2.22. Columnar dendritic, (Chalmers' and Savage's "cellular dendritic") growth. **1** Schematically. **2 & 3:** Photomicrographs. **2A**: TIG weld Si-Fe surface **2B**: TIG welded Fe-49Ni. Three micro-fissures; apparently associated with GB's. ***3:*** *α-steel weld structure changing from cellular* to *columnar dendritic* at line A-B. **1:** [Savage, Nippes, Miller 1976 [34] **2:** Savage 1980 [12], **3:** Sivonen, Suutala, Moisio 1975 [84]

2.7.7. Savage's "*Culumnar dendritic"* growth

At still larger **CS,** the dendrite width grows and even the entire grain may solidify dendritic (Fig. 2.23A). The misprint from [12] is preserved here to differentiate this growth mode from its mainstream namesake.

Savage wrote about this controversial morphology: "... we searched nearly two years before finding examples of an actual columnar dendritic structure" [12]. Its existence has not been verified by others and after 1990 it was removed from mainstream classification Kou [3], Messler [4], David, Vitek 1989 [61], Kostrivas, Lippold 2000 [33](Appendix 37) and Koseki 2002 [83] (Fig. 5.1). The structure or something resembling it is occasionally referred to, as in Fig. 1.43.

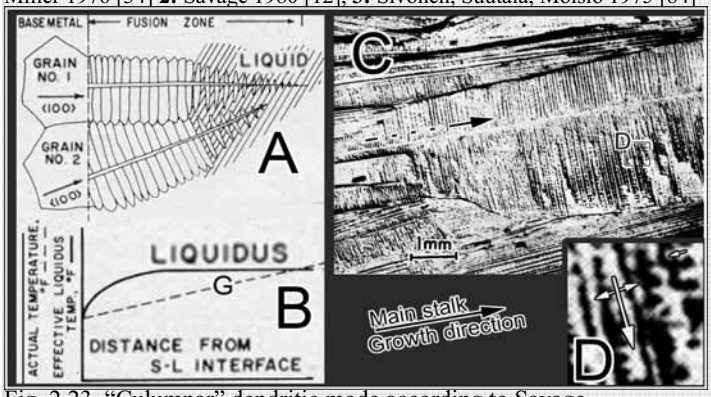

Fig. 2.23. "Culumnar" dendritic mode according to Savage.
A: Schematics, **B:** Thermal regime, **C:** Micrograph suggests that the dendrite is a grain, not a cell in a grain (Ti6Mn-alloy TIG (GTAW) weld), **D:** The arms on the main stalk grow "secondary" arms.

2.7.8 Equiaxed dendritic

With a large constitutional supercooling, the growing grains may form equiaxed dendrites (Fig 2.24). They are free from constriction and choose their orientation freely [73a]. Required circumstances are likely to form in the weld centerline area and at the end of a weld, as the extinguishing arc stops maintaining the temperature gradient.

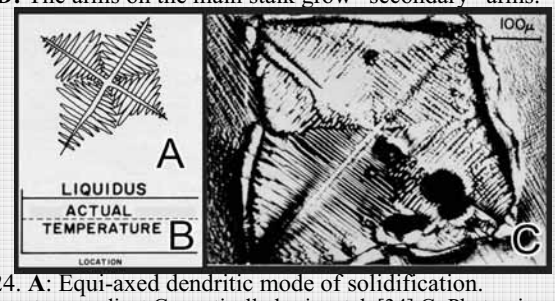

Fig. 2.24. **A**: Equi-axed dendritic mode of solidification.
B: Temperature gradient G practically horizontal. [34] C: Photomicrographs of an equi-axed -dendritic microstructure. Savage, Nippes, Miller 1976 [34] and Savage 1980[12]

2.7.9 Lippold & Savage model

Lippold & Savage modeled weld according to *Case 3,* Fig. 2.25. This is the trademark of the RPI-approach. It is one of the two reference-models we use in this dissertation. The other is the *Case 2*-based Koseki's model in Fig. 5.3.

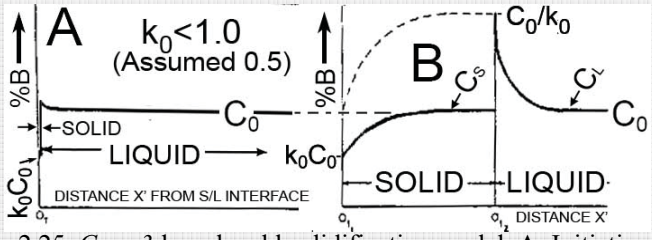

Fig. 2.25. *Case 3*-based weld solidification model. **A**: Initiation, **B**: From start to the steady state. In the steady state $\mathbf{C_S} = \mathbf{C_0}$ and $\mathbf{C_L} = \mathbf{C_0}/\mathbf{k_0}$. Lippold, Savage 1980 [85]

2.8 Lausanne – EPFL; Kurz

The work done in *Ecole Polytechnique Fédérale de Lausanne* is the trunk of today's mainstream understanding of solidification. It combines the classic works of the Toronto pioneers, Flemings, Brody and Mullins & Sekerka. EPFL-work includes a vivid global co-operation. Out of this massive body of solidification research, we limit to their **(i)** classification of solidification regimes and morphologies (Ch. 2.8.1), **(ii)** discussion of *Case 2* solidification with some solid diffusion (our *Sub-Case 2(-)DS,* Ch's 2.8.2…2.8.4), **(iii)** *Case 2* with a concentration gradient (our *Sub-Case 2(+)CG,* Ch. 2.8.5), **(iv)** EPFL-approach to welding. (Ch. 2.8.6), **(v)** multi-component systems with Miettinen's derivative of *Lausanne* work (Ch. 2.8.7), **(vi)** solidification kinetics with diminishing dendrite tips (Ch. 2.8.8) and **(vii)** small- and large systems, referring to *Case 2*- and *Case 3*-based systems (2.8.9).

(vi) *leads to a discussion of solidification with acceleration of* ***R*** *-induced morphological changes, discussed further in Ch.4.2.1 and Appendix 43*

(vii) *leads to a discussion of the differences between the solute profiles in the x-axis (longitudinal) direction and the perpendicular direction in needle like cells (Ch.6.3.3) and* ***(2)*** *in the final transient (Ch. 5.6.6).*

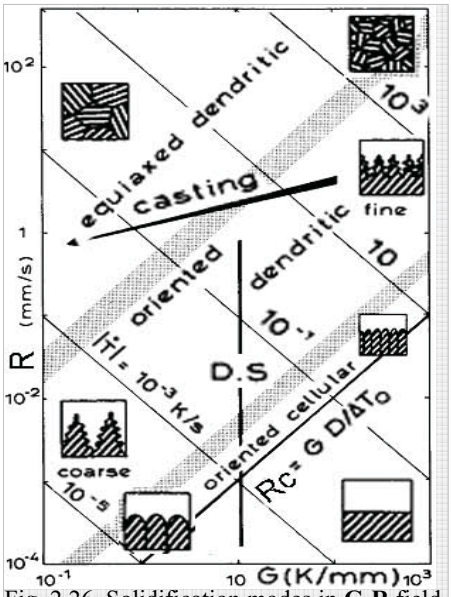

Fig. 2.26. Solidification modes in **G-R** field. Increasing **G**/**R** leads from planar to cellular to columnar dendritic to equiaxed dendrite. Kurz&Fisher [5 1989 edition.] referred to. by Koseki 2002 [83].

2.8.1 Solidification regimes and morphologies

The *Lausanne-research line* classifies solidification regimes in the classic mainstream manner with detailed descriptions; the *SCS Cases*, *Sub-Cases* and use of "**R**" instead of "**v"** for growth rate in the following are added by us to keep this dissertation uniform.

Morphologies are planar, oriented cellular, oriented dendritic and equiaxed dendritic Fig. 2.26. Later the third type is named Columnar Dendritic (Fig. 5.1).

2.8.2 Clyne-Kurz – *Case 2* with some solid diffusion

The paper Clyne and Kurz [86] is not made for welds and their **R** accelerating from 0 to **v**. However, it suits well for the initially low **R** in fusion welds**;** it adds *incomplete solid-state back-diffusion* to *Case 2*, making it approach *Case 1*. The *SCS2* term for this is *Sub-Case 2(-)DS,* a Sub-Case joining *Cases 1* and *2* (see Ch. 4.1.1).

The solid line in Fig 2.27 represents pure *Case 2,* the dashed line *Sub-Case 2(-)DS.* Equation 2.8.2A gives the solid solute concentration – the dashed line in Fig. 2.27. The diffusion is introduced into the analysis by the factor α, Equation 2.8.2B.

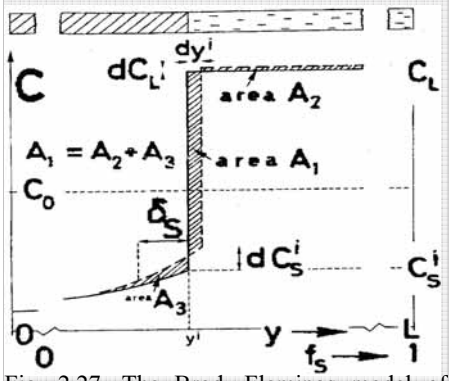

Fig. 2.27. The Brody-Flemings model of solute concentration at solid-liquid interface at *Case* 2 solidification (solid line) and *Sub-Case 2(-)DS* (dashed line, Ch. 4.1.1)[86].

$$C_s^i = k_0 C_o \left(1 - \frac{f_s}{1 + \alpha k_0}\right)^{k_0 - 1}$$

Eq. 2.8.2A. *The Brody-Flemings model* solute concentration at S/L interface, *Sub-Case 2(-)DS*. $\mathbf{k_0}$= equilibrium distribution coefficient. [86][20][5p. 421]

$$\alpha = \frac{D_s t_f}{L^2}$$

Eq. 2.8.2B. The term α, (~Diff. length) of the previous equation. **D** = diffusion coefficient, **L** = length of the solidifying element, $\mathbf{t_f}$ =time unit. Clyne, Kurz, 1981 [86], based on theory of Brody, Flemings 1966 [20].

To bring *Case 2* to this *Sub-Case 2(-)DS*, the circumstances must change to enhance solid diffusion; this may occur with decreasing **R**. The time available for solidification reduces in order *Case 1* →, *Case 2(-)DS* → *Case* 2.

2.8.3 Paradox in *Brody and Flemings model*

The Brody and Flemings model is an elaborate combination of *lever rule, Gulliver-Scheil-equation*, and *Fick's second law* for limited solid diffusion. The combination, as expressed in Equation. 2.8.2A and Fig. 2.27 contains a paradox: the conservation of solute boundary conditions is violated. Clyne and Kurz show this mathematically [86 p.966].This paradox was corrected by Clyne and Kurz.

2.8.4 "Σ"-solution for *Cases 2 to 1*- Clyne-Kurz

To overcome the paradox Clyne and Kurz introduced a corrective term **Σ,** which is 0 with "Gulliver-Scheil" (*Case 2*), and 1 with lever rule (*Case 1* solidification, *[86 p.967 Eq. 12]*). Connection between **Σ** and dendrite arm spacing (~**α**) is studied. This term facilitates locating *Sub-Case 2(-)DS* between *Cases 2* and ***1*** quantitatively.

2.8.5 "Ω"-solution of *Case 2 to Case 3* and beyond

Kurz and Fisher present a synthesis of - and elaborate - the theory widening Gulliver-Scheil equation towards faster growth rates and *Case 3*. They introduced the S/L interface concentration gradient **CG** with the *solute supersaturation* **Ω**, [5 p.72] (**Ω**=1 corresponds to *Case 3:* **Ω**=0 to *Case 2*, Fig. 2.29). The cell formation prerequisites were added with **CS** similarly as in the classic *Case 3* (Eq. 2.5.12)[71]. *The Mullins —Sekerka approach was added into the model later [5 p.226-].*

Cells and dendrite trunks are considered as parabolic needles with tip radius **r** protruding into the melt to the undercooled depth. The concentration gradient around the tip follows the Ivantsov-solution [5 p.73], giving the relation between **Ω,** growth rate **R** and the tip radius **r:** $\Omega = R \cdot r/2D$ **Eq. 2.8.5**

A sharper tipped cell rejects solute (and heat) into the melt faster and grows faster (Fig. 2.30). There is a minimum r^0 for the tip radius; the *capillarity limit, which is* ~ the *critical nucleation radius.* The maximum growth rate is R_e; at that critical points the tip radius either **(i)** grows abruptly making the cellular structure planar and move slowly, or **(ii)** retains the *marginal stability* tip radius ~r_e and supports growth with rate ~ R_e (Langer & Müller-Krumbhaar 1978). In either case the law $R \cdot r = 2D \cdot \Omega$ is valid.

(i) *is assumed in our Model Frame-A (Fig. 5.4), allowing for growth rates reaching this solidification mode, albeit R so high seldom exist in contemporary fusion welding.*

2.8.6 Lausanne and welding

The Lausanne method – including the **Ω**-solution presented above - is advocated to welding [50]. Taking into account the curvature of **G** and its effect on R, as in Fig. 2.31, the model suits to the specifics of fusion welds. Fig 2.31 **c)** considers also the easy growth direction $\mathbf{v_{hkl}}$ and its deviation from direction of **G** with an angle **Ψ** [50]. This is in accordance with the general approach of e.g. [4][5] and Fig. 1.24, with the difference of a larger role of *Case 2* in Lausanne.

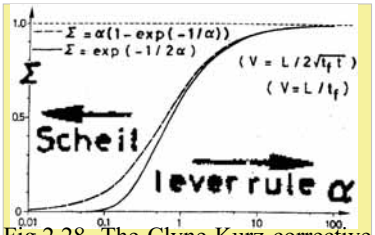

Fig.2.28. The Clyne-Kurz corrective factor **Σ** as a function of **α**, a constant, related to dendrite arm spacing. *Clyne, Kurz, 1981 [86], correction to theory of Brody, Flemings 1966 [20]*

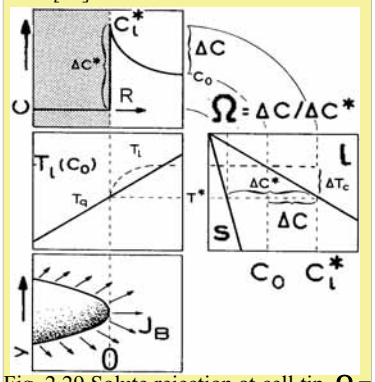

Fig. 2.29 Solute rejection at cell tip. **Ω** = solutesupersaturation Kurz, Fisher [5 p.72]

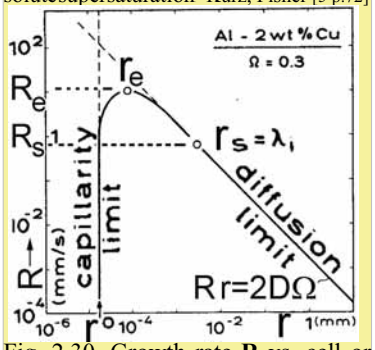

Fig. 2.30. Growth rate **R** vs. cell or dendrite tip radius **r**. K&F [5 p. 75]

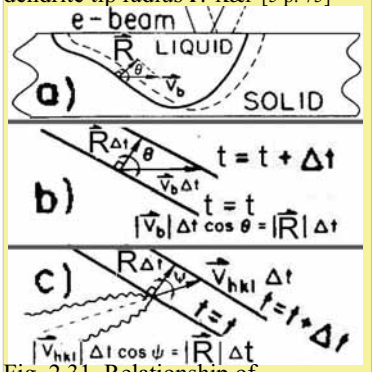

Fig. 2.31. Relationship of
b) welding speed v_b, and growth rate **R**,
c) easy growth direction $\mathbf{v_{hkl}}$.
and growth rate **R**
a) weld pool. Kurz 1995 [50]

2.8.7 Multicomponent systems - Miettinen

The Lausanne research has proliferated in several directions; Jyrki Miettinen developed further the Kurz model, taking into account **G**, cells, capillarity limit, and *internal friction* (Fig 2.32 A). His system for multicomponent systems, Eq. 2.8.7E, was obtained using **Ω** (Eq. 2.8.7A) and equations 2.8.7B, 2.8.7C and 2.8.7D. The model was brought in "CDG" software form (Miettinen 1999 [87]). Excellent correlation was obtained with experimental data, Fig. 2.32 **B),** Vilpas 1999 [51]. **C/P**-line denotes *cellular* to *planar* break-down at capillarity limit.

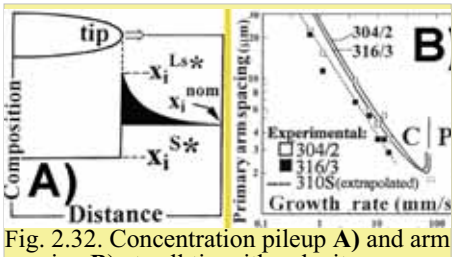

Fig. 2.32. Concentration pileup **A)** and arm spacing **B**) at cell tip with velocity **v**, experim. dots, calcul. lines. Miettinen [87] and Vilpas [51]

$$\Omega_i = \frac{x_i^{Ls*} - x_i^{nom}}{x_i^{Ls*} - x_i^{S*}}$$

Eq. 2.8.7A. Steady state supersaturation Ω_i (relative height of the pileup) Terms in Fig. 2.32

$$\Omega_i = P_i \exp(P_i) \int_{P_i}^{\infty} \frac{\exp(-z)}{z}\, \partial z$$

Eq. 2.8.7B. Supersaturat. **Ω** of paraboloid tip

$$P_i = \frac{VR_t}{2D_i^L}$$

Eq. 2.8.7C. Péclet number of previous Eq.

$$\mu_i^L(T^{S*}, x_2^{Ls*}, \ldots, x_n^{Ls*}) = \mu_i^S(T^{S*}, x_2^{S*}, \ldots, x_n^{S*}) + \Delta G_f + \Delta G_\sigma + \Delta\mu_i^*$$

Eq. 2.8.7D.

$$\sum_{i=2}^{n} \frac{m_i^S (C_i^{Ls*} - C_i^{S*}) V/D_i^L \left(\sqrt{1 + (4\pi D_i^L/VR_t)^2} - 1\right)}{2C_i^{S*}/C_i^{Ls*} + \sqrt{1 + (4\pi D_i^L/VR_t)^2} - 1} + \frac{\Gamma^{Ls}}{\sigma^* R_t^2} + G = 0 \quad [5]$$

Eq. 2.8.7E. Relation of **R** (dendrite tip radius), **G** (S/L temperat. gradient in L), $\mathbf{m}^S$ (liquidus slope), **C** (concentration), **V** (growth velocity), **D** (Diffusion coefficient in liquid), for solute **i**. **Γ** is Gibbs-Thompson coefficient for S/L line and **σ*** is a constant = ¼ Π^2. Miettinen 2000 [88]

2.8.8 Concentration of a needle-like dendrite tip

Dendrite tip radius reduces with increasing growth rate **R** [5 Fig. 4.11, not presented]. Concentration near a small, needle-like tip C_l^* may drop down to C_0 from the usual solute pile-up concentration C_0/k_0 (Fig. 2.33). If this happens, *the planar* ***(p)*** $\rightarrow$ *cellular* ***(c)****- transformation* ends and the solute pile-up disappears; the concentration gradient evens out from in front of the needle-like tips of the S/L front. In reality, dendrite tips do not act as isolated needles, so the pile-up is not evened out totally.

The prediction of the solid concentration in the cell/dendrite C/L – and the amount of solute fenced-in between the cells – is complex and not yet fully solved.

2.8.9 Solute redistribution in large and small systems

Lausanne line discusses solute redistribution with solute pileup [5 pp.117-122] and without it [pp. 122-126], the latter titled *Rapid Diffusion in the Liquid – Small Systems.* The ***pileup-approach*** is based on the classic Eq. 2.5.12; it is a *Case 3* solution. The model includes the solute profile for the final transient III in Fig. 2.34, (see Fig. 5.16).

The ***Rapid Diffusion - Small System*-approach** adds *some solid diffusion* into the Gulliver-Scheil solution, which we categorize as *Sub-Case 2(-)DS* in Ch. 4.1.1.The most natural area for the *Small System*-approach in welding is in between the cells and dendrites as well as in the final transient, where the diffusion distances are microscopic.

Note 1: *EPFL, K&F and associated to them research defies rigorous categorization because of its proliferation. However, the common denominator is the tendency to favor Case 2 - regime. With the term* **Ω***, the Case 2 is extended to Case 3 and beyond. The value of* **Ω** *defines the operation point between the two cases. One line of the Lausanne-EPFL lines, followed in the previous and continued in Ch. 4.2.1, uses the approximation* $\mathbf{\Omega} \cong \boldsymbol{P_C}$ *[5, Eq. 4.5 p.73&242].*

Note 2: *The Lausanne-EPFL approach comes close to the RPI-approach in the needle-tip analysis in Fig. 2.33, using the initial value* $C_l = C_0/k_0$ *which is the steady state condition of Case 3. It is evidently the Langer & Müller-Krumpbhaar-argument [5 Eq.4.6], which nears the Lausanne-EPFL-approach to the Case 3-based RPI-approach (Appendix 43).*

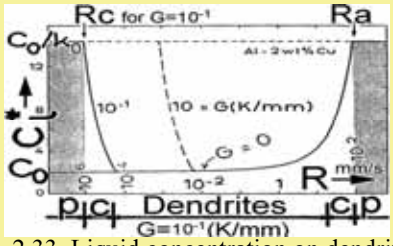

Fig. 2.33. Liquid concentration on dendrite tip may fall from C_0/k_0 to C_0. [5 p.81]

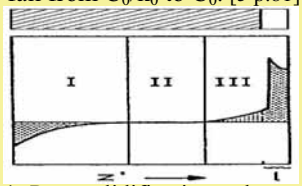

Fig. 2.34. Post solidification solute redistribution in *Case 3*. [5 p. 119].

2.9 David & Vitek 1989; NEGS to EGS transformation

It is generally agreed that grains and cells apply *easy growth solidification* (**EGS)**, growing in the *easy growth direction* **(EGD)** nearest to the temperature gradient **G.** *This is shown e.g. in Fig's 2.21, 5.2 and A7.1A (Cells A1 & A2), the cells of adjacent grains grow in slightly separate directions adopting an **EGD** nearest to **G**.*

However - several studies show that <u>at slow growth rates **R**</u>, the growth - *ignoring the easy growth directions* - proceeds in the temperature gradient **G** direction only, (non-easy growth solidification **NEGS**). <u>Increasing **R** changes the solidification regime to **EGS**</u>. Such studies are – Rutter & Chalmers 1953 [69] (Fig. 2.9a), Teghtsoonian & Chalmers 1951 [70], David & Vitek 1989 [61] (Fig. 2.35), and Morris & Winegard 1969 [61a] (Fig. 2.36).

*The change from **NEGS** to **EGS** occurred at a limiting rate $R_{NEGS\text{-}EGS}$ = ~ 1 cm/min for Sn in [69]. This limiting rate is low with respect to the speeds in common welding. For welding speed of say 100 cm/min, the limiting angle ϕ in Equation 1.1.18 would be 89^0. In our tests on copper (Fig 6.5e), the width of the zone, in which the **G** curves from 90^0 (at the weld interface WiF) to 89^0 (above the WIF), is < 10µm: very narrow indeed; the **NEGS** prevails only in a very limited zone next to WIF, which - if this would apply for copper - would never extend beyond the planar zone. This might be why **NEGS** is not widely recognized.*

We propose – based on [61][61a][69][70] – that cells grow **NEGS** at sufficiently low rates, ignoring the easy growth directions of their lattice. Further, we propose, that there is **(i)** a limiting – material specific - growth rate $\mathbf{R_{NEGS\text{-}EGS}}$, above which solidification transforms to **EGS**, and **(ii)** a driving force $\mathbf{E_{EGS}}$, associated with this transformation (see ***Note*** in Ch. A39.1).

The difference between our proposal and that of David & Vitek (D&V, [61]) is the following. D&V [61 pp.227-228] associates the cellular growth to **NEGS** and the dendritic growth to **EGS**, Fig. 2.35 b and c. We propose that if the **NEGS-EGS**-transition exists in copper, it is independent of the *cellular → dendritic* transition and happens prior to it in the planar growth zone.

In systems, having the **NEGS-EGS**-transition in the planar zone prior to the forming of cells, the **NEGS** would not manifest itself in any metallographically detectable way.

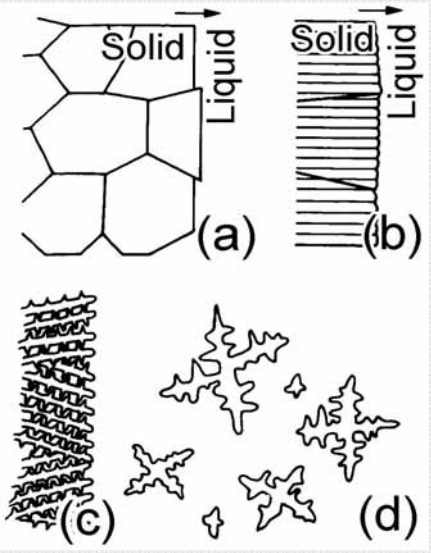

Fig. 2.35. Solidification modes: **(a)** Planar (**b)** cellular, **(c)** columnar dendritic **(d)** equiaxed dendritic.
David & Vitek 1989 [61] referred by DebRoy & David 1995 [80] and Koseki 2002 [83]

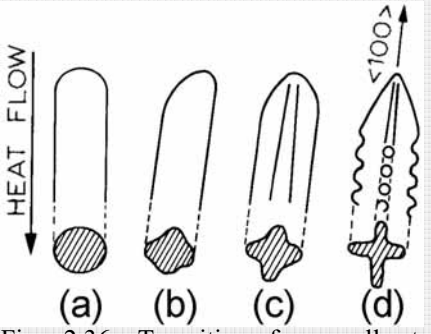

Fig. 2.36. Transition from cells to dendritic cells. The secondary dendrite arms form at higher growth rate. **(a**) Cell. Growth is antiparallel to heat flow regardless of the easy growth direction. **(b)** Cell with deformed cross section. The direction has changed to the easy growth direction. **(c)** and **(d)** forming of the secondary dendrite arms.
The growth rate increases from **(a)** to **(d)**.
Morris & Winegard 1969 [61a]

Prominent authors do not refer to this phenomenon. Mysteriously enough, professor Chalmers left it out of his Principles of Solidification 1964, although he published the paper describing the phenomenon in 1953. We propose that $\mathbf{R_{NEGS\text{-}EGS}}$ often exists in the planar zone and thus remains concealed. *(Further discussion with the Model Frame-B in Fig. 5.5.)*

2.10 Tokyo University; Koseki

This dissertation is greatly indebted to The Tokyo University Professor Toshihiko Koseki's review of present solidification study from 2002 [83], tying the earlier solidification studies with the future production technologies and mathematical modeling methods. The review reflects an understanding coherent with the understanding discussed earlier – especially in Ch. 2.8 - in this dissertation. The review stresses fast solidification rates; some beam and PVD methods reach high speeds (Fig. 2.37). Modern modeling techniques have a central role.

The review portrays four solidification morphologies with the help of Fig. 2.26 from Kurz and Fisher [5, 1992] and Fig. 2.35 from David & Vitek [61]. *(The latter is presented without going into the details of the **NEGS-EGS-transition.)*** These morphologies are identical with the four in Fig. 1.45.

The review presents solute distribution from start to end based on Flemings' analysis [1 p.47]. We use this analysis as the starting point for our *Weld Solidification Continuum Model* (Fig. 5.3).

Koseki modifies Gulliver-Scheil equation (*Case 2*) with solid diffusion, making the model work from *Cases 2* to *Case 1*. [83 Eq. 12 and 14]. This model is similar to the Kurz approach *(Ch's 2.8.2…2.8.5. We call this the Sub-Case 2(-)Solid Diffusion)*

Prof. Koseki has given significant contribution in the field of free and constrained dendrite tip thermodynamics (Fig. 2.38).

The review introduces the basics for two prospective mathematical approaches quantifying the solidification models: the Phase Field method (Fig. 2.39) and "Cellular Automaton" method (Fig. 2.40). This theme is continued in Ch. 5.5.1.

The Tokyo University has long span contacts with the leading metallurgical institutions, including *MIT* (Flemings) and *Lausanne* (Kurz). This work, with the work done in The Osaka University presented in the following, has given guidelines to this dissertation. The Japanese approach is quite in line with the Lausanne understanding;

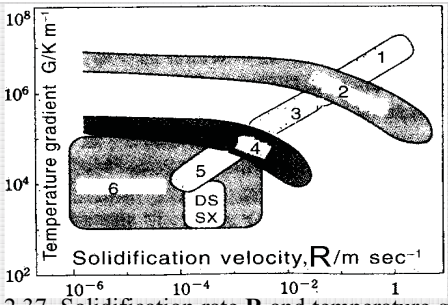

Fig. 2.37. Solidification rate **R** and temperature gradient **G** in various solidification processes. **(1)** Melt spinning; **(2)** Laser treatment; **(3)** Strip casting; **(4)** Welding **(5)** Continuous casting **(6)**. [83] ref. Fukumoto, Umeda 2001 [83c].

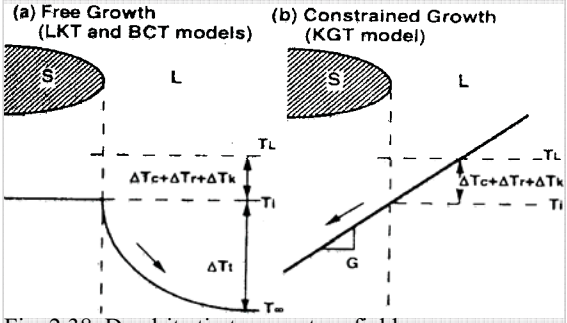

Fig. 2.38. Dendrite tip temperature field.
Koseki 2002 [83] ref. Koseki, Flemings 1995 [83a]

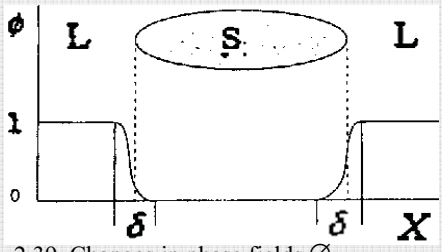

Fig. 2.39. Changes in phase fields ∅
At solid (**S**), liquid (**L**) and S/L interface **δ**. [83][83d]

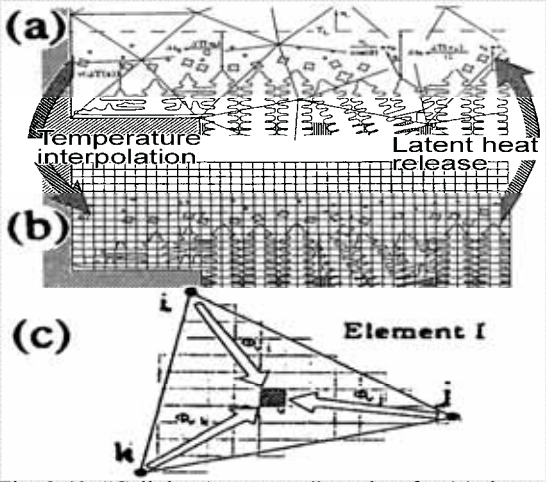

Fig. 2.40. "Cellular Automaton" meshes for (**a**) thermal conduction and diffusion, (**b**) nucleation and growth, (**c**) a+b. Koseki 2002 [83] ref. Gandin , Rappaz 1992 [83b]

2.11 Osaka University; Nishimoto, Mori

Using the Kurz-Giovanola-Trivedi equation [100] and derivatives of it (Equations 2.11.(1) through (3)), the authors deduce the relationship between the dendrite growth velocity and dendrite tip radius in type 304 austenitic steel (Fig. 2.41). This approach recognizes the capillary effect-induced cellular substructure breakdown to planar with a high solidification rate, establishing a quantitative value for it ~ 10 mm/s (Fig. 2.41). This phenomenon was discussed in Ch. 2.8.5 and it is included in our *Model Frame-A* Fig. 5.4 as $\mathbf{R_a}$ in the insert. The subsequent equations 2.11.(2) and (3) appear to be in co ordinance with the *Lausanne research* and Ch. 2.8.7. Eq. (1) is the *coupling Condition* [5 p.186], Eq. (2) is a new solution to [5 Eq. A9.36p.255] and Eq. (3) is evidently a new solution for tip radius obviously well suited for stainless steel. In our *SCS2* system, this analysis belongs to group *Case 2(+)CG*.

The abrupt change from cellular to planar growth in Fig. 2.41 may bring about an abrupt change in hot cracking susceptibility and morphology – probably towards increasing centerline cracking (depicted in Fig's 2.42 A and B).The growth rate ~10 mm/s (for stainless steel) is realistic in modern welding. (The C/L-crack tendency is higher, if the solute pileup is associated with a planar – not cellular or dendritic - S/L-front.)

$$\Delta T = m(C_0 - C_l) + \frac{2\Gamma}{R} \quad (1)$$

$$\frac{\pi^2\Gamma}{P^2 D^2}V^2 + \frac{mC_0(1-K)\xi_c}{D[1-(1-K)I(P)]}V + G = 0 \quad (2)$$

$$R = 2\pi \cdot \sqrt{\frac{\Gamma}{\frac{mC_0(1-K)\xi_c V}{D[1-(1-K)I(P)]}}} \quad (3)$$

Equations 2.11. (1), (2) and (3). **R**=tip radius, **V**=growth velocity. The terms follow EPFL approach as in Eq. 2.8.7E. Nishimoto, Mori 2002 [89]

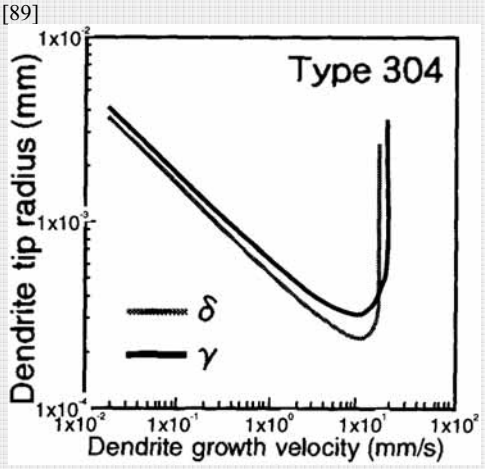

Fig. 2.41. Dendrite tip radius **R** as a function of growth velocity **V** in stainless steel 304**.** Abrupt change at 10 mm/s leads to planar growth, Nishimoto, Mori 2002 [89]

Equiaxed grains

Equiaxed grains along weld centerline reduce risk of centerline hot cracking. Koseki et al. managed to increase equiaxed grains by Ti-micro-alloy stainless steel (Fig's 2.42 C and D).

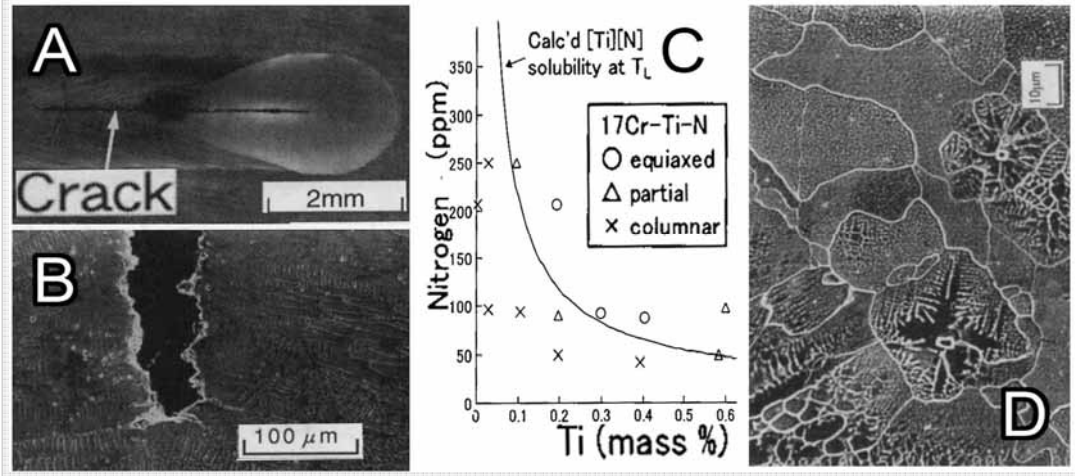

Fig. 2.42. **A and B)** 304 stainless steel weld crack. Nishimoto & Mori [89] **C)** Effect of Ti on formation of equiaxed grains in stainless steel **D)** Equiaxed grains, including dendrites nucleated on TiN in the melt ahead of S/L front. 19Cr-2Mo TIG weld with 0.19 %Ti and 162ppmN. Koseki, Inoue, Nogami, Fukuda. 2002 [90]

2.12 St. Petersburg State Polytechnic University

Welding was a central research area in the former Soviet science. The largest research institutes were the Paton Institute in Kiev, Ukraine, St. Petersburg State Polytechnic University (St.PSPU), and The Bauman Institute in Moscow. Specific issues were studied in several locations. Both political and linguistic barriers hampered communication with the west. We interviewed specialists of the two first named institutions.

Works in St.PSPU [27][115] assume strong, **dR/dt** – associated, concentration fluctuations in the initial transient of a fusion weld, Fig's 2.43 and 2.44. The approach is analogous with that of Flemings in Fig. 4.4.

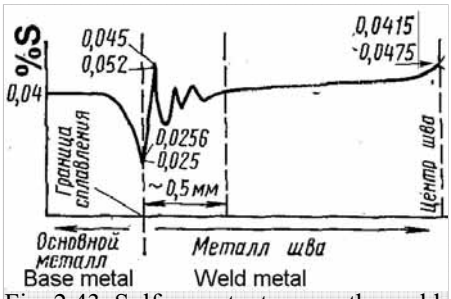

Fig. 2.43. Sulfur content across the weld. Fusion line is the dashed line on the left, center of the weld on the right. [27]

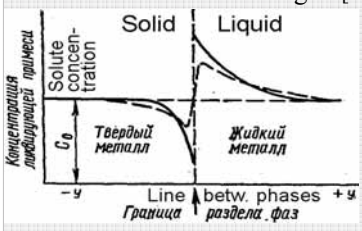

$$\text{а)}\quad C_{т\,(y,\,t)} = C_{т_0} - \frac{C_{т_0} - \varkappa C_{ж_0}}{\varkappa\sqrt{D_т/D_ж}+1}\left[1-\operatorname{erf}\left(\frac{y}{2\sqrt{D_т t}}\right)\right] \quad \text{for } y<0$$

$$\text{б)}\quad C_{ж\,(y,\,t)} = C_{ж_0} - \frac{\varkappa C_{ж_0} - C_{т_0}}{\varkappa+\sqrt{D_ж/D_т}}\left[1-\operatorname{erf}\left(\frac{y}{2\sqrt{D_ж t}}\right)\right] \quad \text{for } y>0 \qquad \text{(VI.23)}$$

Fig. 2.44. dR/dt–associated concentration profile at FL, and its mathematical models (a, b). Petrov, Tumarev 1977 [27]

2.13 Inverse modeling of temperature field

St.PSPU has a long tradition of studies of the interaction of the heat source with the weld pool. With the term *apparent (effective) volume heat source* q_{3app} they study the questions of the weld pool shape and size, latent heat, heating and cooling phenomena (Fig. 2.45) [110, 118, 122].

The energy conservation equation in a moving reference frame can be written as [118, 122]:

$$\frac{\partial T}{\partial t} = a\nabla^2 T + v\frac{\partial T}{\partial x} + \frac{q_{3app}}{c\rho}$$

(a = the thermal diffusivity, v = the welding velocity and $c\rho$ = the volume-specific heat capacity). The unknown parameters (vector **p**) of the apparent heat source q_{3app} can be found by solving the inverse heat conduction problem using measured temperature-related (heat-induced) weld characteristics (temperature, weld penetration, weld pool length, etc.).

The corresponding optimization problem (minimization of the objective function F) with a set of inequality constraints of physical nature is presented as [110][118] [122]:

$$F(\mathbf{p}) = \sum_{n=1}^{N} w_n^f \left[f_n^m - f_n(\mathbf{p})\right]^2 + \sum_{k=1}^{K} w_k^p \left(p_k^0 - p_k\right)^2 \to \min$$

$$q \le q_{\max}, \text{ etc,}$$

(N = the number of observations, K = the number of unknown parameters, f_n^m and f_n = the measured and calculated weld characteristics respectively, w_n^f and w_k^p = the weighting factors, p_k^0 = the guessed value of the k:th parameter p_k, $q_{\max}$ = the peak allowable value of the power q). The global minimum of the objective function (true optimum) can be found by using numerical optimization.

As an example, Fig. 2.46 shows the quasi-stationary temperature field in the solid part of the work piece in laser welding of 2 mm thick low-alloy steel. Similar analyses for copper are in Fig's 6.5 and A31B.

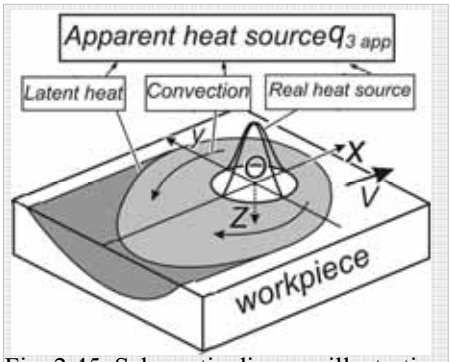

Fig. 2.45. Schematic diagram illustrating a moving reference frame and apparent heat source.

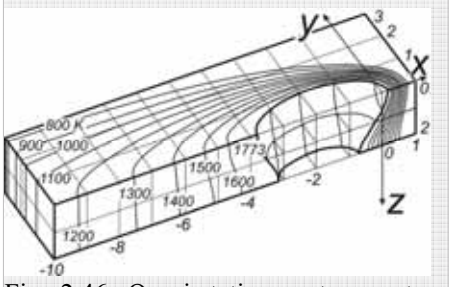

Fig. 2.46. Quasi-stationary temperature field in the solid part of the work piece in laser welding, steel S355J2C3 [118].

2.14 Paton institute; Demchenko

Vladimir Demchenko presents a solution for *Case 3*-based model, including solid diffusion and thermal conduction[92,pp.151-].

η is the phase volume fraction, subscripts **L** and **S** refer to liquid and solid, respectively. Ω_S and Ω_L are the volumes of the phases. **F** = coordinates of the system moving with the S/L interface. $\mathbf{C_0}$ $\mathbf{C_S}$, $\mathbf{C_L}$, **T** and **t** are the concentrations – nominal, in solid & in liquid - temperature and time, respectively. $\mathbf{D_S}$, $\mathbf{D_L}$ are the diffusion coefficients. **c**, **λ** and **ρ** are volumetric enthalpy, heat conductivity and density, respectively. $\mathcal{H}$ = volumetric heat of solidification. **k** – the *equilibrium distribution coefficient* (named $\mathbf{k_0}$ in Fig.1.9).

The mass balance is defined on both sides of the S/L interface, starting from Equation 2.14.B, which appears to be the Fick's second law of diffusion, resembling Eq. 2.5.12, including diffusion in solid. Equations 2.14D and 2.14E&F are two pairs of its solutions. Unfortunately we are unable to follow the reasoning completely; this approach seems to be a 3-D model for *Case 3* solidification including diffusion in solid; this obviously is a *Sub-Case 3(-)DS*-type model (Ch. 4.1.4). If initial conditions $D_L = \infty$, D_L= zero lead it to *Case 2*, it would be an ideal tool to connect *Cases 3* and 2. The used ***SCV***, volume fraction **η** could evidently help join this model with *Case 2,* using the volume fraction $\mathbf{f_S}$ in analyses like the one in Fig A41.

Fig. 2.47 presents a perpendicular and a longitudinal cross section of the growing cells at the S/L interface. If the solute redistribution scheme in Fig.2.47 a) is continuous from the start of the weld in longitudinal (grain/cell) direction, and if – as it seems - it may be used in the perpendicular direction as well, the model may give a remarkable contribution to weld metal solidification.

$$\frac{|\Omega_L|}{|\Omega|} = \eta \quad \text{and} \quad \frac{|\Omega_S|}{|\Omega|} = 1-\eta$$

Eq's 2.14A. See text. [92 p.153]

$$\frac{\partial}{\partial t}\left\{\frac{1}{|\Omega|}\left(\int_{\Omega_S} C_S\,dF + \int_{\Omega_L} C_L\,dF\right)\right\} = \frac{\partial}{\partial x}\left\{\frac{1}{|\Omega|}\left(\int_{\Omega_S} D_S\frac{\partial C_S}{\partial x}\,dF + \int_{\Omega_L} D_L\frac{\partial C_L}{\partial x}\,dF\right)\right\} \quad (4.6)$$

Eq. 2.14B. Solid/liquid ratio and solute redistribution. [92 p.152 Eq. 2.6]

$$\eta(T) = \exp\left\{-\int_{T_L^*}^{T}\frac{d\varphi_L}{dT}\,\frac{1}{\varphi_L(T)-\varphi_S(T)}\right\}$$

Eq. 2.14C. A differential equation, deduced from Eq. 2.14B [92 p154 Eq. 4.13]

$$\eta(T) = \left(\frac{T_L^*-T^*}{T_L^*-T}\right)^{\frac{1}{1-K}};\quad \eta(C_L) = \left(\frac{C_0}{C_L}\right)^{\frac{1}{1-K}} \quad (4.14)$$

Eq. 2.14D. Two solutions of the equation 2.14C. [92 p.154 Eq. 4.14]

$$\eta(C_L) = \left[\frac{C_0(1-C_L)}{C_L(1-C_0)}\right]^{\frac{1}{R_L}} \quad \text{and}$$

$$\eta = \left(\frac{C_0}{C_{LP}}\right)^{\frac{1}{1-K_1}}\cdot\left(\frac{\Delta C_B}{\Delta C}\right)^{\frac{1}{1-K_2}}$$

Eq's 2.14E&F. Two solutions of the differential Eq. 2.14C. [92 p.155 Eq's 4.15 and 4.16]

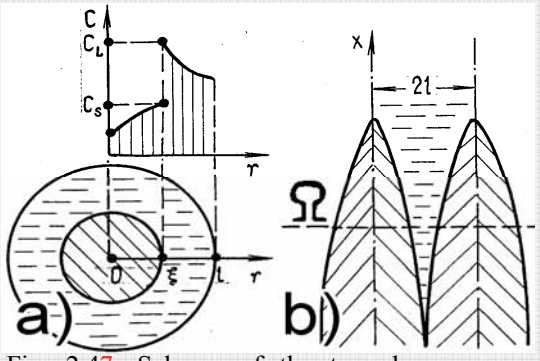

Fig. 2.47. Scheme of the two-phase zone. a) section **Ω** and the concentration distribution in **Ω**; b) cells from side. [92 p.156]

This is an incomplete analysis of Demchenko's impressive model. It seems ***(i)*** *original,* ***(ii)*** *to model the solute concentration in cell growth- and perpendicular direction,* ***(iii)*** *to take into account the solid state back-diffusion and* ***(iv)*** *to model dendrite spacing. Demchenko's model is worth of further and a more profound acquaintance.*

2.15 Phase-Field simulation

Phase-Field method - a recent diffuse interface physical theory - starts from the free energy of the phase and concentration fields. This vividly expanding method is successfully applied on equiaxial solidification in melt interior (Fig. 2.48), proposing that seeds of the crystalline phase nucleate homogenously via *thermal fluctuations*, which have a decisive role in dendrite side-branching, Karma & Rappel 1999 [93]. Other concepts in the area the *sharp interface* and *diffuse interface models,* referring to the concentration distribution at *Case 3*-type S/L-interface.

Hungarian Granacy et al. 2002 [94] extend the *Phase Field theory* to the nucleation and growth, using *diffusion controlled "soft impingement" of growing crystals.* This approach extends to nanocrystalline materials. It creates quite plausible models of equiaxed crystals, as in Fig. 2.49 (a) through (d). A good compatibility is reached between calculated and experimental values of **p,** which is *Kolmogovorov exponent*, a central factor in this model, Fig. 2.49 (e) and (f).

.

Phase Field simulation has expanded lately into the constrained solidification. In the future, it may become a tool for visualizing complex 3-D columnar grains and their more complex substructures; we return to this perspective method and its derivatives in the discussion of our proposed *Model Frame,* Fig. 5.4 and Ch. 5.5.2.

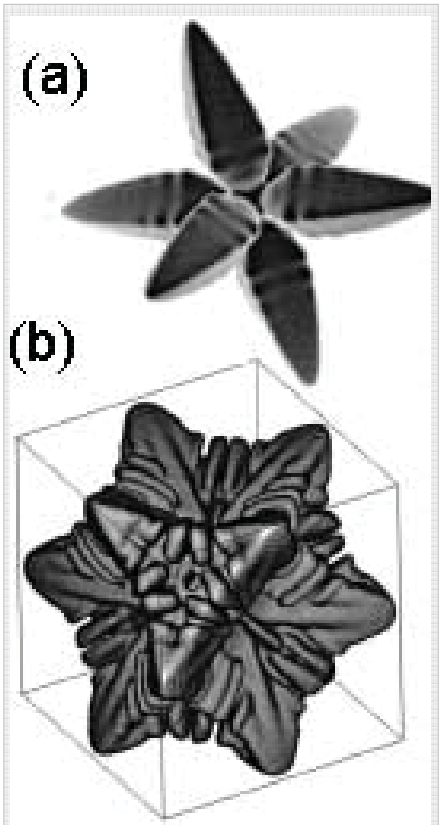

Fig. 2.48. Phase-Field method modeled equiaxed dendrites. **(a)** Karma, Rappel 1996 **(b)** Henry, EPFL, Lausanne 1999-. 2000 [93]

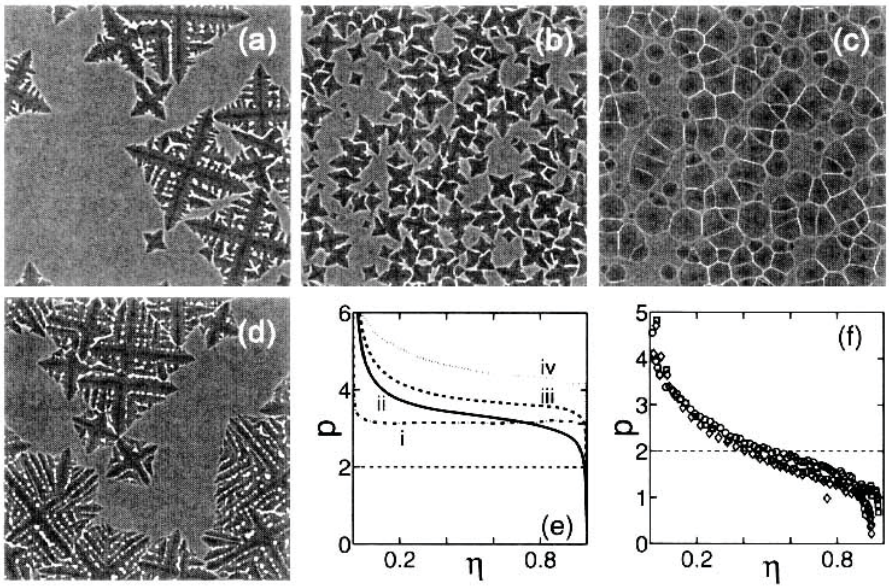

Fig. 2.49. Nucleation and bulk crystallization in binary phase field. Figures (e) and (f) approach the -solid concentrations of Cases 3 and 2 respectively. [94]

2.16 Bimetallic surfaces: Special phase diagrams and anomalous nano-particles

Development of surface study, high-resolution microscopy and modern physics help study nuclei at the initial stage (few atoms). Fig. 2.50 presents two models of alloy equilibrium surfaces five atom layers thick. The atomic structure of the surface is complicated and the authors advocate special phase diagrams for the surface.

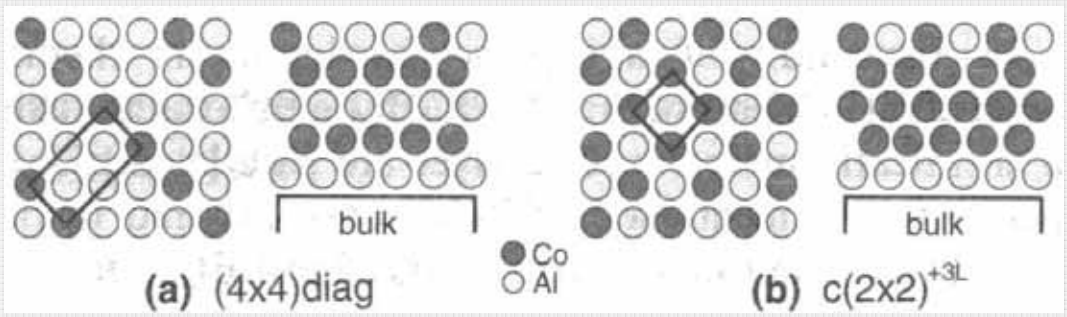

Fig. 2.50. Ball models of two different types of equilibrium surface on CoAl-alloy surface. The surface has a more complicated equilibrium structure than does the bulk metal. The lateral surface unit cells are indicated in the top views. Crystal growth here occurs from gas phase; applicability not known. Wieckhorst, Müller, Hammer, Heinz 2004 [95]

Fig. 2.51 **a)** shows an actual micrograph of three nuclei at early stages – diameter under 4 nm.

Such nanotechnological research may and will eventually contribute to our understanding of solidification.

Microscopic study with simulation led to the model in Fig. 2.51 e). The last atom layer does not follow the fcc-pattern. The atomic arrangement within the nano-particle has fivefold symmetry, differing from the FCC lattice of the bulk metal.

This research is an example of a multitude of different *research lines* in solidification. The solidification process is not just nuclei growing in size; the early stage appears to follow yet unknown laws.

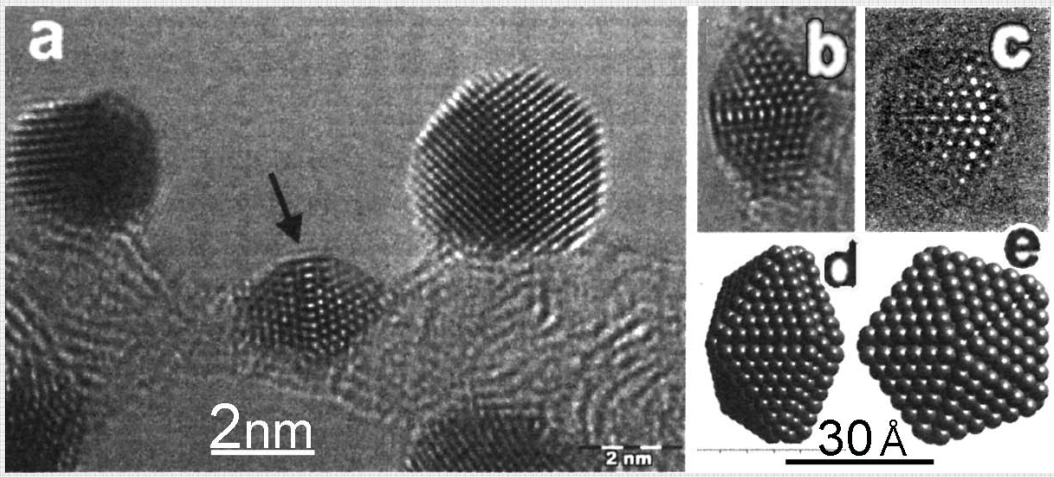

Fig. 2.51. **a) b) and c)** High-resolution micrographs of AuPd-nuclei on amorphous carbon d) and **e)** Phase Field models. Rodriguez-Lopez, et al. 2004 [96]

Chapter 3 THE FOUR *CASES* OF SOLIDIFICATION

The historical approach of this dissertation left Savage's *Cases* scattered in the text; we give here a brief summary of their essence. The *Cases* form the end points for the *Sub-Cases* presented in the next chapter.

3.1 Case 1: Equilibrium solidification

Equilibrium solidification corresponds to how nature would redistribute the solute with ample time. It requires complete diffusion in solid and complete diffusion or stirring in liquid: this is seldom accomplished in pieces of any practical size.

Fig. 3.1 shows the solute composition in a unit cell at start (**a**), at temperature T* (**b**) and after the solidification (**c**). The constitutional diagram is in (**d**).

The solid solute concentration obeys the lever rule equation, Eq. 2.1

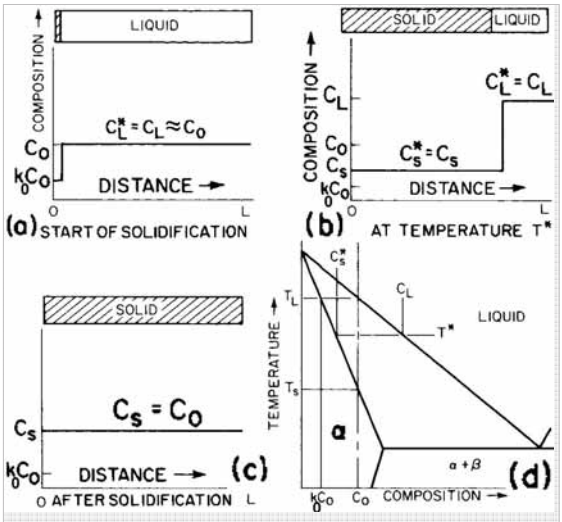

Fig. 3.1*:* Equilibrium maintained at all stages, *Case 1* solidification. : **(a)** Solute profile at start. **(b)** Solute distribution at **T=T***. **(c)** Solid concentration after solidification. **(d)** The constitutional diagram with the basic parameters.
$\mathbf{k_0}$ = equilibrium distribution coefficient**.** Flemings 1974 [1]

3.2 Case 2: No diffusion in solid, total mixing in liquid

Fig. 3.2 shows the solute composition in a unit cell at start (**a**), at temperature T* (**b**) and after solidification (**c**). The constitutional diagram is in (**d**).The solute distribution in *Case 2* is strongly concentrated to the end (Fig. 3.2 **c**), which makes it interesting for zone refining purposes. As it enhances planar growth with no cell lines participating in the distribution of the solute along the path, it increases the risk for centerline cracking in welding.

In Fig. 3.2 (**c**) the after solidification solid concentration between $\mathbf{k_0C_0 \ldots C_{sM}}$ follows the Gulliver-Scheil (Equation $2.4.1_{GS}$).

The validity of *Case 2* in the macroscopic distribution of the solute in welding can be disputed: can you expect the rejected solute to be totally mixed in any practical-sized weld? We include it with the presumption that it exists until the amount of the expelled solute is enough to form a gradient in front of S/L interface. Its zone is of infinitesimal width in the start. In the end – at the final pileup CE in Fig. 3.2 (**c**) – the circumstances may again be feasible for *Case 2*.

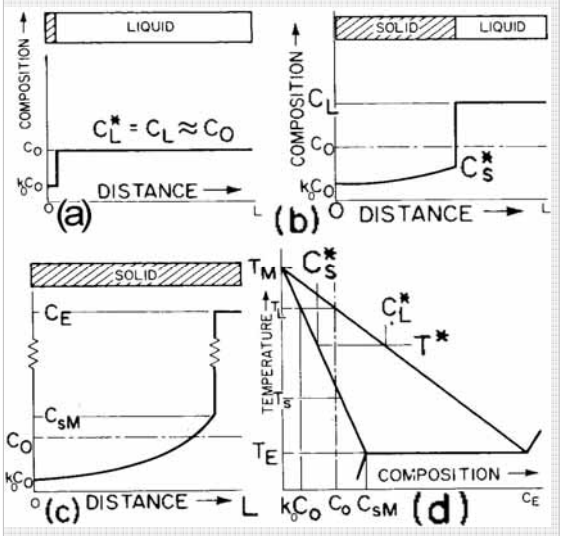

Fig. 3.2. No diffusion in solid, total mixing in liquid, *Case 2* solidification. **(a)** Solute profile at start. **(b)** Solute distribution at **T=T***. **(c)** Solid concentration after solidification. **(d)** The constitutional diagram with the basic parameters. Flemings 1974 [1]

Total mixing is not to be expected in welds of any practical size having a stagnant layer in the liquid ahead the S/L interface. If such a layer exists, the rejected solute piles up in this layer – and the following Case 3 will take effect. The prerequisite for this is that the stagnant layer width δ_h is greater than the solute pileup width (see Appendix 42).

3.3 Case 3: No diffusion in solid, partial diffusion in liquid

3.3.1 Stagnant layer

Partial diffusion and the solute pile-up in Fig. 3.3(a) occur in the stagnant layer at the S/L-interface. The width of this layer δ_h is seldom defined but it is assumed greater than the width of the concentration gradient (Appendix 42).

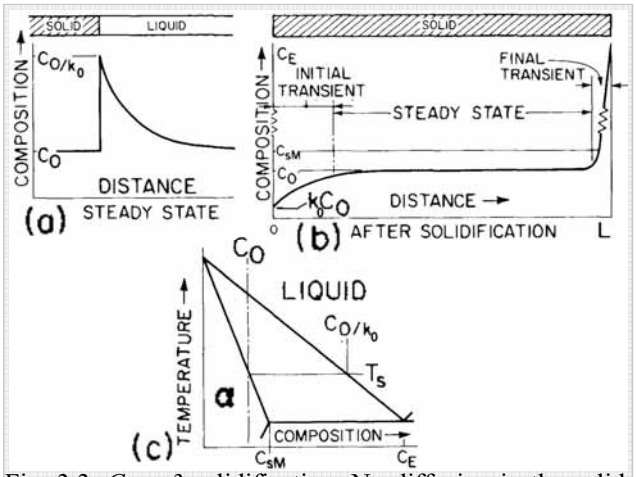

Fig. 3.3. *Case 3* solidification; No diffusion in the solid, partial diffusion in the liquid. **(a)** The concentration gradient (solute pileup) during the steady state. **(b)** The distribution of the solute after *Case 3* solidification. **(c)** The constitutional diagram with the basic parameters. Flemings 1974 [1]

3.3.2 Solute distribution in *Case 3 – classic CS-based model*

The mathematical expression for the liquid concentration in Fig. 3.3(a) is the Equation 2.5.13. The final solid concentrations of the initial and final transients are the Equations 2.5.14 and 2.5.15.

Role of constitutional supercooling (CS) in Case 3

Constitutional supercooling (CS) is necessary for the planar S/L-front to break down to "protrusions", the *cells* (Ch. 1.1.5). The other *Cases 1, 2* and *4* do not form cells, which is easily forgotten [5 p.423].

3.3.3 Mullins & Sekerka and the interface stability

The M&S model (Ch. 2.6.2) develops the classic CS-based *Case 3*-model (above and in detail in Ch.2.5.11) further, preserving the concept of the solute pileup, traveling in front of the S/L interface.

The development to this theory is associated with high growth rates; a dramatic change comes with the capillary effect, eventually rendering the S/L interface planar. This theory has evolved from the research line Brody & Flemings [20] - Clyne & Kurz [86] - Kurz & Fisher 1998 [5 pp. 123-126, 74-84 & Fig. 4.15] Fig's 4.5 & 5.4 in this dissertation)

3.4 Case 4: Splat cooling

We propose extending the Savage's *Case 4,* splat cooling, from the onset of *solute trapping* ($\mathbf{R_{st}}$) to an "ultimate splat cooling" with rate $\mathbf{R_\infty}$, inducing a massive transformation, with no diffusion, no lattice formation and no diffusion associated atom reorientation. Increasing $\mathbf{R > R_\infty}$ brings no further metallurgical effects (Fig. 3.4).

There are processes reaching solidification rates exceeding that of solute trapping $\mathbf{R_{st}}$, but none of them involve fusion welding (Kurz, Trivedi 1994 [97], Trivedi, Sekhar and Seetharaman 1989 [98]). Cells cease to exist and the S/L interface becomes planar with an ideally **NEGS** orientation.

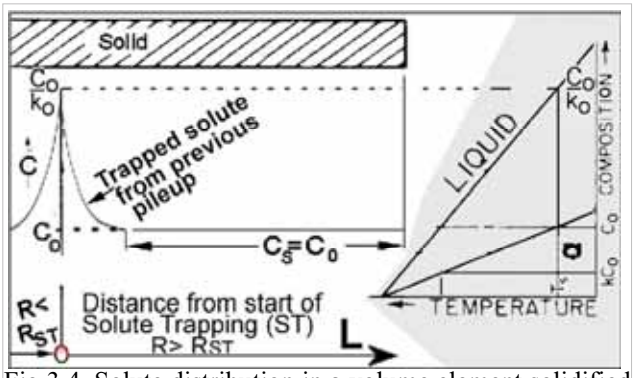

Fig 3.4. Solute distribution in a volume element solidified with accelerating growth rate **R**. reaching the Solute Trapping onset rate $\mathbf{R_{ST}}$ at **L**=0. *Case 4* (*splat cooling*) starts at L=0, increasing **R** brings solidification towards *Case* ∞ (u*ltimate splat cooling*). The previously piled-up solute gradient evens out, after which C_S remains C_0.

The cellular-to-planar-transformation associated with cell capillarity effect (at $\boldsymbol{R_a}$ in Fig. 4.5) happens in accelerating solidification prior to the onset of Case 4. The two should not be confused with one another.

Chapter 4 INTERMEDIATE *SUB-CASES*

The *SCS2* (*Savage Classification System* version *2*) adds to *SCS* the regimes falling in between the discrete *Cases*, mostly operating with variables not included in the *Cases*. *(We name these variables Sub-Case Variables **SCV**'s; they help study the correlations between Cases and Sub-Cases, as in Appendix 41.*

A *Sub-Case* is identified with the *Case number* and a (+) or (-)-sign for increasing or decreasing *Case number*. After it comes the *Sub-Case Variable* (***SCV***) of the particular *Sub-Case.*

4.1 Sub-Cases below Case 3

4.1.1 *Sub-Case 2(-)solid diffusion*

DebRoy & David [80 p.104] and **Kurz & Fisher** [5 p 124] extend *Case 2* assuming "*some Solid-State diffusion"*. As this model starts from *Case 2* (and from Gulliver-Scheil equation) "downwards" (towards *Case 1*), and uses Solid Diffusion (DS) as the **SC*V***, we call it *Sub-Case2(-)DS.*

Either of the two mentioned analyzes may be chosen; we choose the **Kurz & Fisher-**approach, which starts from Fig. 4.1. and leads to the parameter **α'**, equal to:

$$\alpha' = \alpha\left[1-\exp\left(-\frac{1}{\alpha}\right)\right]-0.5\exp\left(-\frac{1}{2\alpha}\right) \qquad \text{Eq. 4.1.1}$$

defining the operation point of the solidification in between *Cases 1* and *2*; value **α'** = 0.5 corresponds to *Case 1* and **α'** = 0 to *Case 2*. Value for **α** is given by Equation 2.8.2B. The liquid composition at S/L line $\mathbf{C_l}$ is given in Fig. 4.2 for the equilibrium distribution coefficient $\mathbf{k_0}$ = 0.14. The solid concentration during solidification $\mathbf{C_{S,S/L}}$ is equal to $\mathbf{k_0 C_l}$. *There is a slight violation of solid solute mass balance between the initial and final transients, which we handle in Appendix 40.*

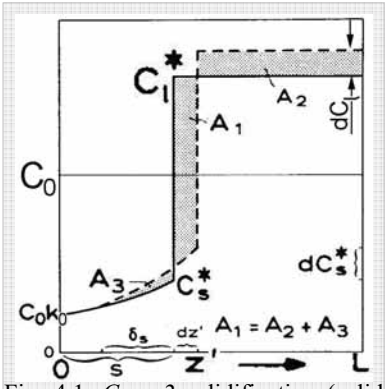

Fig. 4.1. *Case 2* solidification (solid line) with solid diffusion (dashed). Kurz, Fisher 1998 [5, p.124]

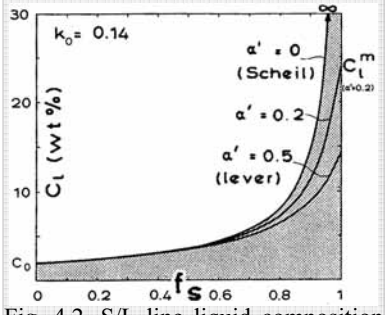

Fig. 4.2. S/L line liquid composition vs. solidified fraction $\mathbf{f_s}$. **α'** is 0.5 at *Case1* and 0 at *Case2. Solution of Kurz & Fisher* [5] Eq.6.9 p. 123

4.1.2 *Sub-Case 2*(+)concentration gradient

There are two models eligible for the *Sub-Case 2(+)CG*; the Pfann model discussed in Ch. 2.4.2 and Kurz & Fisher Ω-solution discussed in Ch. 2.8.5. The latter is newer and further developed. It **(i)** goes from *Case 2* to beyond *Case 3* all the way up to the capillarity limit and **(ii)** has been brought to quantitative level. The Ω-solution is presented briefly in Ch. 2.8.5 and Fig. 2.29. Fig. 4.3 presents the Pfann model with Verhoeven's clarification, showing the essence of this *Sub-Case* more in detail.

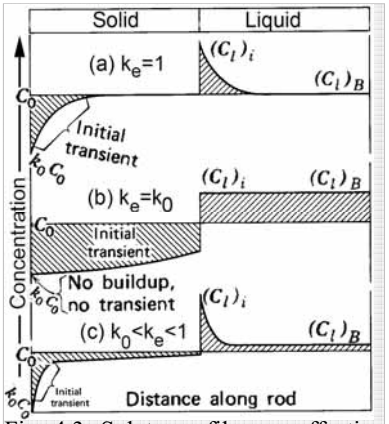

Fig. 4.3. Solute profiles vs. effective distribution coefficient $\mathbf{k_e}$. **(a)** *Case 3*, **(b)** *Case 2* and **(c)** *Sub-Case 2(+)CG* solidification. Verhoeven 1975 [8 p.251-257].

In *Case 2*, Fig. 4.3**(b)**, the Gulliver-Scheil equation determines the solute distribution. **In *Case 3***, Fig. 4.3**(a)**, the classic equations 2.5.13 and 2.5.14 determine the solute distribution.

In between *Cases 2* and *3*, in Fig. 4.3 **(c)**, the *Pfann & Burton-Primm-Slichter-equation* $2.4.2_{BPS}$ determines the solute distribution, adding a concentration gradient *CG* to *Case 2.* We call his new solidification regime *Sub-Case 2*(+)*CG*.

The *Sub-Case 2(+)CG* is the Gulliver-Scheil equation equipped with an *effective distribution coefficient* (Equation $2.4.2_{BPS}$) [67] and [2 p.13].

*The effective distribution coefficient $\mathbf{k_e}$ determines the operation point of the Sub-Case. In Case 2 $\mathbf{k_e}$ is $\mathbf{k_0}$, in Case 3 $\mathbf{k_e}$ = **1.** In between, the solidification occurs according to the determined Sub-Case. This operation point is determined by the term Ω in the Clyne-Kurz-Fisher Ω-solution*

4.1.3 Growth rate Acceleration and Deceleration $\dot{R}$: *Sub-Cases 3(-)Dec* and *3(+)Acc*

In Fig. 4.4, the solidification is presented during **(a)** a steady **R**, **(b)** an accelerating **R**, and **(c)** decelerating **R**. The solidification regime is in **(a)** pure *Case 3*, in **(b)** a higher *Sub-Case 3(+)*, and in **(c)** a lower *Sub-Case3(-)*.

"Higher" means a shift towards a higher energy state and Case 4. "lower" means a shift towards a lower energy state, Case 2 and 1.

The *Sub-Case Variable, SCV,* after the (+) and (-)-signs in this occasion is *dR/dt,* which we call *Acc* with accelerating and *Dec* with decelerating solidification. Therefore, the solidification regime in **(b)** is called *Sub-Case 3(+)Acc,* and in **(c)** *Sub-Case 3(-)Dec.*

ΔC depends on the term **dR/dt**. The relation $\mathbf{C_{S0}/C_{L0}}$ is $\mathbf{k_0}$ on the S/L-line, the *microscopic equilibrium* is preserved (Ch. 1.1.9).

The in the previous chapter presented *Sub-Case 2(+)CG* nears *Case 3* and this *Sub-Case 3(-)Dec* nears *Case 2; they* appear to near one another in between. However, they never meet; they exist in different multi-dimensional spaces. Appendix 41 attempts to visualize the operation paths in solidification.

$\dot{R}$ has been discussed further for two solutes [49 p.738] and for rapid changes [1 p.39]. The latter may be the cause of bands. However important, we leave these themes out of this discussion.

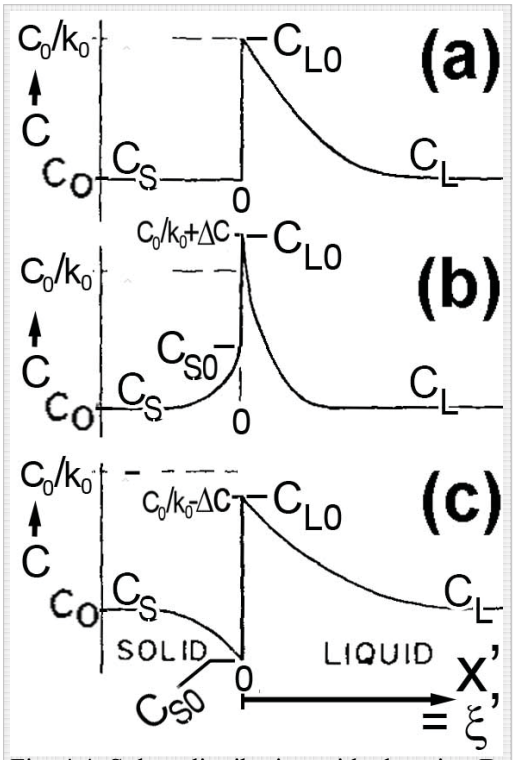

Fig. 4.4. Solute distribution with changing **R**. **(a)** Steady, **(b)** accelerating; **(c)** decelerating growth rate. Acceleration and deceleration start where the $\mathbf{C_S}$ starts curving from $\mathbf{C_0}$.
Developed from Flemings [1 p.116]. The basis for this analysis is from Smith et al. [49]

4.1.4 *Sub-Cases & SCV's - basic features*

Before continuing, we discuss some basic features of the *Sub-Cases* and their variables, which we call *Sub-Case Variables, **SCV**'s.*

A Sub-Case is always based on one Case. The term *Sub-Case* denotes a mathematical equation modeling some aspect (phenomenon) of solidification. Associated with a *Sub-Case*, this aspect is called a *Sub-Case Aspect, **SCA***. The ***SCA*** is – at the present time – almost solely the post-solidification solute profile, mostly only in the longitudinal direction. Future ***SCA***'s can be expected to be the solute profile in the perpendicular direction, distribution of the solute *fenced-in* between the cell-, dendrite- and grain boundaries, micrographic morphologies and their dimensions (such as the locations and widths of the planar, cellular and dendritic zones, as well as the dimensions and geometry of the individual cells and dendrites).

All the *Sub-Cases* are based, so far, on one of the four *Cases*, this *Case* without exception being either the *Case 2* or *3*. *It is probable that other initial conditions for solidification will be thought of; so far the three first ones, by Chalmers [35 pp. 251-256], complemented with the fourth one by Savage (Ch.2.7.1) have no rivals.* It is to be expect that the studying of exceptionally slow and fast welding methods (such as *diffusion welds* and slow *electro-slag/–gas welds*, following near *Case 1*-, and rapid *beam welds* and *explosion welds* following near *Case 4* solidification) will require extending of the scope of the *Sub-Cases* in the future.

As a *Sub-Case* always is based on one *Case,* the *Cases* exclude one another; there can be only one *Case* as the basis, albeit the *Sub-Case* may bring the operation point of the model from its basic *Case* to another *Case*[13]. For example, the *Pfann model* in Fig. 4.3C extends from *Case 2* to *Case 3*, but it is based on *Case 2*, and uses the *Case 2* algorithm – the *Gulliver- Scheil model* – to acquire the model (which solves the solute profile)[14]. The ***Sub-Case Variable SCV*** – in this occasion - is the operation point between the *Cases*, or the "strength", in a scale from 0 to 1, of the concentration gradient, which is brought into the model with the Burton-Primm-Slichter-equation. Mathematically speaking, its ***SCV*** is the B-P-S-equation. Its *algorithm* is the B-P-S-modified Gulliver-Scheil-equation.

Single- and multi-element SCV's. The study of the Burton-Primm-Slichter- equation $2.4.2_{BPS}$ includes the result k_e and its four variables, $\mathbf{k_0}$, **f**, $\boldsymbol{\delta}$ and $\mathbf{D_L}$. It goes without saying that the total comprehension of this crystal-pulling-oriented model is complicated, but remembering that $k_e = k_o$ means *Case 2 -,* and k_e=1 *Case 3* solidification, and the values in between give an operation point of the solidification in between those *Cases*, is sufficient.

The ***SCV*** may consist of one single thermo-metallurgical variable (such as **R** or $\mathbf{D_L}$,) or a combination of them (as the $\mathbf{D_L/R}$ in Fig. A41A). The B-P-R-equation, above, is a complicated combination of the elements $\mathbf{k_0}$, **f**, $\boldsymbol{\delta}$ and $\mathbf{D_L}$. Appendixes 40 and 41 - discussing the visualization and the joining of the solidification models – point out that successful combination of variables decreases the dimensionality of the model and helps its graphical presentation and handling.

Single- and multi-SCV Sub-Cases. It is possible to design *Sub-Cases* with more than one *Sub-Case Variables*. For example, the *M/S-model* – which we present in Chapter 5.6 and in Appendix 38 – has three *SCV*'s: the ones calculating how the solute profile is affected by: **(i)** the melting stage, **(ii)**, the post-solidification diffusion in the solid and **(iii)** the acceleration of **R**. In retrospect it appears that it would have been more reader- and user-friendly to present those three relations as separate *Sub-Cases*; one should avoid multi-*SCV Sub-Cases* whenever possible.

A Sub-Case may be valid only in a restricted section of the solidification continuum. There may be restrictions in the applicability of a *Sub-Case*. For example, the *M/S-model* has a restriction; its initial conditions assume 1-D solidification, which means planar growth with no cell formation; it is limited to planar growth. In a weld, it is applicable only in between WiF and the start of the cellular growth.

Such restrictions must be kept in mind, because **(1)** a model may not warn, if you apply values exceeding the limits of the initial values, and **(2)** outside the validity of one *Sub-Case*, you have to apply another, and the solidification continuum requires the joining of the two.

4.2 Sub-Cases above Case 3: Mullins & Sekerka / Lausanne / Solute Trapping

The Mullins & Sekerka as well as the Lausanne approaches with their derivatives may be classified as *Sub-Cases*, inasmuch as they contain terms adapting to changes of *SCV's*, which they invariably do (at least **R** usually is a variable). When these models function with increasing **R**, leading towards a higher free energy level, we call them "above *Case 3*".

The region at and above *Case 3* can be reached with two models: *Case 3 (proper)* and *Case 2,* equipped with a concentration gradient, i.e. *Sub-Case 2(+)CG*. Both approaches are used. The Lippold–Savage-model (Fig.2.25) use *Case 3*, while EPFL (Ch.2.8), Miettinen (Fig.2.32), Nishimoto & Mori (Fig.2.41) and Koseki (Fig.5.3) use *Sub-Case 2(+CG)*[15]).

There is a fundamental difference in the solute distribution of the Case 2- and Case 3-based approaches (see Ch. 5.5.3). The Case 2-based Sub-Case(+)CG "bulldozes" more solute to weld C/L than does Case 3 and its derivatives. The difference diminishes as the operation point of the Sub-Case(+)CG approaches Case 3. In terms of the Ω-approach, the mentioned difference of "bulldozed" solute diminishes to nil as $\boldsymbol{\Omega}$ *approaches unity. If the operation point is chosen by the approximation* $\boldsymbol{\Omega \cong P_C}$*, as in [5, Eq. 4.5 p.73&242], the whole solidification continuum can be modeled without Case 3, which would become obsolete. Do the Gulliver-Scheil-based Case 2 with its derivatives and the Péclet number model solidification more accurately than does Case 3 and its derivatives? We do not know; this question needs an experimental answer.*

---

[13] All *Sub-Cases* do not lead from their base *Case* to the next.
[14] The same applies to the Clyne-Kurz Ω-model in Ch. 2.8.5.
[15] Koseki actually uses pure *Case 2*. We argue that pure *Case 2* is unable to form cells or columnar dendrites. Here is a contradiction, extending to e.g. [4 Ch.13.5.1 p.423 and Fig. 13.25] also referring to *Case 2* – induced cells and dendrites.

4.2.1 Solidification according to *Sub-Case 2(+)CG"K&F"*: Rise and Fall of cells

Growth rate $\mathbf{R_C}$ in Fig.4.5 divides planar growth from cellular, but does not necessarily divide *Cases 2* and *3*. The former – not having *CS* – can be only planar, but *Case 3* may be planar, cellular or dendritic, depending on the steepness of **G** in Fig's 1.33 and 1.45: *Case 3* starts at $\mathbf{R = R_3 < R_c}$ (not shown in Fig. 4.5, shown in Fig's 5.4, 5.5 and 5.6.)

Increasing growth rate above **Ra** breaks cellular growth to planar due to *capillarity effect* (Fig.4.5). This may happen with cell tip radius **r** reducing to size of the critical radius of nucleation [5 p. 74]. The solute pileup in liquid and *Case3* continue existing at **R > Ra**.

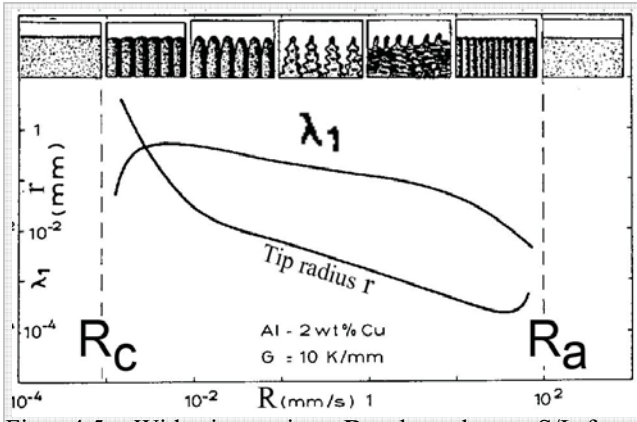

Fig. 4.5. With increasing **R**, the planar S/L-front transforms at $\mathbf{R_C}$ to cellular, then to columnar dendritic, back to cellular, until at **Ra** cells disappear and front becomes planar.
Kurz and Fisher 1998 [5 pp.74- 84] R=growth rate

The impressive analysis between $\mathbf{R_C < R < R_a}$ in Fig. 4.5 widen the range of *Case 2* to and over the range of *Case 3* [71][49]. This Kurz & Fisher (K&F)-approach rivals *Case 3*, by adding a concentration gradient (CG) to *Case2,* using **Ω**. It forms a *Sub-Case 2.* Its ***SCV*** is **R** t, making it *Sub-Case 2(+)CG"K&F".*

The Sub-Case 2(+)CG"K&F" has a parameter $\boldsymbol{\Omega} = f(R, r)$ *(defined in Fig. 2.29 and Eq. 2.8.5), adding a free variable to the analysis. We attempt to visualize the relations of the models in Appendix 41.*
This wide-ranging Sub-Case performs tasks of Case 3 and has the capacity to make it obsolete.

4.2.2 *Sub-Case 3(+)M&S*

The Mullins & Sekerka-solution 1964 [77] forms a continuum from *Case 3* upwards, towards *Case 4*, starting from the break-down of the planar S/L-front to cells; the **M&S**-approach is just the *Sub-Case3(+)M&S*; it uses the same *Fick's diffusion law*-algorithm as the classic *Case 3* (Eq's. 2.5.12 and 2.6.2[a]), so the continuity is guaranteed. Since the post-solidification solid solute profile $\mathbf{C_S}$ is assumed constant $\mathbf{C_0}$ in the steady state of the *Case 3*, the fact that **M&S**-solution does not solve $\mathbf{C_S}$ does not matter; the solution assumes $\mathbf{C_S=C_0}$. The primary *Sub-Case Aspect (SCA)* for the *Sub-Case 3(+)"MS"* is the cell width or tip radius, which the model solves elegantly.

Lausanne has introduced a wide set of ***SCV***'s including, the *Péclet*-number (relation of the flow rate to the diffusion rate), the Ivantsov-function [5 p.73] and the *marginal stability* [5 p.74]; if – or rather as - these are acting laws of nature, they should be adopted in the *Sub-Case 3(+)M&S.*

*Comparison of the results of this proposed Sub-Case 3(+)M&S-model with the results of the Gulliver-Scheil-based Sub-Case 2(+)**CG**"K&F"-model should be interesting. The latter might have a tendency to "bulldoze" more solute to the weld C/L due to its Case 2 legacy.*

4.2.3 Case 4: From *Solute trapping* to ultimate massive solidification

Increasing **R** will eventually lead to the onset of *solute trapping* at rate $\mathbf{R_{st}}$ and its increasing towards ultimate massive transformation at $\mathbf{R_\infty}$. We define $\mathbf{R_{st}}$ as the end of *Case 3* and start of *Case 4*. $\mathbf{R_\infty}$ is the end of *Case 4* and any diffusion-induced metallurgical phenomena.

What happens as $\boldsymbol{R}$ *reaches and surpasses* $\boldsymbol{R_{st}}$ *depends largely on how the solute atoms adapt to the matrix lattice. In carbon steel, we may see a dramatic increase of hardness in martensite-reaction, while in say Cu-Ni-alloys very little happens. If rapid cooling subdues crystallization and an amorphous metal glass forms, the resulting structure may have extraordinary features; there may be several material-specific Sub-Cases between the onset of Case 4 and Case ∞. This range of growth rates is beyond normal fusion welding and this dissertation.*

Chapter 5 WELD SOLIDIFICATION CONTINUUM AND ITS MODELING

With the term *weld solidification continuum*, we mean and emphasize the continuity of the chain of thermo-metallurgical events leading to the solidification of a grain from start to end. Its model should have the same continuity, but this is seldom completely achieved. The model should **(a)** plot the composition profile, **(b)** visualize the micro structural morphologies **(c)** accept as input the pertinent thermo-metallurgical variables, forming the "*Sub-Case Variable*", ***SCV***, and **(d)** show the solidification *Cases* and *Sub-Cases;* all this preferably at any point of the 3-dimensional weld. Some of the pertinent variables are **(i)** the solidification rate **R, (ii)** the temperature gradient **G**, **(iii)** the fluctuations of **R**, **(iv, v)** the pre- and post-solidification back-diffusion in solid, **(vi)** the liquid stirring, as well as in quite rapid welding **(vii)** the capillary effect, solute trapping a.s.o.. In the near future, terms like the *Péclet-number* and *Ivantsov-solution* and many others will be widely included. We look at three types of models visualizing solidification continuum on 2-D figures, Chapters 5.1,5.2 and 5.3.

5.1 Rate-Gradient analyses

Solidification can be visualized in **R-G-**coordinates, as in Fig 5.1 by Kou, Kurz and Pavlyk. There is a good agreement in this field in today's mainstream thinking. This analysis shows best the influence of **R** and **G** on morphology and cell width, but lends itself poorly on locating these in weld geometry.

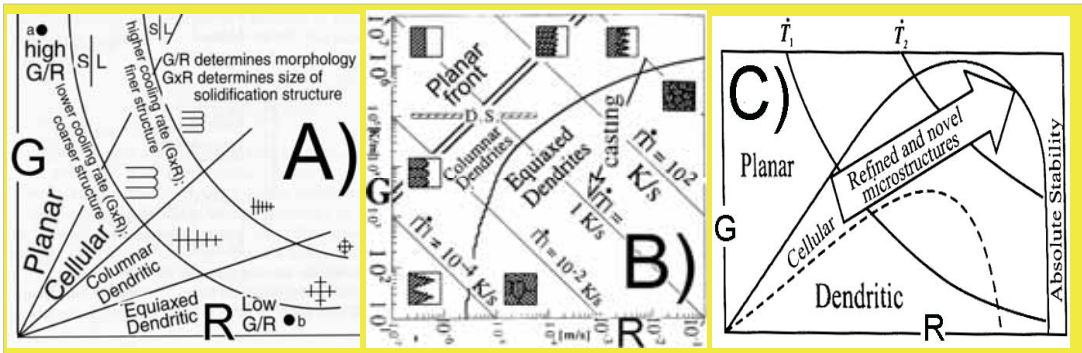

Fig. 5.1. Weld metal morphologies in R–G– coordinates by Kou (A), Kurz (B) and Pavlyk (C). The two first show the *planar → cellular → columnar dendritic → equiaxed dendritic* –continuum and the cell structure growing finer with increasing R*G. The third (**C**) adds the *capillary effect* - induced cellular → planar transition. **A):** Kou 2003 [3], **B):** Kurz, Fisher 1998 [5] (the figure is mirrored) and **C:** Pavlyk 2004 [99]

5.2 Geometric morphology-model

Fig. 5.2 models the morphologies along the weld geometry. The *planar→cellular→ columnar dendritic → equiaxed dendrite*-continuum from **FL** (**R** = 0) to centerline ($\mathbf{R_{Max}}$ = **v**) is clear.

This presentation is geometrically informative: the forms, directions and locations of the constituents - in the weld and within the grains - are clear.

Solute concentration profiles and factors governing the solidification are difficult to present in this model.

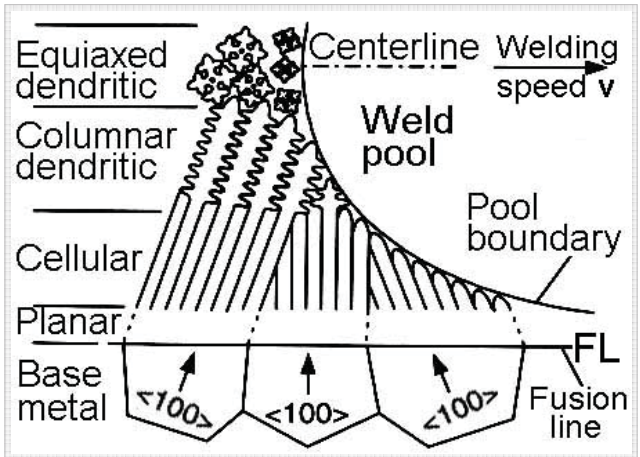

Fig. 5.2. Growth morphologies across weld fusion zone. Kou 2003 [3]

5.3 Solid solute profile–model: One Case

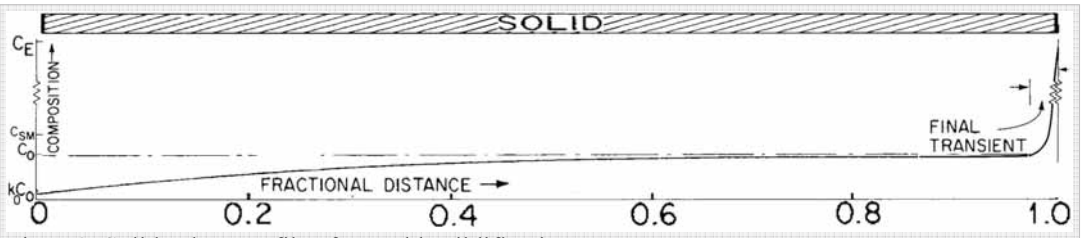

Fig. 5.3. Solid solute profile after weld solidification. Koseki 2002 [83] from Flemings 1974 [1]

Solid solute spectrums from start to end of the solidification are irreplaceable (Fig's 5.3 and 2.25). They give the solute profile along the grain but have no information of the grain/cell geometry. In cellular and dendritic structures, they depict the average solute profile only near the cell or dendrite stem centerline, which may give incomplete information of the solute distribution as a whole.

This longitudinal solute distribution - and the process leading to it - is also called the "macrosegregation" as opposed to the inter-cellular/dendritic perpendicular solute distribution, called "microsegregation" [4][14][124][3, our Fig.1.27].

5.4 Weld Solidification Continuum Model Frame – a tool for modeling

The *Weld Solidification Continuum Model Frame* (in short *Model Frame*) attempts to combine the three presented afore models, handling the solidification from start to end. A model of the solidification of an actual weld is created from this *Model Frame* by excluding – after conscious deliberation - non-pertinent components and arranging the pertinent ones in a logical sequence and proportion.

Three *Model Frame*-versions are presented, the main version **A** is for elliptic weld pools, version **B** for teardrop-shaped weld pools and version **C** for welds forming equiaxed dendrites in the middle. The versions **B** and **C** may be regarded as braches diverging from a common trunk.

Model Frame A includes a range of growth rates R, extending so high that the solidification shifts to either Model Frame B or Model Frame C in practically all fusion welding occasions.

5.4.1 *Model Frame*-A: Elliptic pool – Solute profile, grain & cell geometry, Four Cases and R & G

The *Model Frame-A* in Fig. 5.4 incorporates the solid solute profile of Fig. 5.3, the grain and cell geometry of Fig. 5.2, the modeling of cell morphology and size of Fig. 5.1, as well as the four *Cases* and a selection of their *Sub-Cases*.

The *Model Frame* should include all pertinent *Sub-Cases; we present only two basic ones.* Also all the *SCV*'s should be presented; the *Model-Frame-A* presents only their elements, the thermo-metallurgical variables *TMV's* **R** and **G**.

The *model* of an actual weld is derived from a *Model Frame* by excluding the obsolete *Cases* or *Sub-Cases* and arranging the ones regarded pertinent in logical sequences. If different *Cases* or *Sub-Cases* are placed one after one other, their continuity at the joint must be given special attention. The *model* for the actual weld thus acquired, is the result of the chosen *Cases/Sub-Cases*; the only completely reliable verification of the rightness of the choices is through welding experiments.

Model Frame-A assumes welding speed low enough to invite *Case 1* at start, and high enough to invite capillary effect and *Case 4* at the end. Obviously, one or both of these must be discarded in the modeling of most actual welds.

The x-axis scale x=0 is located at the weld interface WiF and x=1.0 at the weld centerline. A rough estimate for the widths of the initial– and final transients are of the order of 15…20µm (Ch's 2.5.13 and 2.5.12 [12 p.19]) If the total length of the depicted grain is, say 10 mm or 10000µm, it is obvious, that the start and the end of the x-scale are greatly enlarged.

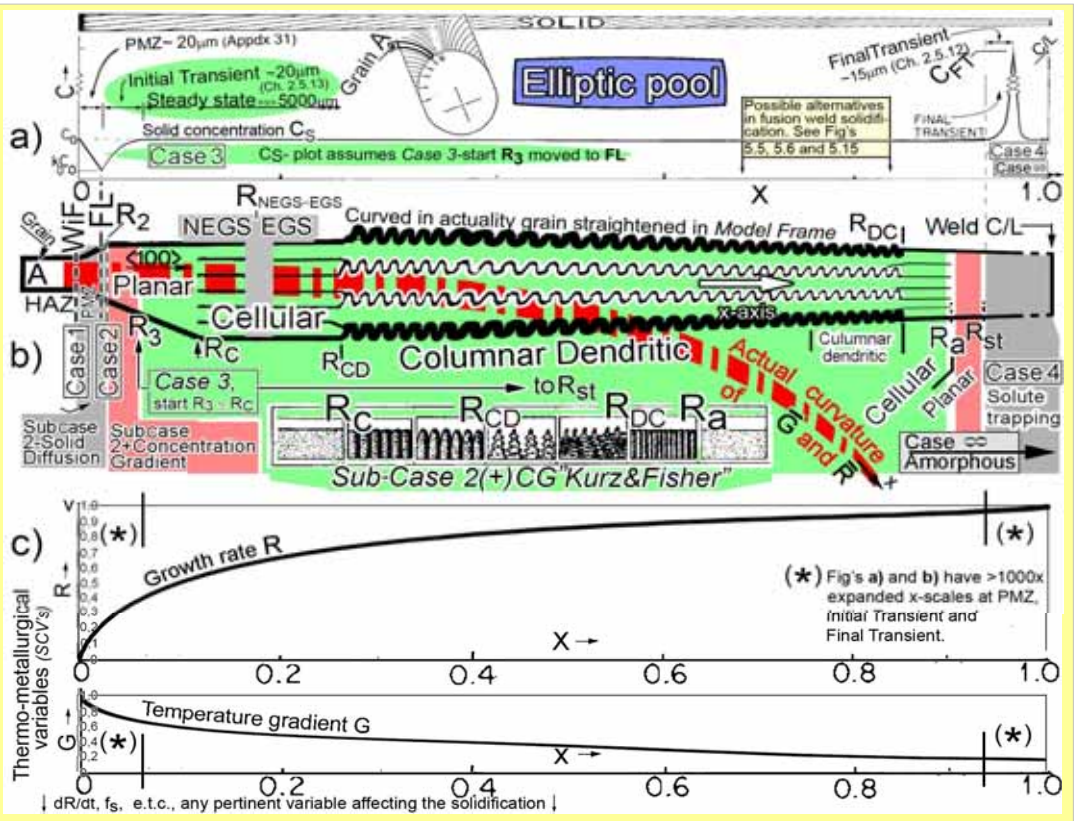

Fig.5.4. The ***Model Frame-A*** for a weld with an elliptic pool, including four *basic model-element-groups:* **(a)** solute profile, **(b)** solidification modes & microstructures, **(c)** thermo-metallurgical variables (of which *Sub-Case Variables, or SCV*'s are formed) and **(d)** *Cases* & *Sub-Cases* (presented with group **b**). The curved grain is straightened. $\boldsymbol{R = R_{min} = 0}$ *at x=0.* $\boldsymbol{R = R_{Max}}$ *(=* $\boldsymbol{v}$*, Eq.1.7) at the weld C/L.* $\boldsymbol{R_{Max} > R_{ST} > R_a > R_{DC}}$.

a): The longitudinal solid solute concentration profile **C** of the narrowing grain **A**; $\mathbf{k_0C_0 \rightarrow C_0 \rightarrow C_{FT} \rightarrow C_0}$. Assumed is solidification up to solute trapping. Solidification will at some $R_{critical}$ swift to the alternative Model *Frame-B or C* in Fig's 5.5 and 5.6, in most fusion welding occasions.

Case 3 may start at **WiF**, **FL**, **R3,** or, but no later than $\mathbf{R_C}$. C_S-plot assumes *Case 3*-start at **FL**.

b): Grain **A** in HAZ (as the grain **A** in Fig. 1.26a) has an *easy growth direction* ***EGD*** in $\overline{G}$ direction. It out-competes its neighbors; its growth is *planar* from **WiF** until $\mathbf{R_C}$, where *cells* emerge and solidification continues with *Sub-Case 2(+)CGK&F* in the insert (Ch. 4.2.1). At $\mathbf{R_a}$ the growth turns *planar* due to the *"capillarity effect"*. *Case 4* starts at $\mathbf{R_{ST}}$, with *solute trapping*. The *Cases* are stitched together with the *Sub-Cases* (Ch. 4), to create an uninterrupted continuum from start of the solidification to its end. *(The Case 3-based solute profile in a) and the Case 2-based Sub-Case 2(+)CG"K&F" in b) conflict slightly: the latter does not recognize the steady state of the former.)*

The solidification is marked to start with *Case 1*, changing to *Case 2* at $\mathbf{R_2}$ and to *Case 3* at $\mathbf{R_3}$. As long as the moot between *Cases* 2 and *3* exists, the *Model Frame* only reminds of the existence of the various models; it does not advice in their choice and locating. At least one *Case* must be chosen and if this is done, the rest must be discarded. *Multiple-Case*-systems require continuum through the transition area. If the modeled solidification is estimated to happen with *Case 3* from start to end, *Cases 1, 2 and 4* (and *their Sub-Cases*) are discarded and $\mathbf{R_3}$ extends from **WiF** to the weld C/L.

The $\mathbf{R_{NEGS-EGS}}$ is the rate, below which the growth is proposed to follow the $\overline{G}$ only, with no regard to the easy growth direction **EGD**. Above $\mathbf{R_{NEGS-EGS}}$ the growth does follow the **EGD** (Ch's 1.1.20 and 2.9). *In our experiments, the* $\mathbf{R_{NEGS-EGS}}$ *was always* $< R_C$*, i.e. all detected cells followed their EGD's.*

c): Of the thermo-metallurgical variables only **R** and **G** are shown. All pertinent variables affecting the particular solidification modeled should be exhibited. These variables or their combinations are the variables in the *Sub-Cases* and in this capacity we call them *Sub-Case Variables, SCV's*, essential for relating the *Sub-Cases* with one another. *[FRAME All v3.jpg]*

5.4.2 Model Frame-B: Teardrop pool

In the *Model Frame-B,* the solidification starts as in the *Model Frame-A,* but diverges from it at some $R_{Critical}$. Increasing **R** *leads to latent heat evolution exceeding the ability to of the system to dissipate it, which hampers the growth to the welding direction* $\boldsymbol{R_y}$, *making the grain grow straight and* giving the weld pool a teardrop shape *[4 p.329]*. This pool form is often associated with a greater susceptibility to hot cracking.

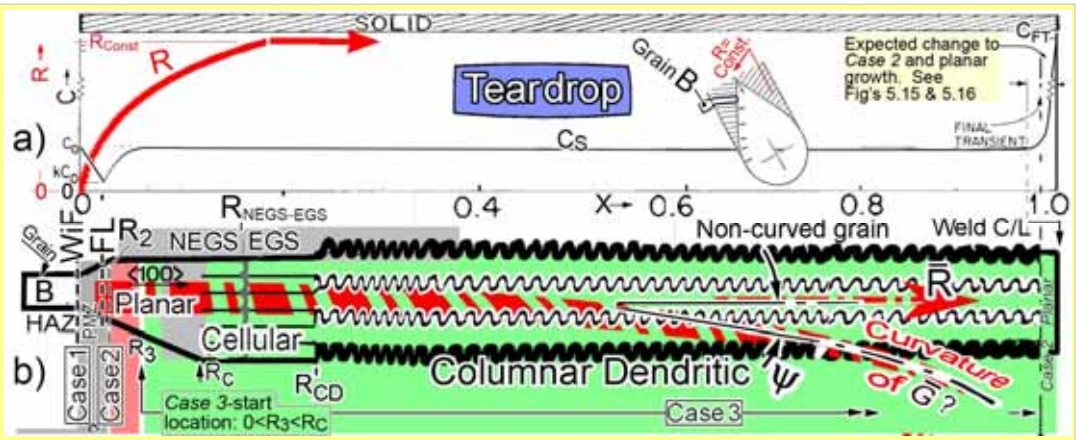

Fig.5.5. The ***Model Frame–B*** for solidification of a teardrop-formed weld pool, as the grain **B** in Fig.1.26b. The grain **B** does not curve after $R \geq R_{Const}$.

a): Solid solute concentration profile **C** decreases from $\mathbf{C_0}$ at **WiF**, and increases from $\mathbf{k_0C_0}$ at **FL** to $\mathbf{C_0}$ at steady-state *Case3* region. In the end of the final transient, $\mathbf{C_S}$ reaches $\mathbf{C_{FT}}$ with ***Case 2***.

b) The trailing end of the pool is straight and the growth rate $\overline{R}$ – being perpendicular to it – is straight and const. Grain **B** in HAZ, having an advantageous easy growth direction **EGD** in the initial **G** – perpendicular to **WiF** direction, grows from weld interface **WiF** to the weld C/L.

Planar → *cellular* → *columnar dendritic*-transformations occur as in the *Frame-A*. In this teardrop model, we assume that $\mathbf{R_{DC}}$, $\mathbf{R_a}$ and $\mathbf{R_{st}}$ will not be reached and no Equiaxed dendrites will appear.

It is possible to place a transformation to *Case 2* at the end of the final transient; the continuum must be preserved in the process.

A reducing to below the diffusion distance width of the remaining melt suggests Case 2, small systems [5 p.122]. We propose that Case 2 renders the solidification mode planar; as it does not create any constitutional supercooling, Fig. 1.33.

The classic explanation for the teardrop shape is that the latent heat evolution exceeds the ability of the system to dissipate it, and the growth rate component to the welding direction $\mathbf{R_y}$ becomes zero [4 p.329]. This seems to imply that the temperature gradient vector $\overline{R}$ stops changing its direction. An advantage of this theory is that no metallurgical phenomena are required to explain the pool form: grains grow straight because $\overline{R}$ advances straight. Appendix 39 presents an alternative proposal, based on an analysis stating that a non-curving $\overline{G}$ is thermodynamically highly unlikely. The problem with this theory is that it requires a non-thermodynamic – metallurgical – phenomenon to explain the straightening of the grain. For this we propose the energy $\mathbf{E_{EGS}}$, favoring growth to an **EGD;** increasing with **R**, $\mathbf{E_{EGS}}$ tends to hamper the curving of the grain.

R is presented with the Fig. a). **G** is assumed as in Fig. 5.4 c).

The substantial differences from the previous figure are **(i)** the straightness and the more even width of the grain, and **(ii)** the head-on-head collision with the grains from the opposing side, at the weld centerline, in the final transient. This solidification type is believed to increase susceptibility to hot cracking. *[FRAMETear v3.jpg]*

5.4.3 Model Frame-C: Equiaxed dendrites - elliptic pool

Solidification starts as depicted in *Model Frame-A,* but shifts to forming equiaxed dendrites near the weld centerline, as depicted in the *Model Frame-C* in Fig.5.6.

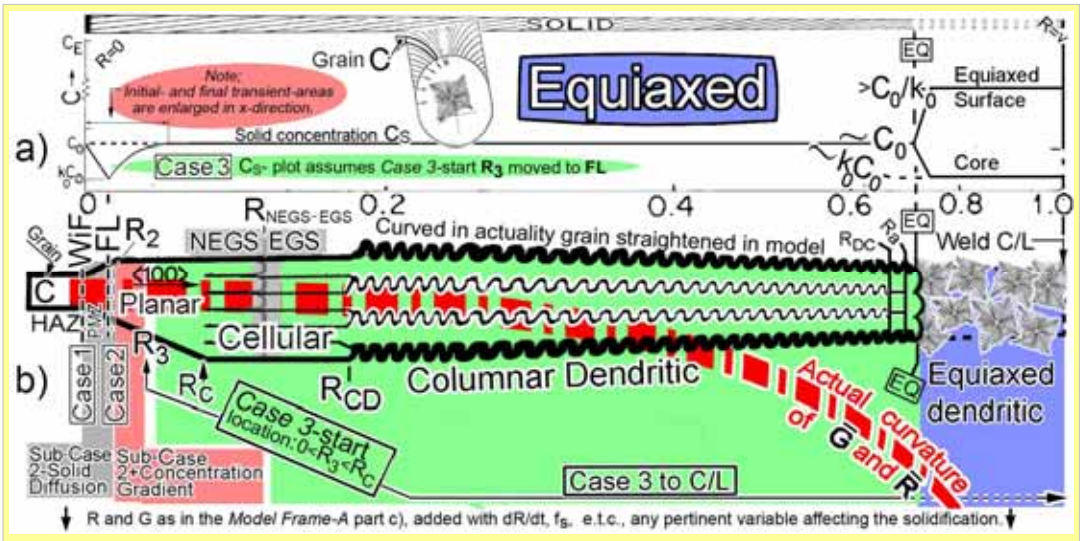

Fig.5.6. The ***Model Frame-C*** for solidification of welds developing equiaxed dendrites near the weld centerline. Weld pool is assumed elliptic and the curved in actuality grains are straightened in the figure. The *Frame-C* assumes that $\mathbf{R_{DC}}$ and $\mathbf{R_a}$ have been reached. This obviously is rare in actual welds; either or both of the lines $\mathbf{R_a}$ or $\mathbf{R_{DC}}$ probably lie beyond to the right of the line **EQ** and must be discarded from most occasions of fusion welding.

a): Solid solute concentration profile **C** is as in Fig. 5.4 up until the line **EQ** (the start of the equiaxed zone), after which **C** divides into two: the concentrations of the dendrite arm centers and their surfaces. Total micro-segregation is assumed, which in reality seldom may be the situation. However, the diffusion has a relative long time to act due to the small diffusion distances from the dendrite arm center to its surface. The shallow **G** near the weld centerline provides time for the diffusion.

b) Grain **C**, growing from HAZ at **WiF**, experiences the same solidification history as Grain **A** in Fig 5.4, up until the line **EQ**. It is generally agreed that very little solute piles up on the weld centerline; the rejected solute tends to be finely dispersed in between the equiaxed dendrites. This type of solidification generally reduces the susceptibility to centerline hot cracking [3 p.188]. A contradicting view is presented in [31 p.179-s].

c) The thermo-metallurgical variables **R** and **G** are assumed as in Fig.5.4 c). *The Model Frame would obviously work more flexibly as a computer program than in this paper form.* [FRAME EquiAxed v2.jpg]

5.4.4 Axial grains

Further solidification types, requiring a *Model Frame* modification are **(i)** the weld pool, forming axial grains ([3 pp.176-178] and Fig. 2.18a), and **(ii)** the weld pool, forming a tail [4 pp.399-400], not presented here (the tailed pool is briefly discussed in Appendix 39).

The axial grains obviously act as exceptionally long grains facilitating long-distance solute transport from the start of the weld even to the end crater. Their *Model Frame* is curbed outside the scope of this work.

5.5.2 Completing the Model Frames with mathematical modeling.

The presented semi-quantitative *Model Frames* may be quantified with mathematical modeling; of such the *phase-field* (PF) *modeling* appears perspective [99][83][106]**.** Gandin and Rappaz developed from it the *cellular automaton modeling,* facilitating grain orientation simulation [83b]. Figs 5.7 and 5.8 depict cells 2 and 3-dimensionally and Fig. 5.9 compares real micrograph **A** with model **B**, while **C** and **D** map orientations with different test parameters. These modeling techniques develop with a pace making any overview of them out of date by the time it is printed.

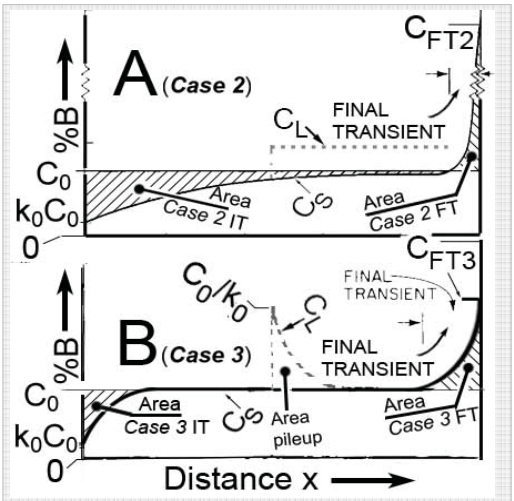

Fig. 5.10. Solid solute profiles of *Case 2* (**A**) and *Case 3* (**B**). Area ***Case2 IT*** = **Area *Case 2* FT** >>> **Area *Case* 3 IT** = Area Pileup =**Area *Case* 3 FT** *in planar growth.* If the *Case 3* solidification enters the cellular/dendritic mode, the area ***Case 3 FT*** reduces by the amount of solute *fenced-in* between cells/ dendrites.

5.5.3 *Cases 2 and 3 in weld solidification*

The *Cases 1* and *4* in the *Model Frames-A…C* are obsolete in the models of most practical welds, as was discussed in Ch. 4.1.4. Fig. 5.10 compares *Cases 2* and *3*. The choice between these *Cases* has a great influence on modeling; of the two, *Case 2* segregates a much larger amount of solute to the final transient, and it is unable to form cells or dendrites. If *Case 3* shifts to the cellular or dendritic growth mode, this difference in macrosegregation increases further: part of the solute becomes *fenced-in* between the cells or dendrites, and this may reduce the amount of *Case 3*-induced solute in the final transient to negligible.

Modeling of an actual weld - choosing arbitrarily between the mathematical models associated with either of the two *Cases* and their *Sub-Cases* - leads to the solution of the chosen model. The *Model Frame*-analysis gives erroneous result for erroneously chosen *Cases/Sub-Cases*; the choice is crucial.

5.5.4 Role of the stagnant layer

A stagnant layer wider than the solute pileup extinguishes any non-diffusional mixing of the rejected solute, the pileup remains and the solidification follows *Case 3*. If the pileup is wider of the two – or the stagnant layer is totally absent – and the pool is heftily mixed (as a weld pool almost invariably is), then *Case 2* and its *Sub-Cases* are feasible (see Appendix 42).

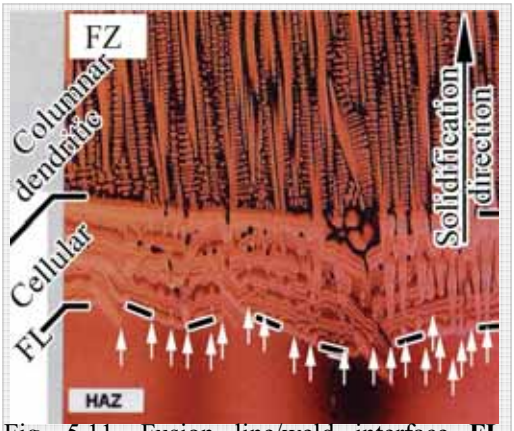

Fig. 5.11. Fusion line/weld interface **FL,** Cellular and columnar dendritic areas and cells (white arrows) as marked by the author on a micrograph of a Ni-superalloy spot weld. David, Babu, Vitek2001 [105]. No distinct planar zone is detected.

The start of the longitudinal growth from WiF with *Case 2* seems improbable. The PMZ-archipelago of solid peninsulas and islands probably extinguishes even the heftiest mixing even with no stagnant layer at all, making *Case 3* probable. *Case 2* does not appear feasible until the length of the remaining melt reduces sufficiently, as in **(i)** the final transient, or **(ii)** in the transverse growth between sharp-tipped cells, taking place in a limited amount of melt with distances coverable with diffusion ([5], "small systems", p.122). Hence, we assume that the dominating *Case* of the longitudinal solidification of a grain in a fusion weld – from the weld interface to the final transient - is the *Case 3*. In the final transient, the *Case 2* may replace *Case 3*.

5.5.5 Planar growth start in *Case 3*-dominated fusion weld solidification

The assumed domination of *Case 3* makes no restrictions to the selection of the micrographic morphologies of the solidified structure; the growth modes of Fig. 1.45 may all be results of *Case 3* solidification, including the planar growth. We presume, and our results corroborate, that the fusion weld solidification starts with planar growth. This is not self evident in weld solidification; Fig. 5.11 shows a weld with no planar zone at all. It is a spot weld, but even in fusion welds, the planar zone may be so small that its existence is questionable, as the hardly detectable ~ 3 µm wide one in Fig. 2.21.

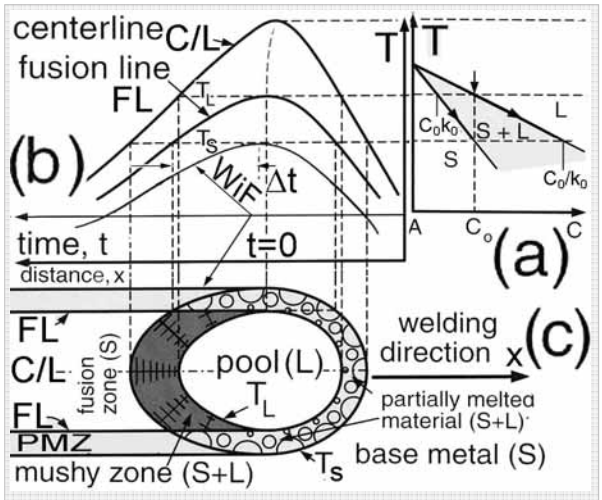

Fig.5.12. Bead-on-plate-weld solidification from weld interface **WiF** through partially melted zone **PMZ** to fusion line **FL** .**(a)** phase diagram, **(b)** thermal cycle, **(c)** microstructure with emphasis on **PMZ**.
Based on Kou 2003 [3 p.180 Fig. 7.12]. *WiF and thermal cycle for T_E in (b) added. Welding direction is reversed from left to right and eutectic reaction neglected*

5.6 The melting stage and Melting/ Solidification- (M/S-) model

5.6.1 Melting prior to solidification

The weld pool is surrounded by a partially melted zone **PMZ.** We call the locus of its solidus weld interface **WiF** and liquidus the fusion line **FL**, Fig. 5.12. We intend to point out that the melting stage plays a significant role in the solute distribution at the start of the solidification next to the weld interface **WiF**.

5.6.2 The Melting/Solidification or M/S – model

We propose a quantitative *Melting/Solidification (M/S)*-model, taking into account the melting stage near the weld interface in fusion weld solidification [91]. A detailed description of the model is in Appendix 38, here we limit to the essence of the mechanism, by which the melting stage affects the solidification.

Fig. 5.13 a) shows the trajectory ***ABE*** of the point ***A*** of the melting front. Its growth rate (marked ***–R***) follows Eq. 1.1.18A and decelerates to zero as the trajectory reaches the point ***E*** **(**Fig. 5.13 b**),** where starts the solidification along the trajectory ***EFH***.

The model assumes that:

(a) The melting and solidification fronts are normal to liquidus isotherm $T_L(C_{L0})$ = const, (C_{L0} is the initial solute concentration in the weld pool).

(b) The melting or solidification proceeds in the temperature gradient direction only, i.e. growth in the easy growth direction ***EGD*** is not assumed (assumed is ***NEGS*** only, Ch. 1.1.20).

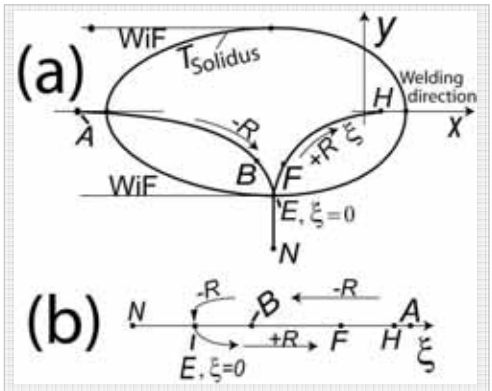

Fig.5.13. The trajectory of a point in the melting front is depicted as **ABC** (a). The ξ-axis is the straightened distance of the melting front (after t=0 the solidification front) from the weld interface WiF.

(c) Solidification occurs with *Case 3* and with a planar solid/ liquid interface moving with a solute pileup in front. (This model applies to near-WiF regions with temperature gradients ***G*** higher than the limiting gradient for constitutional supercooling, as in Fig. 1.45 "Planar").

5.6.3 M/S-model: a model with melting stage, solid diffusion and acceleration of R

The proposed *Melting/Solidification- or M/S-model* for the solute distribution near a fusion weld interface was designed on the principle of prior-to-solidification solid diffusion forming an upside-down solute-lean concentration gradient with minimum $\mathbf{C_S}$ at ~ $\mathbf{k_0C_0}$, Fig. 5.14. The horizontal **ξ**-axis is the distance from **WiF**, along the straightened melting trajectory

The *M/S-model* takes into consideration **(i)** the melting stage, **(ii)** the post-solidification solute back-diffusion in the solid, **(iii)** the growth rate acceleration, typical to fusion welds[16]. **(iv)** the temperature dependency of the solute solubilities and diffusion coefficients in both liquid and solid, as well as **(v)** the welding speed and heat input and heat conduction kinetics (Appendix 38).

The mass transfer solution is of type *Case 3,* solved with numerical *finite difference method* solution. The concentration gradient is solved with the algorithm of the Toronto-pioneers [49][71], with the difference that the concentration ***C*** is replaced with *the mass transfer potential* ***U,***

Eq. 2.13 $U(x', t) = C(x', t) / S(x', t)$,

where **S** is the solute solubility. The benefit is that **U** is continuous through the S/L-interface facilitating the solving of the solute concentration continuously through the interface.

*A detailed description of the M/S-model is given in Appendix 38. The effects of the phenomena **(i)**, **(ii)** and **(iii)** above are depicted separately; the first in Fig. 5.14, and the second and third in Appendix 38 as Fig's A38.3 and A38.4.*

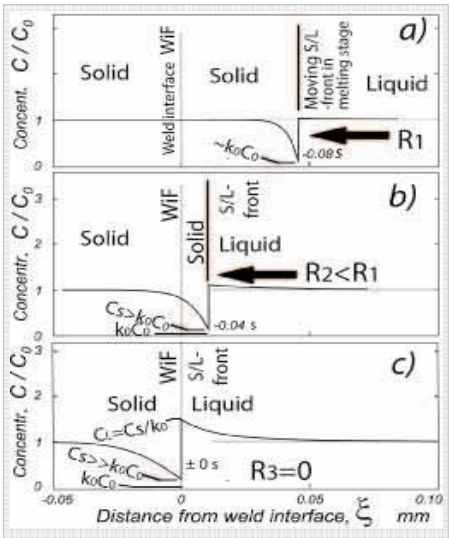

Fig. 5.14. The melting stage prior to solidification. The advancing S/L-front forms an upside-down solute-lean concentration gradient due to prior-to solidification diffusion in solid. The rejected solute piles in the liquid. Diffusion starts smoothening this pile-up, when melting turns to solidification at WiF.

5.6.4 The solidification starting with the M/S-model

Fig. 5.15**a** compares the *M/S model* with the classic *Case 3* model (e.g. Fig. Lippold & Savage, Fig. 2.25B.)

Fig. 5.15 shows the solidification continuum from the *Case 3*-based **M/S-**model at start, until the end of the planar zone. From there, the Mullins&Sekerka-*Sub-Case 3(+)M&S* model[17] reigns until the final transient. The model assumes a transformation of the solidification mode to *Case 2* at the end of the final transient (*small systems* [5 p. 122-126]).

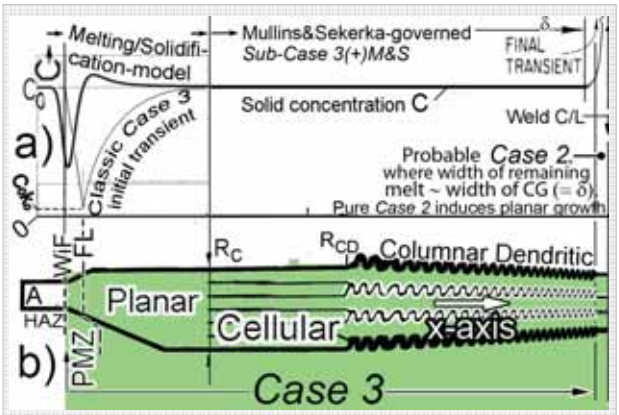

Fig. 5.15. A *model* developed in the *Model Frame* for a fusion weld. The *Melting/Solidification-model* (*M/S model*) governs solidification from start until the start of the cellular growth at $\mathbf{R}=\mathbf{R_C}$. From $\mathbf{R_C}$ to the final transient, the solidification follows the Mullins&Sekerka-solution, which in the SCS2-classification is the *Sub-Case 3(+)M&S* (See Ch. 4.2.2). The Final transient solidifies according to *Case 2*.

a): The left side of the upper plot is the solid solute profile according to the *Melting/ Solidification*- model, taking into consideration the factors **(i)-(v)** .listed in Ch. 5.6.3 Below it is – for comparison – the solute profile of the classic *Case 3* initial transient. **b):** a rough qualitative picture of the microstructure.

[16] To be exact, the *M/S-model* takes into consideration also the deceleration of the upside-down CG during melting.
[17] The *Sub-Case 3(+)M&S, does not consider the marginal stability effect* starting at Ra in Fig's.4.5 and 5.4**b**.

5.6.5 From *M/S-model* to pure *Case* 3.

We – as said - propose fusion weld solidification starting with *Case 3*. To be exact, the very start of the solidification occurs not by pure *Case 3*, but with its *Sub-Case,* we call *M/S-model*. This may sound confusing, but a *Sub-Case* is - by definition - a mathematical equation modeling the effect on the solidification of some *Sub-Case variable* or in this occasion *variables, SCV*'s. The variables in the *M/S*-model are **(i)** the melting stage, **(ii)** the acceleration of **R**, and **(iii)** the back-diffusion in the solid DS. This was described above in this Ch. 5.6, and in more detail in Appendix 38. The effect of all of these three variables diminishes to negligible with growing time and distance from the WiF, and the *Case* approaches pure *Case 3*. This approaching is asymptotic and presents no conflicts in the continuum, which continues as *Case 3* to the final transient.

5.6.6 From *Case 3* to *Case 2* in the Final Transient

The problem in preserving the continuum arises in the *final transient* **FT**, where – as we propose – the *Case 3* transforms to *Case 2*, with the mechanism presented in Fig. 5.16. The part **A** of this figure has the *concentration gradient* **CG** barely colliding with the weld C/L, i.e. the **CG** approaching from the opposite side. At this point, the solidification *Case* starts transforming from *3* towards *2.*

Fig. 5.16 **B** shows the **CG** after it has advanced a distance "**CG cut-off"** after the collision. An amount of solute, proportional to the **"Cut-off Area 2"** has been added to the remaining pileup, evening out with a mechanism approaching *Case 2* as the distance Δ_B diminishes.

The presented model is a *Sub-Case 3(-)"CG cut-off",* which takes the operation point from *Case 3* to *Case 2*[18]. The profile for the C_L of his model has been solved [49][5 Fig. A11.2 and Eq. A11.13 p.279].

Note: *The solute concentrations in the final transient - in the liquid C_{FT} and in the solid $k_0 C_{FT}$ - tend to grow so high, that in most practical systems some phase transformation – e.g. eutectic reaction – intervenes and stops further concentration increase. This dissertation is restricted to single-phase alloys and such phenomena are not regarded.*

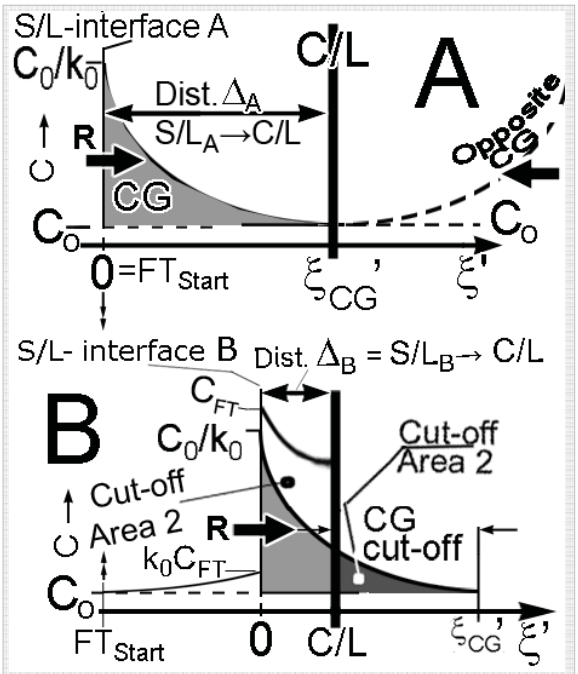

Fig. 5.16. **(A):** The ***S/L-interface A*** (with concentration gradient **CG)** colliding with the weld centerline **C/L** at distance Δ_A with rate **R;** start of the final transient FT. end of pure *Case 3* solidification.
(B): The distance of the S/L_B-interface to weld C/L = Δ_B has diminished < (CG-width = ξ_{CG}'). Part of the solute pileup, corresponding to the *Cut-off Area 2*, is re-located into the remaining solute pileup between S/L_B- interface and the weld **C/L**. Diffusion evens out the gradient, leading to an increasingly pure *Case 2*-solidification.

[18] It can be readily joined as a continuation to the Mullins & Sekerka-solution and its derivatives, all being *Case 3*-based models.

5.7 About the Model Frame, Cases, Sub-Cases, Sub-Case Variables and the Lausanne and RPI approaches

This dissertation is based on concepts of *Cases*, *Sub-Cases* (a system for categorization of existing and new models of the solidification) and *Sub-Case Variables SCV's*. The *Model Frame* is a tool utilizing these concepts together. Its philosophy is that the modeler finds easily - and is even forced to either include, or discard - elements, easily left without attention. For example, when modeling welds with exceptionally low or high growth rates, it is convenient to have the whole known palette of models for growth rates from zero to ∞ in front of you, as in the *Model Frame-A*. As new *Sub-Cases* emerge, they should be included in the *Model Frame*. The *M/S-model* is such a new *Sub-Case*. It is obvious that the *Model Frame* should be presented as a computer program, the paper presentations in Fig's 5.4 – 5.6 lack the needed flexibility.

The *Cases*. The concept of ***Case*** is indispensable when different solidification models are analyzed and compared with one another. This dissertation would be impossible to write, replacing the approximately five hundred references to the *Cases* with the corresponding *descriptive classifications* (Ch. 1.2). We attribute the casing system to Professor Savage, and call it the *Savage Casing System SCS*. The fact is that David & Vitek [62], DebRoy & David [80 p.104], Messler [4] and Lippold & Kotecki [11] present or refer to a similar or identical classification. It may well be that several researchers have independently come to this concept; the first seems - however - to have been Savage, who – from his part, most certainly - based his first three *Cases* on Chalmers [13 and 35][19].

The consecutiveness of the *Cases* (*Case 4* being "above" *Case 3* a.s.o.) comes from their free energy, but may still be somewhat misleading. The *Case 4* has obviously the highest free energy of the four. Similarly, *Case 1* – the *Case* of equilibrium - has undoubtedly the lowest free energy. Moreover, the solute pileup in *Case 3* represents higher free energy than the completely mixed melt in *Case 2*. However, it is a mistake to take the four *Cases* as consecutive stations on one railroad. *Cases 1* and *4* would indeed represent the end stations of such a railroad, but you have to build shrewd tracks to place *Cases 2* and *3* on the same railroad. An idea of two tracks from *Case 1* to *4*, the first through *Case 2* and the second through *Case 3* would be less erroneous. Appendix 40 suggests that the probably best one of the present models joining *Cases 2* and *1* is not a mathematically rigorous analytic solution. The discussion continues in Appendix 41 by visualizing the mutual relations of all four *Cases*. The conclusion is, that the *Cases* operate in different multi-D spaces, between which analytic continuums are impossible (with the *SCV*'s used). If our presumption - of solidification changing *Cases* during the process – is correct, there probably must be a rigorous solution for the said continuum. We obviously should find *SCV*'s bringing the different *Sub-Cases* into one and the same multi-D space. If this line of thinking is correct, this problem surely will find its solution. The situation reminds of the emergence of the term $\mathbf{k_0}$ facilitating the analytical solution of the *Gulliver-Scheil-equation*, for which its pioneers had only numerical solutions.

The *Sub-Case Variables, SCV*'s, consist of either thermodynamic (as **G, R**, *welding parameters*, *solidified fraction*, a.s.o.), or metallurgical (as the $\mathbf{C_0}$, **D**'s, $\mathbf{k_0}$, a.s.o.) elements[20]. These elements are called *TMV*'s. In the *Sub-Cases*, the *TMV's* are used either alone or in combinations and in that capacity they are called ***SCV's***. Appendix 41 visualizes the *Cases*, *Sub-Cases*, their mutual relations and the operation paths in a weld. Fig. A41 shows, that the ratios $\mathbf{D_L / R}$ and $\mathbf{D_S / R}$ are more usable as ***SCV's*** than the *TMV's* $\mathbf{D_L}$, $\mathbf{D_S}$ and **R** would be alone.

The drawback of complex ***SCV***-combinations is the complexity they bring into the model. The Burton-Primm-Slichter-factor (Eq. $2.4.2_{BPS}$), for example, is a historic corner-stone as the first ***SCV*** widening *Case 2* towards *Case 3*, but it is too complex and crystal-pulling-oriented for practical use in welding.

---

[19] There is no reference for this, but Chalmers' Physical Metallurgy [35], including its pages 251-253, was intellectual capital for Savage as it is for all of us. The three first *Cases* stem from there, and to them Savage added his fourth *one*.

[20] We frame out stresses from this dissertation, albeit they may and do affect the solidification.

The continuum of the fusion weld solidification and *Sub-Cases*. The growth rate **R** in a fusion weld accelerates from zero to **v**. We propose that the fusion weld solidification starts with the *Case 3*-based *M/S-model*, turns to *Case 3*, and ends at the final transient with *Case 2*. (If there are zones of *Cases 1* and/or *2* at the start, due to the **v=** ~0, they are of negligible width. With extremely high **v**, the solidification may follow the *Case 4* regime, as presented in Fig. 5.4, but usually either of the models in Fig's 5.5 or 5.6 intervenes before that).

The ***Lausanne-approach***, centered in EPFL, solves the problem of the continuum *Case 2→Case 3* by adding a concentration gradient to the *Gulliver-Scheil*-equation, forming the *Sub-Case2 (+)CG"K&F"* (Ch. 4.2.1).

Our assessment fails to properly credit professor Kurz's associates in the development. The scientists below and several others have either taken part of the development or exploited this approach.

1981	*Clyne, Kurz*	*[86]*	*2000*	*Boettinger, Coriell, Greer, Karma, Kurz, Rappaz, Trivedi*	*[19]*
1986	*Kurz, Giovanola, Trivedi*	*[100]*	*2000*	*Miettinen*	*[88]*
1989	*Trivedi, Sekhar, Seetharaman*	*[98]*	*2002*	*Koseki*	*[83]*
1992	*Gandin, Rappaz*	*[83b]*	*2002*	*Nishimoto, Mori*	*[89]*
1994	*Kurz. Trivedi*	*[97]*	*2002*	*Koseki, Inoue, Nogami, Fukuda*	*[90]*
1997	*Winkler, Amberg, Inoue, Koseki*	*[44]*	*2004*	*Pavlyk*	*[99]*
1999	*Karma, Rappel*	*[93]*	*2004*	*Dejmek, Folch, Parisi, Plapp*	*[106]*

These works form the core of what we call the Lausanne approach. They differ from one another, and crediting this all on EPFL can be disputed. There is a tendency to prefer Case 2 over Case 3, as in Fig. 5.3.

The *Lausanne approach* extends the solidification theory to the area of rapid cooling. Many of its features (*Péclet-number*, *Ivantsov-solution, capillarity limit or marginal stability limit* etc.) are seldom adopted into the fusion weld solidification research, except in Japan. The terms are associated with high solidification rates. The R=10 mm/s (60 cm/min) marginal stability limit for stainless steels of Nishimoto and Mori determined (Fig. 2.41) is well in the range of modern welding.

The Appendix 41 visualizes the difficulty of linking the Sub-Cases between Cases 2 and 3; these exist in different spaces with two alien to one another free SCV's: Ω and f_s. This discrepancy is associated with the presently used SCV's; it is assumably solvable. The Case 2 – associated f_s can obviously be adapted to Case 3, as it relates to the grain length. It seems possible to make Case 3 adopt Ω, e.g. the way outlined in Chapter A42.3 We will leave this topic with a note that Ω is a critical variable, as it determines the operation point of the solidification between the Cases 2 and 3,which strongly affects the amount of solute bulldozed to the weld centerline, as discussed in Ch. 5.5.3. Before solving the problem of the operation point of Ω, the question should be asked: is this necessary? Case 3 assumes $C_s=C_0$ in the steady state, which extends from the initial to the final transient. The Case 3 of the Toronto pioneers adopts readily the 3-based Mullins & Sekerka approach, and this, we assume, adopts readily new features; it contains the idea of absolute stability in higher growth rates [77 p.449].

So, choosing Case 3 would be simpler. Unfortunately the nature does not do things the ways simpler for us, and the possibility of Case 2 and its Sub-Cases reigning fusion weld solidification is very real. Maybe the estimates $\Omega \cong P_C$, or the ones discussed by [5 pp. 74-76 and Fig.A8.3], or others, are closer to the truth. Maybe the solidification does reach $C_S=C_0$ later than predicted by Eq. 2.5.14. Maybe the steady state is reduced to the starting point of the final transient as in Fig. 5.3.

The *RPI-(Savage)-approach* assumes that the S/L-interface in a weld pool has *Case 3*-conditions due to a stagnant layer, the width of which (~~~75μm) almost without exception is wider than the width of the pileup ξ_{CG}= *~15μm* (Appendix 42 and Ch. 2.5.12). This makes the solidification follow *Case 3* from start to the final transient **FT.**

This approach is common in the welding research in the U.S.A.. Similarly as the researchers associated with the Lausanne-approach above, the American welding research community is heterogeneous and only loosely or not at all associated with RPI.

Between the cells or dendrites and at the final transient, the diminishing remaining melt solidifies with *Case 2*[21]. A discrete jump from *Case 3* to *Case 2* is unlikely (Appendix 41); Fig. 5.16 outlines a *Sub-Case 3*(-)"reducing CG" for this.

The accuracies of the two modeling approaches in welding should be measured experimentally.

[21] Both research lines agree on this: Kurz&Fisher [5 p.122-] and Lippold&Kotecki [11 p.163].

Chapter 6 EXPERIMENTS ON PURE AND DOPED Cu

The aims of the experiments were to study the solidification continuum of grains of pure and doped Cu welds from weld interface to the weld centerline, and the hot cracking susceptibility of the various microstructures.

6.1 Materials and tests

Variables in the test were **(1)** the dope in the copper, **(2)** *welding speed* ***v*** and **(3)** *ultrasonic irradiation*. Hot crack propensity was tested with *Varestraint* for parallel to weld straining and self-restraint ***R****-test* for perpendicular straining.

Welding speeds were **v** ~ 0 to 5, 10, 100 and 200 cm/min. One weld with **v** = 3000 cm/min and comparable copper type (CuOF) was acquired to the metallographic examination from tube production (Appendixes 8-10).

6.1.1 Materials

Base metals and dopes: Tested coppers were four: **(1 & 2) C & D** = standard CuOF of Outokumpu, **(3) E** = purified copper Table (6.1), and **(4) 30m =** the 3000 cm/min welded tube; its chemical batch analysis is not available, but it is standard Outokumpu CuOF. The dopes are in table 6.2.

OUTOKUMPU 20.4.2005 MLTK 2005/103

Chemical analysis

	C	D	E	Unit
Cu	99,997	99,998	99,9995	%
Ag	15,3	11,3	0,6	ppm
Al	<0,08	<0,08	<0,08	ppm
As	0,94	1,03	0,14	ppm
Bi	0,18	0,36	0,2	ppm
Cd	<0,003	<0,003	<0,003	ppm
Co	<0,006	<0,006	<0,006	ppm
Cr	<0,05	<0,05	<0,05	ppm
Fe	0,4	0,2	<0,2	ppm
H	<0,2	0,5	<0,2	ppm
Hg	<0,5	<0,5	<0,5	ppm
Mg	1,7	1,9	<0,1	ppm
Mn	<0,1	<0,1	<0,1	ppm
Ni	<0,2	0,6	<0,2	ppm
O	1,3	0,4	1	ppm
P	<0,3	<0,3	<0,3	ppm
Pb	0,23	0,39	0,29	ppm
S	5,3	5,9	1,6	ppm
Sb	0,07	0,09	0,63	ppm
Se	0,4	0,7	<0,1	ppm
Si	<0,2	<0,2	<0,2	ppm
Sn	0,11	0,1	0,2	ppm
Te	0,09	0,36	<0,01	ppm
Zn	<0,1	<0,1	<0,1	ppm
Zr	<0,09	<0,09	<0,09	ppm

Table 6.1. Chemical analyses of the welds types **C**, **D** and **E**

		At. nr.	At. wght [amu]	Dens. 20C [G/ml]	Cryst. struct.	Atom. rad. [nm]	Most comm. val.	Melt. point C
	Cu	29	63,6	8,9	FCC	0,13	1+	1085
1	Ag	47	107,9	10,5	FCC	0,14	1+	962
2	B	5	10,8	2,3	Rhmb.	-	3+	-2150
3	Bi	83	209,0					271
4	C	6	12,0	2,3	Hex.	0,07	4+	3367
5	Fe	26	55,9	7,9	BCC	0,12	2+	1534
6	La	57	138,9					~920
7	Li	3	6,9	0,5	BCC	0,15	1+	180
8	Mg	12	24,3	1,7	HCP	0,16	2+	649
9	Mn	25	54,9	7,4	Cubic	0,11	2+	1244
10	P	15	31,0	1,8	Ortho	0,11	5+	44
11	Pb	82	207,2	11,4	FCC	0,18	2+	327
12	Ta	73	181,0					3000
13	W	74	183,9	19,3	BCC	0,14	4+	3410
14	Zn	30	65,4	7,1	HCP	0,13	2+	420
15	Zr	40	91,2	6,5	HCP	0,16	4+	1852

Table 6.2. Dopes and their physical characteristics

The four copper types showed marked differences in the tests – both as such and doped. They are presented mixed under the denomination Cu. Appendixes 1 -35 have an identification in brackets [].The first digit(s) of this identification reveal the copper type.

6.1.2 Test plates and welding

In test was used bead-on-plate, no filler TIG-welding, with Ar + 75% He shield gas (flow 12 l/min + 8 l/min in an 11 mm long shroud trailing the torch). The base plate thickness was 3 ± 0.1 mm.

For dope was drilled a hole at x = 0 (Fig. 6.1). Welding started at x=-5mm. The weld movement was started after the arc was stabilized, which required 0.3…0.7 s. The surface was brushed and cleaned with acetone C_3H_6O prior to welding.

Electrodes had 0.9…1.2%LaO_2 additive (ISO 6848, black,), ∅ 4 mm, with tip angle 60^0. The torch had a trailing shield shroud (L70xW30mm). The average arc voltage was 12,5V.

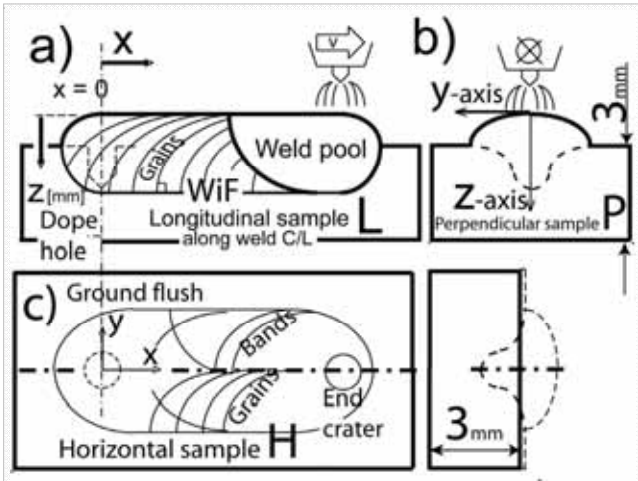

Fig. 6.1 **a)** Longitudinal, **b)** perpendicular and **c)** horizontal sample and the xyz-coordinate system..

Welding speeds were ~0, 5, 10, 100 and 200 cm/min, and one metallographic specimen with v=3000cm/min. The welding voltage and current for this weld are unknown.

6.1.3 Ultrasonic irradiation

Ultrasonic irradiation was carried out with Krautkramer-Branson USN 50 apparatus (Nr. 05296-602304), with 6W electrical and 2.1 W ultrasonic power. The beam with was nominally ∅6 mm beam (Fig's 6.2 and 6.3).

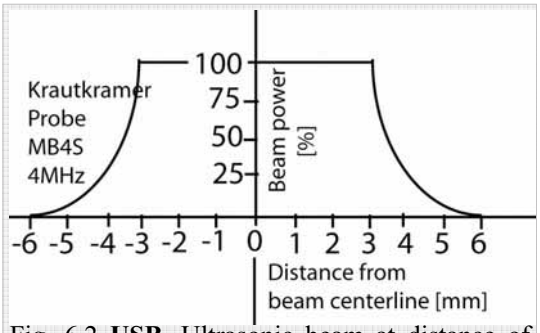

Fig. 6.2 **USB.** Ultrasonic beam at distance of the weld centerline distribution of the used probe. Radiation outside radius 5mm is considered insignificant.
- MB4S probe 4MHz , $-D_{eff.}$= 9.6 mm
- Speed of sound in Cu 20^0C= 3500m/s
- $\lambda_{Cu,\ 20C}$ = 0.88 mm, $-Sin\gamma_6=0{,}5\ \lambda/D_{eff}$
- $Sin\gamma_{20}=0{,}87\ \lambda/D_{eff}$
-Output half angle (6dB stray radiation attenuation => n/s = 0.25) 2.25 Deg.
-Output half angle (20dB stray radiation attenuation => n/s = 0.01) 3.91 Deg.
- radiation power at 40mm Max: ~4.6 mW/mm^2

Width of the weld plate = 80 mm.
Radius of the beam at distance 40mm (weld center line) is ~4.8mm (6 dB) n/s = 0.25
and ~6.0mm (20dB) n/s = 0.01
[Krautkrämer-Branson: Datasheets]

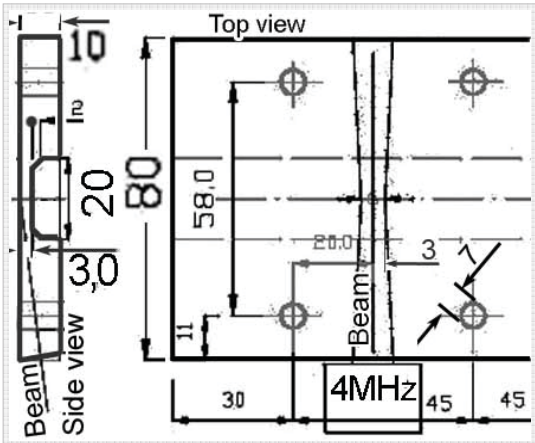

Fig. 6.3. View from side and top of the grooved 3 mm test plate (type D). The 4MHz ultra sonic probe and beam of the irradiated test plates.

6.1.4 Cracking tests

Varestraint test machine was pneumatically actuated, with 100 mm stroke and 6 s piston stroke time. The anvil radius **R=100mm** and the 3mm thickness give maximum strain (*Varestrain*) in flat test pieces ~1.5%.

The **US** irradiation from side required 10mm plate thickness. For this, we milled a 7mm deep and 20mm wide groove along the longitudinal centerline of the 10mm thick plate (Fig. 6.3). These test plates *behave* as 3mm thick in welding and R-testing, and as 10mm thick in Varestraint tests, in which they yield a ~5% *Varestrain*.

The flat 3mm test plate welds (*C-type, 86 pces CuOF, and Type E, 26 pces 99.9995 purified*) and the grooved 10 → 3 mm test welds (*D-type, 82 pces CuOF*) differ slightly in their thermal behavior; weld heat dissipates slightly faster from the grooved *D-type* samples. However, no differences were detected in the basic metallurgical behavior between the two sample types and their results are presented mixed. (The marks C, D and E appear as the firs digit of the codes of the figures in the appendixes). If a weld on a grooved 10 mm test plate cracked in **Varestraint test** or **R-test**, they invariably cracked on a flat 3mm test plate as well.

Restraint test (R-test) is a variation of the *Rigid Restraint Cracking* or *RRC-test* for transverse stresses [108]. The test plates were rigidly bolted to the Varestraint apparatus with *puller grips* and *anvil grips* giving the self-restraint for the R-test (Fig 6.4).

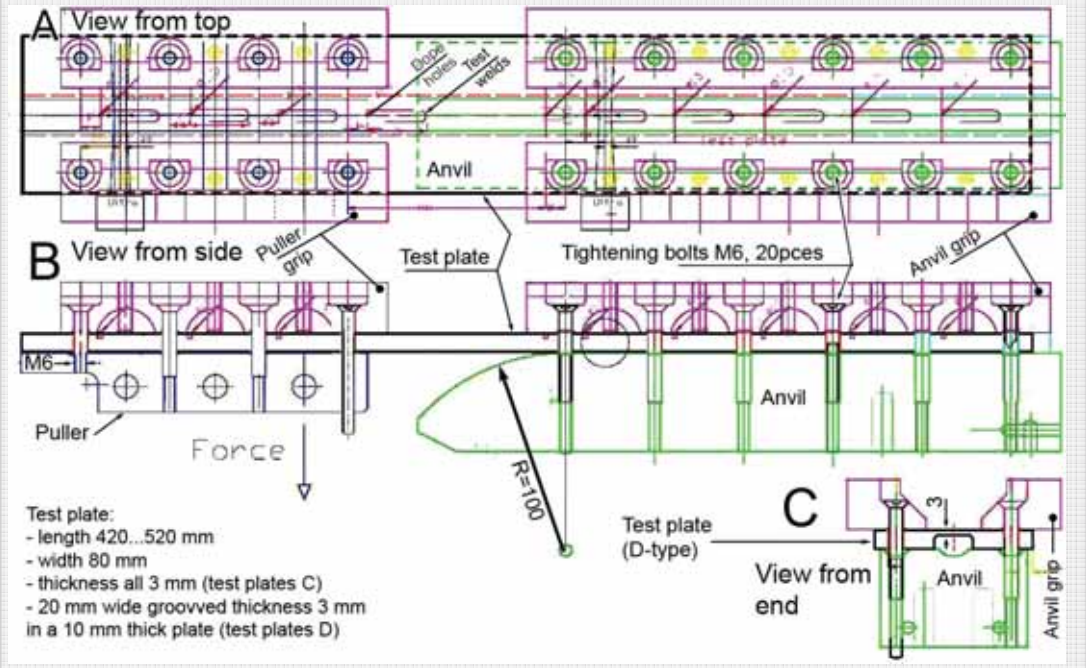

Fig. 6.4. Fixtures of the Varestraint jigs serve as fixtures for the R-test. In insert C is shown a grooved (D-type) test plate. Plain flat 3 mm test plates (of C-type) were fixed similarly.

6.1.5 Metallographic preparation and microscopy

Metallography was performed in two laboratories: LUT and Outokumpu Pori, both using electro-polishing in 850ml H_3PO_4 + 150ml H_20. [15 p.400 Table 2] for 10min at 1.7 V. In search of weld fusion line, the time was tripled. Electro-polish had a specific and vital effect revealing the micro-constituents.

The etchants differed: ***ETCHANT LUT/Cu2*** was: 30ml H_20 (67%WT) 5g + $FeCl_3$ (~11%WT) + 10ml HCl (~22%WT) [15 p.401 Table 3, *Grard's No. 2*]. The etching time was 12…15 seconds,

sometimes doubled or tripled. OK Pori-laboratories achieved excellent results with ***ETCHANT OK Pori***: (in order of mixing): 3500ml H_2O (~70%WT) + 300g $FeCl_3$ (~6%WT) +1200 ml HCl (~24%WT) + rest H_2O to make 5000ml.

Optical micrography was carried out at LUT using Zeiss IM35 microscope. The image processing system automatic focusing caused a ± 15% inaccuracy in the enlargement measurement.
SEM was performed at OK Pori with a PHILIPS XL30 electronic microscope, with acceleration voltage 30 kV, W filament energy-dispersive spectrometer EDS, resolution 0.5 % wt. In the point analysis, the point diameter was ~1μm.

6.1.6 NDT-penetrating fluid test

Cracks in welds (dope/**v**) Bi/100, La/100, Pb/100 and Li/100 were tested with SHERWIN PMUC HM 3A/Pabb Co fluorescent NDT penetrant by applying it on the weld top surface and inspecting the root side surface. Despite the seeming on both sides *spongy crack areas*, no evidence of penetrant seep-through was detected.

6.1.7 Test weld thermal dynamics

The temperature distribution for the test plates with welding speed 100 cm/min is presented in Fig. 6.5. The temperature fields are given in three sections in the Fig's 6.5 **a), b)** and **c). R**, **G**, **G/R** and **GR** are given on the weld surface in **d)** and in the thickness direction in **e)**. The analysis is based on classic weld cooling thermodynamics and inverse problem solution [110].

Fig. A31/B presents the **G/R**-plot with a weld longitudinal section for a Li-doped 100 cm/min test weld. This analysis gives – for example - an estimate for the PMZ width, which we never succeeded to estimate metallographically with any reasonable accuracy.

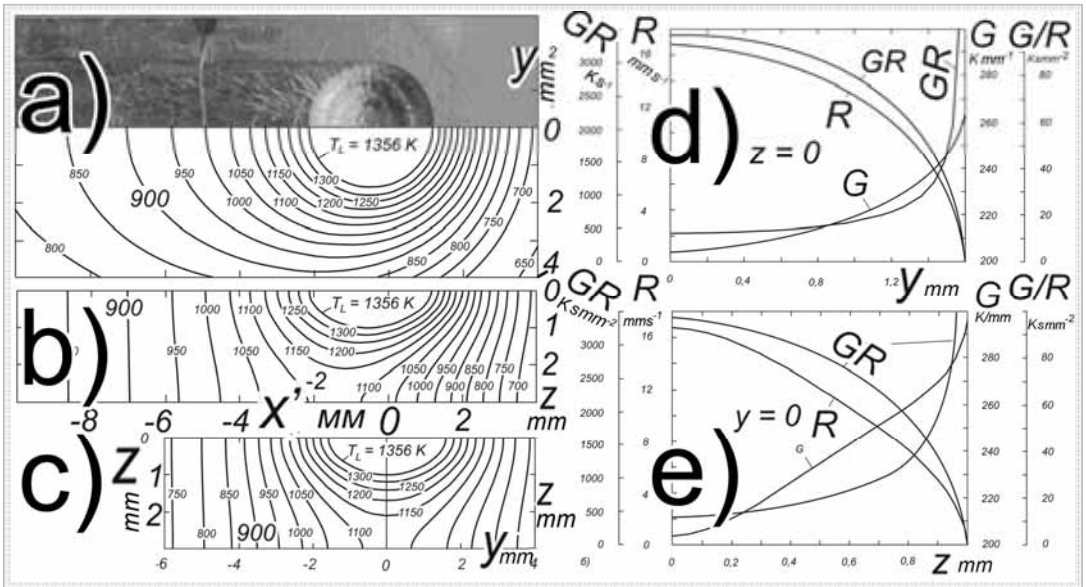

Fig. 6.5. Thermodynamic cooling data of the 100cm/min test welds. Temperature distribution **a)** on the xy-top surface, **b)** in the xz- and **b)** in the yz-cross sections. **R**, **G**, **G/R** and **GR** at the trailing end of the weld pool: **d)** on the plate surface, and **e)** at the weld centerline C/L.

See the **G/R**-plot of **e)** associated with a weld xz-section in Fig. A31/B.

(t=3mm, **I**=320A, **U**=12,5V, welding speed **v**=100cm/min CuOF+Li dope. The copper type and dope are considered not to affect the cooling. The coordinate system is presented in Fig. 6.1, x'=0, is fixed to the arc). [110].

6.2 Metallographic observations

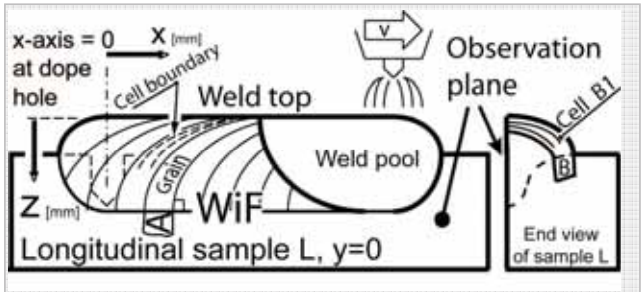

Fig. 6.6. The most informative and most used in the metallographic observations longitudinal xz-section at weld centerline, showing the grain growth from the WiF to the weld top.

We endeavored to see the solidification continuum in copper weld, from weld interface WiF (Fig.1.15) to the weld centerline. We never achieved horizontal 2-D xy-sections showing entire grains as in Fig. 1.26, due to the twofold curvature of the grains. The best cross section for the study of the entire solidification continuum for us was the xz-section along weld C/L in Fig. 6.6, where the grains grow in one plane in a bead-on-plate weld. The growth of the grain **A** - from WiF to the top of the weld - is metallurgically analogous to the growth of the grains **A** from WiF to weld C/L in Fig's 1.26 and 5.4a).

The weld with 3000 cm/min in Appendixes 8…10 is a butt weld; all other test welds were bead-on-plate welds. In the butt weld, the geometry of the very end of the grains at the weld C/L differs from that of the bead-on plate welds. The xz-views in Appendixes 8…10 taken ~200 µm from the C/L are not quite comparable with the xz-views of the other test welds, in which the distance from the C/L is <100µm.

The Appendixes 1…35 present the central results of the metallography. We comment briefly the results of the acquired from them in the following.

6.2.1 Cu-weld metal solidification continuum

The solidification continuum in the copper weld metal consists of two growth modes. Starting from the weld interface towards the end of an individual grain, these growth modes are the *planar growth* and the *cellular growth*. No dendrites – columnar, equiaxed or any other type – were detected in the test welds. This is seen in all Appendixes 1…35 without exception.

6.2.2 The final transient and the *snow cap*

The final transient at the end of the solidification of a grain remained vague. All Appendixes 1…35 reveal - by the change of their coloring from red to tinted (often white or greenish) - a *snow cap* – an obvious concentration pile-up on the weld bead surface, growing thicker and more greenish towards the end of the weld. There appear three separate solute distribution-phenomena:

(i) a grain starts growing from **WiF,** stops growing at the weld centerline and leaves there the solute of its final transient. The entire xz-surface at y=0 is covered with solute; prone to cracking solutes cause centerline hot cracks.

(ii) A 10…200 µm thick *snow cap* covers the entire bead surface fairly evenly from the weld toe to the weld centerline. This – we suppose - is due to the *perpendicular segregation in the grains/cells* bordering the outside surface of the bead. In the *End view* of Fig. 6.6, the grain **B** and the cell **B1** have part of their perpendicular solute transport towards the bead surface. This transport grows as the cell tip radius grows smaller. (*We assume that planar growing grains or blunt cell tips do not cause perpendicular solute transport.)*

(iii) Solute is transported (*macrosegregated*) from the start of the weld to its end; the discoloring increases towards the end of the entire weld (Appendixes 1, 2 and especially 32 Insert M). This obviously is not predicted by the types of model, in which the grain stops growing at the weld centerline.

5.5 Discussion of the proposed Model Frame

5.5.1 General.

The *Solidification Continuum Model Frame* - in short *Model Frame* - is a tool helping in creating models for actual welds. It is divided in *four basic model-element-groups*: **a)** solid solute concentration profile, **b)** geometric variables, **c)** the thermo-metallurgical *Sub-Case Variables* ***SCV***'s and **d)** *Cases* & *Sub-Cases* (located with the group **b)**.

Group **a):** The solid solute composition profiles, if presented only along x-axis, omit the perpendicular solidification of the sharp-tipped cells/dendrites and the solute that these cells/dendrites *fence-in* between one another. Figs 5.9 C and D show a mathematical presentation, which - if applied to solute concentration - would model its distribution in perpendicular direction.

Group **b):** The geometric variables are naturally the geometric forms of the constituents presented in Cartesian coordinates, with curved grains straightened.

Group **c**): The *Sub-Case Variables* (*SCV's*), consisting of *thermo-metallurgical variable*s **(*SCV*)** are complex to present in the *Model Frame*. Examples of ***SCV***'s are **(i)** the growth rate **R** and its acceleration and deceleration, **(ii)** the temperature gradient **G, (iii)** diffusion in solid, **(iv)** weld pool flows and stirring, **(v)** the proportion of the remaining melt, **(vi)** the initial concentration, **(vii)** the capillary effect (with exceptionally rapid welding), **(viii)** the *melting effect* (Ch. 5.6), as well as any pertinent factor influencing the solidification of the particular weld to be modeled. *SCV*'s may also be combinations of the individual thermo-mechanical variables.

Most existing models present these variables only one-dimensionally, in x-axis direction – a lack shared by our Model Frames as well. The problem is non-existent with planar growth, negligible with blunt-tipped cells/dendrites, but may be acute with sharp-tipped cells/dendrites, transporting solute also in transverse direction, towards the cell/dendrite boundaries. The total 3-dimensional modeling is underway, as can be seen in Figs 5.8 and 5.9. The latter illustrates, how some variables are better presented with angular than Cartesian coordinates.

Group **d):** The *Case & Sub-Case*-system – presented in the section **b** in Figs 5.4…5.6 – is the backbone of this approach and solute profile modeling in general. The non-pertinent models are discarded and the pertinent one(s) ordered to create the model of the actual weld. The *Model Frame* sets no restrictions or guidelines: you can discard all others and stretch *Case 2* from WiF to the final transient, which would give the model in Fig. 5.3.

There is no limit to choosing all Cases and Sub-Cases and placing them logically. The best verification of the choice is experimental. Fig. 5.15 is an example of a model developed from the *Model Frame.*

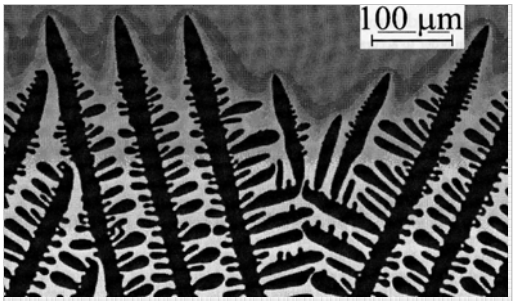

Fig. 5.7. A 2-D Phase-Field (PF) simulation of primary d-ferrite in carbon steel. Pavlyk 2004 [99], Gandin, Rappaz 1992 [83b]

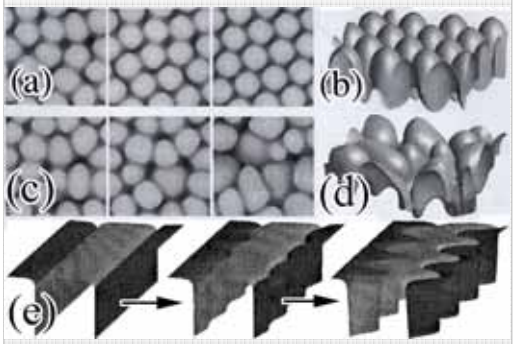

Fig. 5.8. A 3-D PF-simulations of cells. **(a&c)** from end, **(b&d)** 3-D, **(e)** cellular to dendritic transformation. Dejmek, Folch, Parisi, Plapp. 2004 [106]

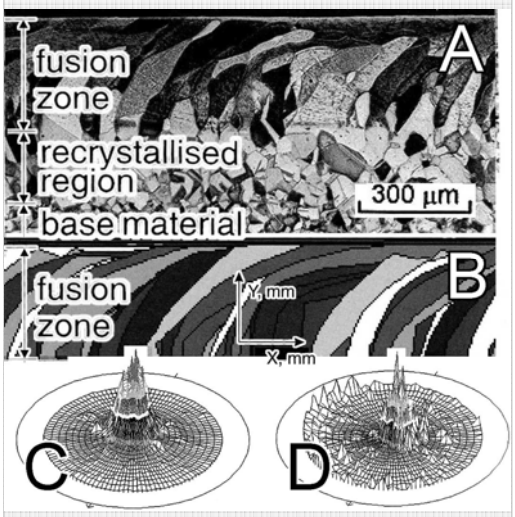

Fig. 5.9. Grain Boundary Evolution (GBE)-model. Bergmann, Mayer, Muller, Ploshikhin 1998 [107]

There were no welds – doped or non-doped not showing any *snow-cap* by discoloring; Even Appendix 5 with non-doped purified 99.9995% copper shows one, marked **Whi**. We cannot be absolutely sure that some of the phenomena we interpret as *snow-caps* are in fact metallographic edge anomalies, but we remained in the impression that there is a discoloring at the weld top even in this sample. The thickest *snow cap* is shown in Fig. A15.2; it has evidently back-filled the C/L crack beneath it.

Appendixes 2, 3 & 4 show micro cracking of the *snow cap (*or *white layer)*, some of it with the *crack-eye*-mechanism, in pure copper welds; these cracks never extended to the bulk weld metal in the tests.

6.2.3 Low welding speed – blurring and porosity

All low-welding-speed samples (**v** ≤ 5cm/min, **Appendixes 1…4, 11…14 & 32**) show blurred microstructures and hefty porosity. Microstructure blurring is probably due to post-solidification SGB-migration (Ch. 1.1.13). The porosity remained mysterious; it would seem improbable that any lack in gas shield would affect most the tests with the lowest welding speeds.

6.2.4 Cubelettes

Fig. A5 Insert D has *cells* (double line B) with *cubelettes* lined-up along their centerlines. The cell boundaries are blurred due to the back-diffusion and the cubelettes are of varying in size, with some at verge of growing over the cell boundaries.

The *cubelettes* are even better seen in Fig. A7.1**.** The existence of the structure we name *cubelette* is recognized, but we found little information of it (Fig.6.7). According to out findings cubelettes act in cellular growth as cubic precipitates. They form rows at the cell centerline and grow, given ample time and temperature.

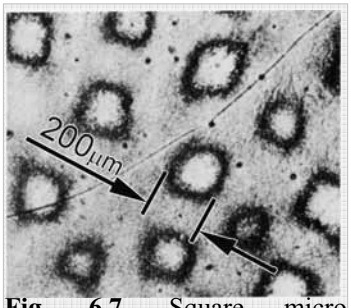

Fig. 6.7. Square micro constituents in cast ingot of DHP copper [14 p.403 Fig. 5]

Smothering. With sufficiently high temperature and time *cubelettes* grow over the boundaries of their cell and *smother* it; what remains are large size cubelettes (Fig's A6.C, A13C, A20C, A21.2B, 24.F, 35.2A&B).

Hollow and flush/protruding cubelettes. Large cubelettes appear hollow, small ones appear flush or protruding (Fig's A5D, A7B, A9B, A10B, A21.2A).

The *cubelettes* resemble the *hopper grains* presented by Flemings in Fig. 2.14**G**.

"Pure copper". The 99.9995 % wt purified Cu was produced in an attempt to make copper pure enough to solidify non-cellular (Ch.1.1.25). Fig. A7.1A shows distinct cells; this metal is an alloy, not "pure copper" in this sense.

No differences were noticed in the microstructures of the 99.9995% purified copper and the 99.998 % pure CuOF, with the exception of the grain **GR1** in Fig. A7.1.

6.2.5 Cell bands

Cells are crosswise intersected by intermittent faint lighter stripes much like grains are intersected by *bands*. The stripes often run through the grain, but they do not cross the grain boundary. Adjacent grains have these stripes with a similar wave length. We call these stripes *cell-bands*; they run parallel to *bands* much like smaller waves on a sea run parallel the every seventh greater wave. Clear *cell bands* can be seen in the Fig's **A7.2 and** A35.1. They may be associated with the *cubelettes*.

6.2.6 Micro-cells

Fig. A5.1C shows contours **C, D** and **E**, which we call *micro-cells*. They are much like *cells* but differ from them by:

(i) their width, which is almost an order of magnitude smaller than that of *cells* (the width of the *micro-cells* is normally <0.1…1.2 µm, while the cells are normally 2-8 µm wide), and

(ii) their *scattered orientation*, not obeying the temperature gradient, as do the *cells*.

More of these *micro-cells* can be seen in Fig's A7C, A9C, A10A&C, A13D, A21A&B, A26B and A27B.

6.2.7 Crack surfaces, *globules*

With dopes causing cracking, especially pronounced weld centerline cracking, the crack surfaces did not give indication of the dope in our chemical analysis. We concentrated on Bi-dope, in which the Bi-content of the crack surface was below the 0.5 % wt resolution of the EDS-apparatus in the SEM-microscope. Bi was detected only in pale *globules*, which were almost pure Bi (Appendixes 16…18).

The only EDS-signal on bulk crack surface was the 0.95 wt% of given by P (Fig. A32/H).

Flemings presents in Fig 2.15 the result of a eutectic reaction with a fan-like eutectic in the cell; in this, the proeutectic reaction (Fig. 2.14 **A** through **C**) has happened before the forming of the cell. We never detected any fan-like structures in cells with doped Cu, but some of our results could be explained with another mechanism presented by Flemings: the globules resemble the *ternary eutectic precipitates* forming from Liquid L_2 (Fig. 2.14 **D** through **F**).

6.2.8 Weld centerline cracking vs. cell boundary & cross-jump cracking

Three basically different cracking modes were detected:

(i) weld centerline cracking, usually accompanied by grain boundary cracks,

(ii) grain- and cell boundary cracks, usually accompanied by perpendicular *cross-jump cracks*, forming grids of microscopic cracks or *spongy crack areas*.

(iii) *Crack-eye* cracking

The centerline cracks are readily visible with bare eye. The *spongy crack areas* often require careful microscopy to be detected. Examples of the first type **(i)** are in Appendixes 11, 12 15, 23, 32, 33/A and 34/1. Examples of the second type **(ii)** are in Appendixes 20/A, D &E, 25/B…E, 28/B&D, 29/B, 30/B, 31/C and 33/B, E&G. Examples of the third type **(iii)** are in Appendixes 16 and 34/Fig.2

The centerline cracks are often accompanied by grain boundary cracks (Appendixes 15/Insert3 and 32A).

6.2.9 Crack-eyes

The Varestraint test revealed a peculiar crack mode, in which the crack grows freely within a grain, but is strongly restricted by what seems to be the grain boundary. Appendixes 2/F&G, 16…18, 22/C and 34/2 show *crack-eyes* in different stages in the bulk weld metal, Fig. A1.A shows them on the weld top surface. Analysis in these appendixes suggests that the cracking nucleates in the immediate vicinity of the grain boundary, but the grain boundary itself remains surprisingly intact and conspicuous; for this we name them *crack eye lids*.

6.2.10 Ultrasonic irradiation of the solidifying weld

Irradiation with 4MHz ultrasonic beam did not cause microstructural changes within the resolution of our test methods (Appendixes 27 and 30. Seven irradiated/non-irradiated-pairs corroborated this result).

6.3 Hot cracking

6.3.1 Low speed vs. visible weld centerline cracking

Visually detected crack-area lengths (length of cracked area in x-direction) in **R-test** in Fig. 6.8 show indisputably that susceptibility to visually detectable cracking is high with low welding speed **v** and reduces with increasing **v**. (Pool shape remained elliptic in the range 5≤v≤200 cm/min)

Visually detectable hot cracking is mainly of centerline type accompanied by grain boundary cracking (See Appendix 32/A).

Fig. 6.9 plots the visually detected Varestraint-test cracks, and it shows dopes with tendency to transverse cracking.

Both figures hide the definite tendency to microscopic spongy cracks, which we were unable to report quantitatively!

The two copper brands – CuOF and 99.9995% Cu – never cracked in our tests un-doped. Doping affected the two brands similarly.

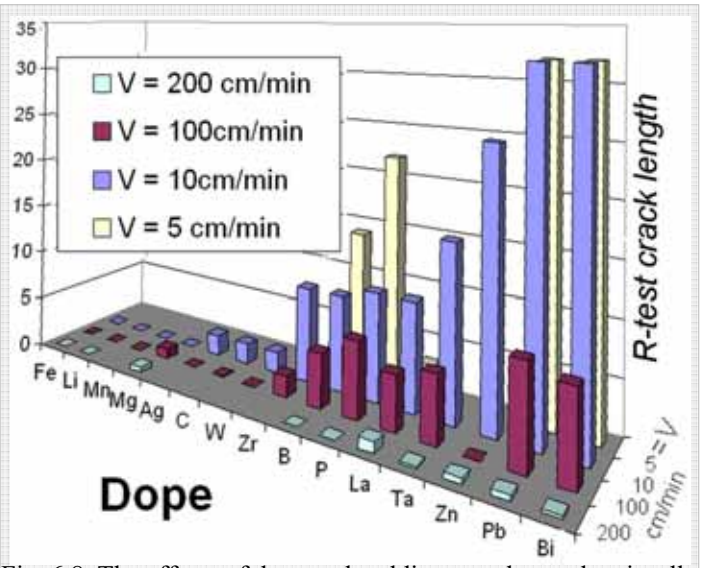

Fig. 6.8. The effects of dope and welding speed **v** on the visually detected crack length in the **R-test.** 15 different dopes.

Susceptibility to visible C/L-hot cracking was invariably smaller with greater welding speeds.

Pure non-doped copper (CuOF and 99.9995 % pure) showed no cracking at any welding speed.

Similar no cracking result were obtained for **Fe- and Li**-doped welds. They were not tested with **v** 5 cm/min: Fe was not tested with 200 cm/mm either.[CrackLengthP6.jpg]

6.3.2. High speed vs. inter-cellular hot cracks

Microscope revealed increasing number of micro-cracks, replacing the visible C/L-cracks, when **v** was increased. The micro-cracks were .evenly distributed across the weld; the hot crack morphology changed from weld centerline- to inter-cellular cracking with increasing **v**.

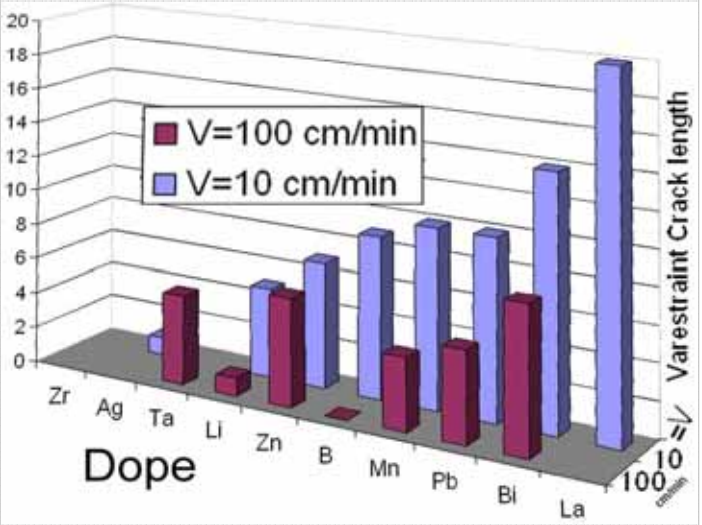

Fig. 6.9. The effects of dope and welding speed **v** on the visually detected **Varestraint test** Crack length with some of the tested above dopes.

Susceptibility to hot cracking was still smaller with greater welding speeds, but the difference was smaller than above.

Pure non-doped copper (CuOF and 99.9995 % pure) showed no cracking at any welding speed. [Vare CrackLength]

Slow **R** induces planar- and blunt-tipped cellular growth, bulldozing the solute pileup to the weld centerline. With increasing **R,** the cell tips sharpen and more solute is *fenced-in* between the cells. This distributes the cracks to the cell boundaries. Cells, surrounded by severely *fenced-in* - prone to cracking - solute, are prone to cracking also crosswise, making transverse *"cross-jump cracks"*, forming the mentioned afore *areas of the spongy cracks,* distributed evenly around the weld metal (see Fig's A18/A, A19/B, A20/D, A23/1-Root & 2A, A26/C, A28/D, A29/1B&3, A30/A, B, C, A31/C, A33/G).

6.3.3 Microscopic cracking - *fencing-in* of dope with increasing R

The results endorse the theory that planar or blunt-tipped cellular solidification fronts *bulldoze* (*referring to leveling off earth by pushing with a broad blunt horizontal blade, as e.g. in road building*) the concentration gradient to the weld centerline, while solidification fronts consisting of needle-tipped cells or dendrites ***fence-in***[22] a part of the solute gradient at the cell/dendrite lines, spreading it evenly across the fusion zone, Fig. 6.10. This can be called *plowing*, referring to the sharp-tipped plows used for plowing dirt in farming [3 p.291][4 p.446].

*This may explain why laser- and EB-welds with high **R** suffer less of centerline hot cracking even with high bead depth/width-ratios, infamous for centerline hot cracking with traditional methods: the finer dendritic microstructures seems to transport less solute to the centerline.*

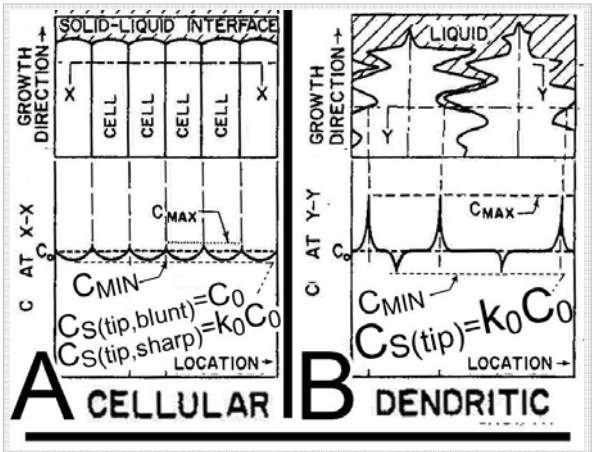

Fig. 6.10. Solute profile in perpendicular to growth direction in **A** cells and **B** in dendrites. Adopted from Savage et al [31].

The mechanism of solute *fencing-in* between cells works in copper not only on the cell- but also on the grain level; not only the cell boundaries, but also the grain boundaries crack [11 Ch. 6.3.2.2].

*In Cu, the very grain boundary **GB** itself (oddly enough) remains intact and the crack appears in its immediate vicinity. The very **GB** forms resilient "crack eye lids" bordering the crack (Appendixes 16 and 22). Crack-inducing solutes seem to enrich not on the **GB** but immediately next to it (Fig's A18 and A22C).*

To summarize, a low speed weld tends to *bulldoze* the solute to the centerline, a high speed weld *fences-in* the solute on the cell-boundaries, distributing it evenly across the weld metal. Fig A35.3 compares the Pb-doped 10 and 200 cm/min welds, showing pronounced C/L-cracking of the slower-**v** weld as compared with the humped but crack-free surface of the faster-**v** weld. (*Comparison of Fig's A15.1 with Fig.A19 & Fig.A21 (Bi-dope), Fig.A23.1 with Fig.25A&D (La-dope), Fig.A28 with 29 (Li-dope) and Fig's A32A with A33A, D and F (P-dope) shows the same)*

6.3.4 *Grain-lag cracks*

The Fig's A9 and A22 suggest that a grain grows individually, without rigorous attention to its neighbors. Since the concentrations and the thermal environments are practically the same, the growth proceeds in average with the same speed, but subtle differences between individual grains appear to occur (*grain growth autonomy)*. This may leave one grain slightly *lagging behind* in approaching the end at the weld centerline. The grain, still bulldozing its - inflated by the final transient - solute pileup to the weld centerline, while its neighbors have already solidified and are contracting. The still liquid pileup grain can not withstand the tensile stress, and a *grain-lag hot crack* – the size of the cross section of the lagging grain - may form.

The Fig. 2.35(a), drawn with the two outer grains *lagging* behind the grain in the center, illustrates the described above. Our findings are too few; this phenomenon must be verified. The ordering of the protruding from the crack surfaces cells raises questions requiring explanation.

6.4 About the experimental method

Welding over a dope-filled hole – as we did - has the draw-back of the concentration differences along the weld. Even so, it gives comparable results of a great number of dopes (solutes) rapidly and economically. It is suitable as a screening test for a large number of solute/base metal combinations.

Light microscopy accentuates the cracks of high-**v** welds; the aggressive chemical attack of the metallographic preparation increases crack indications. High-**v** welds – not subjected to a chemical attack - may be less susceptible to hot cracking than our high-**v** tests report.

---

[22] This phenomenon is sometimes called *trapping* [79] et al.. We use term *fencing-in* to avoid confusion with *solute trapping* of Ch. 1.1.27.

Chapter 7 DISCUSSION

This dissertation attempts to give a wide view of the solidification of single-phase fusion welds. The topic is complex. The basic elements of the theory – starting from the *Cases* and culminating in the *Model Frame* - are discussed in Ch's 5.5 and 5.7. The experimental results are discussed in Ch. 6; the exotic microstructures found deserve further research, but this dissertation is not the forum for it; here the important result is that the bulk fusion weld follows the general theory.

In this final discussion we limit to **(a)** the existence of two approaches or research-lines in weld solidification, and **(b)** how this dissertation relates to the total palette of phenomena occurring in the solidification of fusion welds.

The picture of the solidification of a fusion weld is shattered, like a puzzle with missing parts. Our understanding of solidification is far from complete, and a fundamental division of approaches in this field does exist.

The two approaches. *Case 3* solidification regime can be achieved in two ways. The first is calculating – as the Toronto-pioneers – the concentration gradient from the laws of diffusion and presuming that the solid concentration reaches a steady state with $C_L=C_0|_{Const}$.(Eq's 2.5.12…2.5.14). The RPI-line advocates this *Case 3* approach. The second way is to start form *Case 2,* take the Gulliver-Scheil equation and add a concentration gradient to it. We call this approach *Case 2(+)CG;* it is advocated by the *Lausanne-approach.* Modeling solidification in between the *Cases 2* and *3*, the *Lausanne*-model is more versatile. Its term Ω determines the operation point between the two *Cases*. The value Ω=1 gives as good as perfect a compatibility with *Case 3*; it makes a negligible difference, whether the model is made with genuine *Case 3* or this *Sub-Case 2(+)CG*$|_{\Omega=1}$.

The problem is how to determine the value for the Ω; one estimate for it is the Péclet-number [5 Eq. 4.5 p.73 and A8.13 p.242], or it may be eliminated otherwise e.g. [5 p. 76]. Such estimates may bring the operation point of the used *Sub-Case* rather far from *Case 3*. This means that the *steady state* ceases to exist, and the model starts predicting more solute rejected to the liquid and bulldozed to the final transient. This difference is pronounced in the models in Fig's 2.25 and 5.3, the first being based on *Case 3* and the second on *Case 2*. Both cannot be correct as general models for fusion welding.

We assume that Savage-Lippold model in Fig. 2.25 is valid for fusion welding and the analysis in Appendix 43 suggests that the Lausanne-research line agrees with this for the range of R depicted in Fig. A43C. There is a region in the beginning of slow-speed fusion weld solidification, where the concentration gradient may be too wide to be protected by the stagnant layer; the leading nose of the solute pileup may be stirred into the turbulent weld pool. In this region Fig. 5.3 may be correct, provided it includes a concentration gradient as in Sub-Case 2(+)CG. More light is being shed to the stagnant layer, as discussed in Appendix 42.

The area of this dissertation is restricted to the pre- and at-solidification phenomena of single-phase pure metals and binary alloys. This, however, did not quite succeed: some discussion of eutectic and peritectic systems was not avoided, even in multi-component forms. The solutions for them, by Flemings and Miettinen (Ch's 2.6.1 and 2.8.7 respectively), suggest that the concepts *Case, Sub-Case, SCV, M/S and Model Frame* are applicable for multi-phase, multi-component alloys.

The post-solidification phase changes are more problematic. The single-phase system is rare in everyday welding; there are more post-solidification models for multi-phase systems. These models are – almost without exception – system-specific: they apply for a limited scope of materials, but being – again almost without exception – experimentally verified, they fulfill their task well within their scope. Bhadeshia & Honeycombe present the formation of the post-solidification microstructures and the elements for their modeling for steels [125]; Lippold and Kotecki do in principle the same for stainless steels [11]. The methods and variables used for *post-solidification studies* in these state-of-the art works differ so profoundly from the methods and variables for the *pre-* and *at-solidification studies* that their application to *Model Frame* seems impossible, or at least impractical. It seems that the models of the pre- and at-solidification phenomena and the models of the post-solidification phenomena should be kept separate; both are equally needed.

The *pre-* and *at-solidification* form only one part of solidification, but this part is a vital corner stone. The picture of fusion weld solidification will be smudged and shattered as long as the dualism in the approaches exists.

Chapter 8 SUMMARY OF THE DISSERTATION

1. A historical survey of the theories of fusion weld solidification is made, starting from G.H. Gulliver at the start of the 20th century. It shows that there is a general global agreement in the basics of solidification. Nomenclatural differences do exist.

2. The main solidification regimes are classified throughout this work as *Cases* from *1* to *4*, which are united or expanded with *Sub-Cases*. These are physical and mathematical models, designed by Pfann, Flemings, Kurz and others. We propose one such model (the **M/S**-model) for the start of the solidification.

3. Returning to the historical survey, one basic difference divides the solidification research in two lines: the welding-oriented RPI; Savage approach favors *Case 3*, while the casting- and single-crystal production-oriented Lausanne EPFL; Kurz approach prefers *Case 2* and its derivatives.

4. The two approaches above come to the same final solution of the solute profile. This solution is based on *Case 3* (Appendix 43).

5. Historical research, corroborated by our own results, led to a prolific discussion of when the grain growth follows the *lattice easy growth direction* and when *the temperature gradient direction*.

6. 1-dimensional concentration profiles obviously give a complete view of the total solute distribution only in planar and blunt-dipped cellular growth. In needle-like cellular/dendritic growth, the perpendicular solute transport across the cell/dendrite must be accounted for. Because of the perpendicular transport, some solute is *fenced-in* between the cells, instead of being *bulldozed* to the final transient at the weld centerline.

7. We propose a *Model Frame* as a helping tool for modeling, visualization and discussion of fusion weld solidification. The model follows the growth of one grain from weld fusion line to the weld centerline.

8. We propose that the longitudinal solidification of a fusion weld occurs according to *Case 3* or its *Sub-Cases* from the epitaxial nucleation at the weld interface to the final transient near the weld centerline, where it transforms to *Case 2* or its *Sub-Cases*.

9. Special attention must be paid to the continuity of the models in the areas of transition, e.g. as the one from *Case 3* and its *Sub-Cases* to *Case 2* and its *Sub-Cases.*

10. We propose the *Case 3*-based *melting/solidification model* (**M/S-**model) for the start of solidification. The **M/S**-model takes into consideration the melting stage, the back-diffusion in the solid, the acceleration of the growth rate, and the basic thermodynamic parameters of the weld.

11. Uneven concentration along the solid/liquid front can strongly change the shape of the tail of the molten pool. This can substantially influence the susceptibility to centerline hot cracking.

12. Our preference of *Case 3* over *Case 2* in fusion welding is largely based on two factors: **(i)** the concept of *stagnant layer* which protects the pileup of the rejected solute from being mechanically mixed by the turbulences of the melt, and **(ii)** the rapidness of the process, not giving time for diffusion to even out the composition of the remaining melt.

13. There are three occasions, in which *Case 2* may displace *Case 3* in fusion welding:

14.1 in the final transient as the width of the remaining melt diminishes to a size allowing diffusion to even out the solute composition,

14.2 in the perpendicular to grain growth direction growth of cell- or dendrite tips, where –again – the dimensions of the remaining melt are small enough to allow total mixing by diffusion

14.3 in the start of the solidification, where the near-zero solidification rate may create a width of the solute pileup exceeding the width of the stagnant layer. In this dissertation, we neglect this occasion. The width of the stagnant layer is under dispute, and the area is studied forcefully; slow-speed fusion welds may be found to follow *Case 2* more than we assume.

14. In the experiments, the solidification growth modes in pure and doped copper were planar-, and cellular structures. No dendrites were detected.

15. Pure coppers (99.997- and 99.9995% -pure Cu) solidified as alloys, expressing practically no hot cracking tendency. Doping changed this: the highest susceptibilities to hot cracking gave Bi-, Pb-, Zn-, Ta La-, P-, B- and Zr-dopes.

16. With low welding speeds, the hot cracks were of centerline-type. Increasing speed either extinguished the cracking or distributed the cracks evenly across the weld metal as fine meshes of cracks – unseen by bare eye and barely distinguishable with a light microscope.

17. The pool shape was not found to affect the phenomenon of point 16.

18. A slow welding speed favors planar- and blunt-tipped cellular growth, bulldozing the solute to the weld centerline. An increase of speed enhances growth of cells with sharpening tips, dispersing the solute by fencing it into the cell boundaries across the weld.

19. Peculiar micro-constituents – *cubelettes*, *micro-cells* and *cell-bands* were found in copper. *Cubelettes* form rows in cells and seem to grow and - given time – *smother* their cells, leaving a structure scarcely distinguishable from planar zone.

20. Peculiar crack form *crack-eye* was frequent. The crack was surrounded by resilient grain boundaries, which we call *crack-eye lids*. The crack appeared to initiate from the immediate vicinity or the grain boundary (*crack-eye lid*), but the grain boundary itself remained resilient and intact.

21. The bead surface was susceptible to severe *humping* at high welding speeds $v \geq 100$cm/min.

22. 4 MHz ultrasonic irradiation did not produce effects in weld morphology within the resolution of our test methods.

23. The solidification of pure and doped copper appeared to follow the anticipated regime of individual grains growing from weld interface to the weld centerline. However, a phenomenon we call *snow cap* suggests macrosegregation on the surface bead from the start of the weld to its end.

24. It appears that an individual solidifying grain may slightly lag behind its neighbors, bulldozing its solute pileup, when its neighbors have already solidified and are already contracting. This may form microscopic voids we call *grain-lag cracks.* This phenomenon should be verified; the evidence (Fig's A9 and A22) is too scarce.

REFERENCES

1 Flemings M.C. 1974: Solidification Processing. McGraw-Hill, New York. ISBN 0-07-021283-x, 364 p.

2 Pfann W.G. 1978: Zone melting. Robert E. Krieger Publishing Company. Huntington, N.Y. USA, 310 p.

3 Kou S. 2003: Welding Metallurgy. John Wiley & Sons. ISBN 0-471-43491-4. 461 p. (University of Wisconsin) (First edition 1987.)

4 Messler Robert W. 1999: Principles of welding. Processes, Physics, Chemistry and Metallurgy. John Wiley & Sons, Inc ISBN 0-471-25376-6, 662 p.

5 Kurz, W., Fisher D.J. 1998: Fundamentals of Solidification. 4th edition, Switzerland. Trans Tech Publications. 305p.ISBN 0-87849-804-4. (First edition 1984), 305 p.

6 Cahn R.W. 1970: Physical metallurgy, North Holland Publishing Company Inc., American Elsevier, ISBN 0-7204-0201-8, 1333 p.

7 Aziz, M.J. 1982. Model for solute redistribution during rapid solidification. Journal of Applied physics, Vol. **53**, pp. 1158 – 1168

8 Verhoeven J.D 1975: Fundamentals of Physical Metallurgy. John Wiley & Sons 567 p

9 Hannon J.B., Copel M., Stumpf R., Reuter M.C., Tromp R.M. 2004: Critical Role of Surface Steps in the Alloying of Ge on Si(001). Physics Review Letters Vol. **92** No 21, May 28, pp. 216104-1…4

10 Haasen P. 1996: Physical Metallurgy. 3:rd edition, Translated by Janet Mordike. Cambridge University Press ISBN 0 521 55 92 0, 420 p.

11 Lippold J.C., Kotecki D.J. 2005: Welding Metallurgy and Weldability of Stainless steels. John Wiley & Sons. ISBN 0-471-47379-0. 357 p.

12 Savage, W.F. 1980: Solidification, segregation and weld imperfections. Houdremont lecture Welding in the World No 5/6 pp.89-113

13 Chalmers, Bruce 1964: Principles of Solidification, John Wiley and Sons, New York. Library of Congress No. 64-20079. 319 p.

14 Metals Handbook 1985: Vol. **9** - Metallography and Microstructures. 9:th edition, 8:th printing 1998. ASM, Metals Park, Ohio 44073, USA ISBN 0-87170-007-7 (v.1)

15 Metals Handbook, 1983 Vol. **6** Ed.9 Welding, Brazing and Soldering. ASM, Metals Park, Ohio 44073, USA

16 Metals Handbook, 1985: Vol. **13** Corrosion. 9:th edition. ASM, Metals Park, Ohio 44073, USA

17 Dragnevski K.I., Cochrane R.F., Mullis A.M. 2002: Experimental Evidence of Dendrite Tip Splitting in Deeply Undercooled, Ultrahigh Purity Cu. Physics Review Letters Vol.**8** Nov. 18 pp- 215502-1…4

18 Fleury V., Watters W.A., Allam L., Devers T. 2002: Rapid electroplating of insulators. NatureNoVol. **418**, i.6882, 18Apr .pp716-719

19 Boettinger W.J., Coriell S.R., Greer A.I., Karma A., Kurz W., Rappaz M., Trivedi R., 2000: Solidification microstructures: recent developments, future directions. Acta Materialia Vol.**48** pp. 43-70

20 Brody, H.D., Flemings, M.C. 1966. Solute redistribution in dendritic solidification. Transactions of the Metallurgical Society of AIME, Vol. **236**, pp. 615 – 624

21 Savage W.F., Aronson A.H. 1966: Preferred Orientation in the Weld Fusion Zone. Welding Journal, Feb pp 85-s…89-s

22 Samuel J. 1979: Crystallography in fusion-weld-metal solidification mechanics. Ph.D. diss. RPI, Troy, NY, USA, n.a.

23 Nelson T.W., Lippold J.C., Mills M.J. 1999: Nature and evolution of the fusion boundary in ferritic-austenitic dissimilar weld metals, Part 1-Nucleation and growth. Welding Journal Oct. p329-s

24 Nelson T.W., Lippold J.C., Mills M.J. 2000: Nature and evolution of the Fusion Boundary in Ferritic-Austenitic Dissimilar Metal Welds - Part 2; On-Cooling Transformations. Welding Journal Oct. p. 267-s

25 Davies G.J., Garland J.G. 1975: Solidification structures and properties of fusion welds. International Metallurgical Reviews. Vol. **20**. Jan. pp83-106

26 Lippold J.C., Clark W.A.T., Tumuluru M. 1992: An investigation of weld metal interfaces. pp 141-145 in: The Materials Science of Joining. The Minerals, Metals & Materials Society. (ed. Cieslac M.J., Perepezlo J.H., Glicksman M.E.)

27 Petrov G.L., Tumarev A.S. 1977: Teorija Svarochnih Protsessov. Vyshaja Skola. (2:nd edition) Moscow. UDK 621.791:541 (075.8), 392 p.

28 Metals Handbook, 1993: Vol. **6** Welding, Brazing and Soldering. ASM, Metals Park, Ohio 44073, USA

28a 34 Savage W.F., Nippes E.F., Szekeres E.S. 1976: A Study of Weld Interface Phenomena in a Low-Alloy Steel. Welding Journal l Sept. pp.260-s…268-s

29 SFS 3052 Welding terminology. Finnish Standards Association SFS

30 David, S.A., & Vitek, J.M. 1993. Analysis of weld metal solidification and microstructures. In Cerjak H., Easterling K. (Editors) 1993: Mathematical modeling of weld phenomena. The Institute of Materials Book 533. ISBN 0-901716-16-2, .369 p.

31 Savage, Lundin, Aronson 1965: Weld Metal Solidification Mechanics. Welding Journ. Apr. pp.175…181-s

32 Andersson H.C.M., Facredin Seitisleam F., Sandström Rolf 2005: Creep testing of thick-wall copper electron beam and friction stir welds at 75, 125 and 175°C. Institutet för metallforskning, Swedish Nuclear Fuel and Waste Management Co. Technical ReportTR-05-08

33 Kostrivas A., Lippold J.C. 2000: A Method for Studying Weld Fusion Boundary Microstructure Evolution in Aluminum alloys. Welding Journal January p. 1-s…8-s

34 Savage W.F., Nippes E.F., Miller T.W.1976: Microsegregation in 70Cu-30Ni Weld Metal Welding Journal June 165-s…173-s

35 Chalmers, Bruce 1959: Physical Metallurgy. John Wiley & Sons, USA. Second Edition 1962.Library of Congress No 59-14983, 468p

36 Adams D.E. 1949: Journal of the Institute of Metals, 75 p.809, n.a.

37 Kirkaldy J.S., Youdelis W.V. 1960: Transactions of AIME, 218, p 828.

38 Brooks J.A., Garrison W.M.Jr. 1999: Weld Microstructure Development and Properties of Precipitation Hardening Martensitic Stainless steels, Welding Journal, August. p.280-s…291-s

39 Iirie H., Asai Y., Sare R.J. 1997: Influence of Sulphur content on molten metal flow in cast iron and steel melted by high energy density beams. Welding in the World No.4 pp. 179-186

40 Mundra K., DebRoy T., Babu S.S., David S.A. 1997: Weld Metal Microstructure Calculations from Fundamentals of Transport Phenomena in the Arc Welding of Low-Alloy Steels. Welding Journal Apr, pp.163-s…171-s

41 Limmaneevichitr C, Kou S. 2000: Visualization of Marangoni Convection in Simulated Weld Pools. Welding Journal, May p.126-s…135-s

42 Lin M.L., Eagar T.W. 1986: Influence of Arc Pressure on Weld Pool Geometry. Welding Journal June p.163-s…169-s

43 Choo R.T.C., Szekely J, Westhoff R.C. 1992: On the calculation of the free surface temperature of gas-tungsten-arc weld pools from first principles, Part I. Modelling the welding arc. Metallurgical Transactions. Vol. **23B** pp. 357-369

44 Winkler C., Amberg G., Inoue H., Koseki T. 1997: A numerical and experimental investigation of qualitatively different weld pool shapes 4th Int. Seminar on Numerical Analysis of Weldability, Graz-Seggau, Austria, 39p.

45 Limmaneevichitr C., Kou S. 2000: Visualization of Marangoni Convection in Simulated Weld Pools Containing a Surface-Active Agent. Welding Journal **69** No. 11 pp 324-s…330-s

46 Pierce S., W., Burgardt P., Olson D.L. 1999: Thermocapillary and Arc Phenomena in Stainless Steel Welding. Welding Journal No. 2 p. 45-s…52-s

47 Lichter S., Roxin A., Mandre S.2004: Mechanism of Liquid Slip on Solid Surfaces. Physics Review Letters Vol. **93**, No.08, Aug. 20, pp. 086001-1...4

48 Faisst H., Eckhardt B. 2003: Traveling Waves in Pipe Flow. Physics Review Letters Vol. **91** No. 22, pp 224502-1…-4

49 Smith V.G., Tiller W.A., Rutter J.W. 1955: A Mathematical analysis of solute redistribution during solidification. Canadian Journal of Physics, 33, pp 723-745

50 Kurz W. 1995: Dendrite growth in Welding. In: *Mathematical Modelling of Weld Phenomena 2*. London pp. 40-53. ISBN 0-901716-63-4

51 Vilpas M. 1999: Prediction of microsegregation and pitting corrosion resistance of austenitic stainless steel welds by modeling. Doctor's thesis. Technical research centre of Finland. 139 p.

52 Suutala N, 1981: Effect of manganese and nitrogen on solidification mode in austenitic stainless steel welds. Metallurgical Transactions Vol.**13A**, pp.2121-2130 n.a.

53 Elmer J.W. 1988: The influence of cooling rate on the microstructure of the austenitic stainless steel alloys. Ph.D. Thesis, MIT, USA. 387p. n.a.

54 Katayamaja S., Matsunawa A. 1984: Solidification microstructure of laser welded stainless steels. 4:th International conference on Lasers and Electro-Optics, Boston, Massachusetts, USA, 12-15 November. Ohio: Laser Institute of America. pp.60-67. ISBN 091 203 5269 n.a.

55 Lippold J.C., Lin W. 1996: Weldability of Al-Cu-Li alloys. Aluminum alloys - their physical and mechanical properties. Transtech Pub: 1685-1690 n.a.

56 Cross C.E. 2005: On the Origin of Weld Solidification Cracking. In (pp. 3...18) Böllinghaus T., Herold H. 2005: Hot cracking phenomena in welds. D-10643 Berlin, Springer Verlag. 401p., ISBN 3-54022-332-0, 394 p.

57 Pumphrey W.I., Jennings P.H. 1948: A consideration of the nature of brittleness and temperature above the solidus casting and welds in aluminum alloys. J. Inst. Metals 75: 235-256. n.a. Ref. Böllinghaus, Herold 2005

58 Zacharia T. 1994: Dynamic Stresses in Weld Metal Hot Cracking. Welding Journal No7 pp. 164-s…172-s

59 Dudas J.H., Collins F.R. 1966: Preventing Weld Cracks in High-Strength Aluminum Alloys. Welding Journal 45(6) pp. 241-s…249-s

60 Tamaki K., Kawakami H., Suzuki J. 2003: Effects of carbon content and peritectic reaction on hot cracking of high-carbon steel weld metal. Welding International 17 No.1 pp. 26-35

61 David S.A., Vitek J.M.1989: Correlation between solidification parameters and weld microstructures. International Materials Reviews34 pp 213-245

61a Morris L.R., Winegard W.C. 1969: J. Crystal Growth. 6, 61. n.a.

62 David S.A., Vitek J.M., Babu S.S., Boatner L.A., Reed R.W. 1999: Welding of Nickel-base Superalloy single crystals. Welding in the World No.6 pp. 6-17

63 Gulliver G.H. 1913: The quantitative effect of rapid cooling upon the constitution of binary alloys. Journal of the Institute of Metals, Vol. **9**, pp. 120-157

64 Gulliver G.H. 1921: Metallic Alloys, Chas. Griffin and Company, London, 439 p.

65 Roozeboom 1899: Zeitschrift physikaliche Chemie, n.a.

66 Scheil E. 1942: Bemerkungen zur Schichtkristallbilding. Zeitschrift für Metallkunde, Vol.**34**, pp.70-72

67 Burton J.A., Prim R.C., Slichter W.P. 1953: The Distribution of Solute in Crystals Grown from the Melt. Part I. Theoretical. and part II. Experimental. Journal of Chemical Physics, Vol.**21** No.11 November. pp1987-1991 Theoretical, pp.1991-1996 Experimental.

68 Wagner C. 1954: J. Metals, 6:154 (Trans AIME 200 154) n.a.

69 Rutter J.W., Chalmers B.:1953 A Prismatic Substructure Formed During Solidification of Metals. Canadian Journal of Physics No. 31, pp.15-39

70 Teghtsoonian E., Chalmers B. 1951: Macromosaic structure of tin single crystals. ("Striations"), Can. Journal of. Physics, M67, V29:pp.370-381

71 Tiller W.A., Jackson K.A., Rutter J.W., Chalmers B., 1953: The Redistribution of Solute Atoms During Solidification of Metals. Acta Metallurgica No. 1 pp. 428-

72 Landau A.I. 1958 P O M M, **6,** 132 n.a.

73 Mollard F.R., Flemings M.C.1967: Trans AIME, 239: 1534 n.a.

73a Kattamis T.Z., Flemings M.C. 1965: Dendrite Morphology, Microsegregation, and Homogenization of Low-Alloy Steel. Transactions of AIME. Vol. **233** pp. 992-999

74 Holmes E.L., Rutter J.W., Winegard W.C. 1957: Growth conditions for stability of a cellular S/L-interface. Canadian Journal of Physics, Vol.**35** pp. 1223-1227

75 Tiller W.A., Rutter J.W. 1956: The Effect of Growth Conditions Upon the Solidification of Binary Alloys. Canadian Journal of Physics, pp. 34, 96.

76 Jackson K.A. 1972: in “Solidification”. ASM, Metals Park, Ohio n.a.

77 Mullins W.W., Sekerka R.F. 1964: Stability of planar interface during solidification of a dilute binary alloy. Journal of Applied Physics, 35(2), pp. 444-452

78 Pfann W.G. 1952: Principles of Zone-Melting. Transact. of AIME (Journal of Metals) Vol.**194** pp.747-453

79 Savage, W.F: Lectures of welding metallurgy, Rensselaer Polytechnic Institute, spring 1975.

80 DebRoy T. David, S.A. 1995: Physical processes in fusion welding. Reviews of Modern Physics. Vol.**67** No.1 Jan, pp.82-112

81 Walton, D, Tiller W.A., Rutter J.W. Winegard W.C. 1955. Trans AIME , **203**: 1023. Referred to by Flemings [1] n.a.

82 Moisio T. 1977: Austeniittisen ruostumattoman teräksen hitsin jähmettyminen (Solidification of austenitic stainless steel). Tutkimus ja Tekniikka, No5, pp. 11-15. (In Finnish)

83 Koseki T, 2002: Solidification and solidification structure control of weld metals. Welding International (**16**) No5 pp.347-361

83a Koseki T., Flemings M.C. 1995: Effect of External Heat Extraction on dendritic growth into Undercooled Melts. ISIJ Int. (35) pp. 611-617, n.a.

83b Gandin Ch.-A., Rappaz M.: 1992: A coupled finite element-cellular automaton model for the prediction of dendritic grain structures in solidification processes. Acta Met. Mater. , (**42**) 2233-2246 n.a.

83c Fukumoto, Umeda 2001: Control of Solidification structure of stainless steels. Materia (**40**) pp.150-157 n.a.

83d Kobayashi 1991: Journal of Japan Crystal Growth Society (**18**) n.a.

84 Sivonen S., Suutala N., Moisio T. 1975: Elektronensthralmikroanalytische Untersuchung der Legierungselementeverteilung nahe der Schmelzlinie in Schweissgut aus austenitischem Chrom-Nickel-Molybdän-Stahl. Schweissen und Schneiden, No.6, pp. 1-4

85 Lippold J.C., Savage W.F. 1980: in "Modeling of Casting and Welding Processes" Ed. Brody H.D., Apelian D. 443, Warrendale PA. Metallurgical Society of AIME.

86 Clyne, T.W. Kurz, W. 1981. Solute redistribution during solidification with rapid solid-state diffusion. Metallurgical Transactions, Vol. **12A**, pp. 965-971

87 Miettinen, Jyrki 1999: Thermodynamic-Kinetic Simulation of Solidification and Phase Transformations in Steels. Helsinki University of Technology publication TKK-MK-78, 41 p.

88 Miettinen J. 2000: Thermodynamic-Kinetic Simulation of Constrained Dendrite Growth in Steels. Metallurgical and Materials Transactions B. Vol. **31B**, April pp.365-379

89 Nishimoto K. Mori H. 2002: Prediction of solidification mode and hot cracking susceptibility in laser welds in high nitrogen stainless steels. Trends in Welding Research Proceedings, 6th International Conference, Pine Mountain, GA, 15-19 Apr. 2002. TWR pp.53-58.

90 Koseki T., Inoue H., Nogami A, Fukuda Y. 2002: Columnar-to-equiaxed transition during solidification of steel welds. TWR pp.35-40

91 Rajamaki P., Karkhin V.A., Khomich P.N. 2007: Analysis of chemical inhomogeneity near fusion weld interface. The 3rd Join Conference, Aug. 21-24. Lappeenranta University of technology, Finland

92 Demchenko V.F. 1992: Mathematical experiment in thermal physics of the technological processes of welding and special electrometallurgy (in Russian), Doctoral thesis, Kiev

93 Karma A. Rappel W-J. 1999: Phase-Field Model of Dendritic Sidebranching with Thermal Noise. http://xxx.lanl.gov/PS_cache/cond-mat/pdf/9902/9902017.pdf

94 Granacy L., Börzsönyi T., Puzstai T. 2002: Nucleation and Bulk Crystallization in Binary Phase Field Theory. Physics Review Letters Vol. **88**, No. 20 pp. 206105-1…4

95 Wieckhorst O., Müller S., Hammer L., Heinz K. 2004: First-Principles-Based Surface Phase Diagram of Fully Relaxed Binary Alloy Surfaces. Physics Review Letters No.19 May 19, pp. 195503-1...4

96 Rodriguez-Lopez, J.R., Montejano-Carrizales J.M., Pal U., Sanchez-Ramirez J.F., Troiani H.E., Garcia D., Miki-Yoshida M., Jose-Yacaman M. 2004: Surface reconstruction and Decahedral Structure of Bimetallic Nanoparticles. Physics Review Letters No.19 May 19, pp. 196102-1...4

97 Kurz W. Trivedi R. 1994: Rapid solidification processing and microstructure formation. Mat. Sci. and Eng. A, Vol. **179-80**, Issues pt 1, 1 May. 1994, pp.46-51. Abstr51N3A

98 Trivedi R., Sekhar J.A., Seetharaman V. 1989: Solidification microstructures near the limit of absolute stability. Mat. Sci. and Eng. A, Vol. **20A**, Issues 4, Apr., pp.769-777

99 Pavlyk V. 2004: Modelling and Direct Numerical Simulation of Dendritic Structures under Solidification Conditions during Fusion Welding. Aachen Techn. Hochsch. Doktors Dissertation. Shaker Verlag, D 82 ISBN 3-8322-2585-4, 138 p.

100 Kurz, W., Giovanola B., Trivedi R. 1986: Theory of microstructural development during rapid solidification. Acta Metallurgia, Vol. **34** pp.823-830.

101 Lundin C.D., Quiao C.Y.P., Gill T.P.S., Goodwin G.M. 1993: Hot Ductility and Hot Cracking Behavior of Modified 316 Stainless Steels Designed for High-Temperature Service. Welding Journal No5, p.189-s

102 Brooks J.A., Robino C.V., Headley T.J., Michael J.R. 2003: Weld Solidification and Cracking Behavior of Free-Machining Stainless Steel. Welding Journal March p. 51-s…64-s

103 Feng Z., Zacharia T., David A. 1997: Thermal Stress Development in a Nickel Based Superalloy during Weldability Test. Welding Journal Nov, p 470-s

104 Cam G., Erim S., Yeni C., Kocak M.1999: Determination of Mechanical and Fracture Properties of Laser Beam Welded Steel Joints. Welding Journal June 193-s

105 David, Babu, Vitek 2001: Recent advances in modelling and characterisation of weld microstructures. Science and Technology of Welding and Joining Vol.**6** No. 6 pp. 341-346

106 Dejmek M., Folch R., Parisi A., Plapp M. 2004: Three-Dimensional Phase-Field Simulations of Directional Solidification. A Symposium in Honor of Prof. W. Kurz. TMS Ann. Meeting at N.C., USA. Ed. M. Rappaz and Ch. Beckermann. ISBN 0-87339-572-7

107 Bergmann H.W., Mayer S, Muller K., Ploshikhin V.V. 1998: Texture evolution in laser beam 1welds undergoing the planar solidification mode. In Mathematical Modeling of Weld Phenomena. Ed. Cerjak H. & Bhadeshia H.K.D.H. ISBN1-1-866125-060-6

108 Fikkers A., Muller T. 1976: Cold cracking tests to select welding conditions. IIW-Doc. IX-997-76, 15p

109 Coulthard J.O., Elliot, R. 1967: The Dependence of the Size of the Cellular Interface Structure in Dilute Binary Alloys on Solidification Conditions. Journal of the Institute of Metals, Jan. p.95

110 Rajamaki P., Karkhin V.A., Khomich P.N. 2007: Determination of the main characteristics of the temperature field for the evaluation of the type of solidification of weld metal in fusion welding. Svarochnoe Proizvodstvo (Welding Production), 2007, N 2 (867), p.3-7. Also in Welding International Vol. **21**, Issue 8 August 2007 , pp. 600 - 604

111 Hansen M. 1958: Constitution of Binary Alloys. McGraw-Hill. Libr. of Congress # 56-8862

112 Gutierrez A., Lippold J.C. 1998: A Proposed Mechanism for Equiaxed Grain Formation along the Fusion Boundary in Aluminum-Copper-Lithium Alloys Welding Journal No.3, March, pp.123-s …132-s

113 Rykalin N.N. 1951: *Calculation of Heat Flow in Welding*, Moscow, Mashgiz, 296 p.

114 Rosenthal D. 1946: The theory of moving sources of heat and its application to melt treatment. Transact. of ASME, 68, pp.819-866

115 Petrov, G.L. 1963: Metal inhomogeneity of weld joints. Leningrad Sudpromiz, 206 p. (in Russian)

116 Makhnenko V.I. 1966: Calculation of diffusion in two phase medium with moving phase line. Automatic Welding. №12. pp. 1-5 (in Russian).

117 Demchenko V.F. 1970: On numerical solution of some problems of kinetics of phase transformations. Physics and Chemistry of Material Treatment, №5, p. 128-136 (in Russian).

118 Karkhin V.A., Plochikhine V.V., Ilyin A.S., Bergmann H.W. 2002: Inverse modelling of fusion welding processes. Mathematical Modelling of Weld Phenomena 6. H. Cerjak (ed.). Maney Publishing for The Institute of Materials, Minerals and Mining, London. pp. 1017 – 1042.

119 Prokhorov N.N. 1968: Physical processes in metals in welding. Vol.**1**. Moscow: Metallurgia, 696 p.

120 Kim K., Yeo T., Oh K.H., Lee D.N. 1996: Effect of carbon and sulphur in continuously cast strand on longitudinal surface cracks. ISIJ International. Vol. **36**, №3. 1996. pp. 284-289.

121 Karkhin V.A., Mnushkin O.S., Petrov G.L. 1978: An approximate calculation scheme of hydrogen redistribution in weld joints. Welding Production. Proceedings of LPI №364, pp.3-8.

122 Karkhin V.A., Homich P.N., Michailov V.G. 2007: Analytical-experimental technique for calculating the temperature fields in laser welding. The 11th NOLAP Conference, Aug. 20-22. Lappeenranta University of technology, Lappeenranta, Finland

123 Pesch H.J, Karkhin V.A., Ilin A.S., Prikhodovsky A.A., Plochikhine V.V., Makhutin M.V., Zoch H.-W. 2005: Effects of Latent Heat of Fusion on Thermal Processes During Welding, In: H. Cerjak, H. K. D. H. Bhadeshia, E. Kozeschnik (Ed.): Mathematical Modelling of Weld Phenomena 7. - Graz: Verlag der Technischen Universität Graz, pp. 39-62

124a Kou S., Yang Y.K. 2007: Fusion-Boundary Macrosegregation in Dissimilar-Filler Welds. Welding Journal **86**, No.10, pp. 303-s…312-s

124b Kou S., Yang Y.K. 2007: Fusion-Boundary Macrosegregation in Dissimilar-Filler metal Al-Cu Welds. Welding Journal **86**, No.11, pp. 331-s…339-s

124c Yang Y.K., Kou S. 2007: Weld-Bottom Macrosegregation Caused by Dissimilar-Filler metals. Welding Journal **86**, No.12, pp. 379-s…387-s

125 'Bhadeshia H.K.D.H., Honeycombe R.W.K 2006 Steels - Microstructure and Properties. Elsevier, Butterworth-Heinemann. ISBN-13: 978-0-750-68084-4. 344 p.

126 V.A. Karkhin, P.N. Khomich, P. Rajamaki. Analysis of macrosegregation in fusion welding. . Proceedings of II International Conference "Computer Technologies in Joining of Materials". Tula, Tula State University, December, 2007. 7p.

APPENDIXES

Appendixes 1…10: No dope, Cu

Appendix 1. Cu 5…0 cm/min. Varestrain 0.75%, xy-view from top. Crack-eyes

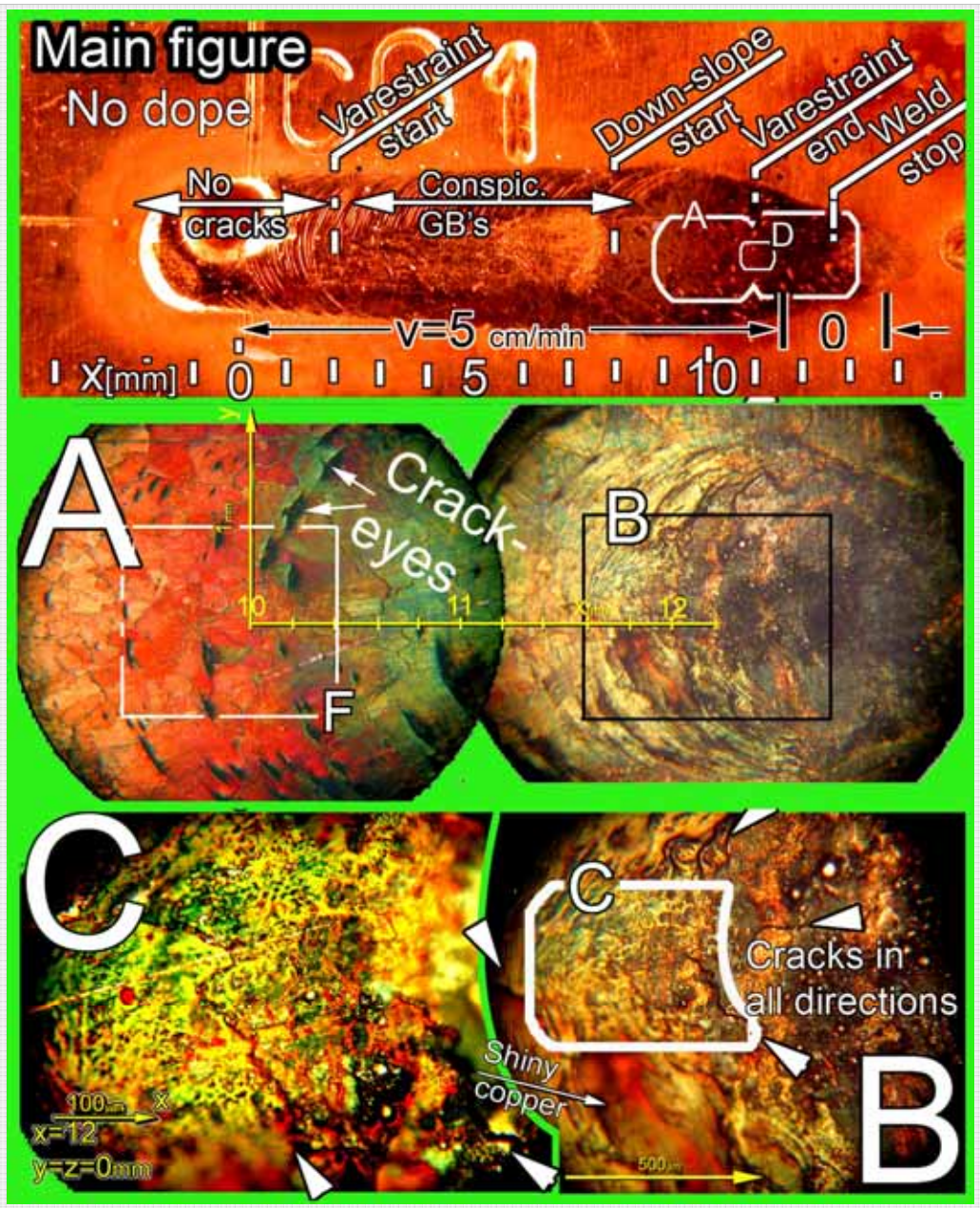

Fig. A1. xy-view of top surface. Welding speed 5 cm/min till x=12.6mm, where the speed was stopped and the power source end-slope automatic maintained a distinguishing arc for 2 sec.
Main fig. (top) has area of conspicuous grain boundaries, but definite cracks were not found with bare eye. No major centreline crack is present.
Inserts A, B and **C:** At **9 < x < 13**, a change of surface coloring from coppery red to greenish is clear. *Crack-eyes*-are obvious at **x < 10.5** and cracks in obscure directions appear at **x > 10.5**. The latter limit to a solute rich *snow cap* on top of the weld (), seen from side in Fig A3A). The solute consists of the impurities of this 99.997%-pure copper. (Areas **D** and **F** are in the Appendix 2.) [CG1_01Tx4.jpg]

Appendix 2. Cu 5…0 cm/min, Varestrain 0.75%, xy-view. Crack-eyes.

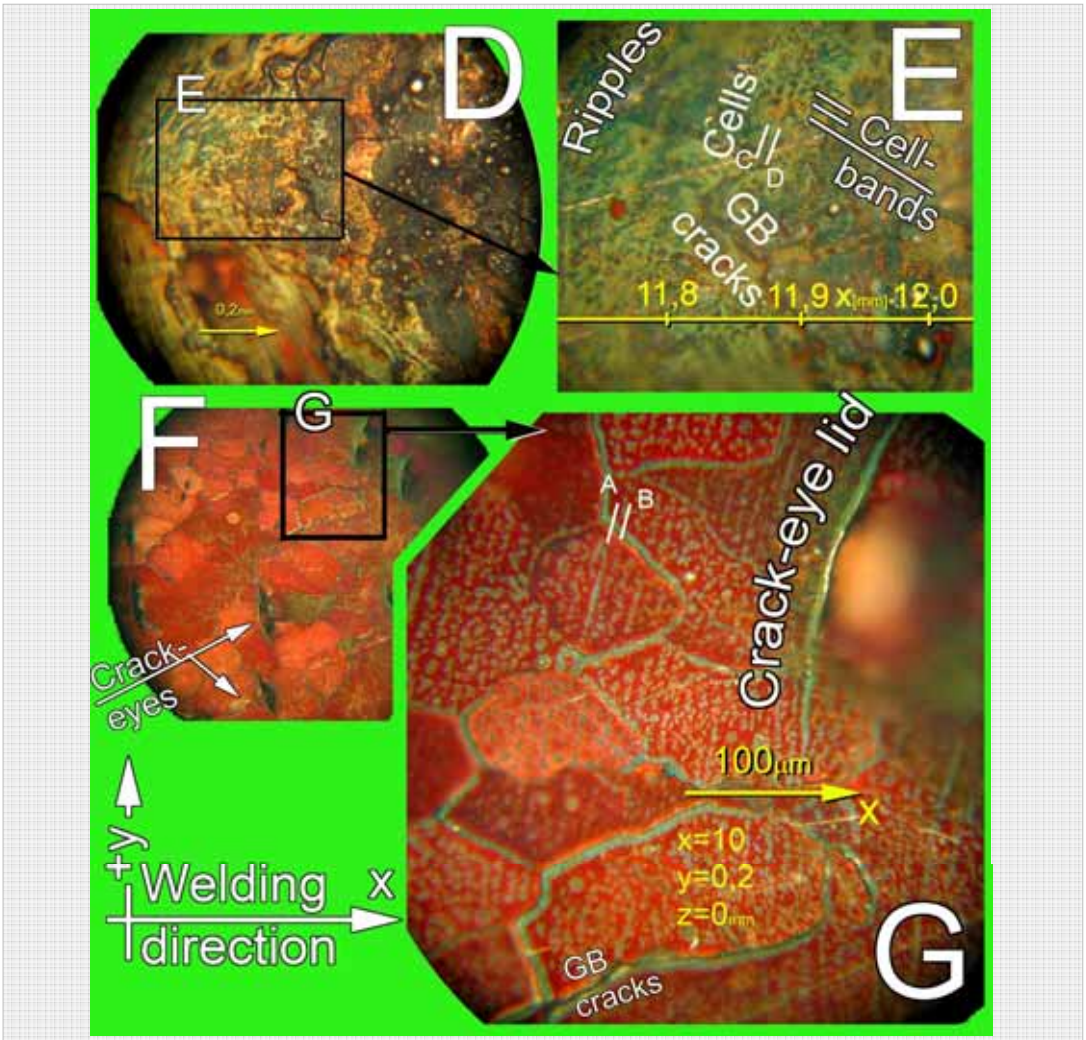

Fig. A2. Insert D of the previous Appendix**,** from area 10.7 < x < 12.7 mm) and **Insert E,** 11.7 < x < 12.1 mm show cracks running in all but center line direction. There is – as improbable as this seems for 99.997 % pure CuOF – a *snow cap*, on top of the weld. This *snow cap* is the *final transient* of the segregation. The segregation is either *perpendicular* to the grain-/cell boundaries or *longitudinal* to the weld centerline. The *snow-cap* reveals that there is a layer of final transient at the end of the weld on its entire surface with a possible exception of the zone adjacent to the weld toe, which – unfortunately – was not studied. It appears, that the grains and cells transport solute macroscopic distances from the start of the weld towards its end. It appears also that most of the surface of the end of the weld is covered with the *snow cap*, not only the centerline. Our theory models poorly the very surface of the weld.

Insert F: Near x=10 mm copper-red surface turns greenish. This is obviously the thin, cracked impurity-rich *snow cap* seen from side in Fig. A3A. It suggests solute (impurity) transport along surface from start of weld to end of weld (not from start of grain to end of grain). This zone has several *line-like cracks* and *crack-eyes*. Most *line-like cracks* may be limited to the *snow cap*-layer; all the *crack-eyes* probably are in the bulk weld metal.

Insert G has a well developed *crack-eye* with a distinct *crack-eye lid*, a grain boundary, framing the crack, but not participating in the cracking itself. The *Cells* (e.g. **AB**) have both centerlines (*cubelettes*) and boundaries of same greenish color. No cracks were detected associated with them.

The grain boundaries - including the *crack-eye lid* – are of same green color as the *snow cap* in **Insert E**; their constitution is obviously similar. Most grain boundaries or their immediate vicinities are cracked, e.g. the one marked **GB cracks.** [CG1_S_x10yz_08x_S_04MiPan4.jpg]

Appendix 3. Cu 5…0 cm/min. Varestrain 0.75%. xz-view. Blurred cells, micro-cells

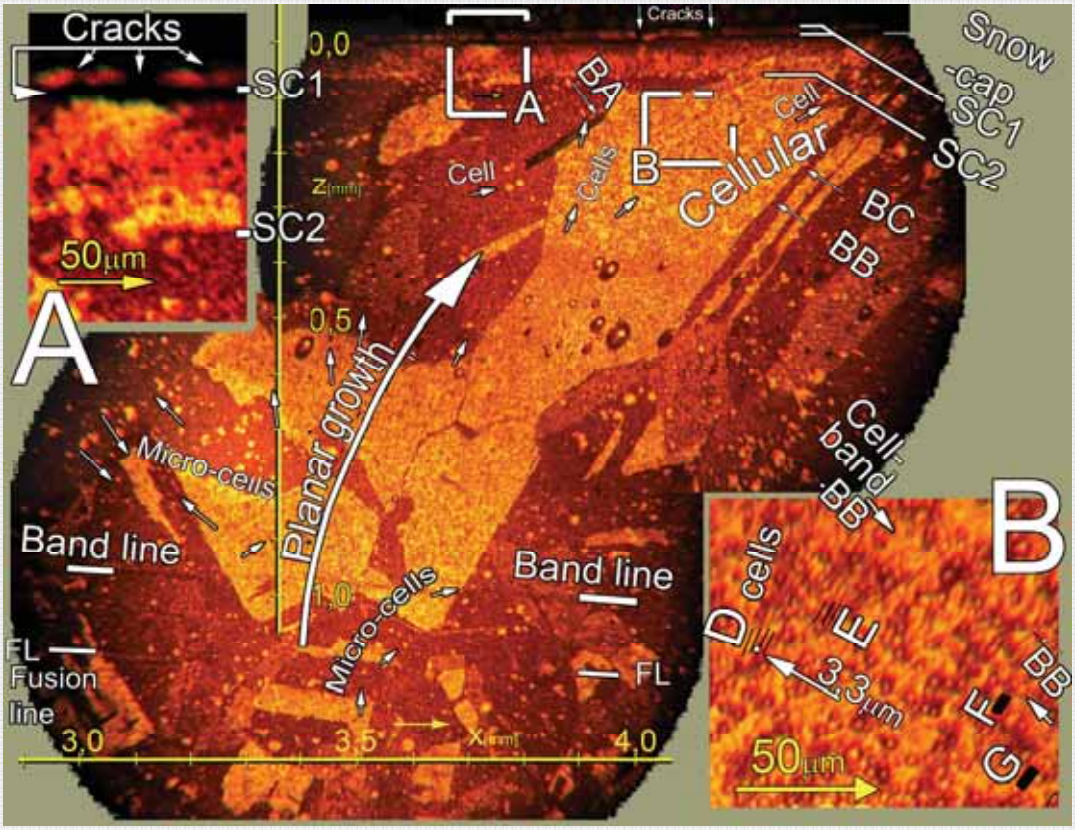

Fig. A3. Longitudinal **xz**-cross section along weld C/L at 3 < x <4 mm. Welding speed in this area was 5 cm/min.

Main figure (center): The fusion line **FL** (z ~ 1.1mm) is intermittently visible. Above it appears to be a band (**band line)** approaching it asymptotically. *(This may be a miss-interpreted planar-to cellular line, above which the cells have been smothered or otherwise mutilated. These slow-**v** welds are difficult to interpret).*

From **FL** to z ~ 0.4mm the growth is planar with ~0.8…1.2 µm wide *micro-cells*. They **(i)** are narrower than usual cell width ~ 2…8 µm. and **(ii)** they have no obedience to temperature gradient **G**. Unnamed white arrows mark the direction of some of them. Some run perpendicular to **G**, which *cells* never do.

Above z ~ 0.4 mm the growth is cellular, the cells being blurred probably by back-diffusion and/or *cubelette smothering* or both.

Cell-bands are marked with white arrows **BA**, **BB**, and **BC**. Their *width* is ~50…100 µm. None of the cell-bands continue from one grain to the neighboring one. The microscopic inspection suggests that cell-bands are restricted to one grain.

Between z ~ 0.4 – 0.6 mm there is a lot of either *porosity* or *crack-eyes*; probably the former. Porosity in slow-speed welds seems improbable, because the better weld gas shield. However, welds with low welding speed (**v**<10cm/min) appeared to be more prone to porosity than welds with high welding speeds (v≥10cm/min).

There is a distinct ***snow-cap***, a layer with elevated solute content. This specific snow-cap was not chemically analyzed. It appears to consist of two layers, **SC1** and **SC2**, the former appears micro cracked.

Insert A shows the *snow-cap* with at least two zone lines, **SC1** and **SC2**. The former is heavily cracked. These cracks are probably line-like, not of the *crack-eye* type.

Insert B: *Cells* are pointed out by sets of black lines **D** through **G**. One of their *cell-bands* is pointed by white arrows **BB**.

Appendix 4. Cu 5…0 cm/min. Varestrain 0.75%, xz-view. Blurred grains, no substructure but nano-cells, severe cell smothering

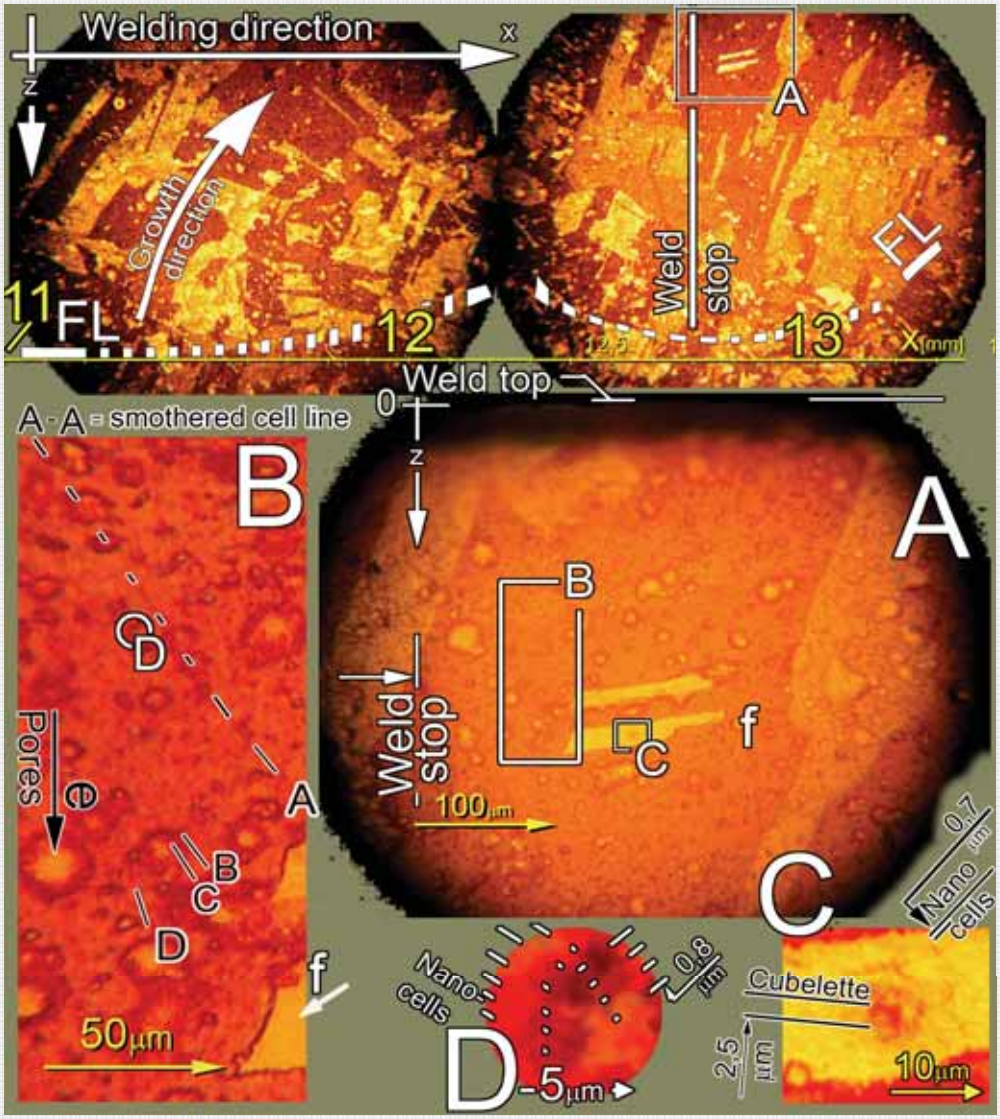

Fig. A4. The region around x~12.7 mm at the **weld stop point**, where diminishing arc provided 2 sec prolonged slow cooling with v~0cm/min.

Insert A: Besides the grain boundaries, and the two twins at **f**, no substructure was detected. There is plenty of porosity. The ones marked **e** in Insert **B** were inspected in SEM, and were interpreted as pores with size up to size ~30 µm. This porosity remained mysterious, because the standing torch should give optimal gas shield.

Insert B: The faint lines **A-A, B, C and D**, running towards the arc (located at "weld stop"), are severely smothered cell lines. The pores seem to be lined in their direction, suggesting that at least some of the contours interpreted as pores are in fact overgrown cubelettes.

No cracks were detected in this strained 0.75% in Varestraint test weld.

Insert C is from one of the twins, which are rare in weld metals inspected in this dissertation. *Cubelettes* appear to be associated with cells: there might have been some cellular activity in the area. **Inserts** C and D have a very faint ~0.8 µm micro-cellular sub structure

We believe this low speed weld has experienced post solidification back-diffusion and SGB migration (see Ch. 1.1.13), possibly also *cubelette growth* and induced by it *cell smothering*. This suggests cellular solidification, which suggests that we were still in *Case 3* and quite far from *Case 1* we aimed to. This kind of tests require enhanced post solidification cooling (see Ch. 1.1.22). [CG1AL_x12yz0_16x_04MiPan3.jpg]

Appendix 5. Cu 10 cm/min, xz-view. *Cubelettes* & *micro-cells*, SEM

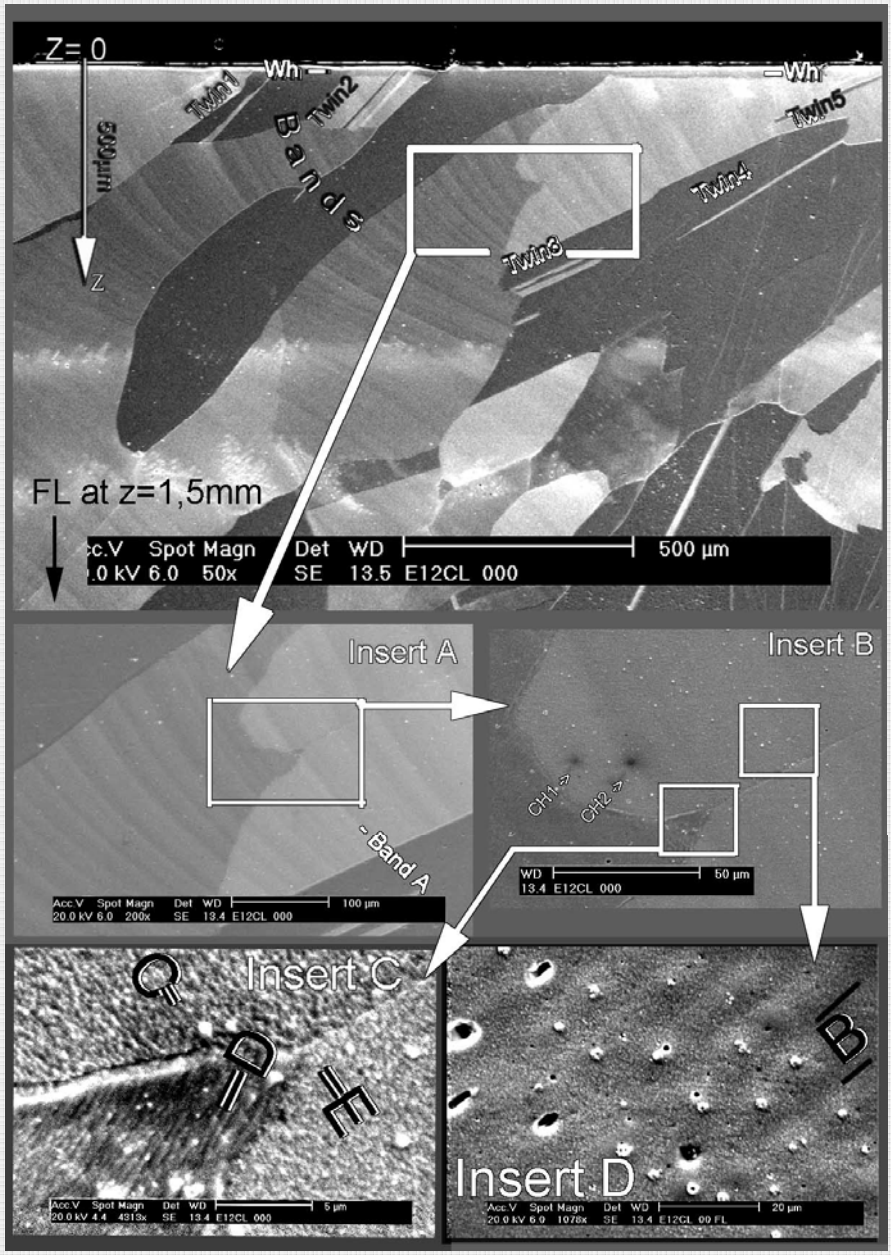

Fig A5. 99.9995% pure Cu, no dope, **v**=10cm/min, **FL** at z=1.5mm. **Main figure** (Top) and Inserts **A** and **B**: Bands are conspicuous. Chemical EDS analysis of spots **CH1** and **CH2** produced no concentration differences.

The double lines **C**, **D** and **E** in the **Insert C** point at *micro- cells,* with width ~ 0.30…0.45µm and widely varying orientations starting from 4 to 11 o'clock (double line **C**). The temperature gradient in this region has been ~ from 7 to 1 o'clock. The $>75^0$ misalignment with temperature gradient is far more than noticed with ordinary *cells*. The micro-cell lines appear decorated with globular precipitates.

Insert D: The double line **B** points at a *cell*. The cell center lines have lined-up *cubelettes,* varying in size. The cell lines are soft, which may be due to back-diffusion. Compared with the next Appendix 6, the latter has sharper and more uniform contours, probably due to lesser amount of back-diffusion with the faster 100 cm/min **v**. [E12CL001MirPan.jpg]

Appendix 6. Cu 100 cm/min, xz-view. Planar to cellular transformation, "cubelettes", heavy & mild cell smothering, grain growth autonomy, grain-lag hot cracks

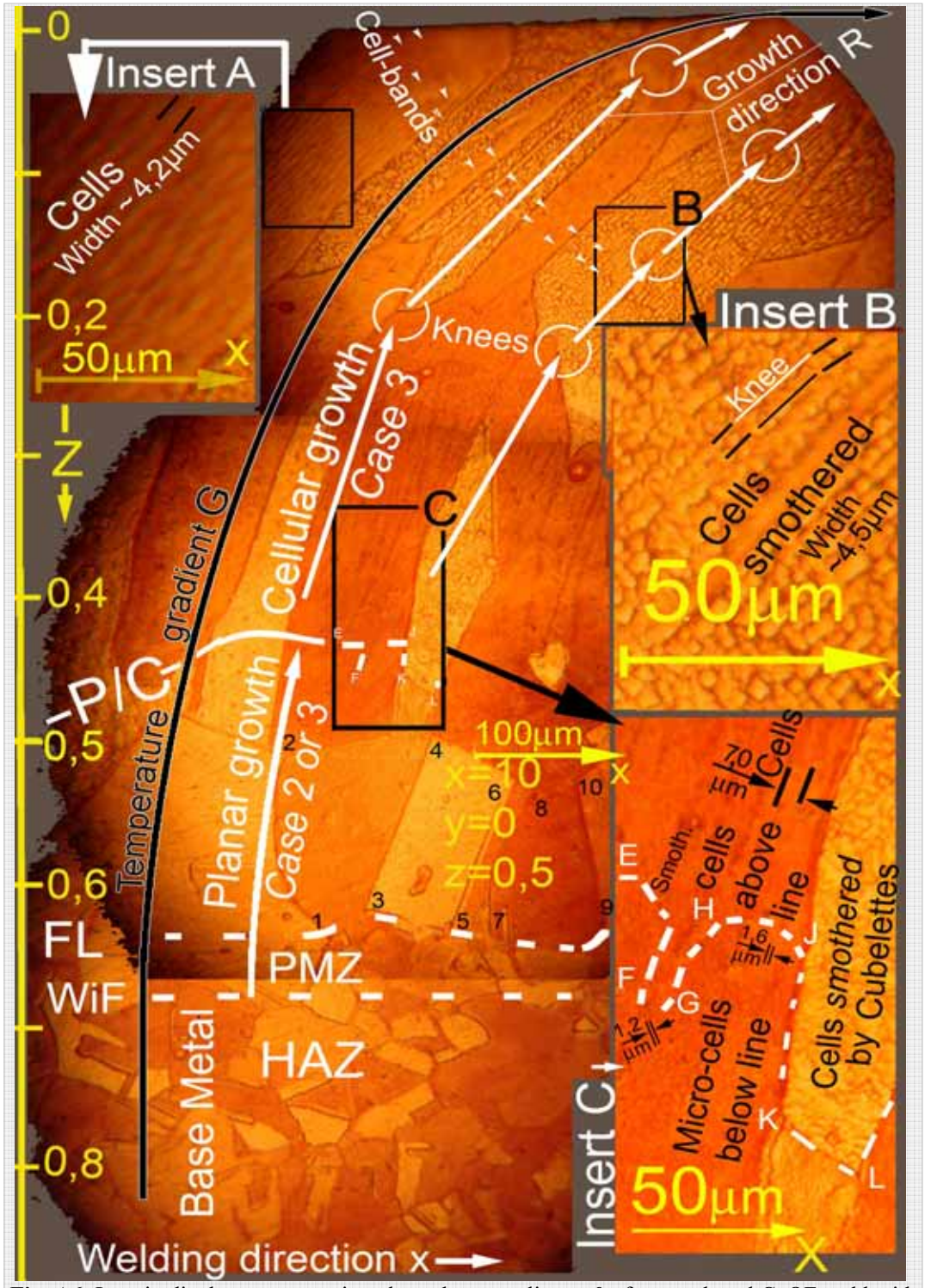

Fig. A6. Longitudinal **xz**-cross section along the centerline **y=0** of a non-doped CuOF weld with welding speed **v**=100 cm/min. (Continued on the next page) [DE6AL_x10y0z10_40x_ML_Panor.jpg

Fig. A6. (Continued from the previous page)

The main figure: The *weld interface*- and *fusion lines* are sketched as lines **WiF** and **FL** respectively. The *planar to cellular growth* transfer line is marked **P/C.**

The Temperature gradient **G** is sketched with a black arrow. The growth direction **R** is depicted with white arrows along the direction of the cells. The growth switches to a new easy growth direction **EGD** at *knees.*

Below **P/C-line**, in the planar growth zone, the growth direction **R** cannot be determined by cell direction and non-easy growth solidification **NEGS** is assumed. The direction of the grain boundaries marked **1** through **10** varies from -40^0 to $+20^0$ with respect to z-direction; this large variance corroborates prevalence of the **NEGS**.

The cellular growth zone consists of two morphologies: **Insert A,** *cells* (*proper*) with clear and straight cell walls, and **Insert B** *cells smothered*, with over-grown *cubelettes* lined up in rows where the cells used to be. The smothering has only just started; the cell walls are still distinguishable (compare with the heavily smothered cells in Fig A4 Insert B).

Cell-bands are faintly distinguishable as darker stripes near the top of the weld. Two such are marked with white rows of arrowheads. The cell-band width is ~ 10…20 μm. Cell-bands continue through grains, but appear misaligned at the grain boundaries.

Insert A shows *cells (*proper, non-smothered). The cell width is 3.9…5.3 μm, average 4.2 μm / Φ 47^0.

Insert B shows *cells* in an early stage of *smothering*. The *smothering* here is mild: the underlying cell structure is yet clearly visible; because the growing *cubelettes* have not totally destroyed the structure; cell width is 2.1…6.2 μm, average 4.5 μm / Φ 45^0. Please, compare with the more destroyed by *smothering* cell-structure in Insert C.

Insert C: The dashed white line **E-F-G-H-J-K-L** shows the border **P/C** between the *planar* and *cellular growth zones.* This often is the most visible line in the weld direction in many micrographs of copper welds; the cellular growth zone (upper side) often is darker because the cell lines etch darker. This line is easy to mistake as the fusion line, which in our case is ~ 200 μm below.

Above the **P/C**-line there is a 20-50 μm wide zone of heavily *smothered* cells, with occasional *cubelettes*. This zone is difficult to distinguish from the planar growth zone, which – however - never contains *cubelettes*.

The *cell width* at >50μm above the **P/C** line at **z** = 0,4mm is 3.6…9.57 μm, average 7.0 μm / Φ 71^0.

The *micro-cell width* below the line **P/C** is 0.71…1.6 μm, average 1.1 μm

Although the line **P/C** is drawn straight line in the main figure, the more accurately drawn dashed line **E…L** in insert **C** shows it quite wiggly. Typically it runs fairly direct in the level of **E-H-J**, but near grain boundaries, the cell boundaries extend further into the planar zone, as at **F-G** and **K-L**. This is a general tendency in these experiments.

Smothering and grain growth autonomy. Part of the line **J-K-L** is a grain boundary, differentiating a grain with microstructure more *smothered* by *overgrown cubelettes* than its vicinity. This is typical in these experiments: inside a grain, the structure is quite homogenous, but adjacent grains may be in a slightly different stage of evolution. We call this the *grain growth autonomy*.

Note on the *grain growth autonomy* and *the grain-lag hot cracks*: It appears that the autonomy may extend to the speed grains grow with, causing lagging of some grains behind the general solidification front. A lagging grain may enter the weld centerline at a stage, when the main front has already crystallized and is contracting. This contraction may tear the still-liquid solute pileup of the lagging grain, causing a hot crack with size of the cross section of the lagging grain. Examples of such microscopic grain-lag cracks are in Fig's A9 Insert A, A10 (Grain A1) and A22 Insert C.

[DE6AL x10y0z10 40x ML Panor.jpg]

Appendix 7. Cu 200 cm/min, xz-view. Cells, cell-bands, cubelettes & micro-cells

In Fig. A7.1**A**, the cells **A1**, **A2**, and **A3** of adjacent grains have slightly different orientations, despite similar $\overline{G}$, due to easy growth solidification **EGS**.

The grain **GR1** is exceptional: there no *cells* exist, only one stray *cubelette*.

We may present only two explanations for this: **(1)** GR1 developed faster than its neighbors (*grain growth autonomy*), the cells were forcefully smothered, and all that was left of the sub structure is the giant, overgrown *cubelette,* **(2)** the grain GR1 is purer than average and the corrosive attack of the metallographic preparation left it untouched with the exception of the cubelette. Neither of the explanations is quite satisfactory, and the grain Gr1 remained slightly mysterious to us.

In Fig. A7.1**B** the grain **Gr2** shows the inner structure of *cells* in the cellular zone. The boundaries of two cells are marked with black dashed lines. At the cell centerlines runs a row *cubelette*s (one is marked Cubel. row). They are obviously not hollow but protruding.

The grain **GR1** has no sub structure except the large and obviously hollow *cubelette*. As impossible as it sounds to propose cubic empty holes in a material, it seems that *cubelettes* grow in size and as they grow they turn hollow[23].

Fig. A7.1C shows that the matrix of the grain **GR2** is formed by a sub structure an order of magnitude finer than the *cells*. We call them *micro-cells*; their width varies typically between 0.15…1.5µm.

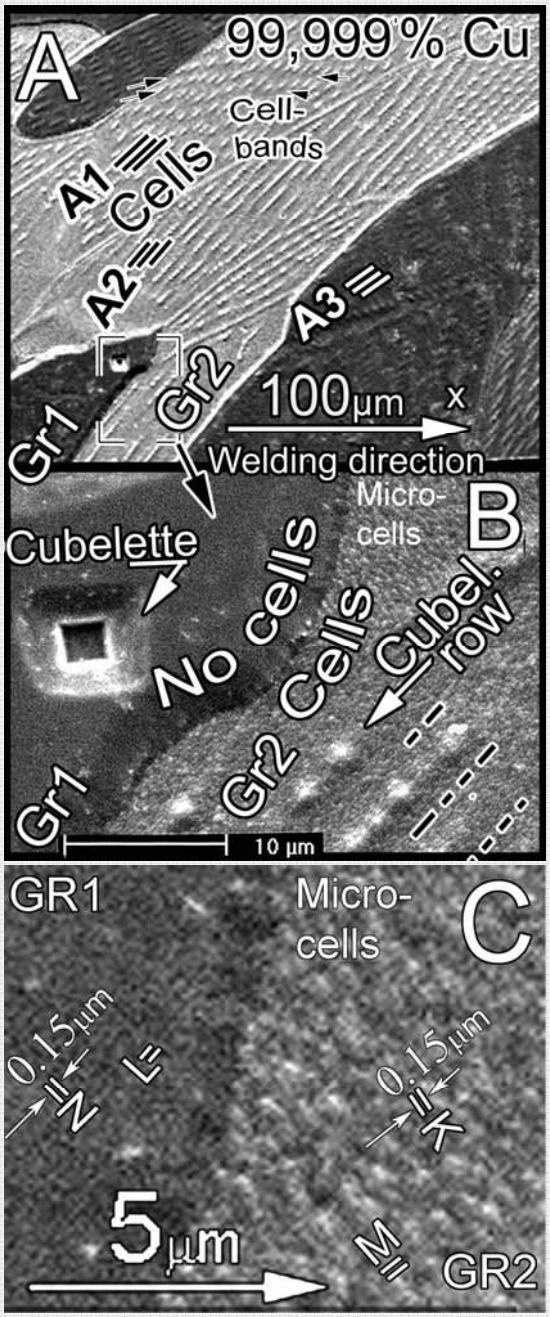

Fig. A7.1. 99.9997%wt Cu, no dope, v = 200 mm/min. xz-section along weld centerline.
A)*: Cells* are marked with triple-lines, *cell bands* with arrowheads.
B): Grain Gr2: The hatched black lines mark cell lines curbing *cubelette rows*. **Grain Gr1** has no *cells* but one large size *cubelette*, which seems hollow. Both grains have *micro-cells* on their floor above the text "Cubel. row"
C): Depicts the area in insert B around the text *Micro-cells.* **K, L, M** and **N** are m*icro-cells* with width ~0.15µm. E51CL001MiPa4.][E51CL001MiPaInsert2.]

[23] Flemings refers to *hopper crystals* found in metals growing facetted, Fig. 2.14 G.

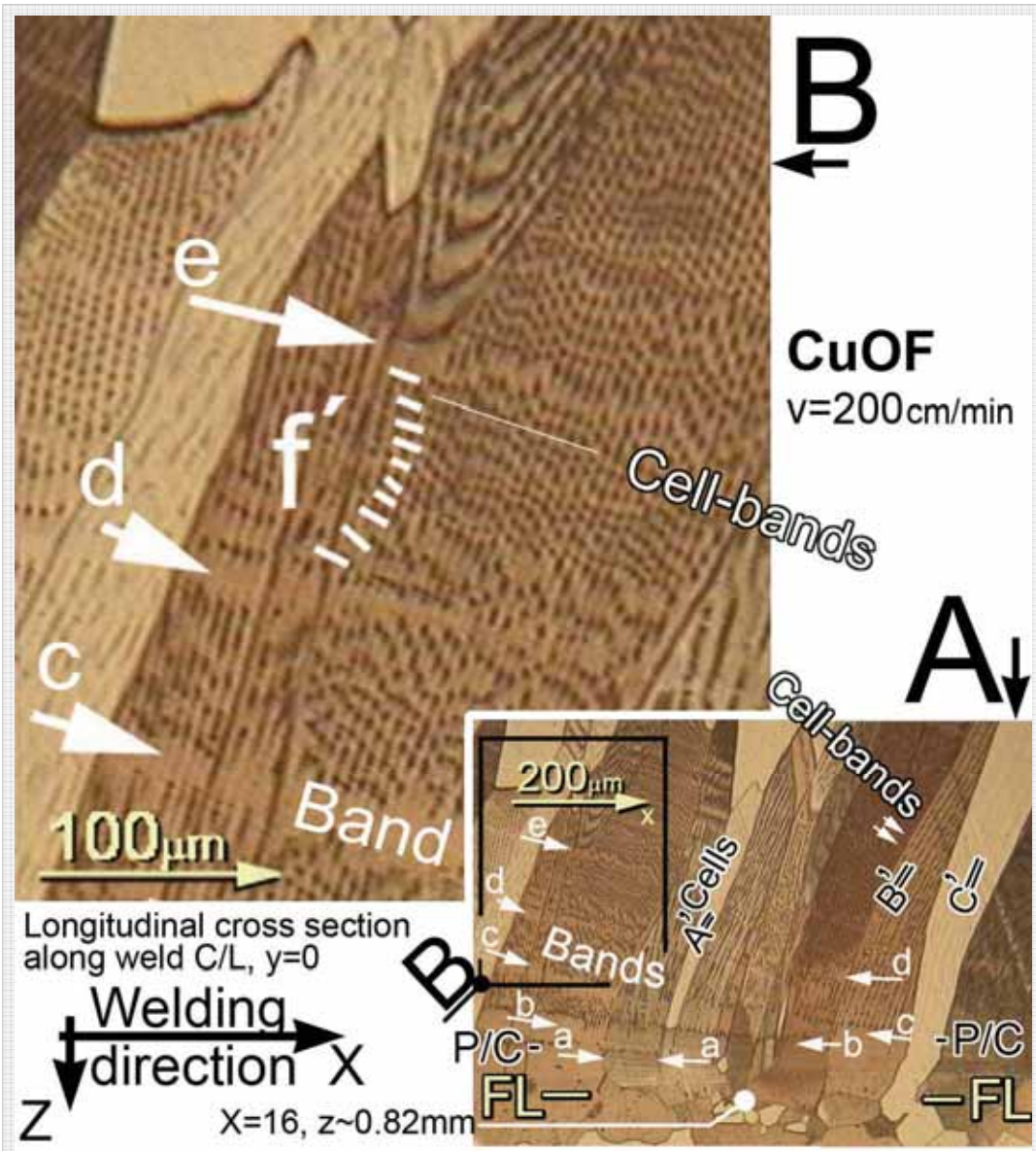

Fig. A7.2. Main figure A: *Fusion line* is at **FL-FL** and the **WiF** a little below it. The planar to cellular growth transition **P/C-P/C** is ~50…100 µm above the **FL-FL**.

The *cells* (**A'**, **B'** and **C')** have a with width ~3…6.3 µm (average 5.5 µm / $\Phi = 70^0$).

The *bands* (**a-a** through **d-d** and **e**) have a mixed planar/cellular structure within the otherwise cellular region. The *cell walls* are faintly visible through the band. The planar fraction of the band diminishes as the distance of the band from line **P/C-P/C** increases. It is as if the **R** had slowed down at the site of the band.

The *bands* intersect the *cells* (and the grains) perpendicularly. The *bands* near the **FL-FL** asymptotically.

The *cells* have *periodicity* in their coloring; the *cell-bands* (double arrowed).

Insert B: The cell width is ~4.0…6.2µm (average 5.45µm / $\Phi \sim 67^0$).

The *cell walls* are faintly visible through the bands **c**, **d** and **e**; those bands have no totally planar fraction.

The *cells* have periodically lighter stripes: *cell-bands* (white lines **f'**), running parallel to the *bands*. There are normally from one to fifteen (typically seven) cell-bands between two bands. The phenomenon appears similar to waves on a sea, every seventh being larger.

The darker spots between the *cell-bands* appear be *cubelettes*. [CG6CL20160xMirTxIns.jpg]

Appendix 8. Cu 3000 cm/min, yz-view. Planar to cellular change. Cubelettes

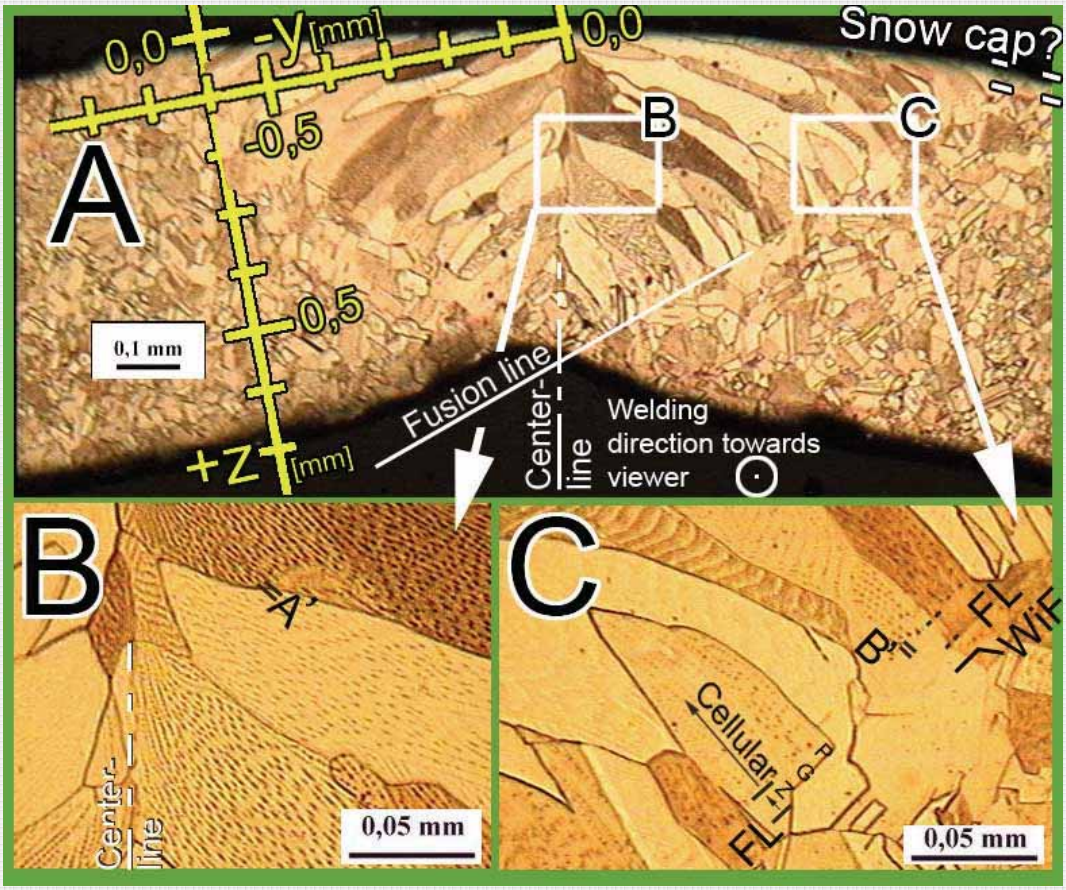

Fig. A8.1. Cu-OF. Longitudinal tube-weld from tube production line. Tube diameter 9,6mm, wall thickness 0.68 mm. Welding speed **v** = 3000 cm/min.

Main figure A: Overview of the perpendicular weld cross section (y-z). Due to full-penetration weld the grains grow from side towards the centerline. Their 3-D form is curved in two directions, so there is no planar 2-D area, which would show the grains from start (fusion line) to end (centerline).

The lines "**Snow cap?"** frame weld top layer, which has a darker greenish tint. This was not further studied; there is no certainty of the existence of a *snow cap* on this weld.

Insert B: Centerline region; clearly *cellular* structure. The grains turn ~ 15…30^0 towards viewer in this region, so the cell image is distorted, but the width (~ 1.9…2.5 µm around cells marked **A'**) is correct.

Insert C: Fusion line **FL-FL** region. The *planar growth zone* is marked **PGZ**. Start of cellular growth is marked with the arrow **Cellular**. The *cell width* (in the region of the *cell* marked **B')** is ~ 2.5…3.2 µm.

The cell centerlines are decorated with even rows of obvious *cubelettes* (darker lined-up spots); they are elongated lengthways, which we cannot fully explain.

No signs of neither cubelette growth or *smothering of cells (by over-grown cubelettes)* is present, which corroborates the assumption that *smothering* requires time for the *cubelettes* to grow.

No sign of start of any dendritic growth was detected, although the range of **R** has obviously been from 0 to 2600cm/min (assuming ϕ=30^0 in Eq. 1.1.18A). [30M, speed30m80xPa.jpg]

Cu 3000 cm/min. Longitudinal xz-view.

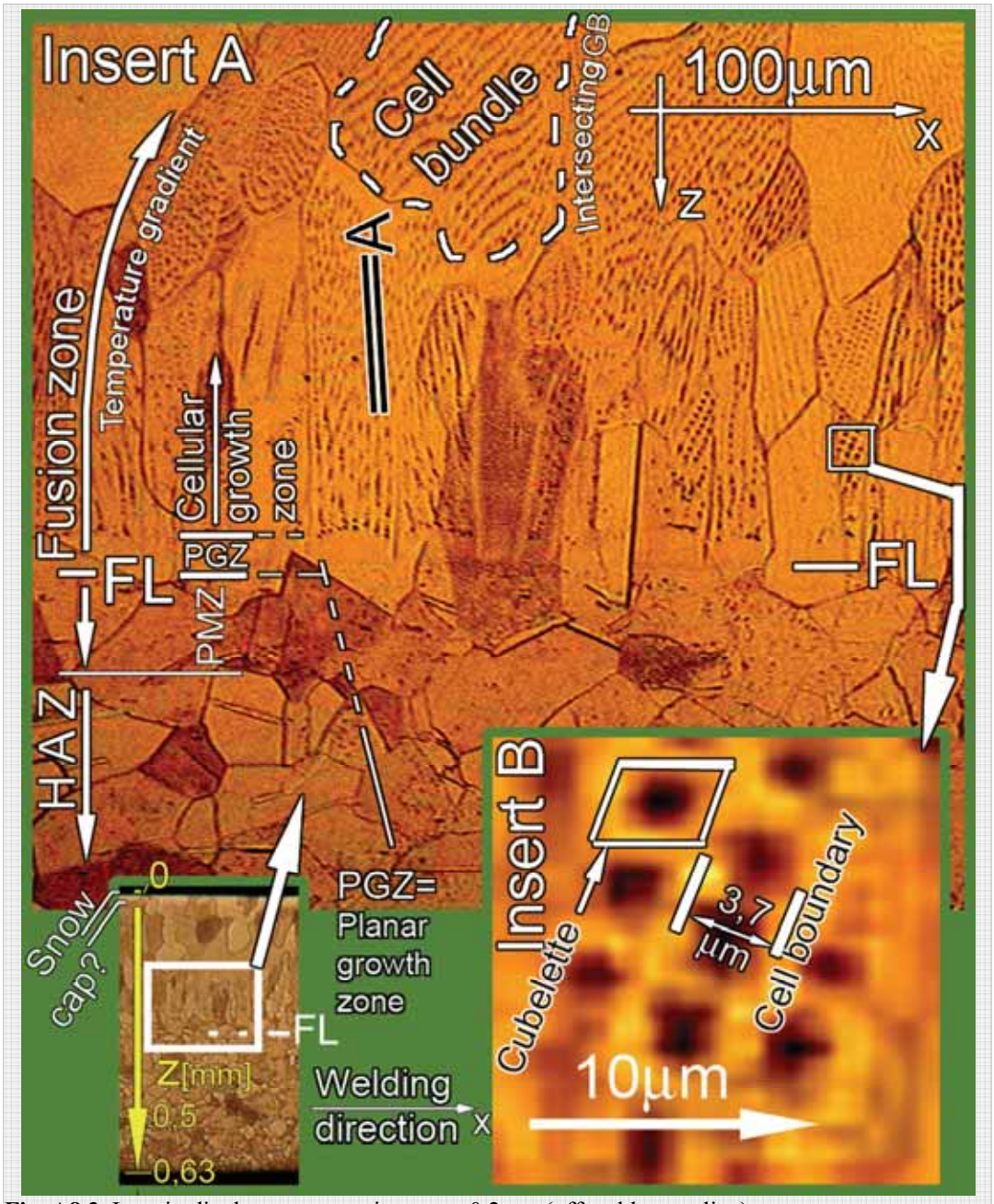

Fig. A8.2. Longitudinal xz-cross section, y= ~ 0.2mm (off weld centerline)
The main figure (lower left): The tube wall thickness is 0.63 mm. The weld has full penetration, but the surface of observation is located off weld CL; the observation surface crosses the *fusion line* at **FL-FL**.
Insert A: Solidification started at *fusion line* **FL-FL** and formed the *planar growth zone* **PGZ**, and continued with *cellular growth* Double line **A** marks a *cell* with width 2.9…4.5 µm / Φ ~90^0. **Cell bundle:** Seen here are not *cells* growing on plane of observation, but cross sections of *bundles of cells* approaching from behind. Adjacent cells lined up accurately and made an illusion of cells.
Insert B: Region of the cellular growth zone. Cell width is 3.7 µm. The inner structure of the cells consists of ***cubelettes***. [30M, Pori_30mpm_F05TX.jpg]

Appendix 9. Cu 3000 cm/min. xz SEM-view. Cell tips in a *grain- lag crack*.

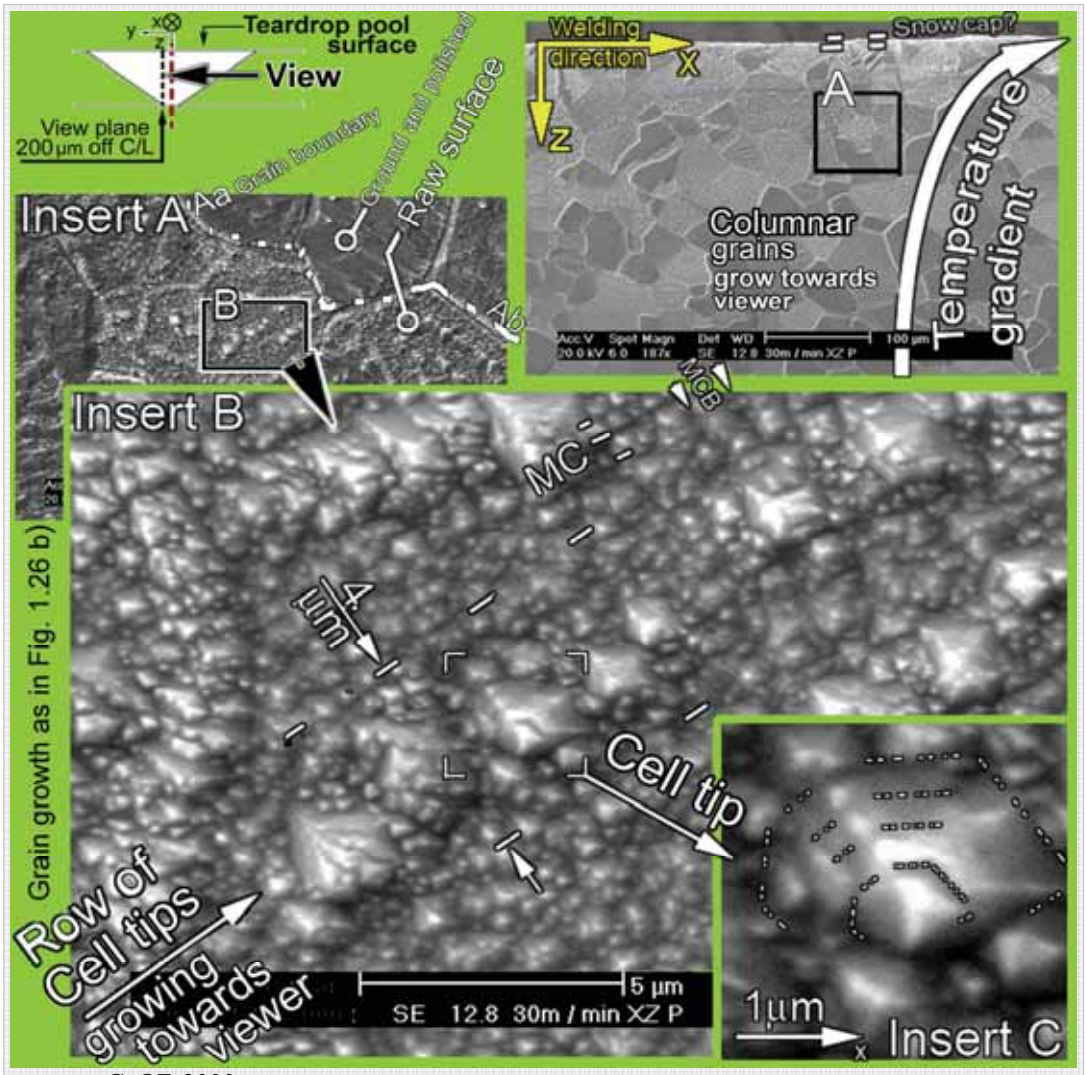

Fig. A9. CuOF 3000**.** (SEM) xz-section, 200 µm off weld centerline. Ground and polished sample, on which a lagging from general S/L front grain has preserved an area of the final solid/liquid interface. **Main figure** (upper right)**:** The columnar grains grow approaching viewer from behind.

Insert A: Grain boundary **Aa-Ab** divides **Ground and polished surface** (above) from **Raw surface** (below) not subjected to mechanical grinding and polishing. The *raw surface* is the end of a grain, which lagged slightly behind its neighbors in arrival to the weld centerline C/L. It pushed its solute pileup (still liquid) to the C/L while its faster neighbor-grains had already solidified and started contracting. This caused tensile stresses, which the still liquid final transient of the lagging grain did not resist and a microscopic crack was formed. The surface we see below the grain boundary Aa-Ab is the raw surface of this crack.

Insert B: *Raw surface* (= S/L front) shows *cell tips* growing slanted towards viewer. The cell width is ~ 4.1 µm). The form of the cell tips is a facetted 6-, 7- or 8-sided pyramid. They protrude above the surface, as is typical for cell tips. Tip form is not accurately definable and tips seem to come in rows – instead of forming neat arrays as in Fig's 2.7 b), 2.12 d) and 2.18 b) - because they do not grow quite directly towards the viewer. This grain never solidified intact with its colleague approaching from the opposite side of weld C/L.

The triple line **MC** points at two *micro-cells* (width ~ 0.4…0.7 µm). The two triangles **MCB** point at a *micro-cell band* (width ~ 0.4…0.7 µm).

Insert C: *Cubelettes* grow facetted. Dashed lines mark four concentric facet lines. The pyramid has 7 or 8 sides. [30M-P_PaTz.jpg]

Appendix10. Cu 3000 cm/min, xy-view. Micro-cells and cubelettes.

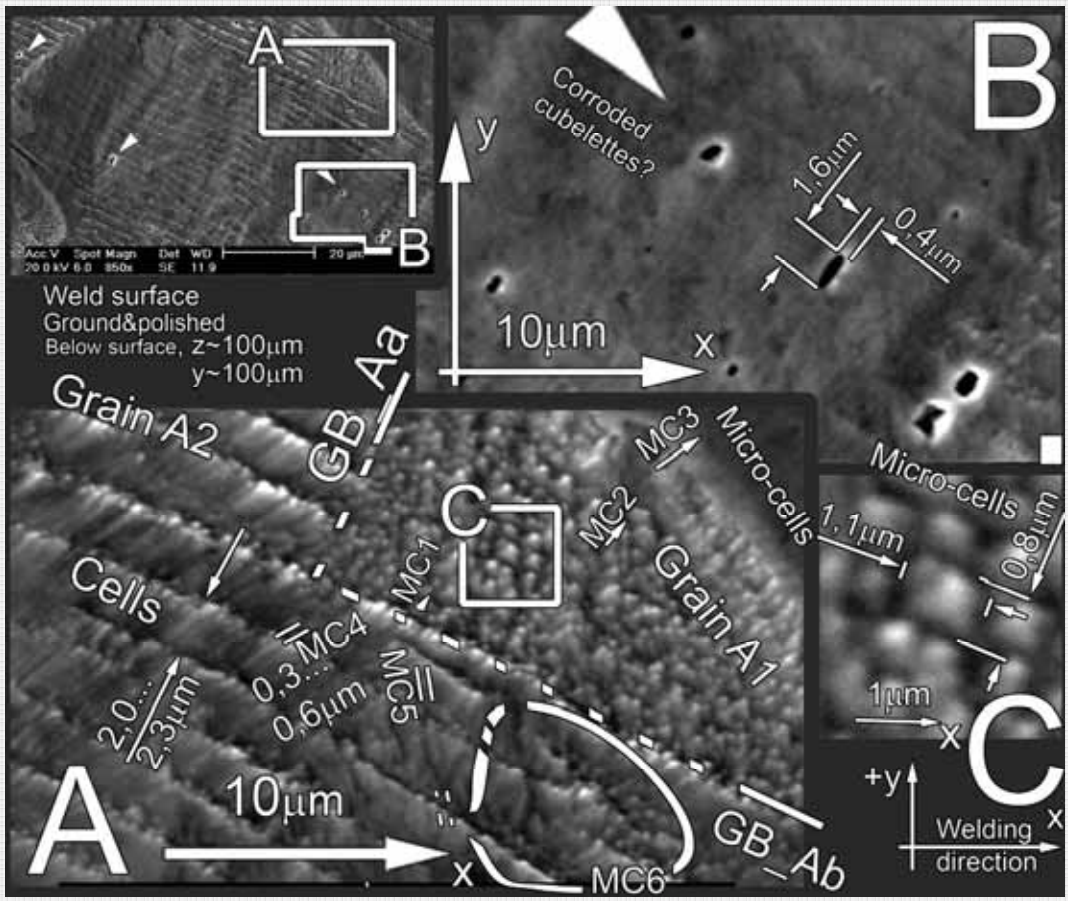

Fig. A10. A SEM-micrograph of a ground and polished horizontal xy-cross section, z ~ 100 µm below the weld top surface, y ~ ±100 µm (off weld C/L).

Main Figure (top left): Mainly cellular structure. White triangles points at *cubelettes*.

Insert A: Boundary **GB_Aa…GB_Ab** separates grains **A1** and **A2** with quite different outlooks. **Grain A1** consists of *micro-cells*, approaching the viewer. Vectors **MC1**, **MC2** and **MC3** depict the scattering of growth directions, typical for *micro-cells*. Dimensions (~1µm) in **Insert C** are typical for *micro-cells*.

Grain A2 (below and to left of **GB_Aa…GB_Ab**) consists of *cells* (2.0…2.4µm). These cells and the spaces between are decorated with *micro-cells* **MC4**, **MC5** and **MC6** (width 0.3…0.6µm).

Insert B: A grain ground & polished flush in the micrographic preparation. A white arrowhead marks a row of *cubelettes* appearing hollow. The elongation suggests the plane of observation tilting with respect to the cubic hole; the shorter side (0.4…0.8 µm in the five largest ones) is probably more accurate.

Insert C: The blow-up of the *micro-cells* shows the tips of the *micro-cells* resembling the tips of the cells, the resolution is poor, but there are faint shadows suggesting facettes on the tip, similar to the ones in Fig. A9 Insert C. It seems not impossible that the *micro-cells* are nuclei of *cells,* having lost a growth competition against their more successfully located and oriented colleagues.

[30M-K02Tx.jpg]

Appendixes 11…22: Bi-dope

Appendix 11. Bi 5…0 cm/min, xy-view from top. C/L cracks

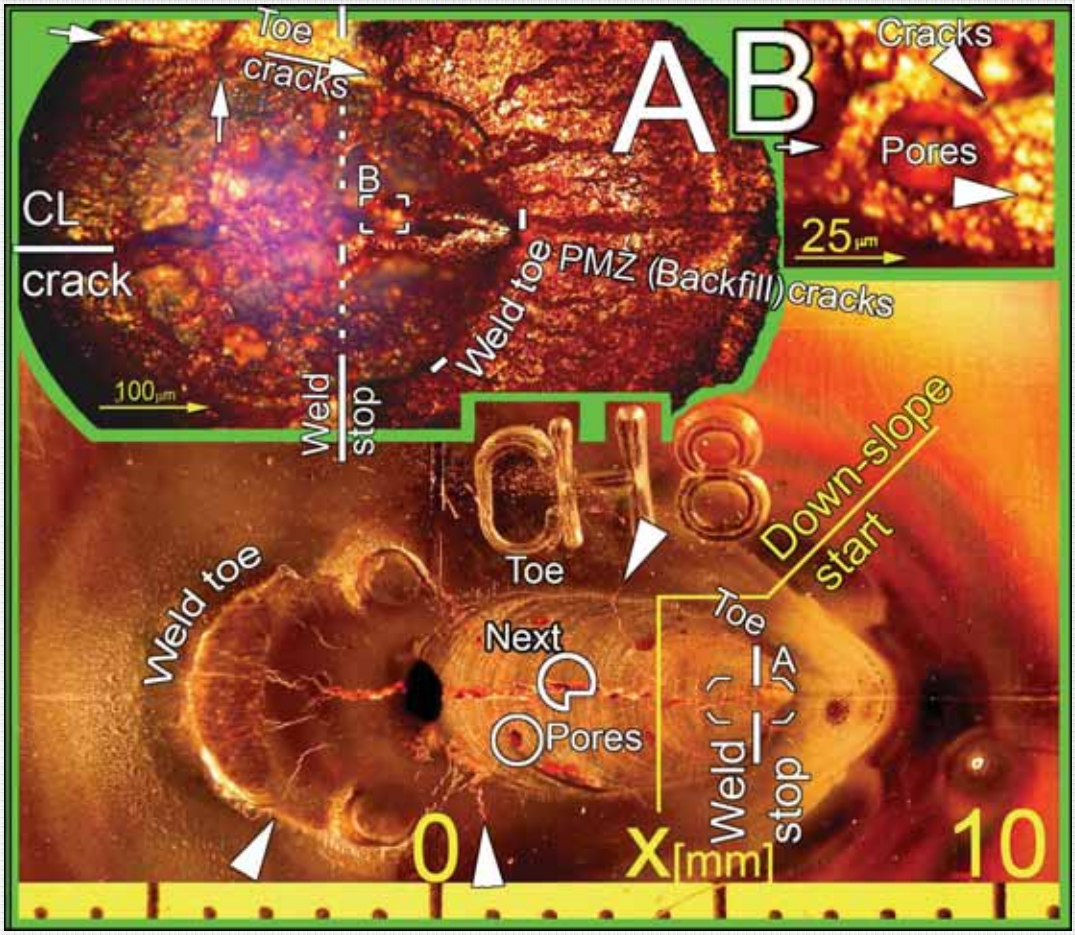

Fig. A11. Weld stops at x= ~6mm.

Regime of welding: Welding speed at **0<x<6**mm = 5cm/min (0.83 mm/s). Time and distance = 0 at **x** = 0.

Prior to x = 0: Welding arc is stricken 0.5 s prior to movement start. Torch reaches location **x**=0 at **t**= 0 s.

After x = 0: Torch movement is stopped at **x=** ~5.5 mm (at **t**= 6.6 s). Current down-slope starts at **x**= ~4.0 mm (at **t**=4.8 s). Down-slope duration 8 s. Down-slope current reduced to 0 [A] at **t** = 12.8 s. The current was extinguished 6.2 s after torch movement stop. This reduced the temperature gradient at the end of the weld (x=5.5mm).

The goal of the test was to create near *Case 1* (equilibrium) solidification at the end of the weld (x=6mm).

Main Figure (Below): Heavy cracking mainly at weld C/L and in its direction. Area **x**<0 is not considered. Cracks extend through the **v**=0cm/min region mainly as centerline cracks and then past the weld toe deep into the base metal with the *adversary backfilling (GB-liquation) mechanism* discussed in Ch. 1.1.16. Besides the C/L-crack, grain boundary cracks are abundant. *Case 1* was clearly not achieved. Porosity is severe.

Insert A: The centerline crack appears to discontinue at the very weld stop. The crack did continue there but was back-filled from the lastly solidifying pool and *snow cap* similarly as in Fig. A15.2. Note the PMZ-(also called Liquation- or Backfill-) cracks crossing the weld toe deep into the PMZ of the base metal. They may broaden the normal partially melted zone several times (Ch. 1.1.16).

Insert B: The immediate vicinity of the weld stop is cracked and porous. [CH8_18APaTx.JPG]

Appendix 12. Bi 5…0 cm/min, xy-view from top. Cell boundary & cell band cracks

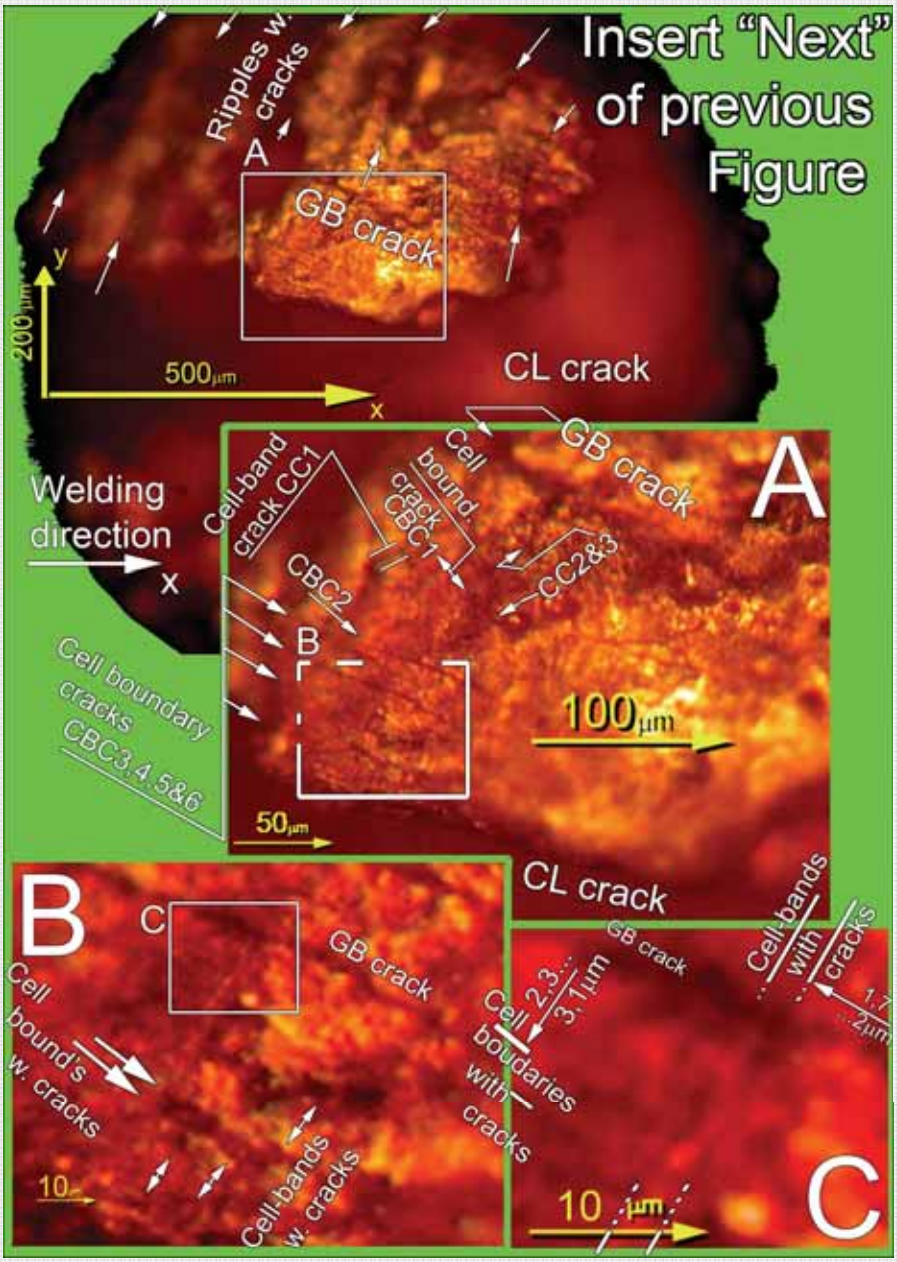

Fig. A12. Insert "Next" of Fig. A11 (on top)**:** The weld top surface. Next to centerline (**CL**) crack, cracks associated with *ripples* are evident. These are – we believe – the same as the perpendicular *cell-band cracks* below. Non-polished/etched raw top surface.

Insert A: *Cell boundary cracks* **CBC** and perpendicular to them *cell-band cracks* **CC** are marked.

Inserts B and **C:** As above, note the sharp *cell-bands* and their cracks. Cell width (2.3 …3.1µmm). Cell-band width (1,7–2µm). Inserts A through B ground, polished and etched.

[CH8_S_x3yz_16x_06Tx.jpg]

Appendix 13. Bi 5…0 cm/min, xz-view. Pores, GB cracks, vague *cells* and *micro-cells*, remnants of *cubelette* rows

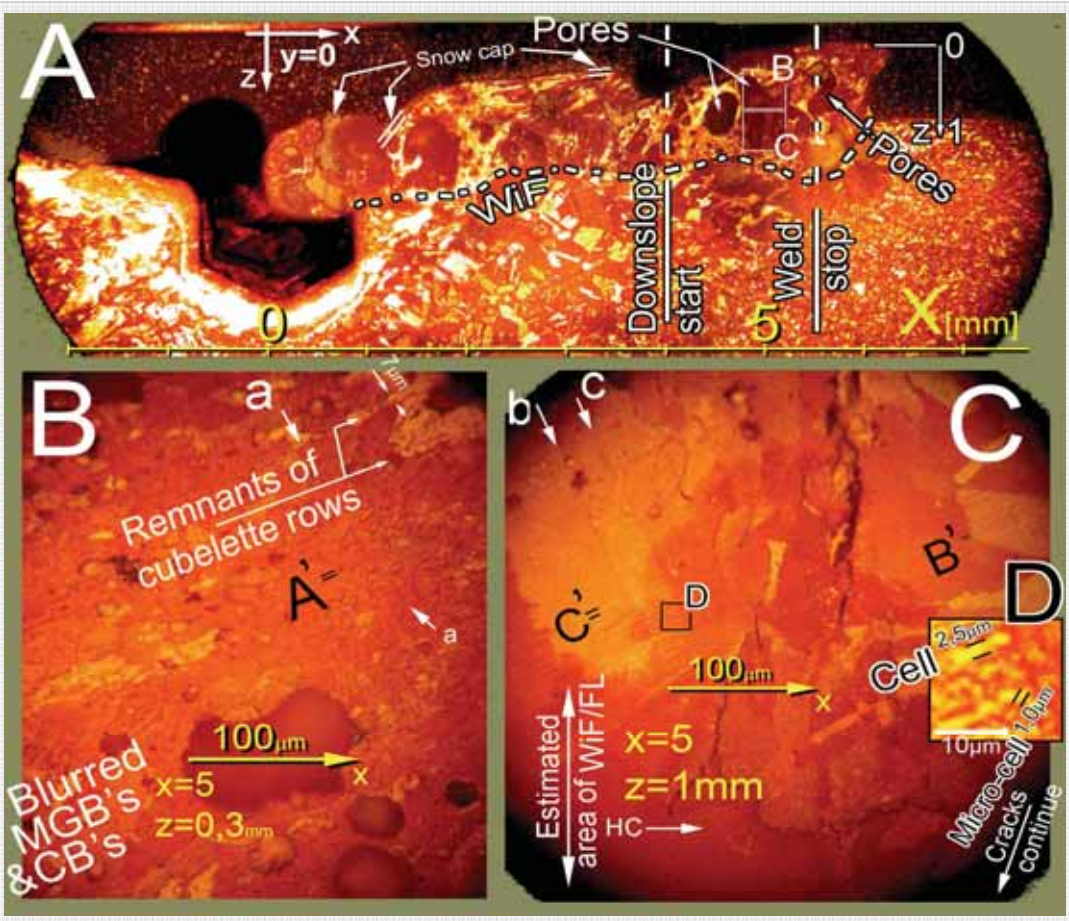

Fig. A13. As seen in this and the previous appendix, the almost 0 welding speed at x ~ 5...6 mm did not bring about near equilibrium *Case 1 solidification*, which would have no segregation and no hot cracking. **Main figure A:** The micro structure is porous and cracked, cracks running mainly in centreline direction with several cracks in grain (and cell) boundary direction.

Insert B: near weld top, at z ~ 0.3mm, porosity is abundant, with few visible cracks. The general view presented In Fig. A12 shows cracks near weld top as well; they do not come visible on a plane parallel to these same cracks. *Grains* are blurred probably because of *GB*-migration (Ch. 1.1.3 and Fig. A6C). *Cells* (**A'**) are vague; *smothered* by *cubelette over- growth* (Ch. 6.2.4). Remnants of cubelette rows are seen.

Insert C: Closer to the WiF/FL, at z ~ 1mm, cracks are more conspicuous, obviously following grain boundaries. The seeming procreation of cracks at a distance from the surface may be connected to the diversification of their directions; near top they run in C/L-direction, not crossing the plane of observation. Deeper they run in all the directions of the grain boundaries, some of which cross the said plane. It is certain – based on Appendix 12 – that in this structure, there are more cracks than seen in this cross section.

The general direction of both **GB**'s and cracks is vertically up. The **WiF/FL**-zone runs somewhere between z = 1.0…1.1mm. The cracks proceed straight through it into the HAZ, presumably with *backfill cracking (liquation) mechanism* (Kou 2003 [3 p.307 Fig.12.4 "Mechanism (a)"]. A crack turns horizontal at arrow **HC** in the region of **WiF/FL**. *Bands* are scarce; arrows **a**, **b** and **c** point at some of them. *Cells*, pointed out by the double lines **A'**, **B'** and **C'** (width 2.0 to 6µm), are mixed with *micro-cells* (width 0.8 to 1.3 µm..

Insert D: The mixed structure of *cells* with *micro-cells* is seen vaguely. [CH8AL_x00yz_04x_01PanMiTxCo.jpg]

Appendix 14. Bi 0 cm/min, xz-view. C/L cracks

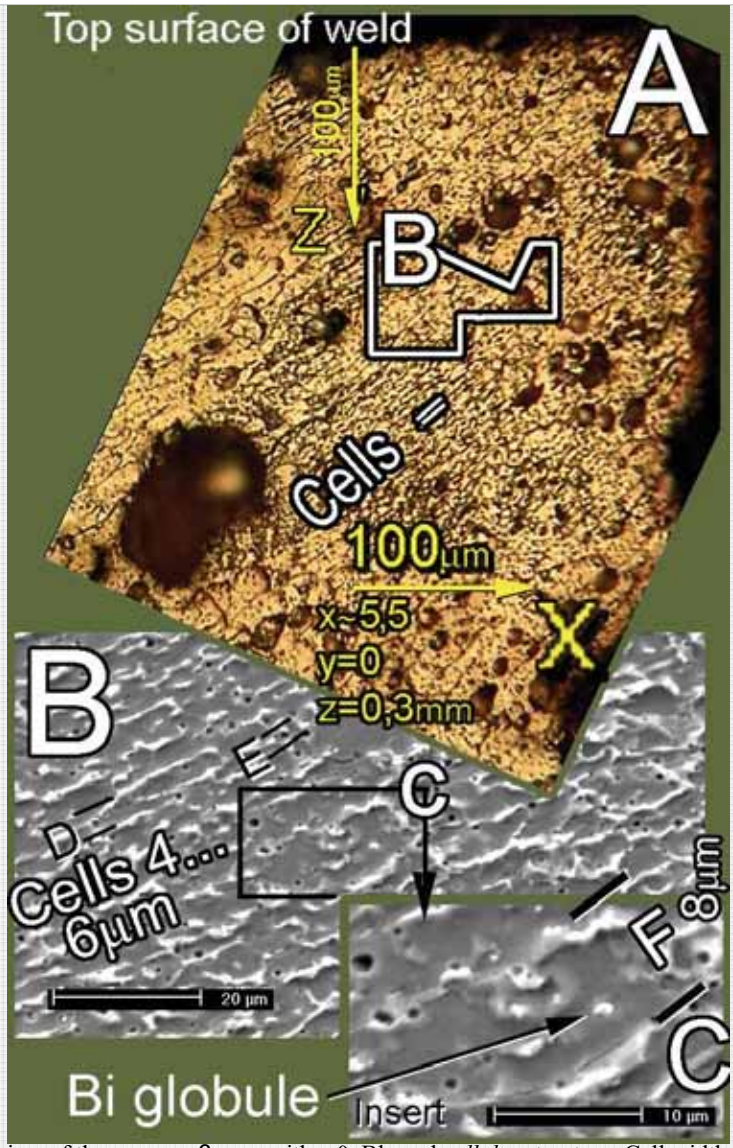

Fig. A14. Optical view of the area x ~ 6 mm, with **v** 0. Blurred *cellular* structure. Cell width at area marked **Cells** ~4…9 µm. Near the top the cell width is ~ 2 ... 3 µm.

Main figure A Grain boundaries are poorly seen. Pores are abundant; several of them house a seemingly incoherent *globule;* probably the same ~ 100% Bi- globules measured in other samples. They appear associated with the severe porosity.

Insert B: A SEM-micrograph of the area of double line. The form of cell boundaries is more distorted than with faster welding speeds, but does not resemble secondary arms. Cell width is ~4…6 µm (cells **D** and **E**). This is a mechanically prepared sample, but cell boundaries are above the body of the cell; this may be a crack surface parallel to the plane of observation.

Insert C: The area marked with double line **F** is a cell, with width 8 µm. The *globule* in it (**Bi globule)** has a diameter ~ 1.5 µm. This particular precipitate was not analyzed, but globules analyzed elsewhere in this work were almost pure Bi.

While many pores have a *globule* in them, many have not; the *globules* may be so incoherently attached that they fall of their socket. The set up of these globules in their sockets is similar to *dimples* on ductile crack surfaces. [CH8AL 06 320xTy.tif]

.

Appendix 15. Bi 10 cm/min, xy view from top. Weld centerline hot crack

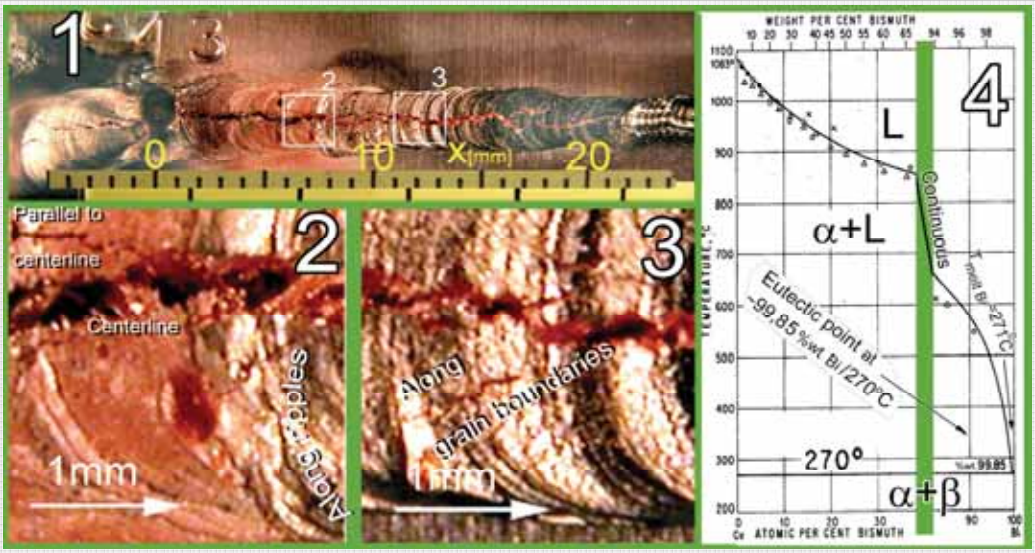

Fig. A15.1. Main figure 1: The Bi-dope causes severe cracking with welding speed **v** =10 cm/min. The major void is the centerline crack extending through the total length of the weld (40mm). **Inserts 2** and **3** point out other cracks - besides the parallel to centerline - along grain boundaries and along ripples. **Insert 4:**:Left and right end of the Cu-Bi eutectic equilibrium diagram [/25B/].

Fig. A15.2. (to the right): A weld, with identical parameters as in the one above, had its centerline crack, back-filled with lighter in color material. This material was not chemically examined, but the coloring reveals that it is evidently Bi-rich Cu-Bi alloy from an exceptionally thick (~100-200µm) *snow cap* on top of the weld.

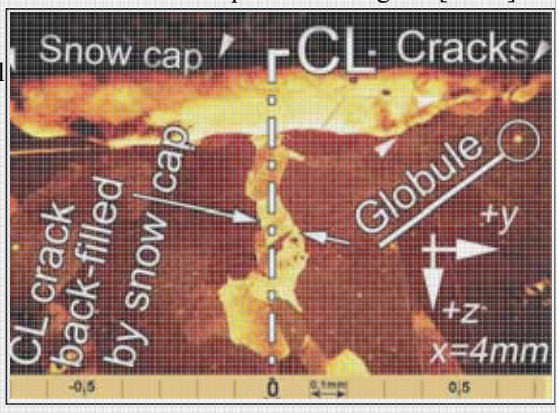

[C73_DSCN0856Tx CuBi.jpg] [C41C_MUTx.jpg]

Legend of Fig. A16: **Main figure** (Lower left): SEM micrograph of an **xz-**crack surface at weld centerline (**y=0**). 180^0 bending after welding in ambient temperature opened the centerline crack and the **Left** and **Right crack surfaces** are on opposite sides of the **Weld CL.** The stress needed was negligible.

Insert A contains two *crack-eyes*. The crack-eyes are bordered by conspicuously intact grain boundaries - *crack-eye lids*- two of which are marked **GB1** and **GB2**. The fusion line is marked **FL**.

Insert B depicts the *crack-eye lid* **GB1**.

Insert C a still closer look at the grain boundary **GB1**. The *globule* with ~ 20µm diameter is a spherical precipitate of >99%wt pure bismuth (measured with EDS). Despite bismuth's devastating propensity to hot cracking, the Bi-level anywhere in the bulk weld metal remained below the EDS 0.5%wt resolution. (The concentration measurement area was 10 µm x10 µm. Measurements of the Bi-concentration across the grain or cell boundaries yielded invariably nil-values, both on polished and cracked surfaces. Even so, the cracks surely are caused by an elevated Bi-concentration and we state that Bi-concentrations < 0.5% wt are sufficient to cause hot cracking in copper welds. Solubility of Bi in Cu is practically nil [111p.308]; all Bi segregates to the eutecticum. Cu-Bi eutecticum forms at 270^0C with C_e 99.98 wt% Bi; this we see as the mentioned above *globules* and the *snow cap* on top of the weld (Fig. A15.4).

.

Appendix 16. Bi 10 cm/min, xz-view. Crack surfaces, crack-eyes, Bi globules

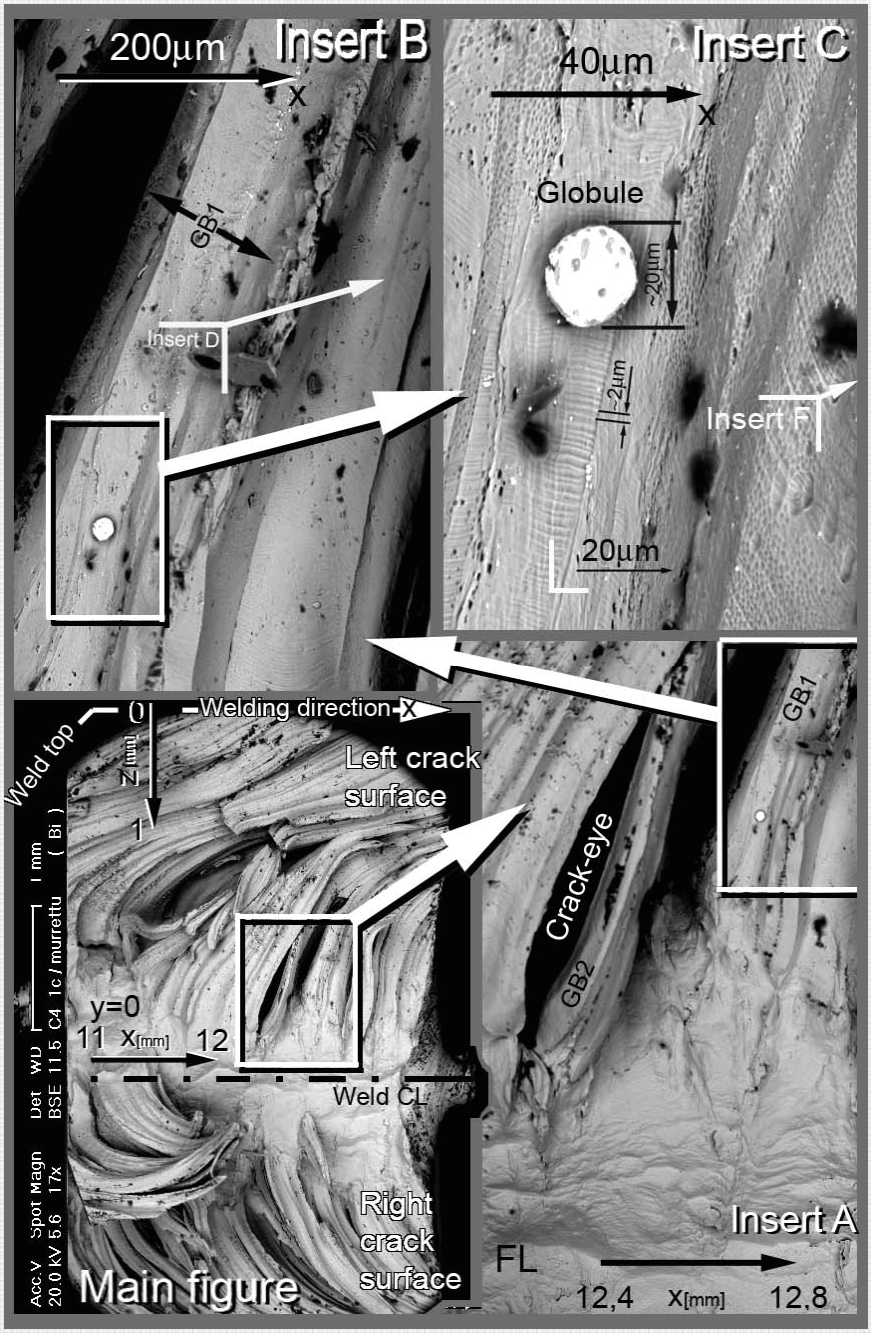

Fig. A16. SEM micrograph of the crack-surface. Bi-dope, 10 cm/min (Legend on the previous Appendix)
[C41C_MUTx.jpg]

Appendix 17. Bi 10 cm/min, xz-view. Crack surfaces, crack-eyes

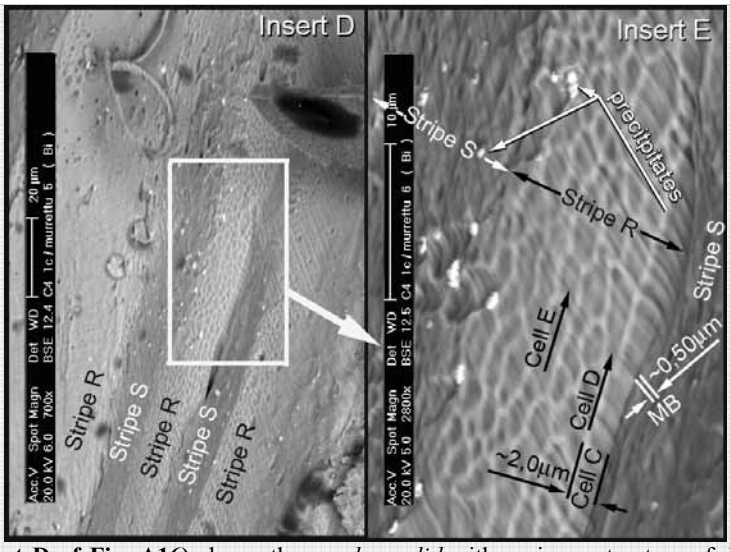

Fig. A17.1 (**Insert D of Fig. A16)** shows the *crack-eye lid* with an inner structure of darker and lighter stripes marked **Stripe R** and **Stripe S**.

Insert E: The lighter **Stripe R** has a cellular substructure, three units of which are marked ***Cells C, Cell D and Cell E***. The cell width is ~ 2.0 µm, which fall within the limits of normal *cells* measured in this dissertation. The direction of these cells is unknown; they may be cell tips growing from below. The relief is much like the cell tips in Fig. 2.12 d).

Cells C, D, E expresses a clear *periodicity*, one period being marked with a double line **MB**. The distance between these periods is ~ 0.50 µm, which typical to *cell-bands.*

The darker **Stripe S** does not show any cellular sub structure.

The white **precipitates** fall below the resolution; they will be discussed with the Appendix 18.

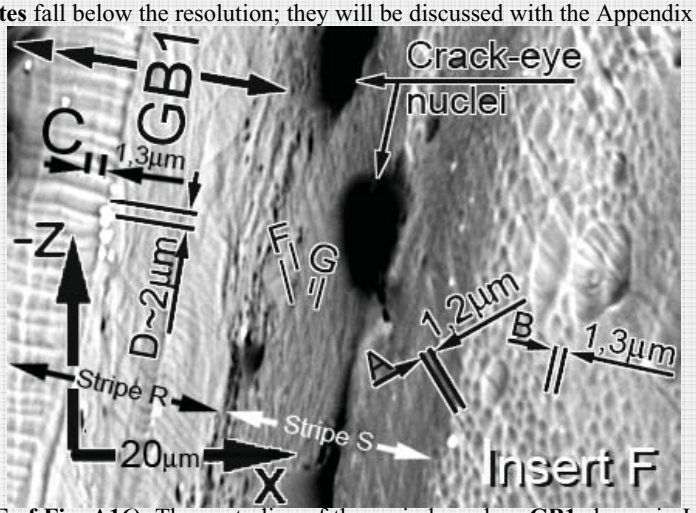

Fig. A17.2 (Insert F of Fig. A16). The centerline of the grain boundary **GB1** shown in Inserts **A B** and **D**. This view corroborates the finding that the grain boundary **GB1** divides into **Stripes R** and **S**. The **Stripe R** obviously is the strong *crack-eye lid* and the **Stripe S** nucleates the *crack-eyes*.

The *cells* are distinct, double lines **B** and **C** point at two. *Width* in **Stripe R** area is ~ 1.3 µm. The cells have a distinct *periodicity*; the *period* (distance between two equally colored areas of a cell) pointed out by the double lines **A** and **D** is ~ 1.2 and 2 µm respectively. The measured *periods* are significantly less than usually measured for the welded copper. Also their appearance is sharp; double lines **A** and **D** probably point at *slip planes.*

The **Stripe S** remains mysterious inasmuch as its sub-structure is concerned. It has a distinct grid-system, pointed our by double lines **F** and **G**, with distances 1.5 and 0.7 µm respectively. *Micro-cells* are not expected in this area, but that is what they resemble. Their obedience to thermal gradient (manifested here by the direction of the 7 to 1 o'clock grain boundary **GB1**) is higher than usually observed in micro-cells.

[C41C-M5Tx.jpg] [C41C_InsF.jpg]

Appendix 18. Bi 10 cm/min, xz-view. Crack surface. Strip lines and ordered micro-cells & flap precipitates

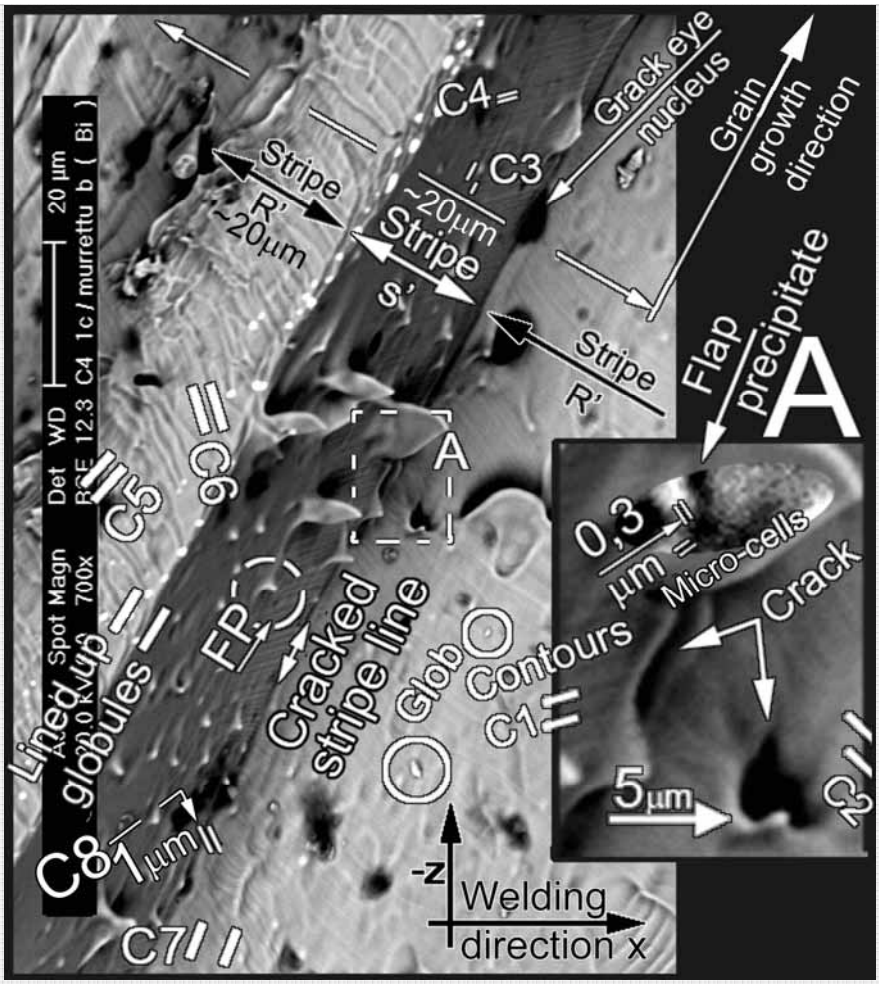

Fig. A18. *Crack-eye* grain boundary area, similar to the one in previous figure.

Main figure (left) corroborates the previous finding: grain boundary area is divided in **stripes R'** and **S',** analogous to the previous **stripes R** and **S**.

Cracked stripe line: Both *stripes* have cracks and *crack-eye* nuclei, but especially prone to them is the *stripe line* between them. One **Crack-eye nucleus** is marked at such a line.

Lined up globules: Sporadic *globules* occur all over the crack surface, but especially frequent they are at the *stripe line*. Two sporadic *globules* are circled and marked **Glob**.

Sub structures of the *stripes R',* (contours **C2, C5, C6, C7** and **C8**) have width 1.1; 1.5; 1.7; 4.7; 0.7 µm respectively and **sub structures of the *stripes S'*** (contours **C1, C3** and **C4)** have widths 1.0; 1.7 and 0.6 µm respectively. The width of both stripes is ~20µm; the stripe lines remain mysterious.

It is probable that the *transverse diffusion* (Ch. 2.5.4), and the *segregation to cell boundaries* forms a perpendicular solute pileup (modeled e.g. by Demchenko, Fig. 2.47 a)), forming a high Bi-content at the grain or cell boundaries. This, however, does not explain the *lined up globules*, of which we know only that they are almost pure Bi.

The structure does not have the features of the normal binary eutectic solidification (Fig. A15.1/4). Where do these Bi *globules* come from? Flemings presents in **Fig. 2.14 E & F** a mechanism, involving a ternary eutectic system, forming globules much like the ones in the upper left line of the ***stripe* S'**. This may be a clue to this problem, but structure evades a thorough explanation. It is evident however that the eutectic reaction - which must exist in the system - does not form the normal fan-like lamellae inside cells as in Fig. 2.15.

Insert A: ***Micro-cracks*** in various directions. *Flap precipitates* with a fine grid of *micro-cells*.

[C41C-MBTx.jpg]

Appendix 19. Bi 100 cm/min, xy-view from top. Centerline crack reducing & cross-jump cracks

.

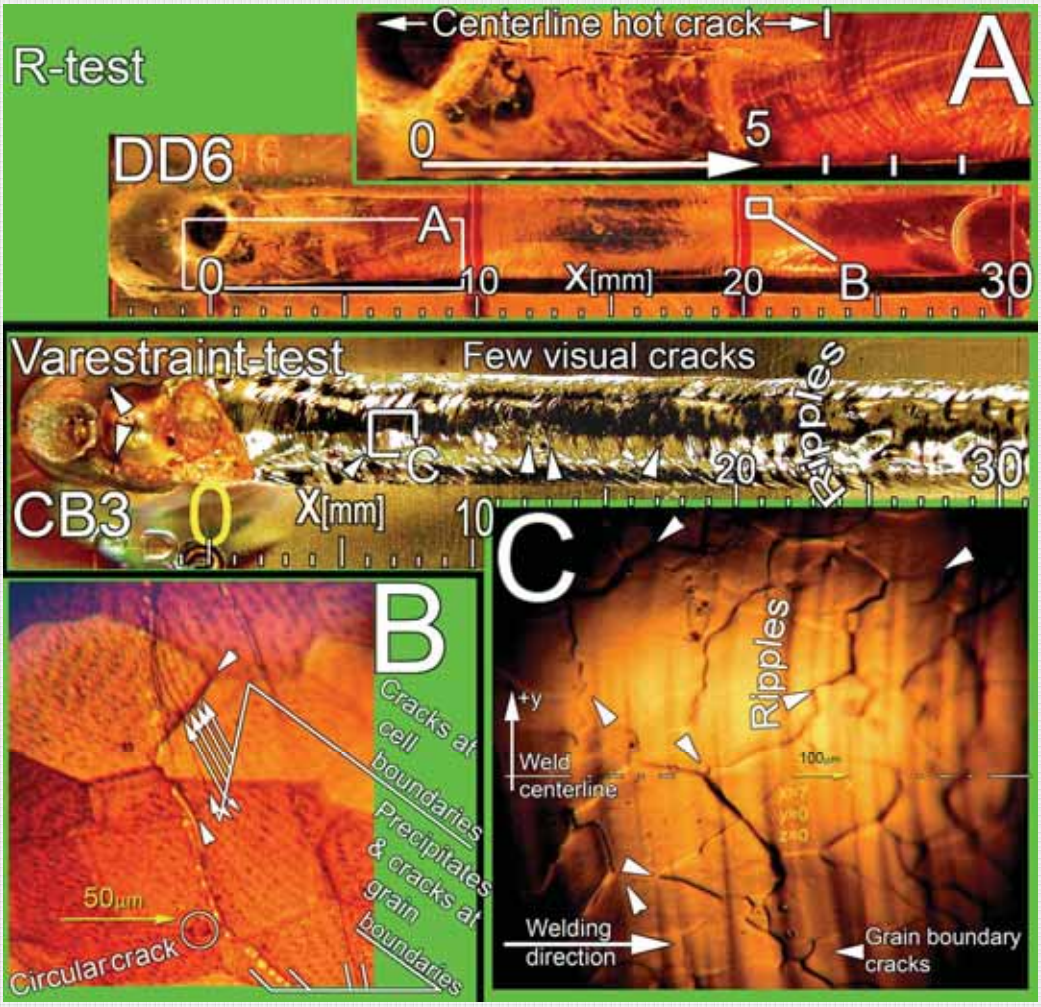

Fig. A19. Bi dope, v=100 cm/min. Weld raw surface **xy**-view. Comparison of R-test and Varestraint-test samples. R-test shows serious centerline (C/L) cracking, Varestraint test does not.

R-test sample DD6 with **Inserts A and B:** The only visually detectable flaw is the C/L hot crack extending to x ~6 mm. **Insert B**: Microscope reveals a fine grid of cracks mainly on grain and cell boundaries (~ *spongy crack* area).

Distinct and cracked precipitation along most grain boundaries; typical back-fill of brittle, high-Bi, low T_m eutecticum**.** Back-filling of cracks is beneficial in e.g. Al-alloys, but this Bi-back-filling is devastating.

Circular crack*s* (*crack-eye* nuclei) are frequent.

Varestraint test sample CB3 with **Insert C:** No flaws are detected visually. Varestraint test makes weld surface is more rippled than the former. **Insert C:** Microscope reveals a grid of mainly grain boundary cracks almost identical with the one in Insert B. Exerting no stress in y-direction, Varestraint test does not reveal a pure C/L crack.

COMPARISON WITH v=10 cm/min WELDS (see Appendixes 15…18): The amount of visual cracks in these faster welded samples is significantly less. Relative amount (both length and opening) of centerline cracks is less; cracks form finely dispersed grids in the weld. Due to small amount of *cross jump cracks*, this is not typical *spongy cracking*. [Dd600_10Tx.jpg].

Appendix 20. Bi 100 cm/min. Varestrain 1.5%, xz-view. FL→ planar→ Cellular growth, crack-eyes

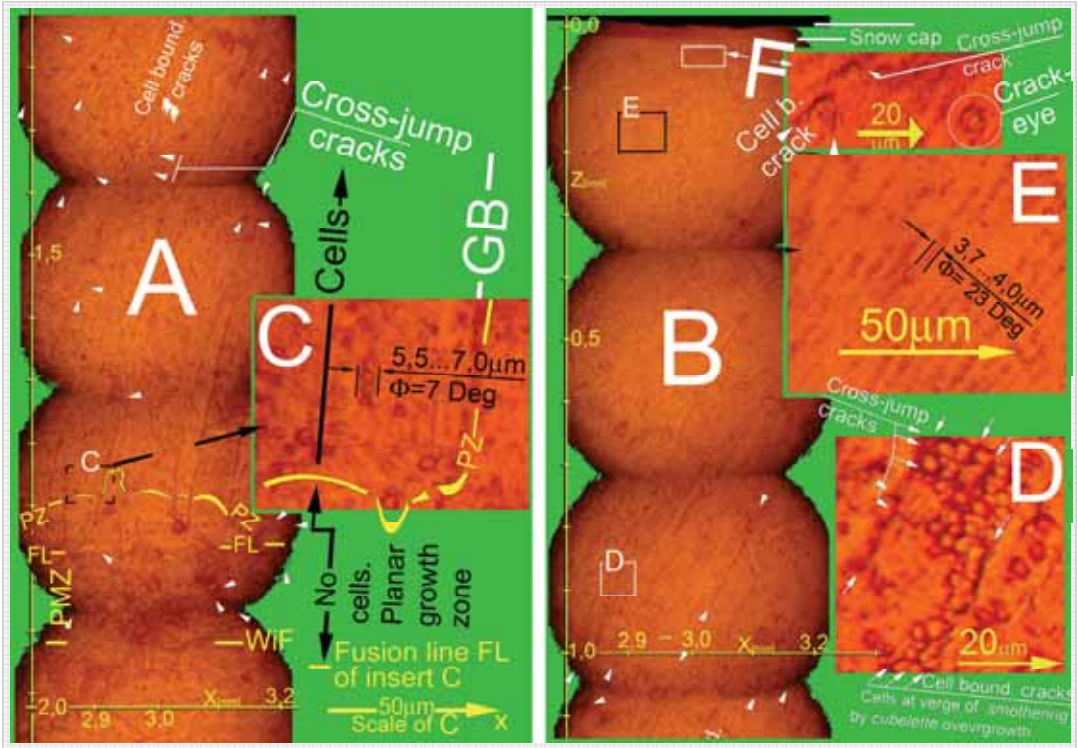

Fig. A20. Bi dope, **v**=100 cm/min, Varestrain 1.5 %. Longitudinal cross section, **xz**-view **y**=0,
View A: Fusion line **FL-FL** area, **View B: Weld Top** continuing from View A**.**

View A: Weld interface **WiF** and fusion line **FL** marked roughly, between them partially melted zone **PMZ.** The zone above **FL** till line **PZ-PZ** is the *planar growth zone*, with no *cells*. *Cells* do exist above **PZ-PZ,** but the line wiggles substantially more than **FL**.

Insert C: Rows of *cubelettes* are distinct; some have grown larger than the others. This suggests *cell smothering (by overgrown cubelettes)*, a phenomenon not expect with **v** as high as 100 cm/min. Ambiguous *cells* make determination of line **PZ** difficult, but it seems to tilt down near **GB**'s. The location may shift substantially in neighboring grains.

View B. Weld top. Distinct cellular structure. There is a darker discoloring – *snow cap* - on top of the weld. A large part of the Bi dope has been transported there in the solute pileup in front of S/L interface.

Insert D: Tiny **cell boundary cracks** and perpendicular **cross-jump cracks** border *cubelettes*. The latter are at verge of out-growing the *cells*, nearly *smothering* them.

Insert E: *Cubelettes* form the core of the *cells*, and are fairly well confined in them. The faster growth rate **R** has not allowed time for cubelettes to grow.

Insert F shows **Cell boundary cracks** and **cross-jump cracks** (perpendicular to the former). Some flaws adopt a **crack-eye** form. This increased cracking is probably due to the vicinity of the snow-cap (final transient). [CB3AL_x03yz00_40x_03Mis.jpg]

Appendix 21. Bi 200 cm/min, xy-view from top. Cubelette rows on Cell centerlines

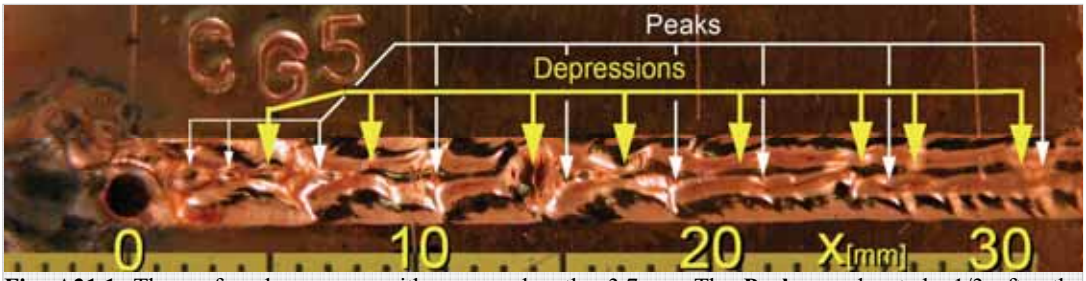

Fig. A21.1. The surface has waves with a wave length ~3.7mm. The **Peaks** are located ~1/3 after the depression on its left and ~2/3 before the depression on its right. This surface form defect is called *humping* or "*strings of pearls*". Increasing welding speed increases its occurrence. Here it is not developed fully.

There is a ridge along the weld centerline. A steep ridge and associated to it undercut is a signal warning of approaching humping ("string of pearls").

No cracks *were detected visually* ***in this 200 cm/min weld****. Please, compare this with the* ***seriously centerline-cracked 10 cm/min weld*** *in Fig. A15.1.This difference is – we propose – due to the fact that* ***slow*** *v enhances planar and blunt-tipped cellular growth, "plowing" most of the solute to the weld centerline.* ***Fast v*** *enhances sharp-tipped cellular growth "fencing-in" much of the solute between the cells, thus distributing it evenly across the weld fusion zone****.***

The stress distribution in the first occasion – with most of the stress concentrated on the lastly solidifying C/L – is probably more crack-inducing. In the latter occasion, the stress is more evenly distributed across the fusion zone, and the densely and evenly distributed cell boundaries – even if contaminated by the "fenced-in" solute – are more likely to be able to relax the stresses.

[CG5_09Tx]

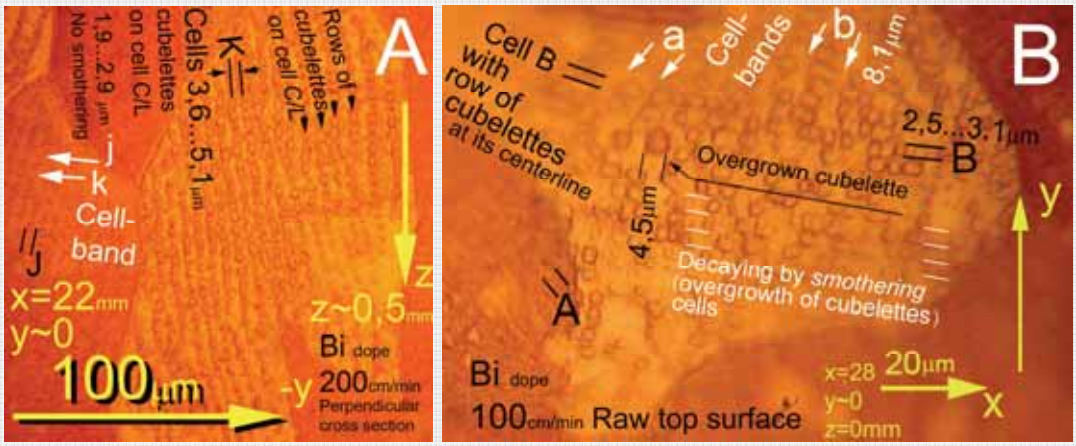

Fig. A21.2. Comparison cell structures of two Bi-doped welds: **v** = 200 and 100cm/min.

A: Perpendicular yz-section of the 200 cm/min weld. The black double lines **K** and **J** point at cells in a colony with cell width 3.6…5.1µm. .The black arrowheads indicate rows of *cubelettes* on the cell centerline. The size of the cubelettes was 1.9…2.9µm; notably less than width of the cells they occupied.

White arrows **j** and **k** point at periodic cell discoloring we call *cell bands*. They run perpendicular to cells and parallel to *bands*.

B: Raw top surface of the 100 cm/min weld. *Cells* (width is 2.5…3.1µm) are not as accurate. Cubelettes are larger up to ~4.5µm. The growth of the *cubelettes* from inside the cells decays the cell; a process we call *cell smothering*.

These view angles differ from the standard xz-section at weld C/L: in **A** welding direction is away from viewer and in **B** shows a view from top. The cubelettes are square regardless of the viewing direction.

[CG5BP_x22y00z_16x_01MiTxInsB][DF7BSurf_x28yz_40x_02BU.jpg]

Appendix 22. Bi 200 cm/min, xz-view. Grain-lag cracks, cell tips, crack-eyes and crack-eye lids

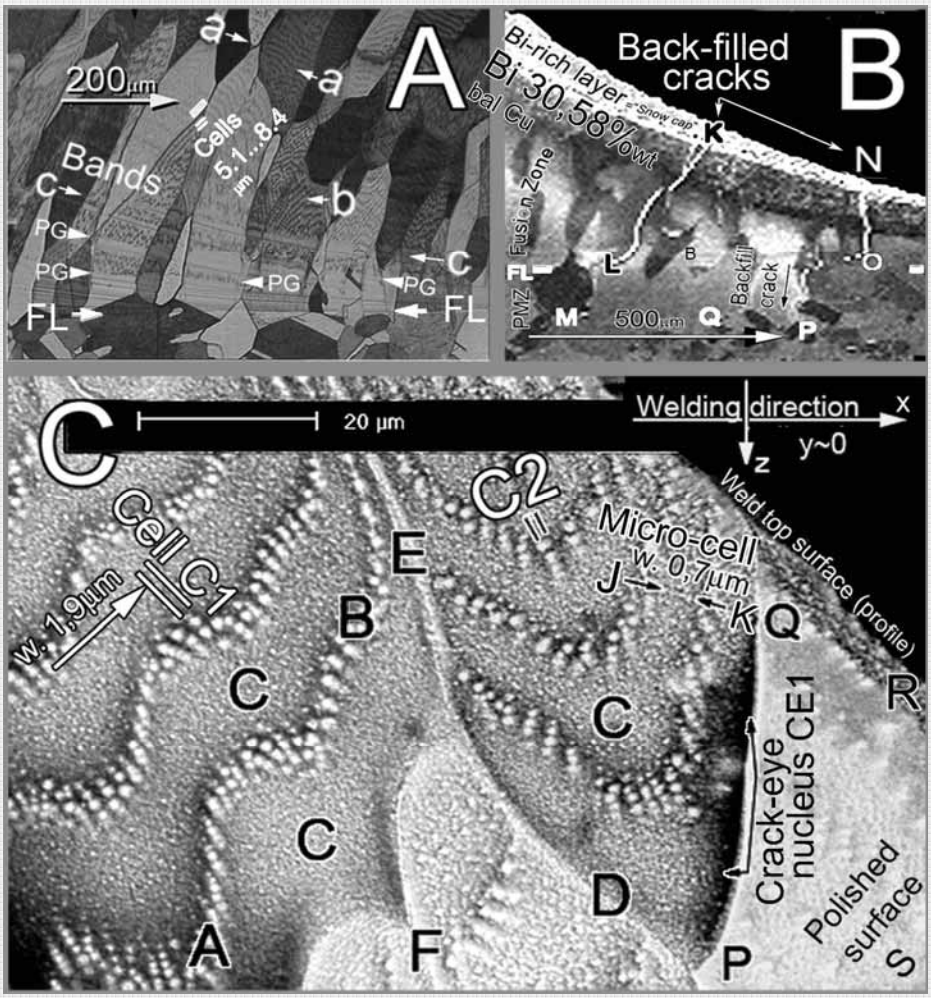

Fig. A22. xz-views along the Bi doped, 200cm/min weld centerline. Severely humped weld surface.

View A: Fusion line **FL**, *planar growth zone* upper limit **PG**, *bands* (planar inner structure) and *cells* clearly visible.

View B: Lines **K-L-M** and **N-O-P** show backfilled with 53.7%wt Bi grain boundary-cracks, extending far beyond **FL**. into the large grain zone of HAZ causing its cracking. (Bi-content was 30.6% in grain and 53.7 %wt at the back-filled GB). Kou 2003 [3 p. 325], Messler 1999 [4 p.508 and 566].

Both lines K-**L-M** and **N-O-P** appear cracked.

View C: (similar to Inserts A&B in Fig. A9). Area to the right of line **PQ** experienced the mechanical polishing. The area to the left of the line **PQ**, marked **C-C-C** is a deeper set S/L interface of a grain, which lagged a little behind its neighbors. By the time the **C-C-C** surface pushed its solute pileup to the weld centerline, its neighbors had already solidified and their contraction created tensile stresses, which tore open the molten areas **C-C-C,** forming a microscopic *hot crack.* We see this crack surface with the protruding from it tips of cells. Being below the surface **S** the crack survived the mechanical metallographic polishing, leaving the protruding cells standing. They (e.g. **C1** and **C2**) are ~1,5…3.5 µm wide in wiggly rows, (e.g. **A-B)** ~7…15 µm apart. The cells look different from the well organized hexagonal cells in e.g. Fig's 2.7b, 2.12c and 2.18b, but such wiggling occurs in copper (Appendix 8, Insert A: "Cell bundle").

The matrix surface **C-C-C** has *micro-cells* (as the ~0.7 µm wide ones pointed out by arrows **J**-**K**).

The lines **D-E**, **E-F** and **P-Q** are *grain boundaries* (GB). Left of **P-Q** there appears to be a ***crack-eye nucleus*** **CE1** (see Appendixes 16 and 34)**. P-Q** appears to be its *crack-eye lid.*

[CG5AL044InsertC_Mi2]

La dope enhances:
- etching of the fusion line
- growth of *cubelettes,* smothering cells
- solidification from *Case 3* to *Case 2*.
- backfill cracking in the PMZ

Appendixes 23…27: La-dope

Appendix 23. La 10 cm/min. Varestrain 5%, xy-view from top. C/L & 45 deg cracks

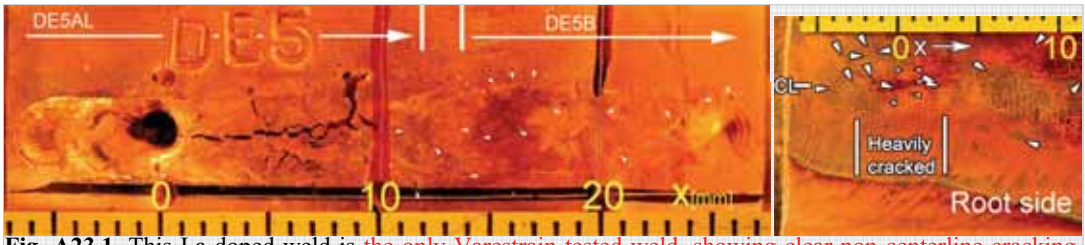

Fig. A23.1. This La-doped weld is the only Varestrain-tested weld, showing clear non-centerline cracking. La causes more arbitrarily oriented cracks than any other of the tested dopes. The cracks advance readily over the weld toe. White triangles point at chosen cracks. After the bend is finished the cracks become all but invisible. Lanthanum causes in copper treacherous cracks so evenly distributed that they probably relax stresses stopping the further opening of the crack. [De500_C10_Tx.jpg] [De501_C10_Tx.jpg]

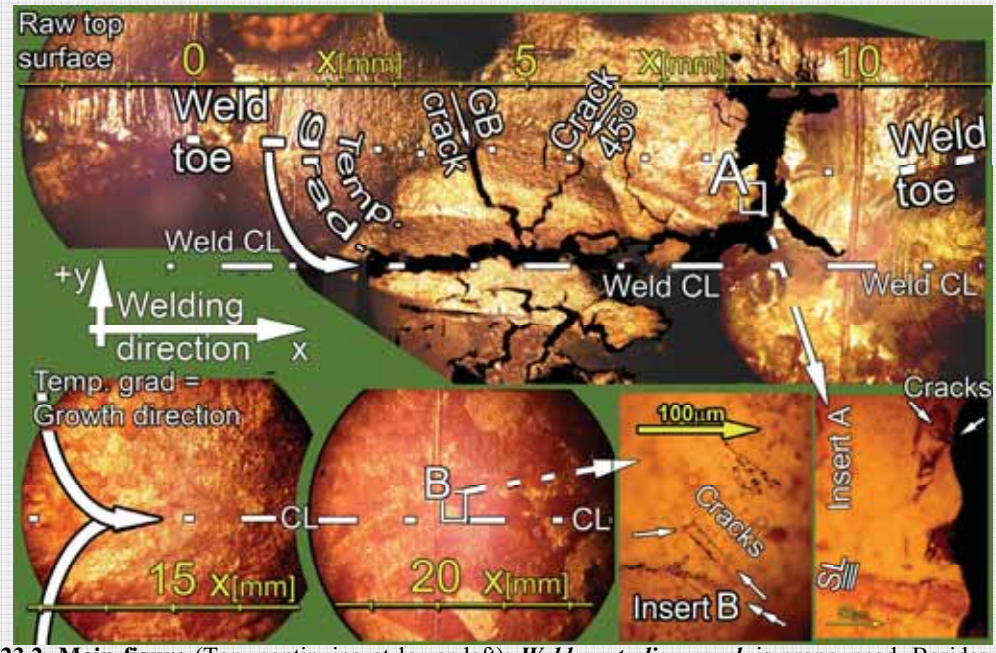

Fig. A23.2. Main figure (Top, continuing at lower left): ***Weld centerline crack*** is pronounced. Besides it there are cracks marked **GB crack,** and **Crack 45^0**.

GB cracks run ~ along grain growth (= **G**) direction. Note their crossing the **Weld toe** into base metal by backfilling mechanism.

Cross-jump cracks run from a GB-crack to another, uniting them, making zigzag cracks.

A fine 3-D mesh of criss-crossing micro cracks facilitates cracks zigzagging into the largest **τ**- resultant of 45^o to the principal stress. There are no metallurgically weaker constituents in this direction. (*Bands* run roughly in this direction, but we never once detected cracks associated to them.)

Out of the 14 dopes, La-dope was fifth worst in overall cracking (weld centerline- and transverse together), but most susceptible to transverse cracking. La differs from other dopes in this sense.

Insert A: The major crack surface is decorated with cracks with 90^0 angles between them. The weld top surface is rather undistorted and planar to the corner of the crack; marked plastic strain has not occurred. However, the surface shows several *slip lines* **SL**.

Insert B: The surface at the distance x=22 mm in this non-US radiated sample is similar to the 4MHz US radiated surface. No effect attributable to the radiation is noted. [DE5_S_Pan_x00yz_04x_01Pa2.jpg]

Appendix 24. La 10 cm/min, xz-view. Inverse segregation

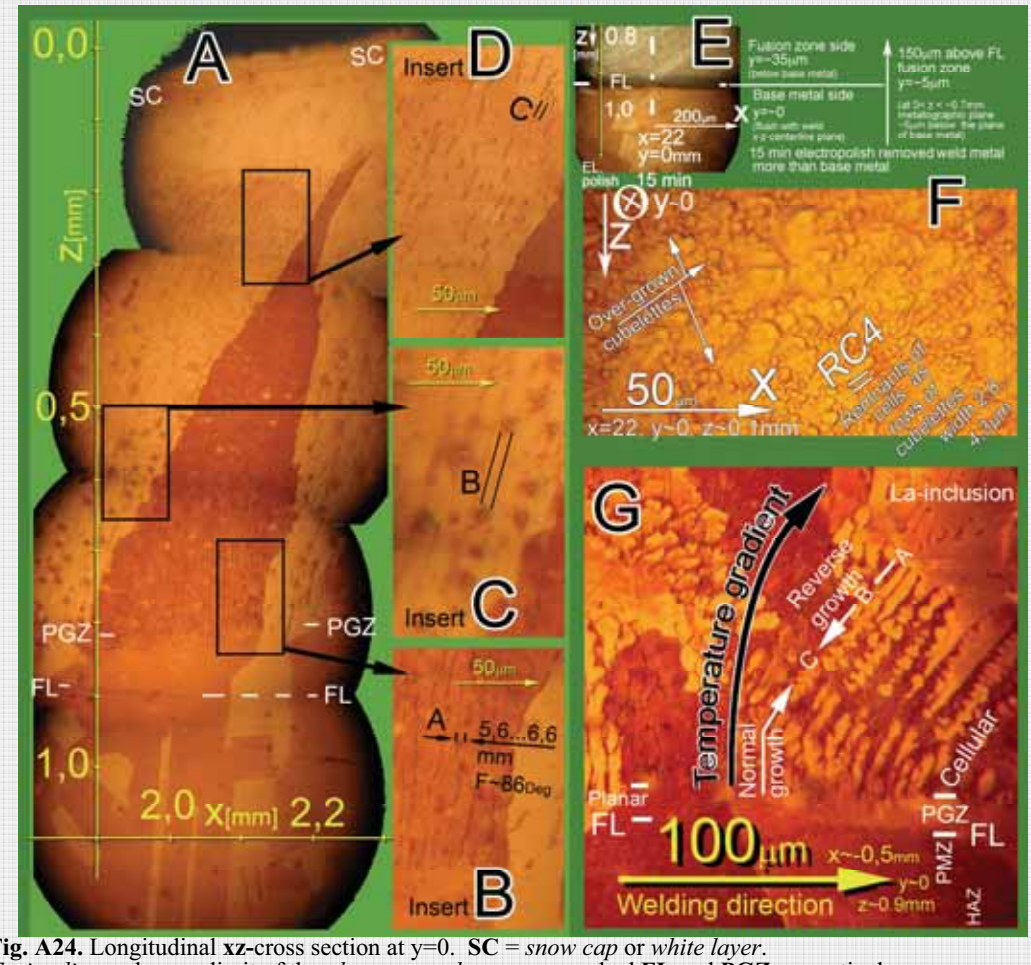

Fig. A24. Longitudinal **xz-**cross section at y=0. **SC** = *snow cap* or *white layer*.
Fusion line and upper limit of the *planar growth zone* are marked **FL** and **PGZ** respectively.
Inserts B and **C:** *Cells* are obvious. *Cubelettes* exist and especially in **Insert B** their width approaches and even exceeds the width of the *cells*.
Insert D: As the previous Inserts but *cubelette* size is small.

Inserts E&F Location x=22, y=0, z=100µm. The distance x=22 mm is beyond the Varestraint bend area; this sample is comparable with the R-test samples. This sample is the un-irradiated reference for the 4MHz ultrasonic irradiated sample.

Insert E: Fusion line at x=22, y=0, z=1mm.Typical to La-dope, the fusion line etches distinct. The valley formed next to **FL** on fusion zone side is ~35µm deep. The whole fusion zone is ~5 µm below base metal surface. We interpret this valley as the fusion line and marked it **FL**. However, it is not certain that nature would humor us by etching just the liquidus line of the **PMZ** so clearly.

Insert F: Location x=22, y=0, z=100µm.Pure copper forms cells at this speed limitedly, but La-dope all but extinguishes them totally. Cells manifest themselves only as *rows of cubelettes*, over-growth of which *smothered* the *cells*. Double line **RC4** points at remnants of a cell, width ~2.8…4.3µm.

Insert G. Location x= -0.5, y ~0. z ~0.9mm, dope-hole area, which is out of the normal test range. A lanthanum inclusion acts as a base for cells appearing to grow against the temperature gradient. At start, the cells beneath point **A** start growing *cellular*. Roughly at point **B** the cells become *columnar dendritic* (start growing side arms). Roughly at point **C** they meet the *cells* growing from *planar to* cellular line in normal direction. *Planar growth zone* is marked **PGZ** and the fusion line **FL**.

It seems that this is a sign of inverse segregation in welding (see Ch. 1.6)

[DE5AL_x02yz00_40x_02MiPaYh.jpg][] [DE5AL_x00M1yz00_40x_01MiTx.jpg]

Appendix 25. La 100 cm/min. R-test, xy-view from top. Micro-cracks. No detectable effect of US irradiation

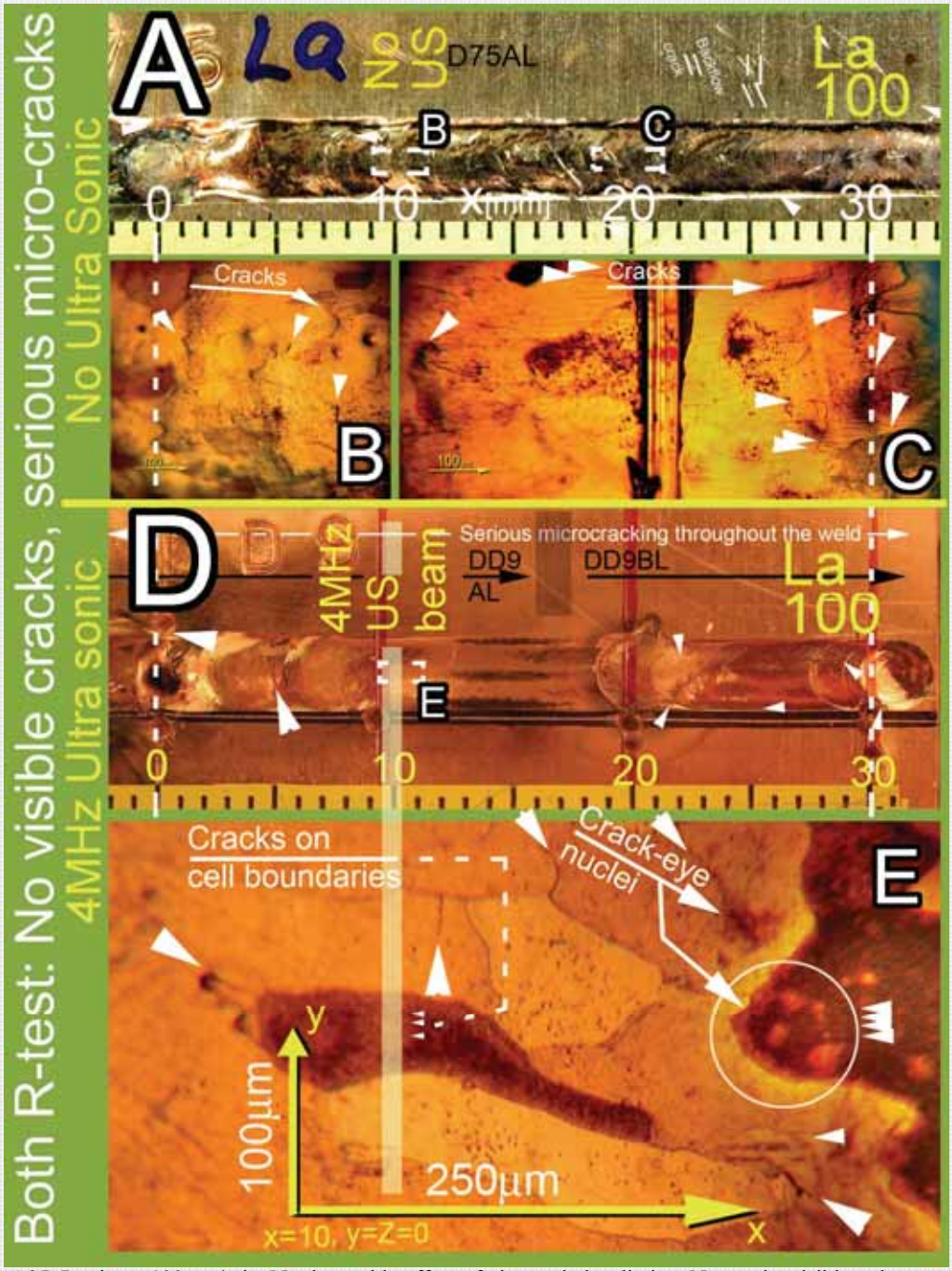

Fig. A25. La-dope, 100 cm/min. No detectable effect of ultrasonic irradiation. No cracks visible to bare eye. Microscope reveals serious micro-cracking. [D75_DSCN1047Tx2.jpg]

Appendix 26. La 100 cm/min. R-test, xz –view, x=3mm. Backfill cracks & cross-jump cracks, Micro-cells

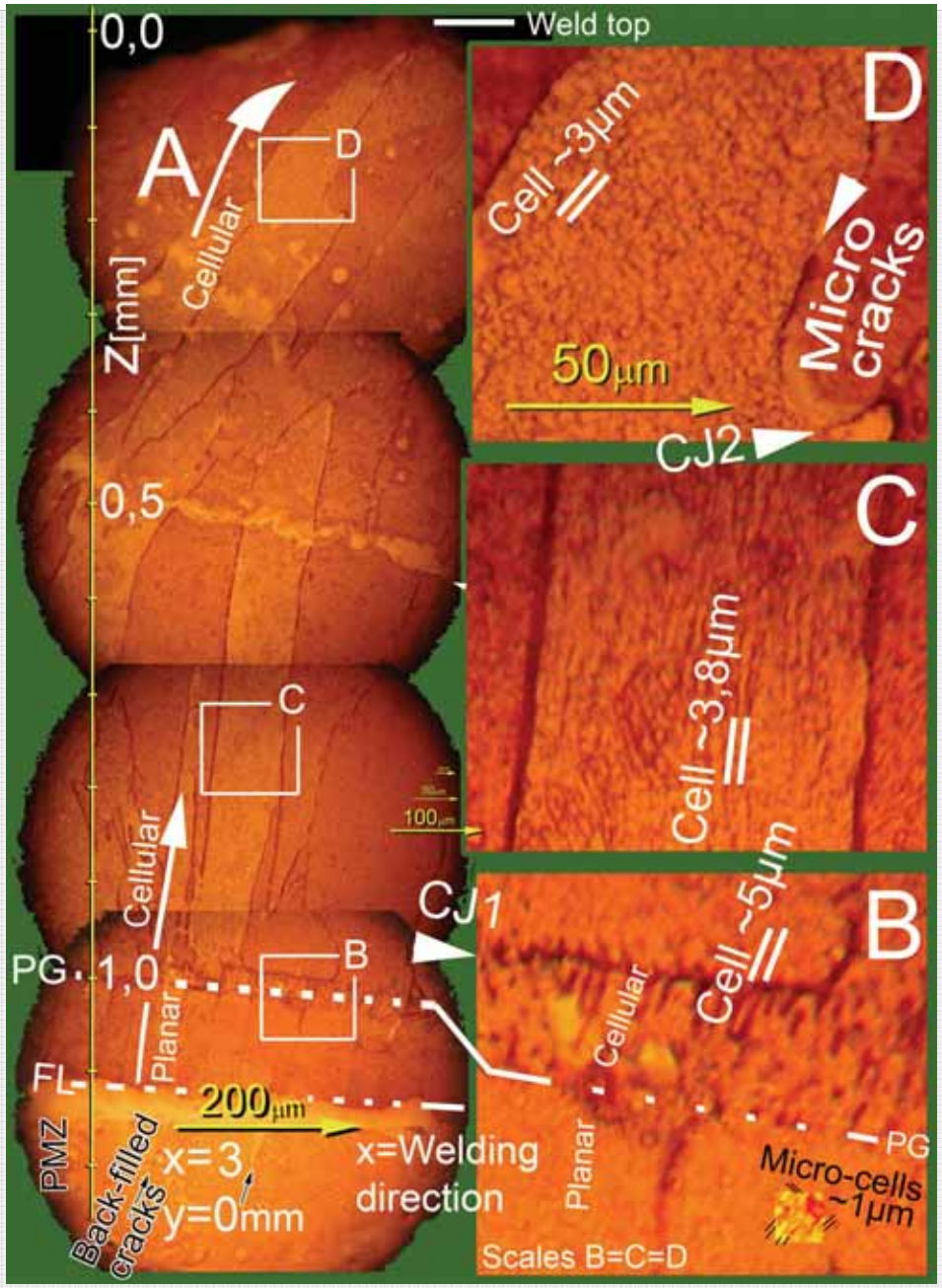

Fig. A26. La-dope, 100cm/min, x-z view at x=3. **Main figure A:** Fusion line **FL** is very distinct. Below it, *back-filled cracks* extend to **PMZ** and further.
From **FL** to **PG** growth was *planar*; structure is *micro cellular*, above it *cellular* to top.
Insert B: Upper line of planar growth zone **PG** divides *micro-cellular* and *cellular* zones. Suspicious and evidently cracked cell lines, including *cross-jump* type, the one marked **CJ1**.
Insert C: Distinctly *cellular* structure. Several cell lines obviously cracked.
Insert D: GB distinctly cracked. The crack **CJ2** runs roughly perpendicular to cell growth direction and is evidently a *cross-jump* crack. Cell width grows smaller and cubelettes grow clearer and more ordered towards the top. [D75AL_x03yz10_40x_08MiPa.jpg]

Appendix 27. La 100 cm/min. R-test xz-view, x=10. Comparison of Non-US vs. 4MHz US irradiation

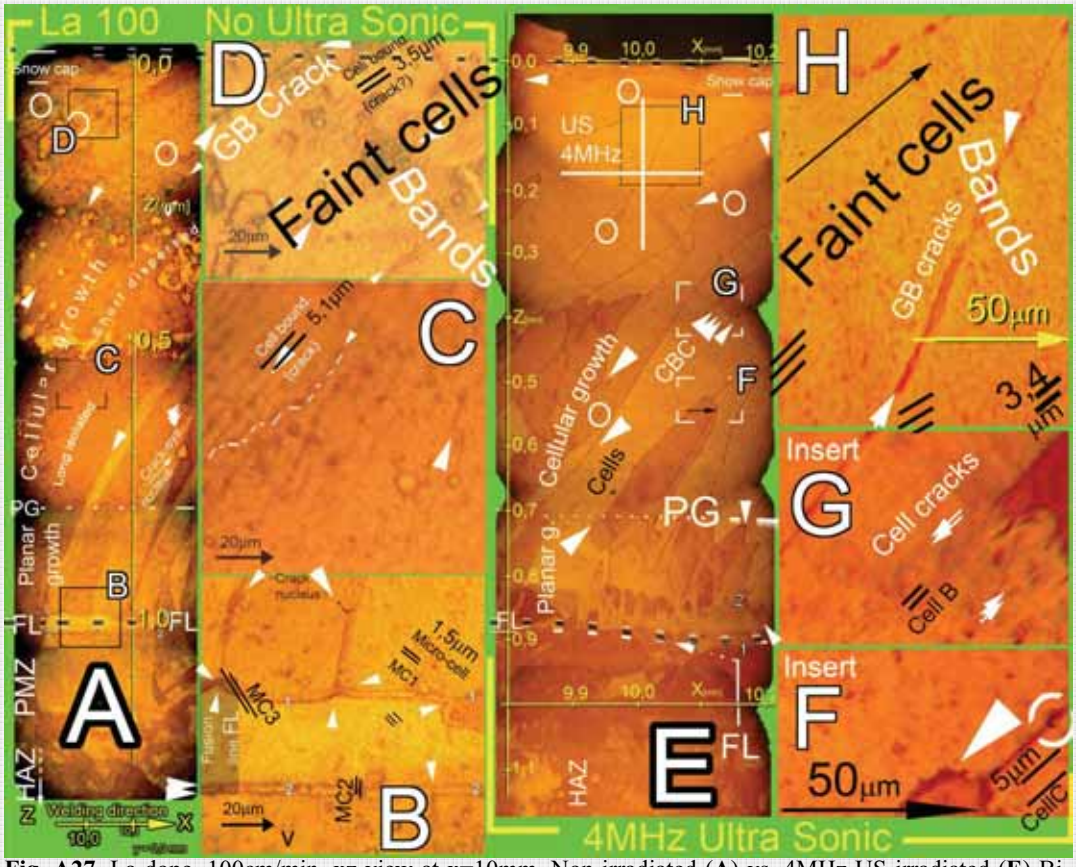

Fig. A27. La-dope, 100cm/min, xz-view at x=10mm. Non-irradiated (**A**) vs. 4MHz US irradiated (**E**) Bi-doped 100cm/min samples.

A: Non-US-irradiated. **FL** at z= ~1.0mm. Planar growth zone width (**FL-PG**) = ~200 µm. Cellular zone continues to the weld top. Cells turn faint towards the end. A ~50 µm wide *snow cap,* probably the final transient, is distinct. Some porosity is apparent.

B: Insert from FL-area reveals a line (marked **1…1**) above **FL**, similar to one Nelson, Lippold and Mills call *Type II Boundary* [23]. Actual **FL** is the one marked **2-2**. Micro-cells, width ~1.5µm visible.

C and D: (Inserts) Faint cellular structure associated with fine cell boundary cracks (white arrow heads)

E: 4MHzUS-irradiated. The structure is less porous, but reducing porosity was not detected in other irradiated samples. Otherwise the structures are similar.

F, G and H: (Inserts) Structures basically similar to the ones in non-irradiated.

Table: Cell width at different height z from top, and the location of planar growth zone top line Z_{PG}.

	Non-irradiated	4MHz irradiated
z [mm]	**Cell width [µm]**	**Cell width [µm]**
0.6	**5.1**	**5.0**
0.1	**3.5**	**3.4**
Loc. of PG	**z_{PG}=0.6 µm**	**z_{PG}=0.7 µm**

We cannot definitely state that there exist no differences – attributable to the irradiation – between the non-irradiated and the 4MHz ultrasonic irradiated samples. The differences between the microstructures fall in the range of scatter. To make a definite determination, the tests must be run with greater repeatability especially in the metallography. However, the measurable variables, cell width and height of the planar growth zone are equal within the measuring accuracy, ~15% (Table)

[D75AL_x10yzNoUS vs

Appendixes 28…31: Li-dope

Appendix 28. Li 10 cm/min, xy- and xz-views. Meshes of cracks with transverse cross-jump cracks

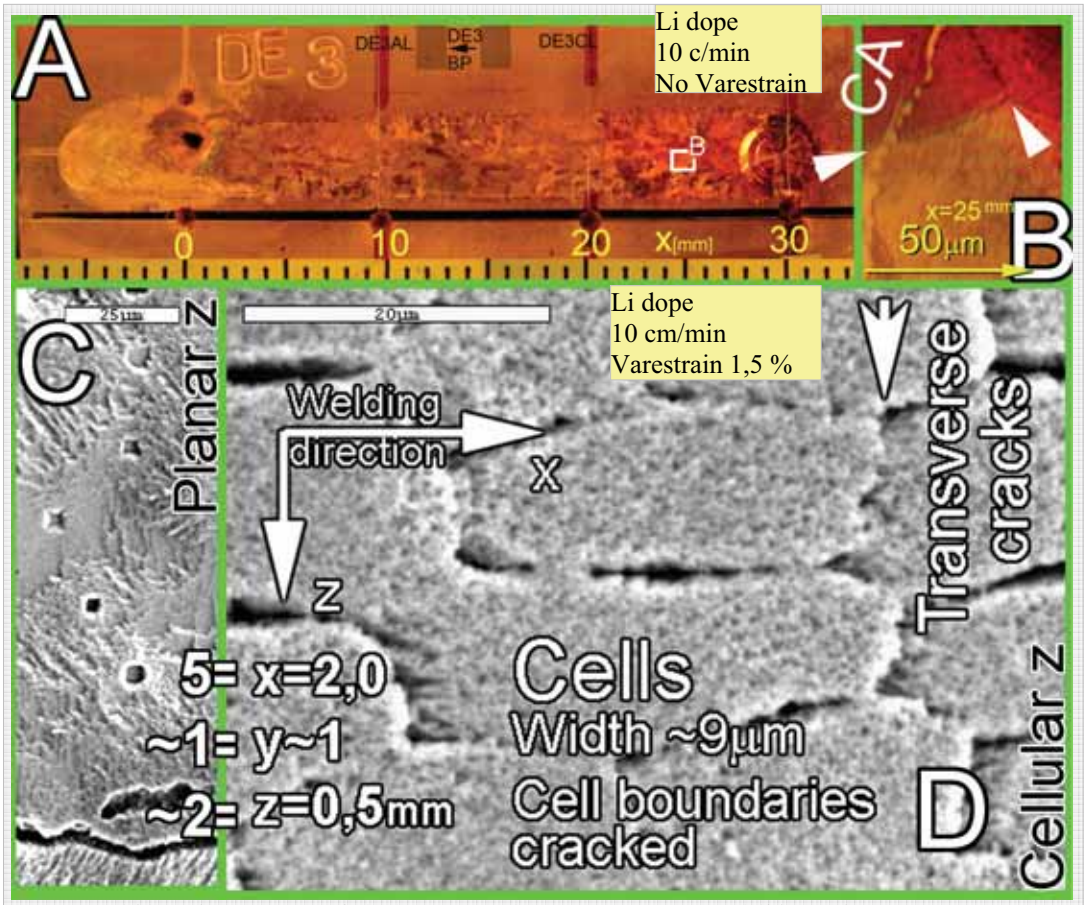

Fig. A28. Lithium dope, v=10 cm/min (no Varestrain). **A: Top view.** No visible cracks.

B: Top view detail: CA is a back-filled grain boundary (**GB**) crack. These seem intact but are brittle and micro crack easily. Li-induced back-filling is <u>not</u> beneficial; it creates a false illusion of a flawless surface.

Arrowheads point at two cracked **GB**'s. A suspected *spongy crack area* of intersecting perpendicular to one another micro cracks is in upper right corner (darker area).

C: Longitudinal xz SEM-view near fusion line at planar zone (**PZ**). A cracked GB, no finer cracks. PZ is not susceptible to spongy cracking.

D: The cellular zone. Cell boundaries (**CB**) are heavily micro-cracked. As serious cell boundary cracking was observed with other dopes (mainly Bi and Pb) as well, but only with welding speeds **v** ≥ 100 cm/min. We call cracks perpendicular to grain or cell growth direction <u>*cross jump cracks.*</u> Such an area, as in this insert D, where *cross jump cracks* intersect with CB cracks and make a 3-D mesh, we call a <u>*spongy crack area*</u>. These were common with other dopes as well, but Li was the only dope, with which spongy crack areas were detected with welding speed **v** < 100 cm/min

Cell surface is decorated with *micro-cells*. [De300_C10UX.jpg][E15AL_01Tx.jpg]

Appendix 29. Li 100 cm/min, xy-view. Cross-jump cracks and spongy areas

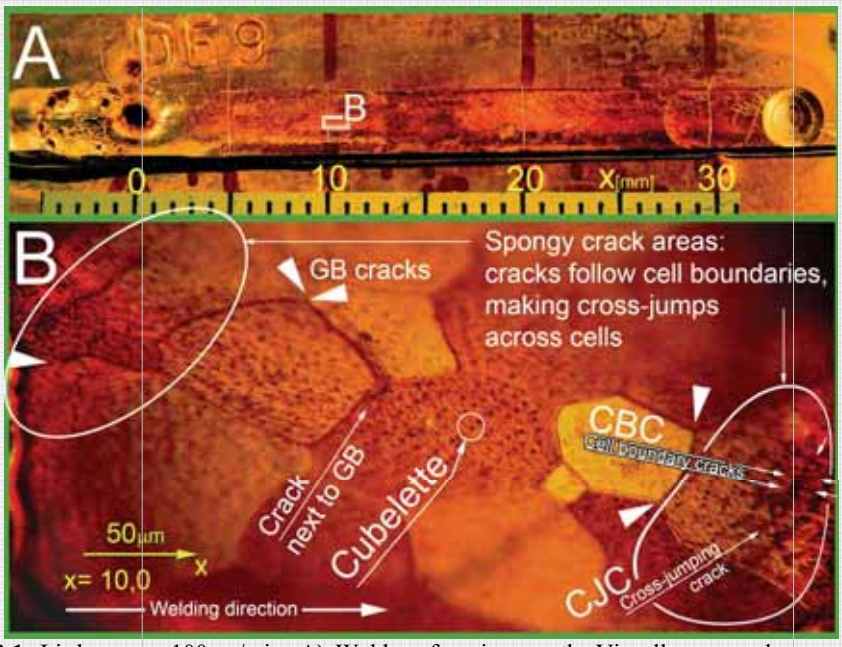

Fig. A29.1. Li-dope, v =100cm/min. **A)** Weld surface is smooth. Visually no cracks are observed (non-etched raw surface). **B)** Macroscopic inspection reveals grain boundary cracks and *spongy crack areas* (etched sample). [De900_C10Tx7.jpg]

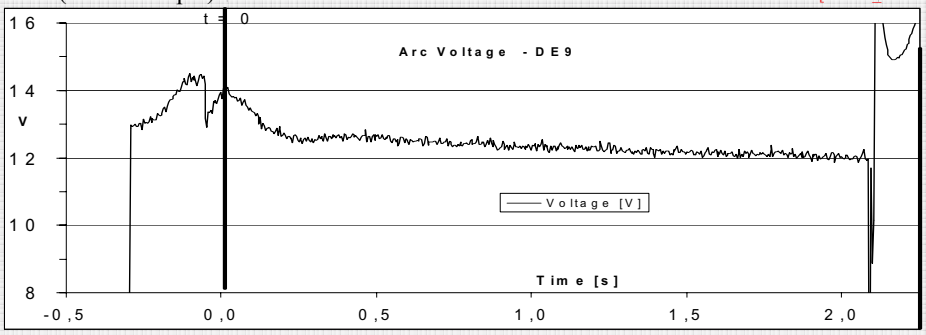

Fig. A29.2. Arc Voltage. Times 0.0 and 2.1 s correspond to x=0.0 mm and end crater respectively. [DE9.xls].

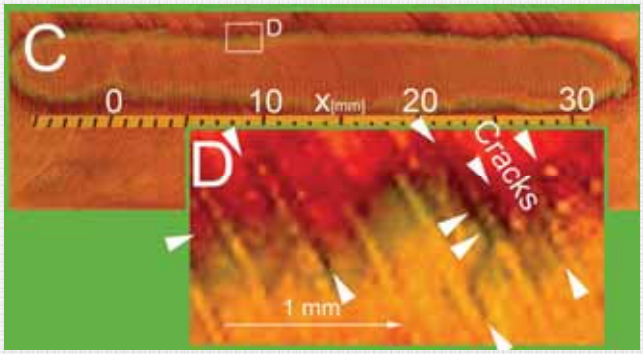

Fig. A29.3. Non-etched root side. **C)** and **D)** Cracks emerge through the ~ 2 mm base metal. Several micro-cracks in *spongy crack* manner (with perpendicular *cross-jump cracks*). The cracks follow machining grooves, albeit they have no metallurgical connection with the weld. NDT penetrant, sprayed on top surface, did not seep through the weld to the root side in a test extended to two months. [De901_C10Tx.jpg].

Appendix 30. Li-dope, 100 cm/min, xz-view. Cross-jump cracks.

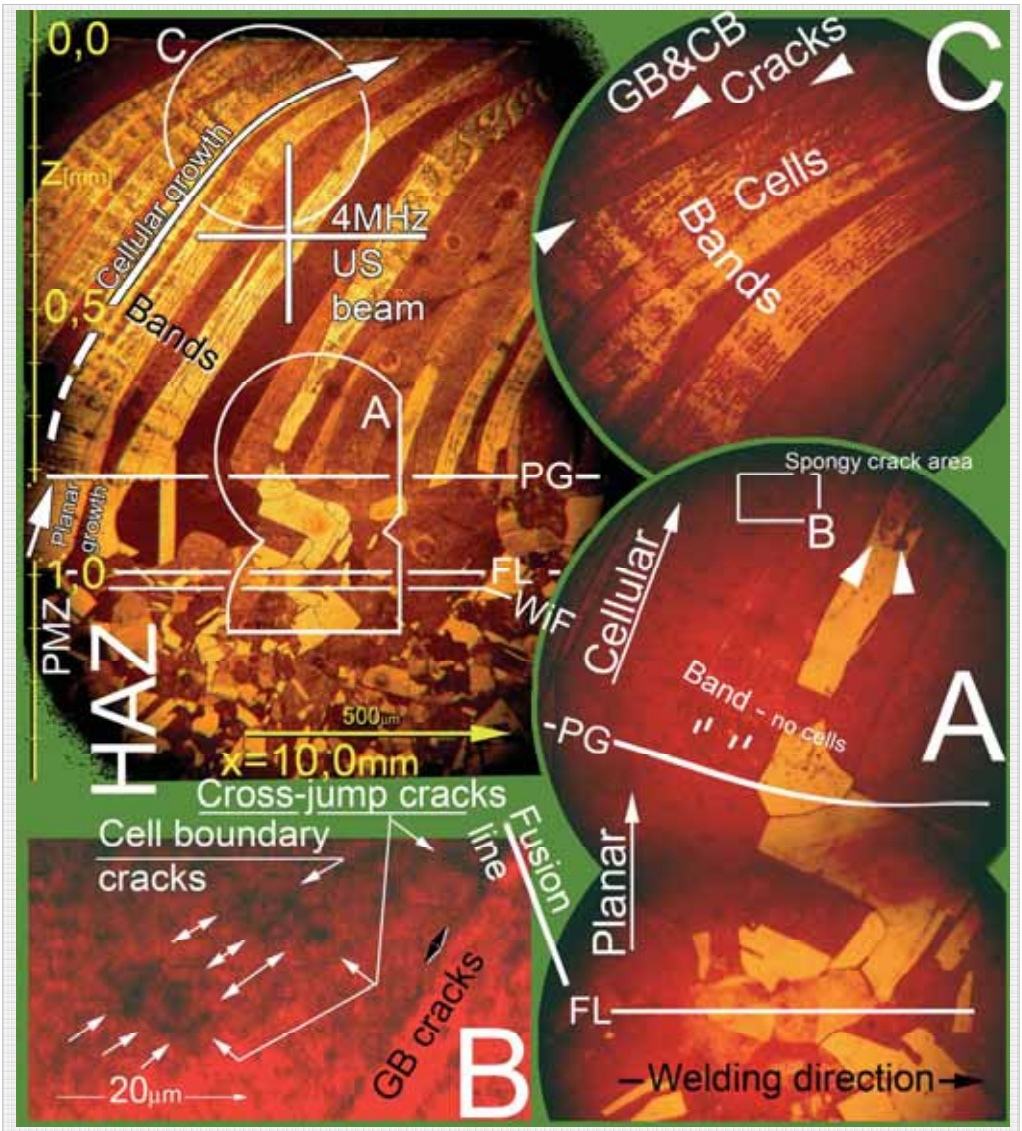

Fig. A30. Li-dope, 100cm/min, 4MHz US. **xz** cross section along weld centerline, **x** = 10mm, the location of the 4MHz US beam. No change attributable to US irradiation is detected in grain or cell morphology. Cell width at z=0.7 and 0.1mm is ~5.1 and ~3.3 µm respectively.

Main figure (top left) several short and intermittent micro-cracks are observed mostly associated with grain boundaries or their immediate vicinity.

WiF is the weld interface, **FL** the fusion line. **PG** is *upper line* of *planar growth zones*. After it grains adopt *cellular substructure.*

Insert A: Above and near **PG** the *cellular growth* is interrupted at location of the first or first two *bands*. The growth rate **G** is less at these locations bringing the solidification *case* from ***3*** towards ***2***-

Some *cell boundary spongy cracks* in circled area depicted in insert **B**.

Insert B: *C*ell *boundaries* are severely cracked and have etched intensely. Some *cross-jump cracks* (**C-JC**) run across the *cells*. There is a distinct period (~ 20 µm) between these **C-JC**'s. This period is of same order of magnitude as *cell-band width*. Marked **GB cracks** appear intermittently with roughly same period.

Insert C: Marked with white triangles **GB&CB cracks** refer to grain boundary- and cell boundary cracks existing also near weld top. [DE9AL_x10yz00_16x_07MiPa.jpg].

Appendix 31. Li 100 cm/min, xz-view. G/R analysis, spongy crack area

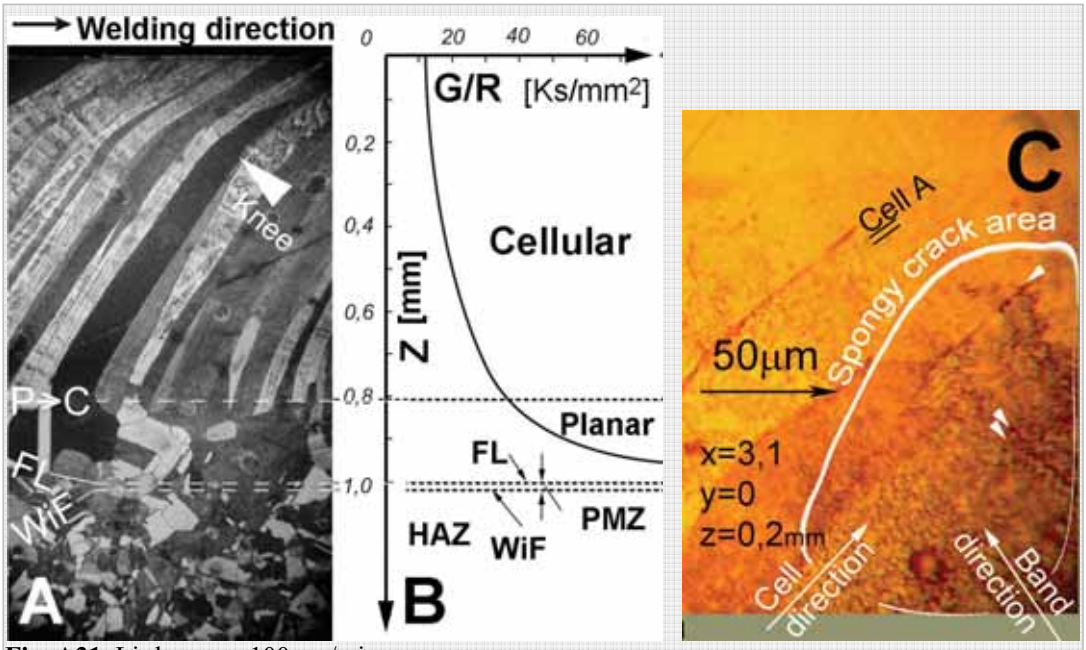

Fig. A31. Li-dope, **v** =100 cm/min.

A) Microstructure, weld interface **WiF**, fusion line **FL** and Planar to cellular transition **P → C** are distinct. No cracks detected visually. No signs of **EQZ** detected (see Fig. 1.21).

B) G/R-z- analysis (see Chapters 2.13.2 and **1.3**). The location of is **FL** estimated and the **PMZ** width (~20 µm) is given by the **G/R-z**-analysis. (R-tested sample)

C) Li-dope causes finely dispersed mesh of cracks in the *spongy crack area*.
(**t**= 3mm, **v**=100cm/min, **U**=12.5 ± 0.4V) [Kar_Paper1_DE9AL_16xF.jpg][DD5AL_x03yz00_40x_03MirPap.jpg]

Appendixes 32…33: P-dope

P-doped welds reveal transformation from clearly visible centerline cracking to microscopic cracking in ambiguous (mostly grain- and cell boundary) directions. This transformation happens with increasing welding speed from 5 to 200 cm/min. ~ 0 cm/min speed at end crater lead to radial micro-cracking

Appendix 32. P-dope with 0 and 5 cm/min, xy-view: *Centerline* & *cell boundary* cracks, xz-view: globules, pronounced *snow cap* and *fusion line*

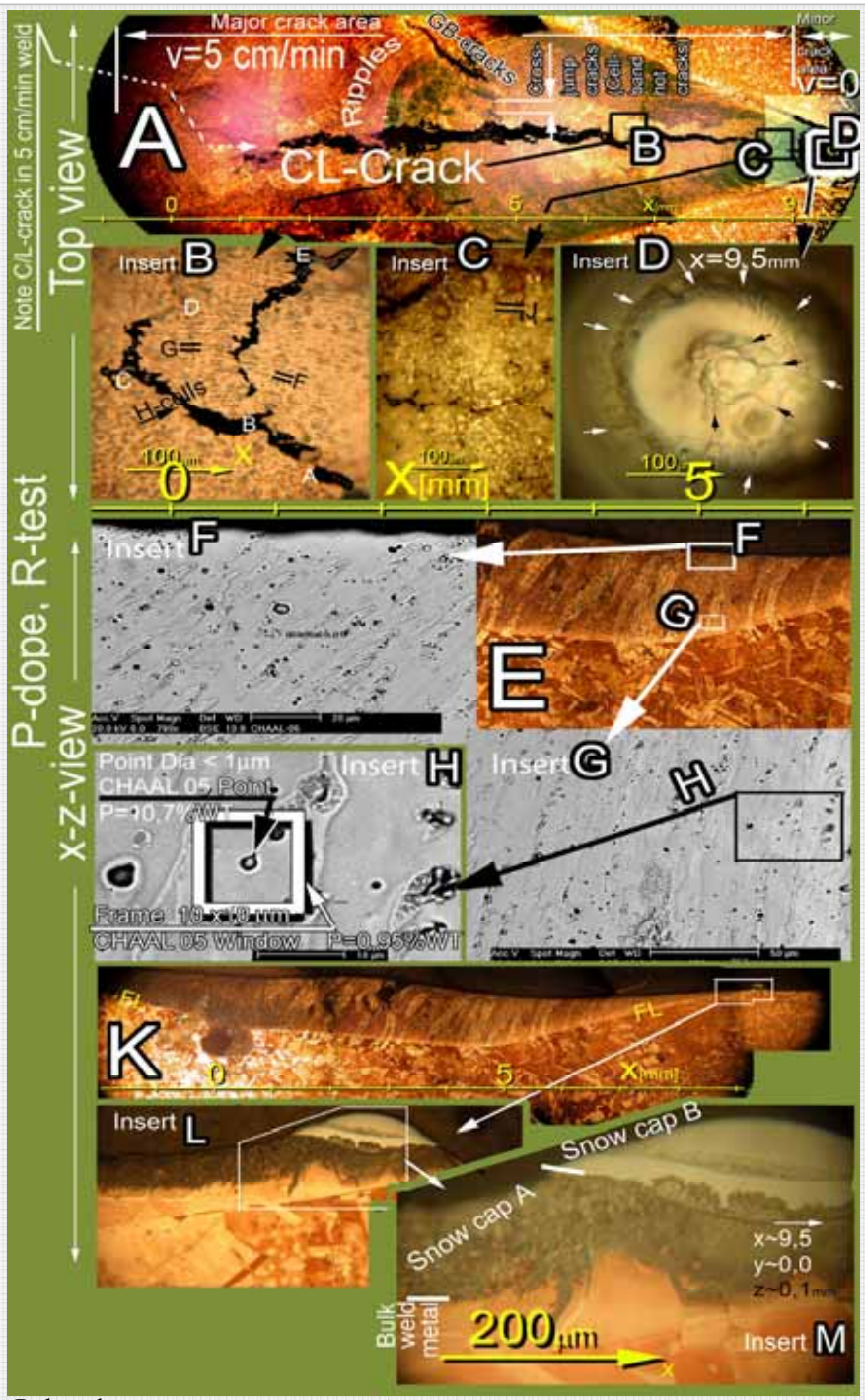

Fig. A32. P-doped. **Welding regime:** v = 5 cm/min till x = 9.5 mm, where the torch movement is stopped for 2 s. **View A:** A centerline crack at 1 < x < 9.1 mm. **Inserts B** and **C:** Details**. Insert D:** The C/L crack is back-filled at the end crater, which does have fine radial cracks. **View E: xz-cross section at y=0.** Distinct fusion line**. Insert H:** chemical analysis of a *globule* and 10x10µm area. **View K and its Inserts L & M:** Distinct *snow caps* at x~9 mm from P-dope transport from x=0. Distinct fusion line. [CHA_S_x0yz_04x_01MiPaALN.jpg]

Appendix 33. P-dope, 10, 100 and 200 cm/min, xy-view from top. Lacking centerline micro cracks at v ≥ 10 cm/min

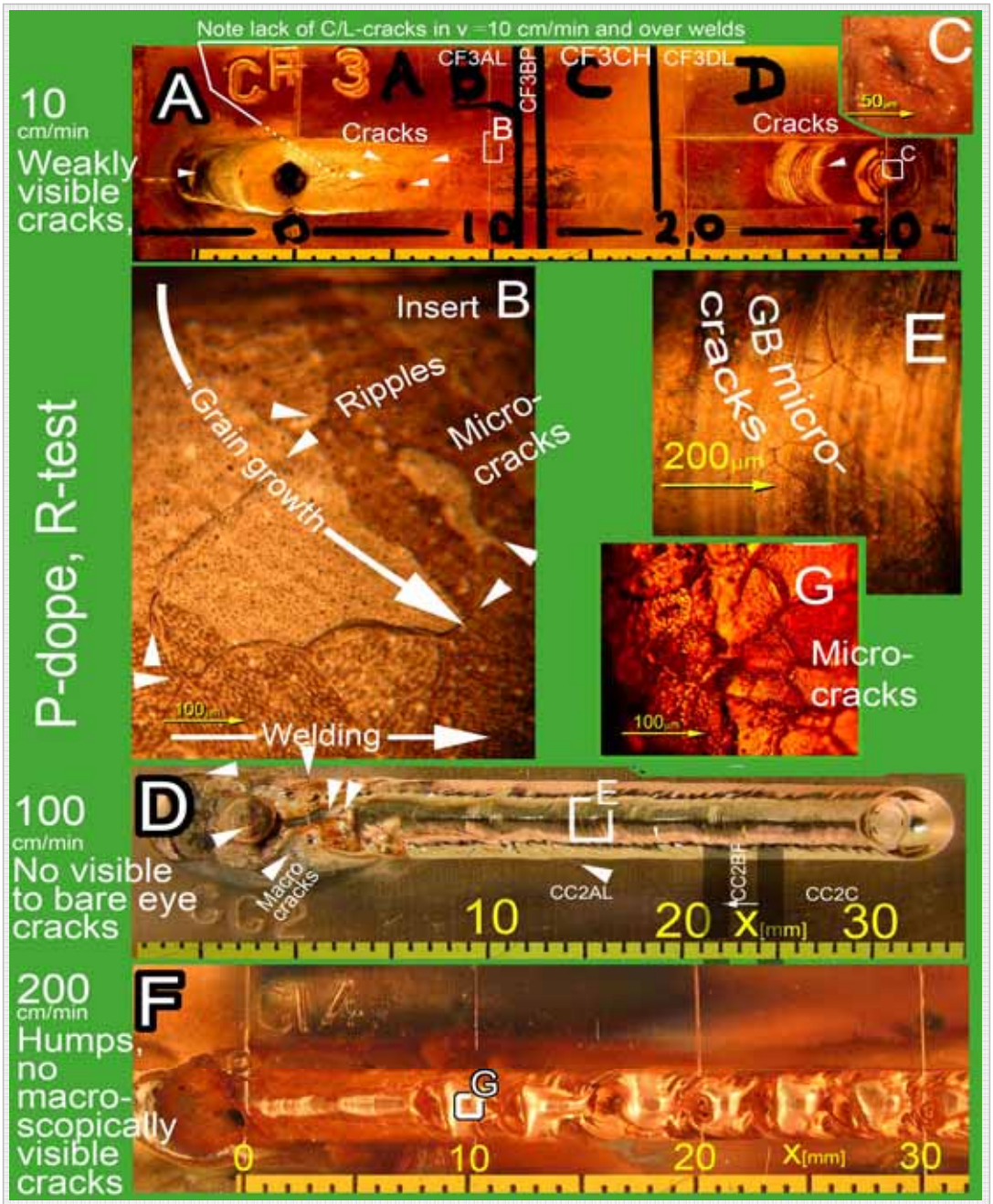

Fig. A 33. P-dope welds, top view, R-test. **A:** 10 cm/min, cracks, visible to bare eye, **D:** 100 cm/min. only macroscopically visible cracks, and **F:** 200 cm/min, no macroscopically detectable cracks. Compare with the 5 cm/min weld, with distinct centerline cracking in Fig. A32A; the cracks in the 10 cm/min weld are less severe. In the 100 and 200 cm/min welds, visible cracks disappear. Microscope reveals micro-cracks in various directions (inserts **B**, **G** and **E**).

*Evidently, a slow **v** causes blunt cells "bulldozing" solute to the C/L, while a fast **v** induces sharp-tipped cells/dendrites "fencing-in" the solute to the cell/ dendrite lines, thus distributing it evenly across the fusion zone, diminishing the propensity to C/L cracking and probably to hot cracking in general.* [CF3_ixVer4.jpg]

Appendixes 34…35 Pb-dope

Appendix 34. Pb 10 cm/min, xy- & xz-cracks. Back-filling & crack-eyes

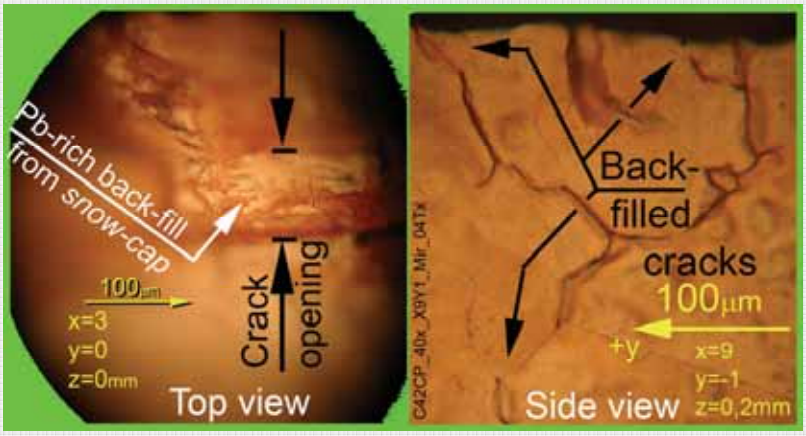

Fig. A34.1 Pb dope was as crack-prone as Bi dope (Fig. A15.2) and was as keen to back-filling of cracks (Appendix 22B). View of raw surface (left) and perpendicular weld cross section (right, welding direction away from viewer) of crack back-filling.

Top view: View of raw surface, crack is *back-filled* from the weld pool. The back-fill is brittle (crack above word "opening").

Side view: *Back-fills* fill the cracks only partially; they may cover cracks at surface and leave the inside open. Bi-dope does the same¸ the back-fill is in these cases not beneficial, it may hamper the crack detection. [D21_S_x03yz_40x_08TxCo.jpg]

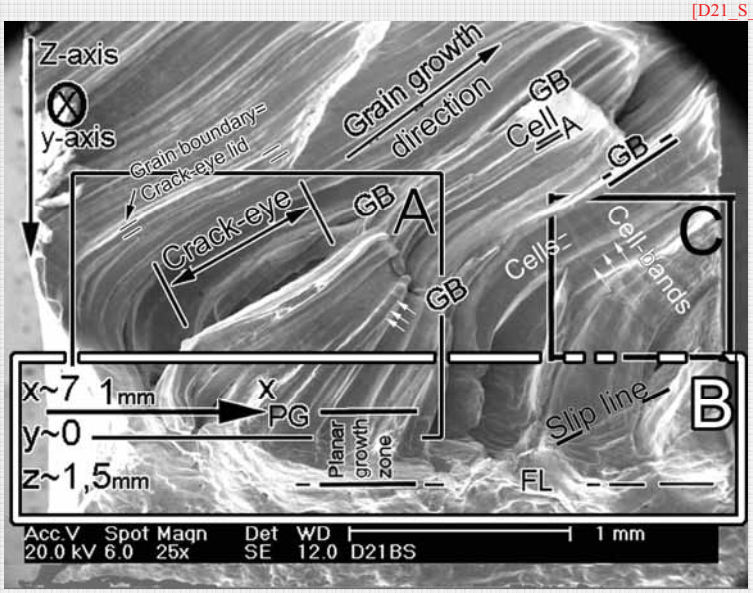

.

Fig. A34.2. Centerline hot crack surface. General view, analysis of details **A**, **B** and **C** not presented here.

Frame A: *Crack-eye* and *crack-eye lid*, (see Appendix 16).

Frame B: Fusion line (**FL**) area with *planar to cellular* transformation at line **PG**. The lines in the planar growth zone **PGZ** on the right were identified and marked *slip lines*.

Frame C: *Cell-bands* running perpendicular to *cells* are marked with white triple arrows. Frame A has such marked slip-lines. [D21BSTx3Top2.jpg]

Appendix 35. Pb 100 cm/min, xz-view. Distinct FL, cells and bands

Longitudinal cross section illustrates best the growth from fusion line **FL** to the end of solidification in bead-on-plate welds. Fig. 1 present such a view with a distinct line we interpret as **FL**, (similar interpretations are in Dig's 1.14…1.20). Bands are also distinct; in Cu the distinct **FL** occurs often with distinct bands.

Grains grow with **EGS** (see Ch. 1.1.20); the white triangles point at knees, formed at change from one **EGD** to another.

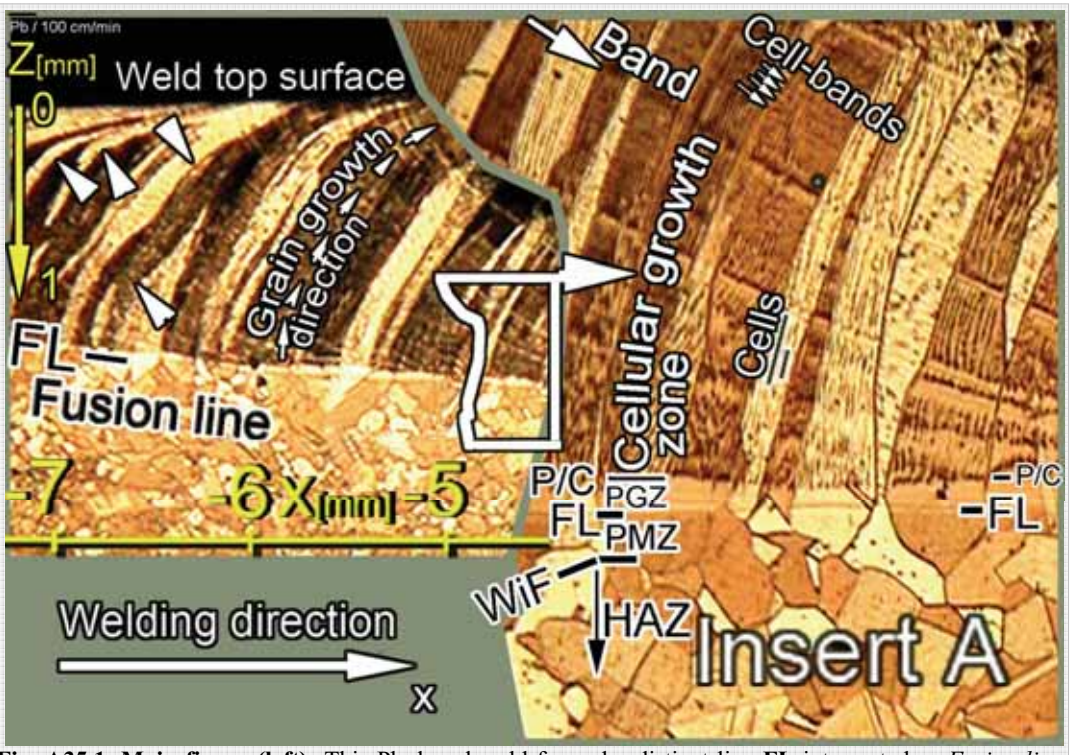

Fig. A35.1. Main figure (left): This Pb-doped weld formed a distinct line **FL** interpreted as *Fusion line*. Above **Fl** is the Planar Growth Zone **PGZ**, and after it the *Cellular Growth Zone*, continuing up to the weld top surface. **Insert A:** Below **FL** there is the *Partially Melted Zone* **PMZ**, and **HAZ.** The line between them, the *weld interface* **WiF** is practically non-determinable with light metallography.
Bands with planar inner structure are readily visible. Finer pitched *Cell Bands* are also detectable.

[C22BL0_PanorSEM4.jpg].

Appendix 35 p.2: (A & B) Cell *smothering,* (C) Revealing of fusion line

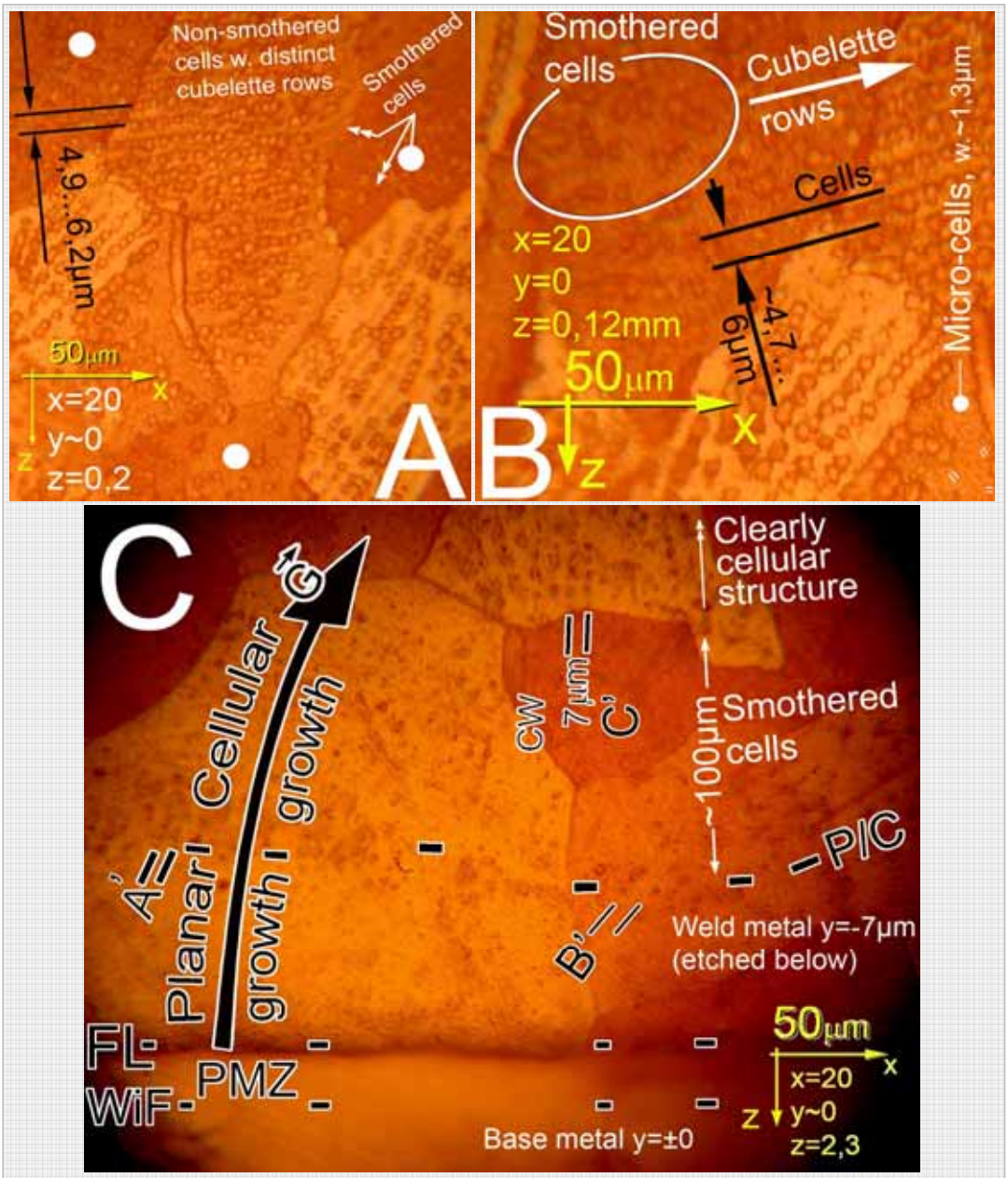

Fig. A35.2. Longitudinal cross section along the weld C/L. Pb-dope, 100 cm/min. **A and B:** View near the weld top. Some grains have their inner structure blurred due to *cell smothering.*

C: View near the weld interface **WiF** and fusion line **FL**. Solidification starts with planar growth. Planar-to-Cellular transition occurs at line **P/C**, that is: at a distance ~ 70…100µm above **FL**. At a ~ 100 µm wide zone at start, the cellular structure is blurred and only localized cells at **A'**, **B'** and **C'** are seen. This is probably due to *cell smothering* by growth of *cubelettes* over the lines of the cells they are lined-up in.

The level of the weld metal surface, located above the line **FL**, is 7µm below the level of the base metal in **y**-direction. This is apparently due to electrolytic polishing 1,72V / 30min (increased to three times the normal to reveal the **FL**). La-, P- and Pb-doping revealed the **FL** best in this manner. The mechanism may be associated with enhanced stress-corrosion of Cu with these dopes. The outlook of the **FL** differs from the **FL**'s revealed in Fig's 1.17, 1.19 and 1.20 to the extent that the mechanisms probably are different.

[D54CL_x20y0z_40x_02Mir_Txt2.jpg][D54CL_x20y0z_40x_02MirWOHZ.jpg][D54CL_x20y0z23_40x_03Mir_Txt.jpg]

Appendix 35 p.3: Comparison of 200 and 10 cm/min welds. Pb-dope

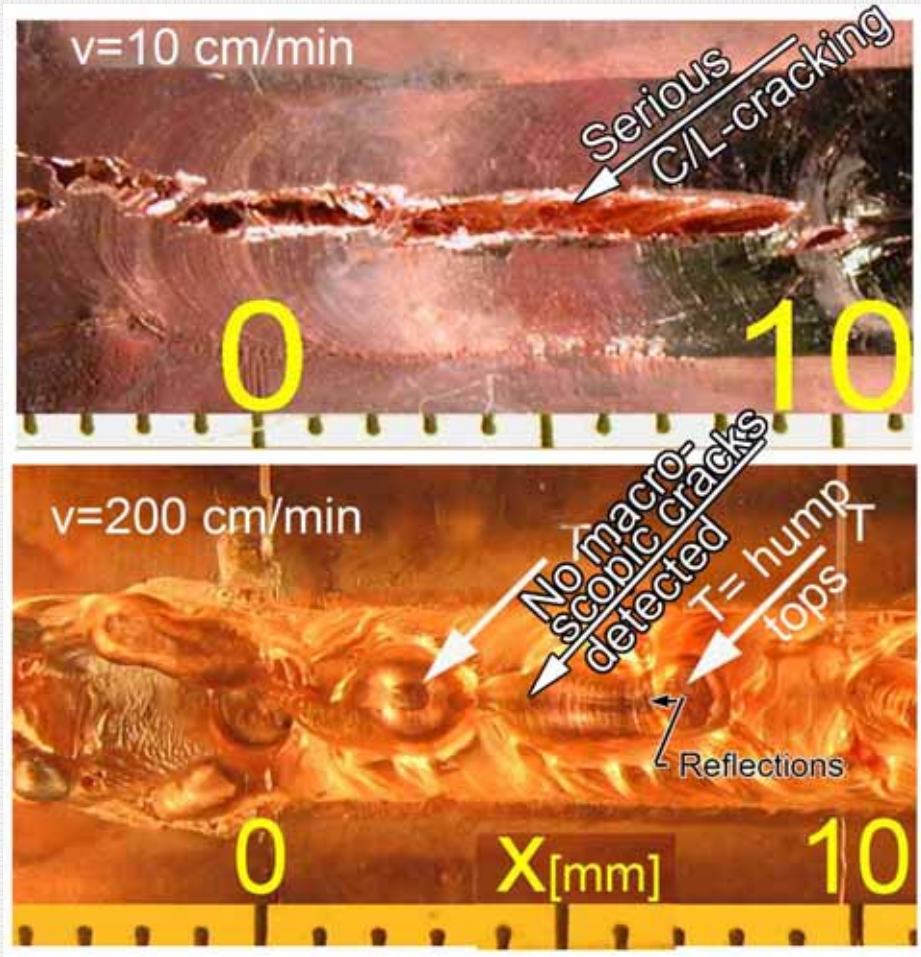

Fig. A35.3. Comparison of 10 cm/min and 200 cm/min welds. The former has a severe C/L-crack, while in the latter; no visible or macroscopic cracks were detected.

The surface of the 200 cm/min weld is severely *humped.* The darker/lighter areas near the hump tops are reflections.

Microscopy of the 200cm/min Pb-doped samples revealed a very faint tendency to spongy crack areas. (Fig. Ci3_28ATx.jpg, not presented).

It is possible that the contours in the spongy crack areas, interpreted as cracks, are in fact indentations formed by the metallographic polishing and etching process. Distinguishing in copper a deeply corroded cell boundary from a fine micro-crack with an optical microscope is difficult. A scanning electron microscope (SEM) gives more reliable results (as in Fig. A28C), but not all samples were examined with SEM. It is possible that in some hot cracking ceased completely in our tests with high welding velocities **v** ≥ 100cm/min. This area should be studied more extensively. [D21_dscn0959_C60Tx2.jpg]

Appendix 36. Ambiguities in the definitions of some central concepts

One of the basic findings of the historic review in this dissertation is the notion of differences - some of which may cause confusion - in nomenclatures.

The concept of *Cases* is an example of the above mentioned differences. It is used among several American weld solidification researchers but seems non-existent in Europe and Japan.

The definitions of the basic metallurgical lines of a weld contain ambiguities. We base on Messler 1999 [4], and name the weld pool solidus[24] *weld interface*, shortening it **WiF** (Fig's A below and 1.15). There are – however – other definitions for *weld interface*, as seen in Fig. A36B.

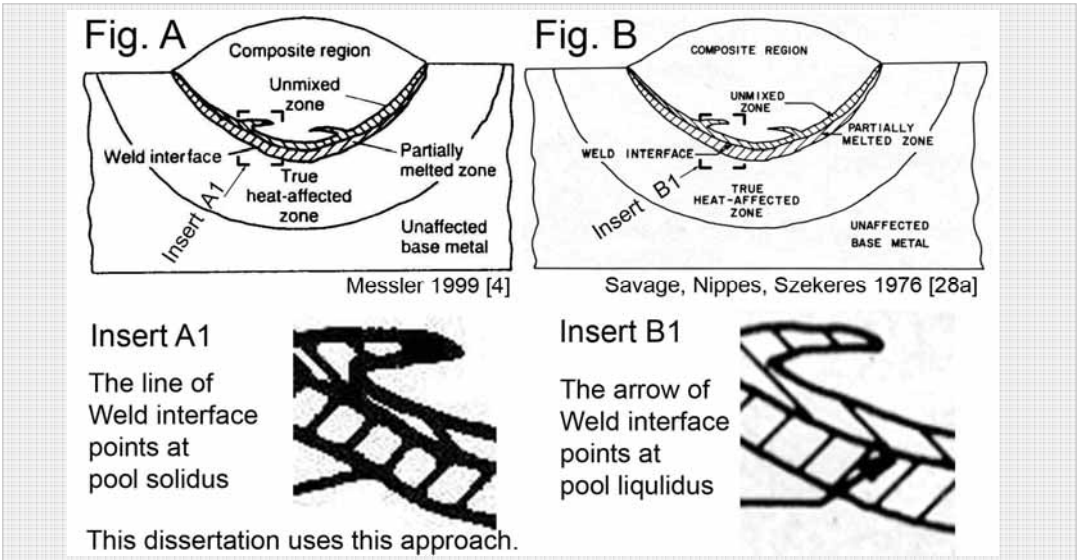

Fig. A36. The lines bordering the weld pool of a metal alloy.
In **Insert A,**. the *Weld interface* is the weld pool solidus.
In **Insert B,** the *Weld interface* is the pool liquidus.
We abide by the newer definition in Fig. A., valid, but this may conflict wit other texts.

For the weld pool liquidus we use the term "*fusion line*", in short **FL** according to Kou [3 p. 180 Fig. 7.12, our Fig. 5.12]; this term is widely used and less prone to conflicts.

Liquation and **liquation cracking** are problematic terms; we avoided them according to Kou, proposing to reserve this term for use in association with constitutional liquation [4 p.509]. We used the term back filling, which could be beneficiary *beneficial* or *adversary* (in more detail in Ch. 1.1.28). This may be conflict with other texts, e.g. [11 Ch. 6.5.3].

[24] and its trace in the longitudinal section of the solidified weld

Appendix 37. The dismissal of the cellular dendritic growth

One nomenclatural change noted in our historical review was the dismissal of the cellular dendritic growth mode. Of the leading weld research institutes, Ohio State University was the last to do this.

2. From five to four solidification modes

In 1998 *OSU* presented the weld solidification modes as in **Fig. A371**, in 2000 as in **Fig. A37.2**. The *Columnar Dendritic Growth* in the former is the proposed by Savage structure. In the latter, the *columnar dendritic growth* is as in the *present mainstream nomenclature* (Fig. 1.45).

3. Nomenclatural ambiguity

It may be that the evidence Savage presented with Fig. 2.23 is insufficient to justify the claim of existence of an entire grain turning dendritic. It does – however – cause nomenclatural clash between the present mainstream research and the older RPI-research.

The nomenclatural ambiguity extends to Chalmers' Principles of Solidification, which first gave the name "cellular dendrites" for what we now call "columnar dendrites", Fig. 1.8B [13 p. 164].

4. The present mainstream nomenclature

The modern nomenclature, into which the *OSU* changed in 2000, was detected by us first in the 1987 edition of Kou [3]. Kurz & Fisher [5] use it (Fig. 5.1C), as does Messler [4]. Thus it may well be called the *present mainstream nomenclature (of solidification growth modes)*.

The first time we detected the term *columnar dendritic* in Savage et al. [31][21][34], with Savage referring to Tiller and Rutter 1956 [75], which – however - does not contain that very term. Therefore, according to this information, the father of the term *columnar dendritic* was W.F Savage and his brain-child[25] lives in the present mainstream usage – slightly in a different usage than originally intended.

Fig. 1.8 presents a proliferation of dendrite morphologies; it may be wise to simplify the general growth mode classification and handle the different dendrite morphologies case by case. For consistency, the cells could be named columnar cells, as "cell" refers also to the product of recovery in metallurgy.

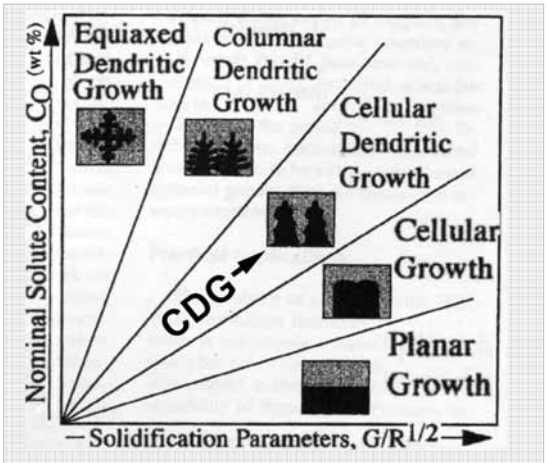

Fig.A37.1 The five weld solidification modes used in Ohio State University. *Gutierrez, Lippold 1998 [112]* The "Savage classification" *1980 [12]* with the difference of "CDG" (added by us) showing poorly developed dendrite arms.

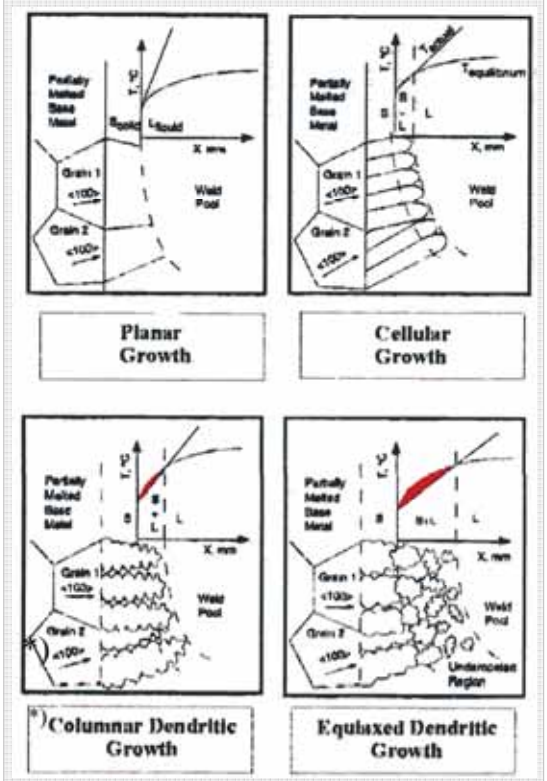

Fig. A37.2. The four solidification modes of a metal alloy used in Ohio State University after the year 2000. *Kostrivas, Lippold 2000 [33] based on Kou 1987 Figure 8.1 [3] First edition.* "**The present mainstream classification**"

[25] Savage's text [31] contains five references, three first of which were not available for us. There is a possibility that S the term *columnar dendrite* derives from one of them.

Appendix 38. The Melting/Solidification- (M/S-) model

The model has been designed as a joint project between the author in Lappeenranta University of Technology and the St. Petersburg State Polytechnic University Professor V.A. Karkhin and his assistant P.N. Homich.

1 Introduction

The *M/S-model* calculates the solute distribution along the longitudinal x-axis across and near the *weld interface* **WiF**[26] . It takes into account **(i)** not only the solidification- but also the melting stage, in other words the pre-solidification (melting stage-induced-) solute redistribution in the base metal as well as in the pool, **(ii)** the post-solidification solid back-diffusion during the cooling of the base and the weld metals, **(iii)** the – typical to a fusion weld – growth rate acceleration from $R = 0$ at the **WiF** to the welding speed v at the weld centerline. Additionally, the principal welding parameters and the –depending from them - weld pool form and size are calculated and taken into account. Further, the temperature dependency of the solute solubilities and the diffusion coefficients in both solid and liquid are accounted for.

The mass-transfer regime of the *M/S-model* is the *Case 3* solidification with allowance to the thermo-metallurgical "Sub-Case Variables" (**SCV**'s) **(i), (ii)** and **(iii)** defined above, the effect of which diminishes rapidly as the S/L-interface recedes from the WiF. This process makes the *M/S-model* continuously to approach pure *Case 3-model*, and the solidification continuum is guaranteed for that solidification regime.

The concentration-calculation for the M/S-model the across the S/L-interface is problematic for **(a)** there is a discontinuity in the concentration at the solid/liquid interface and **(b)** the **WiF** region is located in the initial transient, where the diffusion is non-stationary. The former problem is dodged by replacing the concentration C with the mass transfer potential, which yields uninterrupted solute profiles across the S/L-interface.

The method accepts weld metals with chemistry different from that of the base metal. (The model is prepared for mass transfer induced by formation or disintegration of chemical compounds, albeit we set aside this feature in this dissertation.)

Calculated sulfur distribution in steel is compared with experimental radiographic results.

2 The M/S-model for melting and solidification in fusion welding

We assume:

- Melting and solidification front normal to liquidus isotherm $T_L(C_{L0}) = \text{const}$, in which C_{L0} is the initial solute concentration in the weld pool. (The pool contour dependency on the local concentration is neglected.)
- Melting and solidification in the temperature gradient direction, i.e. growth in the easy growth direction is not assumed [118].
- Planar solid/liquid interface with a *Case 3*-solute pile-up in front. (This model applies to near-**WIF**–regions with temperature gradients G higher than the limiting gradient *for constitutional supercooling* [4].)

The trajectories of the moving points on the solid/liquid interface of melting and solidification are the line ABEFH (**Fig. A38.1a**). Near the **WiF** (point E) these trajectories coincide.

The instantaneous rate of melting and solidification is defined by the speed of the heat source v and direction of the gradient G (**Fig. 1a**).

$$R = \frac{d\xi_{SL}(t)}{dt} = v\cos(\alpha)$$

where $\xi_{SL}(t)$ is the coordinate *(linear distance along the trajectory)* of the S/L interface. Growth rate R changes smoothly along the trajectory ABEF (axis ξ, **Fig. A38.1b**). Near **WiF** the rates of melting and solidification are practically equal.

---

[26] The weld pool-solidus

3 The mass transfer problem

We assume:

- The problem is 1-dimensional; the mass is transported preferentially along the temperature gradient.
- Solute mass transport in solid and in the adjacent stagnant layer with width δ_h follows Fick's second law of diffusion, further in the remaining melt the solute concentration is C_{L0} = const due to fluid flows. Therefore for the analysis of the diffusion near **WiF** (the point E) consideration of the route BEF suffices. If the part BE is relatively short (BE ≈ $10\delta_h$ << $W/2$), it practically equals the part EF. Thus it suffices to pay attention to the diffusion along NEF; so in part BE occurs melting (R<0), in part EF occurs solidification (R>0), while part NE belongs to the base metal (**Fig. A38.1c**). The furthest point N is located outside the diffusion affected zone.
- At any given time t the temperature field and the location of the solid/liquid interface ξ_{SL} (t) are known.
- The distribution coefficient k is constant in time, k<0.
- The density change associated with the phase transformation is ignored.

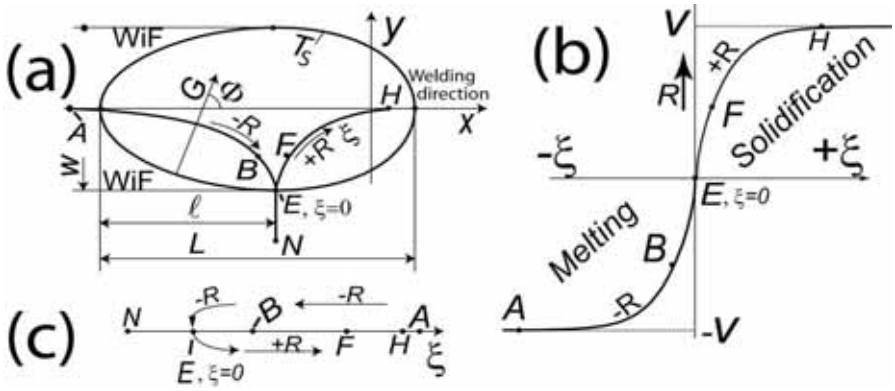

Fig.A38.1 *Weld pool and melting (portion ABE) and solidification (portion EFH) trajectories (a); rate of melting (R <0) and solidification (R > 0) (b), and coordinate system of the diffusion problem with the straightened distance ξ from WIF (c)*

With these assumptions the diffusion problem is the following.

1. The equation in solid (index S) and liquid (index L) is

$$\frac{\partial C_S}{\partial t} = \frac{\partial}{\partial \xi}\left(D_S \frac{\partial C_S}{\partial \xi} \right) + f_S(\xi, t)\,,\ \xi_N < \xi < \xi_{SL}(t) \tag{1}$$

$$\frac{\partial C_L}{\partial t} = \frac{\partial}{\partial \xi}\left(D_L \frac{\partial C_L}{\partial \xi} \right) + f_L(\xi, t)\,,\ \xi_{SL}(t) < \xi < \xi_{SL}(t) + \delta_h \tag{2}$$

where C is the solute concentration; D is the diffusion coefficient, $D = D(\xi, t)$; f is the function taking into account the source (sink) of the solute as a result of the disintegration (formation) of chemical compounds.

2. Initial condition

$$C_S(\xi,0) = C_{S0}(\xi)\,,\ \xi_N < \xi < \xi_{SL}(0) \tag{3}$$
$$C_L(\xi,0) = C_{L0}(\xi)\,,\ \xi_{SL}(0) < \xi < \xi_{SL}(0) + \delta_h \tag{4}$$

3. Boundary conditions

$$C_S(\xi_N,t) = C_{S0} \tag{5}$$
$$C_L(\xi_{SL}(t) + \delta_h,t) = C_{L0} \tag{6}$$
$$\frac{C_S(\xi_{SL}(t),t)}{C_L(\xi_{SL}(t),t)} = k \tag{7}$$
$$D_S \frac{\partial C_S}{\partial \xi}\bigg|_{\xi=\xi_{SL}(t)} - D_L \frac{\partial C_S}{\partial \xi}\bigg|_{\xi=\xi_{SL}(t)} = R\left[C_L(\xi_{SL}(t),t) - C_S(\xi_{SL}(t),t)\right], \qquad R > 0,\ k < 1.0 \tag{8}$$

If $k > 1.0$, the analogous conditions are fulfilled for melting ($R < 0$). Equation (8) reflects the mass balance law at solid/liquid interface.

The discontinuity of the sought function C (ξ, t) at solid/liquid interface (equation (7)) can be eliminated by introducing a new function (mass transfer potential):

$$U(\xi,t) = C(\xi,t) / S(\xi,t) \tag{9}$$

where ***S*** is the *solute solubility*.

The formulation of the mass transfer problem with this $U(\xi, t)$ becomes:

$$1.\ \frac{\partial (SU)}{\partial t} = \frac{\partial}{\partial \xi}\left(SD \frac{\partial U}{\partial \xi} \right) + f(\xi,t)\,,\ \xi_N < \xi < \xi_{SL}(t) + \delta_h \tag{10}$$
$$2.\ U(\xi,0) = C(\xi,0) / S(\xi,0) \tag{11}$$
$$3.\ U(\xi_N,t) = C_{S0} / S(\xi_N,t) \tag{12}$$
$$U(\xi(t) + \delta_h,t) = C_{L0} / S(\xi(t) + \delta_h,t) \tag{13}$$

The problem (9) – (13) generalizes the problem (1) – (8) and facilitates the taking into consideration (a) the dependency of the solubility and (b) diffusion coefficient on temperature and (c) concentration discontinuity at the S/L-interface.

In the specific case when the solubility in the region of each of the phases (solid and liquid) is constant, the solute solubility in solid may be chosen as a unit. Then

$$S(\xi,t) = \begin{cases} 1, & \xi_N \le \xi \le \xi_{SL}(t) \\ 1/k, & \xi_{SL}(t) \le \xi \le \xi_{SL}(t) + \delta_h \end{cases} \tag{14}$$

Solubility S is discontinuous at the solid/liquid interface, but the sought function U (ξ, t) is continuous. Problem (10) – (13) may be solved by the *finite difference method*. Knowing the solution $U(\xi, t)$ the distribution $C(\xi, t)$ can be found by using the equation (9). Therefore may be found the distribution at any weld cross-section at any moment of time, e.g. the post-solidification distribution $C(y, t)$ along the cross section.

4 The temperature problem

In order to solve the mass transfer problem, it is necessary to know in advance the temperature distribution for determining the ξ-axis, the location of the phase interfaces ξ_{SL} (t), growth rate $R(t)$ of this interface and the diffusion coefficient $D(\xi, t)$.

Several experimental and computational methods for defining the temperature field are known. If the law governing the energy input into the body is sufficiently well known, the temperature problem can be solved by numerical or analytical methods. If they are not sufficiently well known, they can be solved by using inverse modeling [118]. We show the technique to solve ξ, ξ_{SL} (t), $R(t)$ and $D(\xi, t)$ with two simple schemes of rapidly moving heat sources in a plate and on a semi-infinite body.

1. Rapidly moving line heat source in a plate.

The temperature field in a moving reference frame (**Fig. A38.2a**, solid lines) is described by the equation [113]:

$$T(x,y)-T_0=\frac{q/(vs)}{c\rho(-4\pi ax/v)^{1/2}}exp\left(\frac{vy^2}{4ax}\right)$$

where s is the plate thickness. Coordinate x is negative behind the source. Out of this the dimensions of the pool can be determined (isotherm $T = T_L$, **Fig. A38.1a**):

$$W=\frac{2}{\sqrt{2\pi e}}\frac{q/(vs)}{c\rho(T_L-T_0)} \tag{15}$$

$$L=\frac{1}{4\pi a}\left[\frac{q/(vs)}{c\rho(T_L-T_0)}\right]^2 v \tag{16}$$

$$l=\frac{e-1}{e}L \tag{17}$$

Weld pool boundary (the isotherm T_L) is defined by the equation

$$y=\pm\left\{\frac{4a}{v}x\ln\left[\frac{(T_L-T_0)c\rho(4\pi a/v)^{1/2}}{q/(vs)}(-x)^{1/2}\right]\right\}^{1/2} \tag{18}$$

If the values of l and W (the length and width of the ripples on the plate surface) are known, it is possible to reconstruct approximately the welding conditions (q/(vs) and v):

$$q/(vs)=W/2(2\pi e)^{1/2}c\rho(T_L-T_0)$$

$$v=l\frac{e}{e-1}4\pi a\left[\frac{c\rho(T_L-T_0)}{q/(vs)}\right]^2 \tag{19}$$

The value of the temperature gradient *grad T* and its direction (angle α) are given by the formulae:

$$gradT = \sqrt{\left(\frac{\partial T}{\partial x}\right)^2 + \left(\frac{\partial T}{\partial y}\right)^2} = \frac{T(x,y) - T_0}{2x}\sqrt{\left(1 + \frac{vy^2}{2ax}\right)^2 + \left(\frac{vy}{a}\right)^2} \tag{20}$$

$$\alpha = \arctan\left(\frac{\partial T / \partial y}{\partial T / \partial x}\right) = \arctan\left(-\frac{a}{vy} - \frac{y}{2x}\right) \tag{21}$$

The rate of melting and solidification are defined by the welding speed v and angle α:

$$R = v\cos\alpha = v\cos\left[\arctan\left(-\frac{a}{vy} - \frac{y}{2x}\right)\right] \tag{22}$$

2. Rapidly moving point source on a semi-infinite body (**Fig. A38.2b**, solid lines).

All values are defined analogously with the case of line source in plate (in the following r is the distance to x-axis):

$$T(x,r) - T_0 = -\frac{q}{2\pi\lambda x}\exp\left(\frac{vr^2}{4ax}\right) \tag{23}$$

$$W = 2\left[\frac{2}{\pi e}\frac{q/v}{c\rho(T_L - T_0)}\right]^{1/2} \tag{24}$$

$$L = \frac{q}{2\pi\lambda(T_L - T_0)} \tag{25}$$

$$l = \frac{e-1}{e}L \tag{26}$$

$$r = \left\{\frac{4a}{v}x\ln\left[-\frac{(T_L - T_0)2\pi\lambda}{q}x\right]\right\}^{1/2} \tag{27}$$

$$gradT = \frac{T(x,r) - T_0}{x}\sqrt{\left(1 + \frac{v}{4a}\frac{r^2}{x}\right)^2 + \left(\frac{vr}{2a}\right)^2} \tag{28}$$

$$\alpha = \arctan\left(-\frac{vr}{2a}\Big/\left(1 + \frac{vr^2}{4ax}\right)\right) \tag{29}$$

$$R = v\cos\left[\arctan\left(-\frac{vr}{2a}\Big/\left(1 + \frac{vr^2}{4ax}\right)\right)\right] \tag{30}$$

If the solution of the temperature problem is numerical, then the derivatives $\partial T/\partial x$ and $\partial T/\partial y$ are defined numerically.

Knowing all necessary characteristics of the temperature field, it is possible to define the trajectories ABEF (**Fig. A38.1a**), location of the solid/liquid interface on the ξ-axis and the growth rate R of the interface (Fig. **A38.**1b). This approach is preserved also in the case of intermittent solidification.

5 Examples

A pool with width $W = 4$ mm and length of the trailing end $l = 4$ mm is formed in welding of a steel plate (a = 7 mm^{2}s^{-1}, $c\rho$ = 0.005 Jmm^{-3}K^{-1}, λ = 0.035 Wmm^{-1}K^{-1}) (**Fig. A38.2**). The initial solute concentration is constant, $C_{S0} = C_{L0} = C_0$. The initial temperature T_0 = 293 K, the liquidus temperature T_L = 1800 K.

Figure A38.2 shows a calculated weld pool formed by a line source in a plate and by a point source on a semi-infinite body. The origin of the coordinates is fixed with the cross section, on which the width of the pool is at maximum. The parameters of the source are defined with the inverse modeling [118].

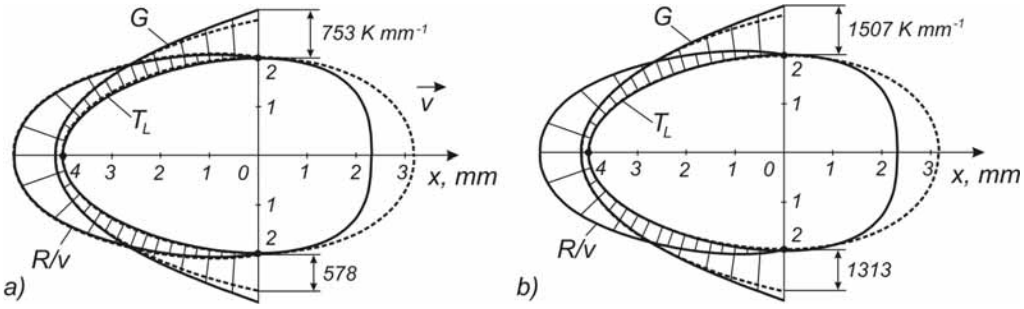

Fig.* A38.*2. *Distribution of the temperature gradient G and relative solidification rate R/v along the trailing solid/liquid interface of the weld pool (T_L isotherms), calculated from the rapidly moving (solid lines) and non-rapidly moving (dashed lines) line sources in a plate (a), and point sources on a semi-infinite body (b).*

It is seen in **Fig. A38.2** that the trailing pool end calculated with schemes of rapidly moving or non-rapidly moving sources are practically identical. The trailing pool end can be approximated sufficiently accurately with an ellipse with semi-axes 4 mm and 2 mm, which facilitates the determination of the trajectories and growth rate of the crystals [119].

The calculated with the two schemes relative solidification rates R/v also are practically identical, but the temperature gradients along the solid/liquid interface somewhat differ. Gradients in the semi-infinite body are 2.0…2.3 times as high as the ones in the plate. Naturally, the parameters of the sources, giving the forms for the pool, differ. From **Fig. A38.2** it follows that the simple scheme of rapidly moving sources can be used in the calculation of the trailing pool contour and crystal growth trajectory and rate.

The diffusion problem was solved for the case of rapidly moving line source in a plate. The heating regime was: $q/(vs)$ = 62.28 Jmm^{-2}, v = 8.15 mms^{-1}. The problem was solved by the finite difference method with 1*10^{-4}...5*10^{-4} mm and 1*10^{-7}...2*10^{-6} s steps. The form of the pool, the diffusion coefficient D and equilibrium distribution coefficient k were varied. The values for the coefficients are in the table based on [115] and [120]. Assumed was $f = 0$. The coordinate of the **WiF** was taken as 0, $\xi_E = 0$.

Figure A38.3b shows the distribution of relative concentrations C/C_0 for carbon at various moments of time t after solidification start (melting stage of the metal is not considered). Solidification front is straight (**Fig. A38.3a**), which corresponds to constant growth rate R =3.635 mms^{-1}. Diffusion coefficients are constant, $D_S = 0$, D_L = 0.005 mm^{2}s^{-1}. The analytical solution was found in [49] (hereafter it is called the classical *Case 3*). The plot C_{Lmax}/C_0 corresponds to the peak concentration in the melt at the moving solid/liquid interface. It follows from **Fig. A38.3b** that after 0.01 s a quasi-stationary (steady) state forms, in which, in a moving with the solidification front coordinate system, the concentration field in front of the solid/liquid interface does not practically change and can be described by the equations [4, 49]:

$$\frac{C_L}{C_0} = 1 + \frac{1-k}{k} \exp\left(-\frac{R}{D_L} \xi' \right) \tag{31}$$

where ξ' is the distance from the solid/liquid interface. The layer of elevated concentration may be characterized with the thickness ξ_0:

$$\xi_0 = C_0 \left(\frac{1-k}{k} \right) \Big/ \left. \frac{dC_L}{d\xi'} \right|_{\xi'=0} = \frac{D_L}{R} \tag{32}$$

In this case ξ_0 = 1.38 μm (**Fig. A38.3b**).

The difference between the calculated and analytical solutions [49] is detectable only at the start of the solidification front movement (at $t \leq 0.001$ s, **Fig. A38.3b**), which witnesses of correctly chosen steps.

Taking into account the diffusion in solid ($D_S = D_L = 0.005$ mm^{2}s^{-1}) leads, naturally, to solute redistribution behind solidification front (**Fig. A38.3c**). The quasi-stationary field does not depend on the solid diffusion and is defined by equation (31).

Explanatory insert for the *M/S-model:* the central terms

The preceding initial conditions are used in forming the *M/S-model*. It will eventually be placed into the *Model Frame*, helping make the final model of the actual weld.

The word "model" has acquired several meanings on different conceptual levels; we call the models of solidification *Cases* or *Sub-Cases*. A *Sub-Case* is a mathematical formula solving some *aspect of solidification*, the aspect most often being the solute profile along a chosen solving path in the weld. At the present, the "chosen solving path" is (almost without exception) the longitudinal direction of the solidification. This is true also for the present *M/S-model:*

- it is a *Sub-Case*, and
- it solves – or its *Sub-Case Aspect* is - the solid solute profile. The "solving path" is the trajectory AB**EFH** (Fig. 1A)**,** straightened in the **ξ**-coordinate system in Fig. 1B of this Appendix.

It should be noted that with no (known to the author) exception, all solidification models solving concentration profiles (for solidification rates, with which the *microscopic equilibrium* exists) stem from the *"Cases"*, defined in Chapter 1.2 and described in detail in Ch. 3.

A *Sub-Case* uses one or more *Sub-Case Variables* ***SCV*'s** to solve its aspect. Such variables may be the *solidification rate* **R**, *temperature gradient* **G**, *diffusion in the solid* $\mathbf{D_S}$, *flows in the liquid* a.s.o. The *M/S-model* uses three such variables: **(1)** the *effect of melting*, **(2)** *the post-solidification diffusion in the solid* (*back-diffusion*) and *the acceleration of R*, the last being mandatory with an oval weld pool (Ch's 1.1.18 and 1.1.19).

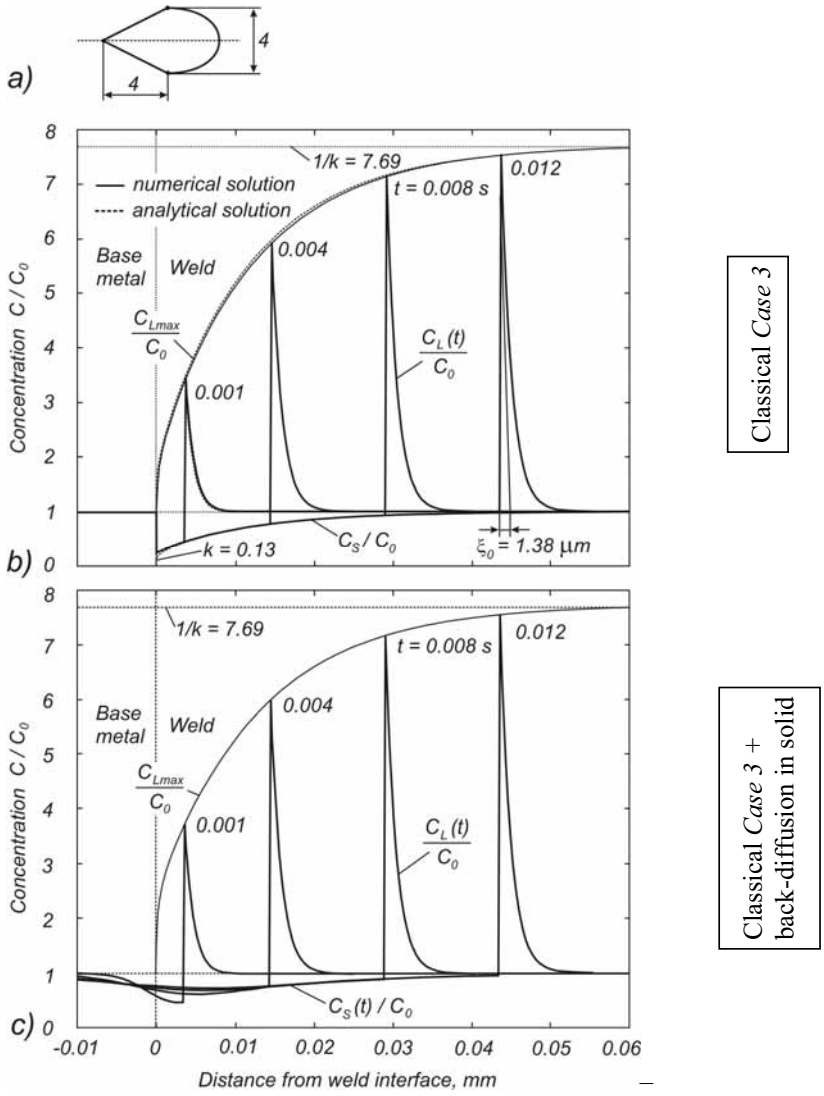

Fig.* A38.*3 *Teardrop weld pool (a) and distribution of the relative concentration of carbon at various moments of time t after solidification start with $D_S = 0$ (b) and $D_S = D_L = 0.005$ mm^2s^{-1} (c). The teardrop is the only feasible pool form for these models for constant R, with no component for modeling $\dot{R}$.*

If the pool form is oval, the solidification rate *R* varies (**Fig. A38.4**). Simultaneously, as *R* grows, the area with elevated concentration contracts, leading to a rise in concentrations in both liquid and solid near the front. Comparing **Figs A38.3b** and **A38.4b** it is seen that in the latter this concentration elevation rate is substantially less. The question rises: is it possible to calculate the thickness of the diffusion layer ξ_0 from equation (32) in the case of the increasing solidification growth rate *R*? In other words: does the quasi-stationary state have time to form, if the front movement changes smoothly (acceleration is relatively small)? The analysis of the results proves that at distance > 0.05 mm from **WiF** with an error < 5%, the equation (32) can be used for both constant and varying growth rate *R*.

In earlier works [4][5][115…117] the melting stage is not accounted for. It follows from **Fig. A38.5** that during the melting stage ($t < 0$) - in the solid - ahead of the melting front forms a zone of reduced concentration, with width proportional to the diffusion coefficient D_S (greater for C than for

S). Therefore the melting stage may trigger a substantial concentration dip – extending to the base metal -in the solid near the **WiF**. In the solidification stage ($t > 0$) the concentration ahead of the solidification front increases, and at $t \geq 0.08$ s ($\xi \geq 0.04$ mm) it is practically identical with the concentration, in which the melting stage is not accounted for (which follows from comparison of **Figs A38.5a** and **A38.4b**). where Q is the activation energy, R is the gas constant. The parameters D_0 and Q are in Table.

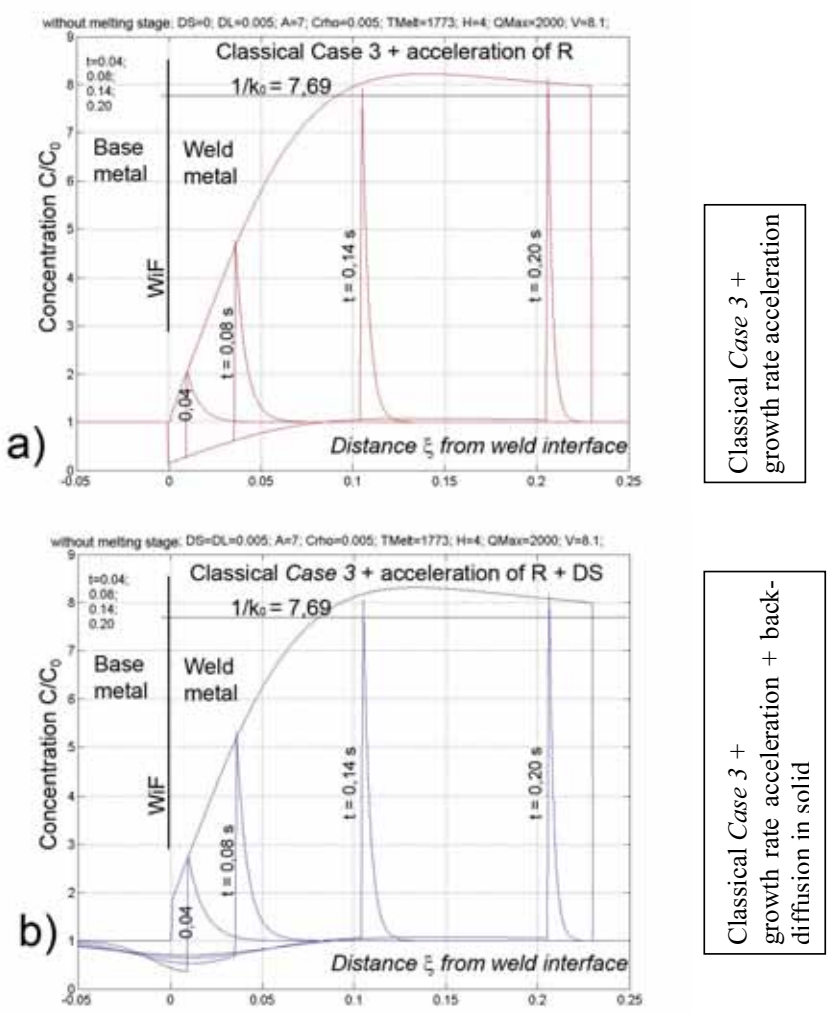

Fig.* A38.*4 *Oval weld pool. Distribution of the relative concentration of carbon at various moments of time t after start of Case 3 solidification with*
(a) acceleration of solidification rate R from 0 (at WiF) to welding speed v.
(b) similar acceleration of R as in (a) and solid diffusion.
Welding speed v =2,2 mm/s. $D_S = 0.005$ mm^2s^{-1}

In the melting stage the dependency $D_S(T)$ does not affect the distribution of the concentration (the plots $t = 0$ in **Figs A38.5a** and **A38.6a)**. In cooling, the intensity of the diffusion process at the **WiF** is governed by the thermal cycle. At time $t = 1$ s the temperature lowers by 400 K, but the diffusion coefficient lowers by an order of magnitude and further cooling brings no changes to the carbon or sulfur distribution. After cooling down, the minimum relative concentration at the **WiF** is 60% for C and 20% for S of the initial. At distance of 0.1…0.5 mm from the **WiF**, the

concentration in the weld metal is slightly over the initial. So, the concentration differences formed at elevated temperatures do not disappear.

In the calculation of the concentration kinetics at the **WiF**, consideration must also be given to the temperature dependency of the diffusion coefficient D_S:

$$D_S(t) = D_0 \exp\left(-\frac{Q}{RT}\right),$$

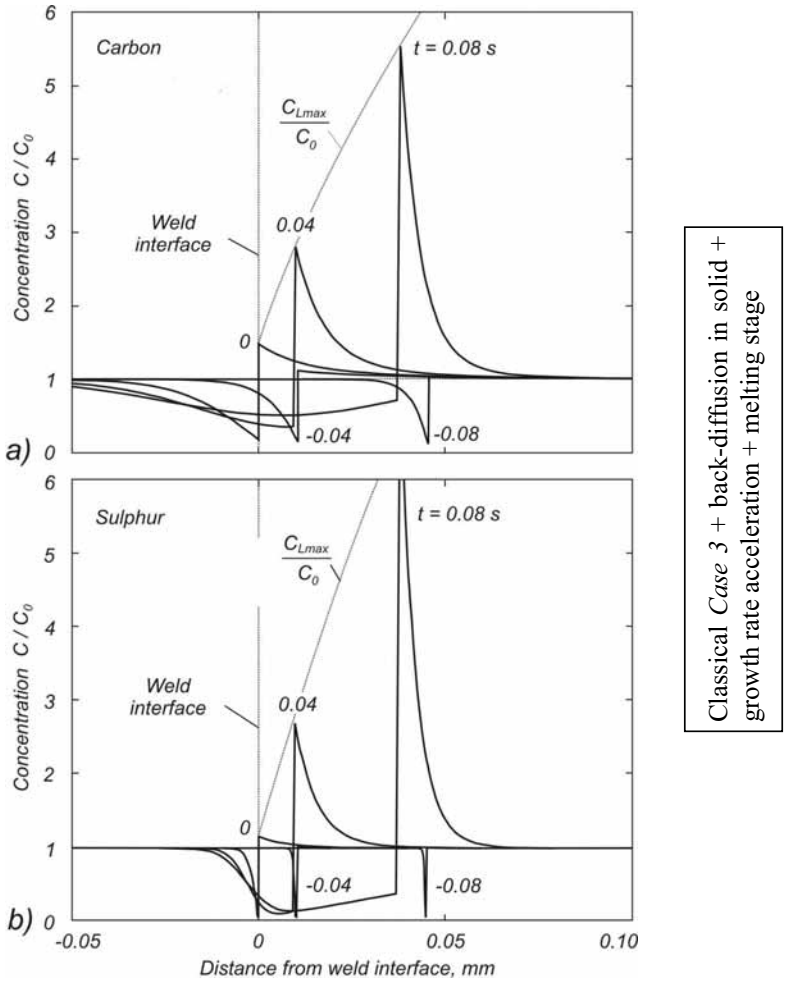

Fig.* A38.*5 *Distribution of the relative concentration of carbon (a) and sulfur (b) at various moments of time t. Moment t = 0 corresponds to the halt of solid/liquid interface (transformation from melting to solidification).*

Table: ***Properties used in the calculations***

Element	k	D_L, mm^2s^{-1}	D_S (T_L), mm^2s^{-1}	D_0, mm^2s^{-1}			Q, $Jmol^{-1}$		
				δ-Fe	γ-Fe	α-Fe	δ-Fe	γ-Fe	α-Fe
C	0.13	$5.52\ 10^{-3}$	$5.52\ 10^{-3}$	1.27	7.61	$5.62\ 10^{-3}$	81379	143511	79773
S	0.05	$5\ 10^{-3}$	$2.69\ 10^{-4}$	456	240	(456)	214639	223425	(214639)

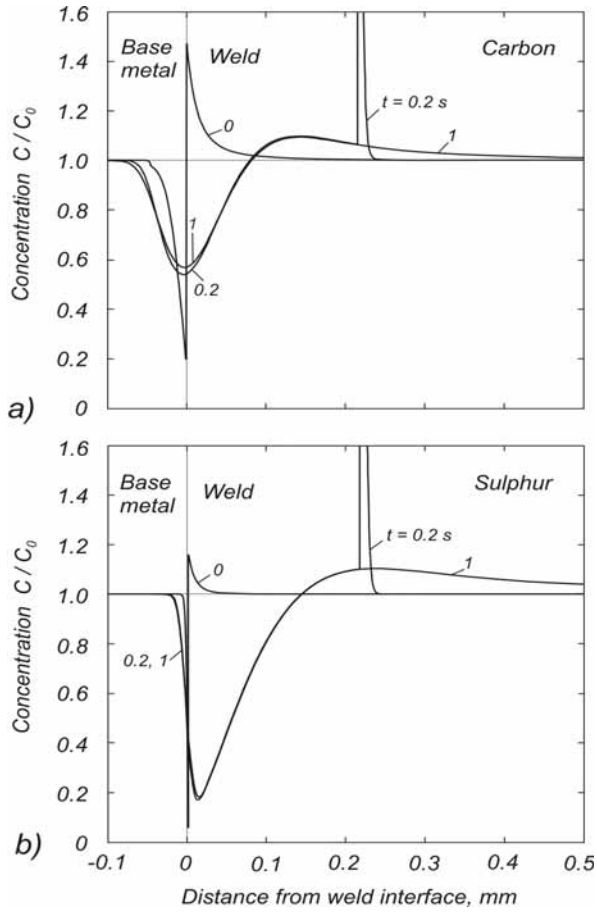

Fig.* A38.*6. *Distribution of carbon concentration (a) and sulfur (b) near the* ***WiF*** *at various moments of time t after start of solidification.*

Because the zone of the chemical unevenness is relatively small, it may be assumed that it is located at a constant temperature field at any moment of time, and then the diffusion during cooling can be regarded as diffusion in a fixed temperature, using the method of equivalent times [121].

As one may expect, doubling v and q (at q/v = const) practically does not affect the macro segregation near the **WiF**.

6 Experimental testing

A thick steel plate was TIG welded with Ar+He shield gas. Bead width W = 10 mm, depth of fusion is 5 mm. Welding regime: q = 3030 W, v = 2.6 mm s^{-1}. The initial concentration C_0 = 0.04 %. The results of radiographic S-content measurements near the **WiF** after cooling down are presented in the **Fig. 7** [1].

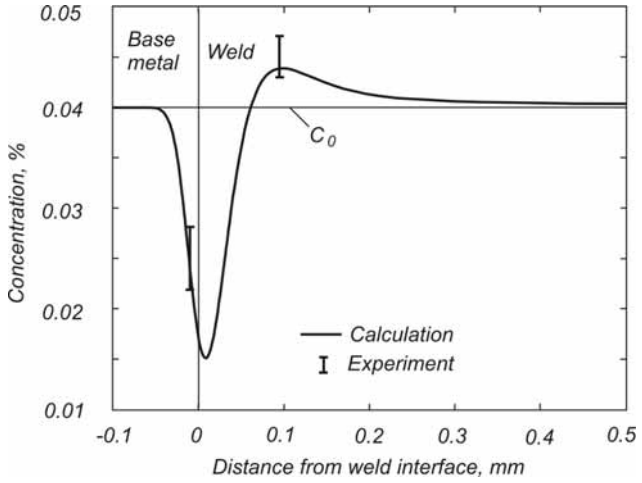

Classical *Case 3* + Back-diffusion in solid + Growth rate acceleration + melting stage + temperature dependency of diffusion

Fig.* A38.*7 *Distribution of sulfur concentration near the* ***WiF****.*

The scheme of a rapidly moving point source on a semi-infinite body was applied. This yielded the calculated bead width W = 9.5 mm, depth of fusion 4.7 mm. The sulfur content profile was calculated with the presented method (**Fig. A38.7**). The S-content near the **WiF** was substantially below the initial on the base metal side, but somewhat above initial on the weld metal side. The width of the zone of unevenness of the S-concentration was roughly 0.5 mm. **Figure A38.7** shows a good agreement between calculation and experiment.

7 Conclusions of the Appendix 38

1. The developed calculation method – we call *Melting/Solidification- or M/S-model* - defines the solute redistribution profile near a fusion **WiF**, taking into consideration **(i)** not only the solidification- but also the melting stage, in other words the pre-solidification (melting stage-induced) solute redistribution in the base metal as well as in the pool, **(ii)** the post-solidification solute back-diffusion in the solid, **(iii)** the growth rate acceleration typical to fusion welds, **(iv)** the form and dimensions of the weld pool, welding speed and heat input and **(v)** the temperature dependency of the solute solubilities and the diffusion coefficients in both solid and liquid.

2. The melting stage forms a concentration dip (upside-down concentration gradient) in the newly formed liquid extending to the base metal near **WiF**. In the solidification stage this dip partially evens out; there is a zone of reduced concentration in the weld metal, but it is limited to the vicinity of the **WiF**.

3. The growth rate acceleration squeezes the solute pile-up ahead the S/L interface in the welding direction, which raises the concentration of both the liquidus and the solidus. This mechanism is explained and modeled by Flemings in Fig. 4.4b .

4. The - formed at the elevated temperature - inhomogeneity of carbon and sulfur near the **WiF**, is partially conserved after the weld has cooled down.

5. The agreement between the calculated results and experimental radiographic measurements of the sulfur profile across the **WiF** is satisfactory.

Appendix 39. Pool Shape

Chapter A39.1 Elliptic to teardrop pool shape

The generally recognized phenomenon of weld pool form changing from elliptic (Fig. A.39.1**B**) to teardrop (Fig. A.39.1**A**) is discussed in Ch. 5.4.2. The reason for this change is increasing welding speed **v,** as discussed in Ch. 1.1.19. Further increase of **v** may lead to a tail forming to the end of the pool (discussed in Ch. A39.2 below).

The classic explanation is based on a *critical growth rate limit, after which the rate of evolution of latent heat (**ΔH**) at the centerline (or center point) of the trailing edge of the weld pool exceeds the ability of the system to dissipate it.* This explanation is contradicted by the solution presented in Fig.A39.2, stating that the latent heat does extend the length of the trailing end of the pool and decreases its curvature, but does not straighten it.

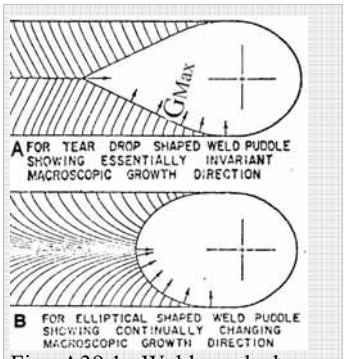

Fig. A39.1. Weld pool shapes. **A:** Teardrop and **B:** elliptical [21]

If the analysis of Fig. A39.2 is correct – as we tend to believe - then **(1)** there is no discrete thermodynamic growth rate limit, after which the trailing edge becomes straight. Moreover – rigorously taken - the analysis of Fig. A39.2 would **(3)** suggest a formation of *axial grains* (see Fig. 2.18) along practically all weld centerlines, because the temperature gradient **G** always has a component in and close to **x**-direction - regardless of how high the **v** is increased.

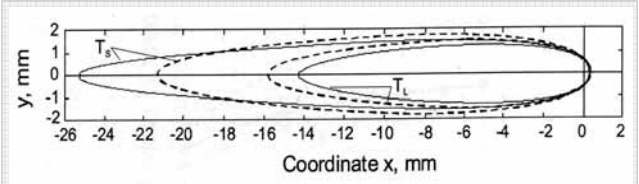

Fig. A39.2. The effect of latent heat on weld pool shape in AISI 304 without (the dashed lines) and with (the solid lines) considering the latent heat. [123]

***Note** In our experiments, the grains never turned perfectly parallel to the welding direction **v** at the end of solidification. At the planar-to-cellular transition line (with low **R**), all grains grew in the obvious **G**-direction[27], curving after that line with the help of knees – obviously in the **EGD** (Appendixes 6, 8, 20, 24, 26, 27, 30, 32 and 35). At the weld top, (with maximum **R**) the grains do not curve parallel to **G**-direction, (= the horizontal welding direction $\vec{v}$ in Appendixes 6, 8, 9, 20, 30, and 32). The Appendixes 2 and 19 show clearly the contours of the grains protruding top surface, not turning into the welding- (and **G**-) direction **x** along the surface.*

*The described above was typical for all our test welds[28]. The **G** – parallel to **v** at the centerline of the top surface – should have bended the grains to its direction, forming axial grains (Fig. 2.18). This did not happen; we are unable to explain fully the phenomena on the very surface of the weld.*

[27] = normal to the mentioned *planar-to-cellular line*, which is easily recognizable in the micrographs.
[28] With a possible exception of Pb-doped weld in Appendix 35

Chapter A39.2 Tail of the pool

Further increase of **v** may lead to a tail forming to the end of the pool (Fig. A39.3).

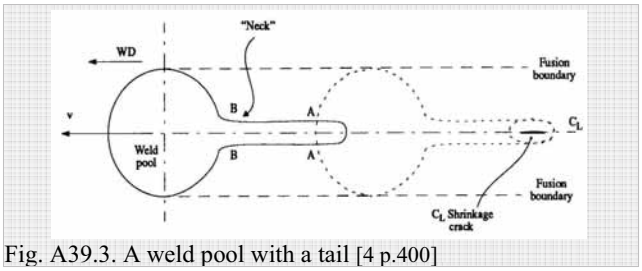

Fig. A39.3. A weld pool with a tail [4 p.400]

The analysis of Fig. A39.2 denies the possibility of formation of the tail depicted in Fig. A39.3: there must be some other explanation for the tail. For this we propose the metallurgical effect of the final transient of Fig. 5.10; it lowers the $\mathbf{T_L}$ enough to be able to cause such a tail.

The solute profile of the weld is shown in Fig. A39.4. The dashed line (analytical) is the classical *Case 3* with constant **R** (2,05 mms^{-1}), without solute back-diffusion. The full line (numerical) is the *M/S-model,* including **(i)** the acceleration of **R**, **(ii)** the solute back-diffusion during cooling to the room temperature, **(iii)** the melting stage upside-down **CG** (Fig. 5.14) and **(iv)** the concentration dependence of $\mathbf{T_L}$, from the phase diagram (Fig. A39.5A). *The weld pool perpendicular cross section is a half-circle, with a point source on the plate surface. This geometry distorts the solute profile form; the volume / Δy near the fusion line is much greater than the volume / Δy near the weld center point; the mass balance is not violated in Fig. A39.4.*

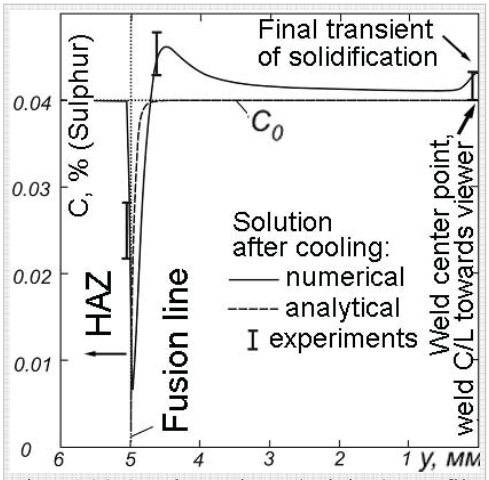

Fig. A39.4. The solute (sulphur) profile after cooling of the weld pool in Fig. A39.5**B**. [126].

The M/S model predicts a tail for a fast-**v** weld, Fig. A39.5**B**. This tail is much like the tail discussed in world literature, Fig. A39.3.

The tail consists of the low-melting solute pileup in the final transient. This solute pileup undergoes a forceful post-solidification back-diffusion during cooling to the room temperature. The peak concentration at the weld C/L has probably reached the eutectic concentration 31%, but the back-diffusion has reduced the post-solidification peak concentration to a mere 0.045%.

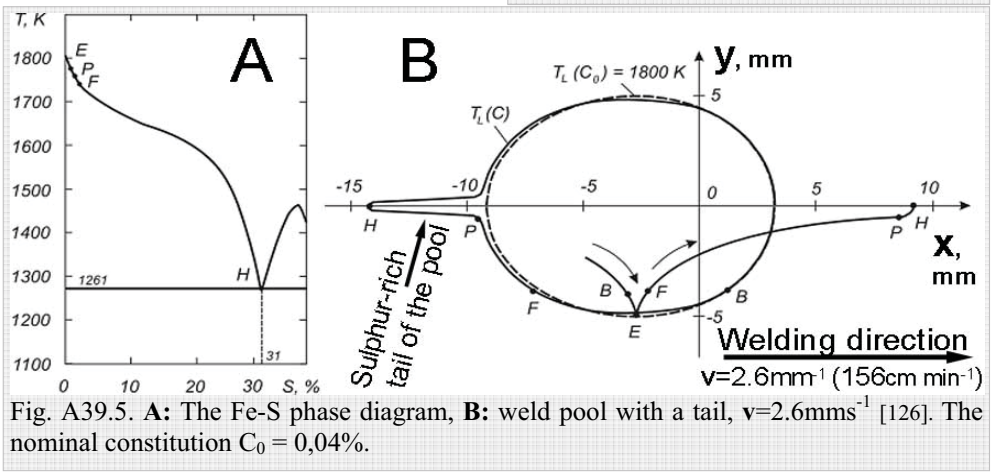

Fig. A39.5. **A:** The Fe-S phase diagram, **B:** weld pool with a tail, **v**=2.6mms^{-1} [126]. The nominal constitution C_0 = 0,04%.

Appendix 40. Joining Case 2 to Case 1 with added solid diffusion, Sub-Case 2(-)Ds

We present in Fig. 4.2 the Kurz & Fisher-analysis of solute profile in *Case 2* with diffusion in solid, making a remark of a slight violation of mass balance. The authors state in the text "*The final solute distribution cannot be determined in this way because it changes with time when a >0 due to back-diffusion…*") This important analysis deserves a closer discussion; it attempts to solve the solute profile in an instance, when the solidification transforms from one *Case* to another, in this instance from *Case2* to *Case 1* or vice versa.

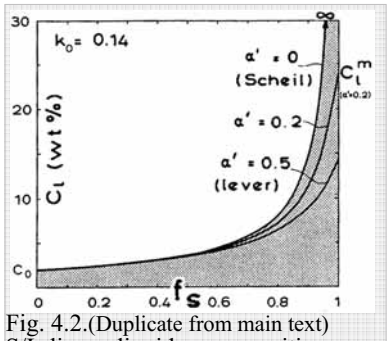

Fig. 4.2.(Duplicate from main text) S/L-line liquid composition vs. solidified fraction $\mathbf{f_s}$. **α'** is 0.5 at *Case 1* and 0 at *Case 2.Solution of Kurz & Fisher* [5] Eq.6.9 p. 123

Kurz & Fisher 1998 [5] – continuing the works of Brody & Flemings 1966 [20] and Clyne & Kurz 1981 [86] - modify the Gulliver-Scheil equation by adding to it the solid back-diffusion with the terms **α** and **α'** (our Equations 2.8.2B and 4.1.1 respectively). The **SCS2** categorizes such a model as *Sub-Case 2(-)Ds. (Sub-Case 2 = Gulliver Scheil equation, (-)* = downwards towards *Case 1*, *Ds* = Diffusion in solid*)*.

This elaborate chain of metallurgical research produces the solute profile in the liquid D_L presented in our Fig. 4.2. If the concentration in the solid were determined from these plots by the equation $\mathbf{D_S = D_L \cdot k_0}$, the mass balance between the start and the end of the solidification would be violated. Kurz & Fisher were well aware of this and note this as pointed out at start of this Appendix.

We do not bring this forth to point out flaws in the text. Brody, Flemings, Clyne, Kurz and Fisher present the best existing theory for determining the said concentration profile. The fact that the end result is not rigorously mathematically flawless means that we are dealing with a phenomenon so complex that at the present time no rigorous mathematical solution exists.

The equation A12.7 of [5 p.282] reveals that the approach is for parabolic growth rate relationship typical of casting: the growth rate **R** at first is at its maximum and decreases with time. The approach is not applicable to fusion welding with is initial growth rate $\mathbf{R_{Initial}}$ = zero growing to its maximum value of $\mathbf{R_{Max}}$ = welding speed according to equation 1.1.18A.

The said afore suggests that leading scientists have not been able to find a rigorously correct mathematical solution for the solid solute profile of the solidification continuum from *Case 2* to *Case 1* for casting (in terms of the SCS2-system *Sub-Case 2(−)D_S*). Such rigorous a solution has not even been sought for fusion welding.

The mentioned above chain of research (Brody & Flemings - Clyne & Kurz - Kurz & Fisher 1998 [5] pp. 123-126 and Figure 6.4 Fig. 4.2 in this dissertation) appears mathematically flawless. The fact that the mass-balance violations in the Brody & Flemings model (Ch. 2.8.3) and in the Kurz & Fisher-approach (our Fig. 4.2 handled above) suggest impossibility of rigorously joining *Case 2* (the Gulliver – Scheil equation) with *Case 1* (the lever rule). The analysis gives a rigorously correct result in the end points: Eq. 2.8.2A does give the Gulliver-Scheil equation with $D_S = 0$ and the lever rule with $D_S=\infty$. However, the Fick's diffusion laws evidently require an addition of differential variables (including time) into the analysis, which seems to make the rigorous analytic solution impossible, calling for a numerical solution.

The *Sub-Case 2(-)Ds* is further discussed in the Appendix 41. Fig. A41**B** shows its relation to the *Cases,* other *Sub-Cases* (which exist in a different coordinate system) and the thermo-metallurgical "Sub-Case Variable" **SCV** *solidified fraction* $\mathbf{f_S}$. The analysis suggests the same as was said above, the analytical joining of the *Cases 2* and *1* is impossible, at least with the ***SCV***'s used at present.

Appendix 41. Visualization of the Cases, Sub-Cases and operation paths of Cases 2 and *3 from solidification start to its end*

Of the *four basic model-element-groups* of the *Model Frame* (Fig. 5.4 and Ch. 5.5.1), namely: **a)** the solid solute concentration profile, **b)** the geometric variables**, c)** the Sub-Case variables (***SCV***'s) and **d)** The *Cases* and *Sub-Cases*, the most complex to visualize are the groups **c)** and **d)**.
Fig. A41 attempts to visualize the *Cases/Sub-Cases* placing them in a xyzΩ-coordinate system, using the *Sub-Case Variables* (*SCV's*) as the coordinates.

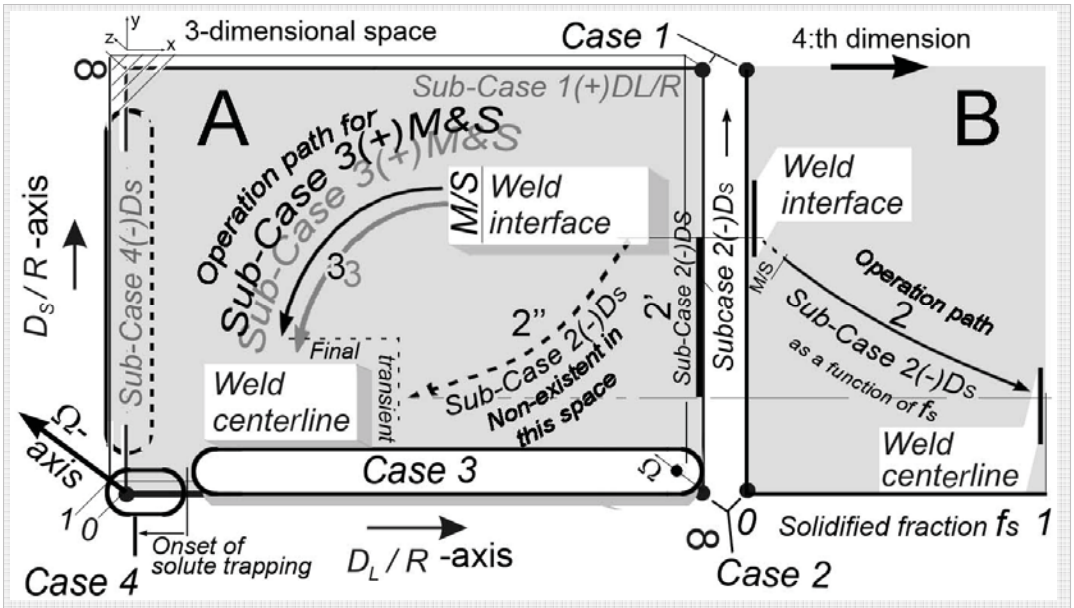

Fig. A41. A visualization of the operation paths of the *Cases 2* and *3* solidification, using a 4-D space with four *Sub-Case Variables* (*SCV*'s) and five *TMV*'s.

A):. The three ***SCV***'s, consisting of four ***TMV***'s ($\mathbf{D_L}$, $\mathbf{D_S}$, **R**, and **Ω**), form a 3-D $\mathbf{D_L/R}$ - $\mathbf{D_S/R}$ - **Ω** coordinate system, accommodating the four *Cases* and the diffusion-related *Sub-Case 2(-)DS* (Ch. 4.1.1) and an ideal *Sub-Case 3(+)M&S* (a Mullins & Sekerka-based model, see Ch. 4.2.2).

The x-axis *SCV*'s: $\mathbf{D_L/R}$ is the *characteristic distance* of the solute pileup (Chapter 2.5.12), appearing as a useful abscissa for this analysis; with this setup it is possible to bring *Cases 1, 2* and *4* on one plane; the corner x, y, z (∞, ∞, 0) is the *Case 1*, the corner (0, ∞, 0) is the *Case 2*, and the corner (0, 0, 0) is the *Case4*. *Case 3* does not exist on the base plane; its shadow has no function - apart helping visualization.

The y-axis is the *Sub-Case 4(-)DS*. It and the *Sub-Case 1(+)D_L/R* have not been solved and are skipped here.

The z-axis: To place *Case 3* into this system, the solute pileup is introduced with **Ω**, which forms a continuous path from no-solute-pileup (*Case 2*) to the solute pileup (*Case 3,* see Chapter 2.8.5). Unfortunately it requires a new dimension, the z-axis and the analysis becomes 3-D. The base plane at **Ω** = 0 houses the *Cases 1, 2*, and *4*, and the *Sub-Case 2(-)DS*. The upper plane at **Ω** = 1 houses the *Case 3* and the ideal *Sub-Case* 3*(+)M&S* (see Ch. 4.2.2).

The solidification starts from and ends at the roughly marked areas *weld interface* (**WiF**)- and *weld centerline* (**C/L**), respectively. The **WiF** is located near – but almost without exception not at – *Case 1*, while the weld **C/L** is located near, but quite seldom at - the *Case 4* (Chapter 4.2.3).

The *operation path **3*** sketches the solidification of *Sub-Case 3(+)M&S*. Note that it is located at the plane (x, y, Ω=1). Its projected shadow on the Ω=0 base plane only emphasizes the difference of the planes, the *Sub-Case* has no component on the base plane.

The ***2'' and 2'*** sketch the operation path of the *Sub-Case 2(-)DS* and its component on the y-axis. The path **2''** is non-existent in the **x**, **y**, **Ω** - system; the 4:th dimension - Fig. **B -** must be prepared for it.

B) To visualize the operation path of *Case 2*, a new variable – the *solidified fraction* $\boldsymbol{f_s}$ – must be added. This fifth ***TMV*** makes the system 4-dimensional.
[Karkhin 20071008 Cases Sub-Cases 7.jpg]

The palette of the pertinent ***SCV's*** changes with respect to the sort of solidification being modeled; a weld with teardrop pool solidifies with a constant **R,** and therefore the term **dR/dt** is not needed in the palette, albeit this ***SCV*** is vital for a weld with an elliptic pool.

The growth mode may – and does - change during fusion weld solidification; it may start with one *Case* or *Sub-Case* and continue with another. Hence, also the model must adapt smoothly from one *Case* or *Sub-Case* to another, to maintain the continuum.

Fig. A41A shows one way to visualize the fusion weld solidification with help of the *Cases* and *Sub-Cases*. Four ***SCV***'s were chosen, namely **R**, $\mathbf{D_L}$, $\mathbf{D_S}$ and **Ω**, for the visualization. ***SCV's*** determine the dimensionality of the figure, and to reduce it to 3-D, $\mathbf{D_L}$ and $\mathbf{D_S}$ were divided by **R**. The quotients $\mathbf{D_L/R}$ and $\mathbf{D_S/R}$ form the x- and y-coordinates. To bring *Case 3* to the system, **Ω** was introduced as the z-axis[29]. The *Cases 1, 2 and 4* are located on the base plane of this coordinate system, but *Case 3* lies on a plane located one **Ω**-unit higher, due to its concentration pileup.

Fig. A41B presents the $\mathbf{y\text{-}f_S}$ _ system and the operation path for the *Case 2*-based *Sub-Case 2(-)*D_S, growing into a fourth dimension: solidified fraction $\mathbf{f_S}$, non-existent in the xyz-system, apart of the 1-D component **2'**.

Let us assume that fusion weld solidification starts with *Case3* and ends with *Case 2*. The number of pertinent ***SCV***'s of such a model is – according to Fig. A41**A** and **B -** at least four. The visualization of the model shows that if the continuum of a fusion weld solidification is pictured as a railroad, then the start and end stations are near (but hardly ever at) the *Cases 1* and *4,* respectively. En route the solidification does pass near (but hardly ever through) the stations of the *Cases 2* and *3*. These two stations – however - are located along separate railroads; if the 3-D space of **A)** is pictured as a room, then the railroad of *Case 3* runs in the ceiling and the railroad of *Case 2* starts from the wall, but vanishes to neighboring room. The joining of these two railroads is imperative for the continuum. We are unable to do this with the setup of the ***SCV***'s of the **Fig. A41**. This has – evidently – never been accomplished rigorously, and a similar problem as in Appendix 40 can be expected. The problem is tolerable and a similar approximate solution would suffice.

The modeling of fusion weld solidification is often choosing between the *Cases 2* and *3* and their *Sub-Cases*. The diminishing portion of the remaining melt at the final transient helps *Case 2* unseat *Case 3* in the end. This may occur in the longitudinal-, as well as in the perpendicular direction (the latter between needle-like cells/dendrites). This introduces the need for a 3-D geometric coordinate system into the model, increasing the number of free *SCV*'s to 7. A complete model would require the **SCV**'s ***dR/dt***, ***G***, and the melting stage effect (M/S-model), rising the number of free variables to 10. This fairly high **SCV** number – which will rise with new **SCV**'s in the future - may not be the key issue in fusion weld modeling, the new applied mathematics and computer technology will solve it. It is – however – difficult to see accurate models for fusion welds without a reasonably accurate solution of the solidification continuum from *Case 3* to *2*.

[29] The *Burton-Primm-Slichter*- solution (Eq. 2.4.2BPS) could also be used for this, as it also unites the *Cases 2* and *3*, but it is so oriented to crystal pulling that its use for fusion welding is not practical.

Appendix 42. The Stagnant Layer and the Concentration Gradient Width

Chapter A42.1. The interpretation and the *width of the stagnant layer* δ_h adopted in this dissertation: A weld pool is usually forcefully stirred by thermal and electro-magnetic currents, which enhance *Case 2* solidification. For the *Case 3* solidification to occur, the rejected solute atoms must remain near the S/L-front and form there a solute pileup. This is believed to occur with the stagnant layer-mechanism depicted in Ch. 1.1.24, assuming the width of the stagnant layer $\delta_h >$ width of the solute pileup.

δ_h has not been solved analytically; a historic solution of Savage, Nippes and Szekeres gives it an estimate ~75µm in a HY-80 steel weld with 165A / 22V / 216 mm/min basic parameters, **Fig. A42,1**. [28a]. Messler presents results of Lundin, which suggest δ_h also roughly ~75µm in SMO-stainless steel base metal / Hastelloy weld metal weld [4 Figure 12.7]. Based on these sources we use an estimate for the width of stagnant layer δ_h the value ~75µm.

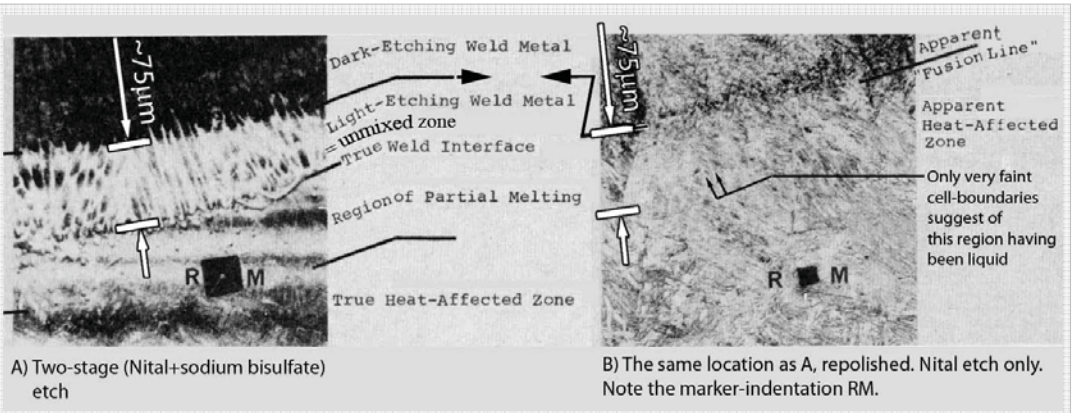

Fig. A42.1. Two micrographs of the same area produced with a "two-stage etch" **(a)**, and a normal "Nital-etch". The "two-stage etch" reveals two different zones in the weld metal: "Dark-Etching" and "Light-Etching". The latter consists of pure molten-and-solidified base metal. It is interpreted in this dissertation as the unmixed zone, caused by a *stagnant layer* next to what we call the *Weld Interface* (t the pool solidus). Savage, Nippes and Szekeres [28a].

*Note that the "True Weld Interface" marked in the figure **a)** refers to the weld pool liquidus, which we call Fusion Line in this dissertation. "Apparent Fusion Line" in Fig. **b)** refers to the line, which would easily have been miss-interpreted as a line between the weld- and base metals, had the special etch not revealed its true nature.*

Chapter A42.2. The *width of the concentration gradient (solute pileup)* ξ_{CG} related to δ_h = 75 µm:

The growth rate $\mathbf{R_{75\mu m}}$, giving the *width 75µm for the solute pileup* comes from:

$$\mathbf{R = 5\ D/\ \xi_{CG}} \qquad \text{(Eq. 2.5.12A rewritten)}$$

$$\mathbf{R_{75\mu m}} = \sim 5\ \mathbf{D/75\mu m}, \qquad \text{(Eq. A42.1)}$$

in which D=~$5 \cdot 10^{-5}$ cm^2/s [4 p.417]. The resulting $\mathbf{R_{75\mu m}}$ =~ 0.33 mm/s or ~2 cm/min. Areas of fusion welds with **R** less than this may have the leading nose of their concentration gradient cut off and mixed with the remaining melt by the weld pool currents. This *c*reates a *Sub-Case 3(-)[*δ_h/ξ_{CG}*]*, discussed briefly in the following.

Chapter A42.3. Leading nose of a concentration gradient (CG) cut-off in the occasion of insufficient stagnant layer width - *Sub-Case 3(-)[δ_h/ξ_{CG}]*.

If the stagnant layer is wider than the concentration gradient **CG**, the **CG** develops fully according the laws of diffusion and *Case 3* (Fig. A42.2A). If the **CG** is wider of the two – as in Fig. A42.2B, its leading nose is cut off and the fluid currents mix it evenly with the remaining melt, raising its concentration by a value **dC**. Increasing *CG cut-off* (in Fig. B) brings the solidification *Case number* down, towards the value *2*. This is an analytically solvable problem; the simplest **SCV** is obviously δ_h / ξ_{CG}, in which a value ≥ 1 corresponds to *Case 3*, and the value 0 to *Case 2*. The mathematical solution would be a *Sub-Case* of type *Sub-Case 3(-)[δ_h/ξ_{CG}]*. We do not attempt to model this mathematically.

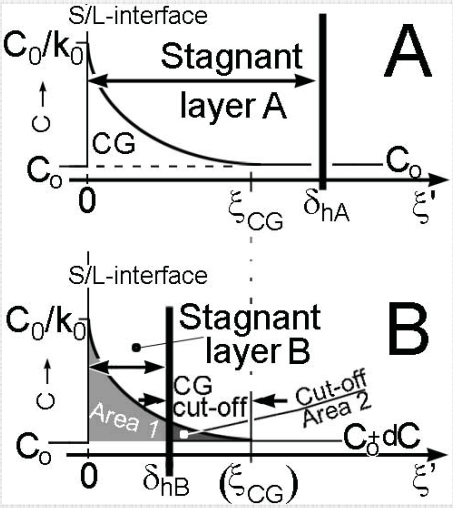

Fig. A42.2. Concentration gradient **CG** and two stagnant layers with different widths.
A): Stagnant layer width δ_{hA} > concentration gradient width ξ_{CG}.
B): $\delta_{hB} < \xi_{CG}$. The leading tip of the concentration gradient is cut off and mixed into the remaining melt, its concentration raises by the solute contained in the cut-off portion.
$\delta_{hB}=½\xi_{CG}$. However, the Cu-off area 2 is only ~10% of the total area of **CG**, *Area 1* = ~90% of the total.
Note. *This analysis illustrates the cutting-off of the solute concentration gradient only approximately. Rigorous mathematical model should consider the effect the steep vertical $dC/D\xi'$ at $\xi = \delta_{hB}$ exerts on the form of the remaining CG. Also the increase of $C_L=C_0+dC$ should be taken into account; this analysis is based on Case 3, but here C_L starts approaching the Case 2-regime; the term $(1-f_S)$, proportion of the remaining melt) should be included in the model. These correctives are ignored her; we limit to pointing out the principle.*

Analyzing Eq.2.5.13 and Fig. 42.2**B**, it can be shown, that even if one half of the **CG** is cut off, only < 10% of the solute of the total amount of solute of the CG is outside the stagnant layer and washed off into the remaining melt.

This approach assumes a constant stagnant layer width δ_h ~ 75 μm. The circumstances for the **CG** to grow wider than that come with slow **R** from Eq. 2.5.12A: $\xi_{CG}=5\ D/R$.

Attention must be paid to the fact that the *CG cut-off* phenomenon creates circumstances favoring *Case 2* over *Case 3*. This is essential for us, who advocate *Case 3* for weld solidification start. Our M/S-model is a *Case 3 Sub-Case*; should it turn out that the *Case 2* indeed controls the weld solidification start, much should be rethought of.

The relation of the **CG** width ξ_{CG} to the stagnant layer width δ_h is important, because without the stagnant layer there is no *Case 3* in the troubled weld pool. The stagnant layer does exist in welding; we know this from the existence of cells and dendrites. There is – however - a minimum **R**, below which *C*ase 3 may not be valid. The limiting **R**, in which the ξ_{CG} reaches the value 75μm, was found 2 cm/min in Ch. A42.2. In Fig. A4.2.2 we see that cutting the speed to one half (increasing ξ_{CG} to 2x75 μm) exposes only <10% of the solute in the **CG** to the pool currents, i.e. with **R**=1 cm/min, we have >90 % of the solute in the pileup. It is below the normal fusion welding speeds, but the problem is that every fusion weld starts with **R**= zero. We cannot rightfully say, which of the *Cases* starts the fusion weld solidification, and judging by the fact that there are models – the Lippold-Savage model (Fig. 2.25) and Koseki-model (Fig. 5.3) – advocating each, this question is open at the present.

Chapter A42.4. The new approach of Kou and Yang [124a-c, 2007] analyzes the stagnant layer near the fusion line **FL** and S/L-interface in much more refined way than we, who present an "on-off" change from 75 μm wide pure non-diffusion *stagnant layer* to a fully mixed weld metal ahead of this layer. Our purpose is to present the basic elements of solidification, and the *stagnant layer* for us is a tool to give reason for the existence of *Case 3* solidification. The mentioned above authoritative series of papers on weld convections corroborates the existence of the *unmixed zone*. In their state-of-the-art résumé the authors found them in various materials and welding methods with width from ~ 10 to150 μm, with an average not far from the ~ 75 μm reported by Savage.

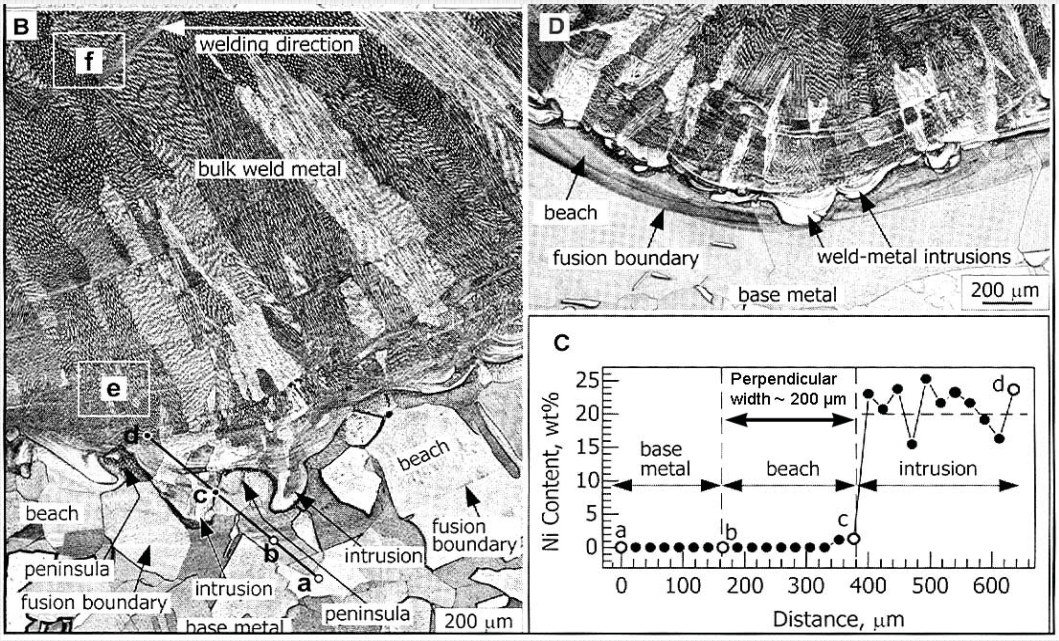

Fig. A42.3. Fusion boundary (base metal liquidus) areas of dissimilar-filler welds in copper welded with Cu-30 Ni. **B):** The higher liquidus temperature in the weld metal T_{LW} as compared with that of the base metal T_{LB} has caused *weld- metal intrusions* into the unmixed base metal *beaches* (of fully molten but unmixed base metal). **C)**: the concentration profile along **b-c** in Fig. **B** shows the complete lack of mixing of Ni from the weld metal. The perpendicular width of the unmixed *beach* is ~ 200 μm. **D):** A *weld-metal intrusion* has penetrated the unmixed *beach* to the fusion boundary. The figure consists of sections B, C and part of D from Kou, Yang 2007 [124]

Fig. A42.3 has some results of the work with dissimilar-filler welds, showing unmixed zones ~0 … ~ 200 mm wide. The authors do not hasten to accredit all for the *stagnant layer*, but even the latest studies suggest that such a layer exists.

- The unmixed zone does not always have an even width. In Fig. A42.3D it reduces locally to ~ zero. A remotely analogous phenomenon is referred to in Fig. 1.32. Our assumption of a 75 μm wide stabile stagnant layer is obviously a rough approximation.

- Often the solidification study is started from the fusion line (liquidus), we start from the base metal solidus, weld interface. The peninsulas and archipelago of islands of solid base metal in the partially melted zone probably form better an environment for a stagnant layer than does the FL, bordering the open weld pool with fluid currents running more freely.

Therefore - even with some still open questions - there is evidence supporting the proposal of *Case 3* or its *Sub-Cases* ruling the longitudinal solidification from the weld interface until the final transient, where *Case 2* and its *Sub-Cases* may take over. The perpendicular solidification of needle-tip cells and dendrites also may end with *Case 2*. The joining of these two *Cases* or *Sub-Cases* – to preserve the solidification continuum from start to end - is a demanding modeling problem still waiting its solution.

Appendix 43. The Lausanne- and RPI-approaches at cell centerline

Kurz & Fisher – central actors of the Lausanne-approach - analyze the $\mathbf{C_L}$ at dendrite tip, as the tip transforms from blunt to needle-like in Fig. 2.33. We added $\mathbf{C_S}$ – assuming *microscopic equilibrium* – to this figure, and present the thus modified result in Fig. A43**C**.

It is worth noticing that both the $\mathbf{C_L}$ and the $\mathbf{C_S}$ of Fig.A43**C** follow the pure *Case 3*-regime. The Kurz & Fisher-analysis, starting with *Sub-Case 2(+)CG*, ends up identical with the *Case 3*-based analysis of Savage et al., presented in the Fig's A43**A** and **B;** the condition $\mathbf{C_{S(tip)}=k_0C_0}$ is valid in both analyses. This implies that **Ω=1** (Fig. 2.29, Ch.2.8.5 and Appendix 41) in the range $\mathbf{R_3<R<Ra'}$ in Fig. A43**C.**[30]. The Lausanne-and RPI-approaches come to the same result via different initial conditions.

The Fig.A.43**C** is limited to the cell centerline, and the identicalness of the approaches is rigorously proven only on that centerline. However, both approaches recognize the probability of the perpendicular cell growth occurring with the Case 2-regime; the *Lausanne line* in e.g. [5 p. 122-] and the *RPI-line* in e.g. [11 p. 163]. Therefore, the identicalness of the two approaches is clear in the range of Fig. A43**C**, which extends from $\mathbf{R=R_3}$.to $\mathbf{R=Ra'}$

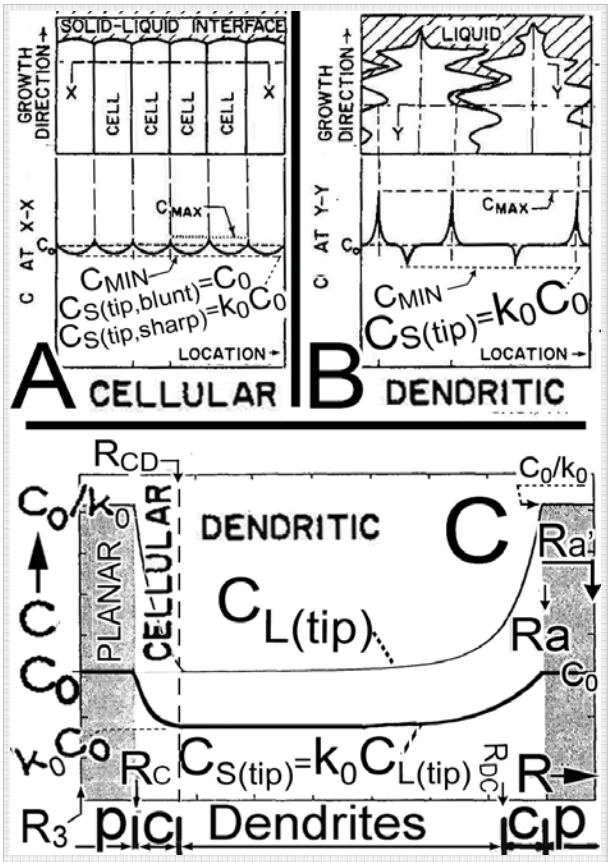

Fig. A43. Comparison of the *Sub-Case 2(+)CG*-based Kurz & Fisher analysis of the cell/dendrite tip concentration (lower, **C**) with the *Case 3*-based Savage et al. analysis of the concentration along the cell/dendrite tip (upper, **A** and **B**). At the cell tip, the analyses are identical and fulfill the *Case 3*-prerequisites.
Adapted from**: A** and **B;** Savage et al. [31], **C;** Kurz & Fisher [5 p. 81].

Résumé of this Appendix: Much of this dissertation handles the differences of what we call the Lausanne- and the RPI-approaches; the first starting from *Case 2* (the Gulliver-Scheil equation), the latter starting from *Case 3*. Fig. A43 shows that the approaches end up identical. This figure suggests the validity of *Case 3* in the growth rate range $\mathbf{R_3 < R < Ra'}$. R3

The two research lines come to as good as an identical solution despite their distinctly different starting points, at least in the range of solidification handled in Fig. A43**C**. The solution is obviously the *Case 3* solution.

[30] Here is a minor discrepancy: Fig. A43**A** allows for sharp cell tips having $C_S=k_0C_0$, while Fig A43**C** limits $C_S=k_0C_0$ only for dendrites. This is ignored here.

Slow growth rate. The start of fusion weld solidification (with $\mathbf{R<R_3}$) is outside the range of Fig. 43A and the discussion above in this Appendix. There, the validity of *Case 3* can be questioned. The width of the concentration gradient ξ_{CG} may be less than the width of the stagnant layer δ_h. There a $\mathbf{\Omega<1}$ solution may become the only possible (Ch. A42.3). In this occasion, the question is, at what point does the solidification turn from *Sub-Case 2 (+)CG* to *Case 3* (Ch.5.6.6). In other words, if indeed, the fusion weld solidification starts with *Sub-Case 2 (+)CG*, at what **R** does the $\mathbf{\Omega}$ rise up to value **1** to allow for the process depicted in Fig. A43G. This question is open, and for its answer, both approaches are needed.

In this dissertation we assume that the ratio δ_h / ξ_{CG} does not go under unity in longitudinal solidification of fusion welds. We even propose the *Case 3*-based *M/S-model*, which must be redesigned if our assumption is incorrect. This area is under vivid research [124a…c]. If our assumption proves wrong, we must do the corrections outlined in Appendix 42.

Fast growth rate. The *Lausanne research line* does invaluable study in the fast solidification range approaching the *marginal stability limit* at $\mathbf{R>R_{DC}}$ in Fig's A43**C** and 5.4. The analysis of Fig. A43 raises the question of the need of the *Gulliver-Scheil*-based *Sub-Case 2 (+)CG*-model in this range. The problem of the term $\mathbf{\Omega}$ would be omitted by using the *Case 3*–initial conditions and model. This would also render the analysis a direct continuation of the *Mullins & Sekerka*–analysis, which is based on pure *Case 3*.

ACTA UNIVERSITATIS LAPPEENRANTAENSIS

258. LIU, JUNHONG. On the differential evolution algorithm and its application to training radial basis function networks. 2006. Diss.

259. LAITINEN, RISTO. Development of LC-MS and extraction methods for the analyses of AKD, ASA, and rosin sizes in paper products. 2006. Diss.

260. KUISMA, PETRI. Seinärakenteen infrapunakontrastin pienentäminen käyttäen ilmajäähdytystä ja säteilysuojausta. 2007. Diss.

261. ELLONEN, HANNA-KAISA. Exploring the strategic impact of technological change – studies on the role of Internet in magazine publishing. 2007. Diss.

262. SOININEN, AURA. Patents in the information and communications technology sector – development trends, problem areas and pressures for change. 2007. Diss.

263. MATTILA, MERITA. Value processing in organizations – individual perceptions in three case companies. 2007. Diss.

264. VARTIAINEN, JARKKO. Measuring irregularities and surface defects from printed patterns. 2007. Diss.

265. VIRKKI-HATAKKA. TERHI. Novel tools for changing chemical engineering practice. 2007. Diss.

266. SEKKI, ANTTI. Successful new venturing process implemented by the founding entrepreneur: A case of Finnish sawmill industry. 2007. Diss.

267. TURKAMA, PETRA. Maximizing benefits in information technology outsourcing. 2007. Diss.

268. BUTYLINA, SVETLANA. Effect of physico-chemical conditions and operating parameters on flux and retention of different components in ultrafiltration and nanofiltration fractionation of sweet whey. 2007. Diss.

269. YOUSEFI, HASSAN. On modelling, system identification and control of servo-systems with a flexible load. 2007. Diss.

270. QU, HAIYAN. Towards desired crystalline product properties: In-situ monitoring of batch crystallization. 2007. Diss.

271. JUSSILA, IIRO. Omistajuus asiakasomisteisissa osuuskunnissa. 2007. Diss.

272. 5th Workshop on Applications of Wireless Communications. Edited by Jouni Ikonen, Matti Juutilainen and Jari Porras. 2007.

273. 11th NOLAMP Conference in Laser Processing of Materials Lappeenranta, August 20-22, 2007. Ed. by Veli Kujanpää and Antti Salminen. 2007.

274. 3rd JOIN Conference Lappeenranta, August 21-24, 2007. International Conference on Total Welding Management in Industrial Applications. Ed. by Jukka Martikainen. 2007.

275. SOUKKA, RISTO. Applying the principles of life cycle assessment and costing in process modeling to examine profit-making capability. 2007. Diss.

276. TAIPALE, OSSI. Observations on software testing practice. 2007. Diss.

277. SAKSA, JUHA-MATTI. Organisaatiokenttä vai paikallisyhteisö: OP-ryhmän strategiat institutionaalisten ja kilpailullisten paineiden ristitulessa. 2007. Diss.

278. NEDEOGLO, NATALIA. Investigation of interaction between native and impurity defects in ZnSe. 2007. Diss.

279. KÄRKKÄINEN, ANTTI. Dynamic simulations of rotors during drop on retainer bearings. 2007. Diss.

280. KARPOVA, TATJANA. Aqueous photocatalytic oxidation of steroid estrogens. 2007. Diss.

281. SHIPILOVA, OLGA. Particle transport method for convection-diffusion-reaction problems. 2007. Diss.

282. ILONEN, JARMO. Supervised local image feature detection. 2007. Diss.

283. BOTAR-JID, CLAUDIU CRISTIAN. Selective catalytic reduction of nitrogen oxides with ammonia in forced unsteady state reactors. Case based and mathematical model simulation reasoning. 2007. Diss.

284. KINNUNEN, JANNE. Direct-on-line axial flux permanent magnet synchronous generator static and dynamic performance. 2007. Diss.

285. VALTONEN, MIKKO. Performance characteristics of an axial-flux solid-rotor-core induction motor. 2007. Diss.

286. PUNNONEN, PEKKA. Impingement jet cooling of end windings in a high-speed electric machine. 2007. Diss.

287. KÄRRI, TIMO. Timing of capacity change: Models for capital intensive industry. 2007. Diss.

288. TUPPURA, ANNI. Market entry order and competitive advantage of the firm. 2007. Diss.

289. TARKIAINEN, ANSSI. Field sales management control: Towards a multi-level theory. 2007. Diss.

290. HUANG, JUN. Analysis of industrial granular flow applications by using advanced collision models. 2007. Diss.

291. SJÖMAN, ELINA. Purification and fractionation by nanofiltration in dairy and sugar and sweetener industry applications. 2007. Diss.

292. AHO, TUOMO. Electromagnetic design of a solid steel rotor motor for demanding operation environments. 2007. Diss.

293. PURHONEN, HEIKKI. Experimental thermal hydraulic studies on the enhancement of safety of LWRs. 2007. Diss.

294. KENGPOL, ATHAKORN. An evaluation of ICTs investment using decision support systems: Case applications from distributor´s and end user´s perspective group decision. 2007. Diss.

295. LASHKUL, ALEXANDER. Quantum transport phenomena and shallow impurity states in CdSb. 2007. Diss.

296. JASTRZĘBSKI, RAFAŁ PIOTR. Design and implementation of FPGA-based LQ control of active magnetic bearings. 2007. Diss.

297. GRÖNLUND, TANJA. Development of advanced silicon radiation detectors for harsh radiation environment. 2007. Diss.

298. RUOKONEN, MIKA. Market orientation in rapidly internationalizing small companies – evidence from the software industry. 2008. Diss.

299. OIKARINEN, TUIJA. Organisatorinen oppiminen – tapaustutkimus oppimisprosessien jännitteistä teollisuusyrityksessä. 2008. Diss.

300. KARHULA, JUKKA. Cardan gear mechanism versus slider-crank mechanism in pumps and engines. 2008. Diss.